A multi-technique investigation of the effect of hydration temperature on the microstructure and mechanical properties of cement paste

Sara Bahafid

UNIVERSITÉ PARIS-EST

École des Ponts ParisTech

Thèse présentée pour obtenir le grade de

Docteur de l'Université Paris-Est

Spécialité: Génie Civil

par

Sara Bahafid

Ecole Doctorale :Sciences, Ingénierie et Environnement

A multi-technique investigation of the effect of hydration temperature on the microstructure and mechanical properties of cement paste

Thèse soutenue le 27/11/2017 devant le jury composé de:

Pr. Bernhard Pichler	*Rapporteur*
Dr. Jean-Baptiste D'ESPINOSE de LACAILLERIE	*Rapporteur*
Pr. Peter McDonald	*Examinateur*
Dr. Thierry Chaussadent	*Examinateur*
Dr. Mateusz wyrzykowski	*Examinateur*
Dr. Myriam Duc	*Examinatrice*
Pr. Jean Sulem	*Directeur de thèse*
Dr. Siavash Ghabezloo	*Co-encadrant de thèse*
Dr. Paméla Faure	*Co-encadrante de thèse*

سورة طه [20:114]

And say, “ O My Lord!
increase my Knowledge”

Surah Taha [20:114]

Pour ma chère mère, elle saura
pourqoui! Et à toute ma
famille…

Abstract

Sara BAHAFID

A multi-technique investigation of the effect of hydration temperature on the microstructure and mechanical properties of cement paste

The cement hydration process and the resulting microstructure are highly dependent on the cement formulation and the hydration conditions. Particularly, the hydration temperature has a significant influence on the cement paste microstructure and its mechanical properties. This is for instance important for understanding the behaviour and properties of oil-well cements which are used to form a cement sheath between the casing and the surrounding formation for stability and sealing purposes. This cement sheath is hydrated under a progressively increasing temperature along the depth of a well due to the geothermal gradient (about 25 °C/km). It results generally in a decrease of the mechanical properties and an increase of permeability along the well. The aim of the present thesis is to investigate the effect of the hydration temperature in the range of 7 °C to 90 °C on the microstructure of a class G cement paste and to establish the link between these temperature dependent microstructure and the elastic properties of the material. The microstructure characterization is done by combining various experimental methods, including X-Ray diffraction associated with the Rietveld analysis, thermogravimetric analysis, mercury intrusion porosimetry, porosity evaluation by freeze-drying or drying at 11% RH, Nitrogen and water vapour sorption experiments and finally ^{1}H nuclear magnetic resonance. The mass assemblage of microstructure phases at different curing temperatures has been evaluated and showed a slight dependence on the hydration temperature. The porosity evaluations show an increase of the capillary porosity and a slight decrease of the total porosity at 28 days, resulting in a decrease of the gel porosity by increasing the hydration temperature. An analysis method has been proposed to evaluate the C-S-H saturated density and chemical composition in terms of H/S and C/S molar ratios. The C-S-H bulk density is increasing with increasing hydration temperature which explains the observed increase of the capillary porosity for higher curing temperatures. The C/S ratio and H/S ratio for both solid and saturated C-S-H are decreasing with increasing curing temperature. The provided quantitative characterization of cement paste microstructure is used in a micromechanical modelling for evaluation of its elastic properties at various hydration temperatures. Two and three-scale self-consistent micromechanical models have shown that the increase of capillary porosity with increasing hydration temperature cannot fully explain the drop of elastic properties. This is mainly due to the increased elastic properties of C-S-H being denser at higher temperature that cancel

the effect of increasing capillary porosity on the overall elastic properties. Another way to fully account for the decrease of the mechanical properties of cement paste is to consider the porosity distribution inside the C-S-H in the form of two distinguished C-S-H types, High Density (HD) and Low Density (LD) C-S-H, as proposed by Tennis and Jennings (2000). This possibility is probed by a combination of various porosity evaluations: Mercury intrusion porosimetry, Nitrogen desorption and water vapour desorption and by a back calculation using micromechanical modelling. The results show that the LD intrinsic porosity is slightly increasing while the HD intrinsic porosity decreases significantly with increasing hydration temperature. The decrease of the elastic properties of cement based materials with increasing hydration temperature is therefore a combined action of the increase of capillary porosity and the changes of intrinsic C-S-H porosities.

Résumé

Sara BAHAFID

Etude multi-technique de l'effet de la température d'hydratation de ciment sur la microstructure et les propriétés mécaniques de la pâte de ciment

Le processus de l'hydratation du ciment et la microstructure qui en résulte, dépendent des conditions au moment de la formulation et de l'hydratation. La température d'hydratation a un effet particulier sur la microstructure et les propriétés physiques et mécaniques des pâtes cimentaires. Ceci est particulièrement important pour l'étude du comportement des ciments pétroliers. En effet, dans un puits pétrolier, une gaine de ciment est coulée entre la roche réservoir et le cuvelage en acier pour assurer entre autre la stabilité et l'étanchéité des puits pétroliers. En raison du gradient géothermique, la gaine de ciment le long d'un puits est exposée à une température d'hydratation qui augmente avec la profondeur menant à une augmentation de perméabilité et une baisse de propriétés mécaniques et mettant en péril les fonctions de la gaine de ciment. L'objectif cette thèse est d'étudier l'effet de la température d'hydratation dans la gamme de 7 °C à 90 °C sur la microstructure d'une pâte de ciment (classe G) et d'établir le lien entre les modifications microstructurales et les variations des propriétés élastiques de cette pâte. L'analyse de la microstructure est basée sur une combinaison de plusieurs méthodes expérimentales, à savoir, la diffraction des rayons X, l'analyse Rietveld, l'analyse thermogravimétrique, l'intrusion au mercure, l'évaluation de la porosité totale par lyophilisation ou par séchage à 11% HR, essais de sorption à l'Azote et à la vapeur d'eau et finalement, la résonance magnétique nucléaire au proton ^{1}H NMR. Les résultats montre que l'assemblage de phases est légèrement modifié par la température d'hydratation. L'étude de la porosité a montré une augmentation de la porosité capillaire et une légère diminution de la porosité totale à 28 jours d'hydratation, ce qui résulte en une diminution de la porosité du gel C-S-H en augmentant la température d'hydratation. Une méthode d'analyse a été proposée pour évaluer la densité du C-S-H saturé et les rapports molaires C/S et H/S pour un C-S-H solide et saturé. Les résultats montrent que la densité de C-S-H augmente avec la température d'hydratation expliquant ainsi l'augmentation observée de la porosité capillaire à températures élevées. Les rapports C/S et H/S pour le C-S-H solide diminuent avec la température. La caractérisation de la microstructure a permis d'alimenter un modèle micromécanique destiné à

prédire les propriétés élastiques de la pâte de ciment pour différentes températures d'hydratation. Des modèles d'homogénéisation auto-cohérents à double et trois échelles ont prouvé que l'augmentation de la porosité capillaire ne suffit pas pour expliquer la baisse des propriétés mécaniques avec la température. En effet, l'augmentation de la température résulte en un C-S-H dense et rigide qui annule l'effet de l'augmentation de la porosité capillaire avec la température sur les propriétés élastiques. La réduction des propriétés mécaniques pourrait être expliquée en considérant une distribution de porosité au sein de C-S-H sous forme de C-S-H basse densité LD et haute densité HD telle que proposée par Tennis and Jennings (2000). Cette possibilité est investiguée par une combinaison de techniques de porosimétrie: porosimétrie d'intrusion de mercure, adsorption d'Azote et désorption de vapeur d'eau et via la modélisation micromécanique. Les résultats montrent que la porosité intrinsèque LD augmente légèrement tandis que la porosité intrinsèque HD diminue de manière significative avec l'augmentation de la température d'hydratation. La perte d'élasticité des matériaux à base de ciment avec l'augmentation de la température d'hydratation s'avère être due à l'action combinée de l'augmentation de la porosité capillaire et des changements de porosités intrinsèques des C-S-H.

Acknowledgements

Arrivée à la partie la plus personnelle d'une thèse, destinée à remercier toutes les personnes ou institutions qui ont contribué de près ou de loin à la réussite de cette thèse.

Ce travail a bénéficié d'une aide de l'état gérée par l'ANR au titre du programme des Investissements d'Avenir ANR-11-LABX-022-01. Je remercie le Labex MMCD d'avoir financé cette thèse. Sans cette aide financière et le caractère fondamental du Labex, ce travail n'aurait pas vu le jour.

Je tiens à remercier très chaleureusement les membres de jury qui ont accepté d'examiner mon mémoire. Je remercie particulièrement Pr. Bernhard Pichler et Pr. Jean Baptiste d'Espinose de Lacaillerie d'avoir rapporté ce travail. Votre relecture méticuleuse et vos questions pertinentes m'ont permis de bien préparer ma soutenance. Je remercie Dr. Thiery Chaussadent d'avoir présidé mon jury de thèse. Je remercie également Pr. Peter McDonald et Dr. Mateusz Wyrzykowski d'avoir examiné mon travail et pour les discussions très enrichissantes qu'on a eu. Merci aux membres de Jury, grâce vous cette expérience était riche en apprentissage jusqu'au dernier moment.

Je tiens à adresser les plus sincères remerciements à mon directeur de thèse, Pr. Jean Sulem, pour m'avoir accordé cette responsabilité, pour sa disponibilité et ses qualités humaines sans pareilles. J'adresse le même niveau de remerciement à mon encadrant, Dr. Siavash Ghabezloo, qui m'a suivi de près tout au long de cette expérience. Ce fut un grand plaisir de travailler avec Dr. Ghabezloo. Son amour dévoué pour la recherche, son esprit pédagogue et curieux, sa rigueur et ses questions très pertinentes, ont bousculé ma vision pour le monde de la recherche. Je ne passerai pas sans mentionner que ses qualités humaines ont rendu le travail durant ses trois années très agréable. Merci Siavash pour tout ce que tu m'as appris ! Je remercie sincèrement mon encadrante, Dr. Paméla Faure pour ses compétences scientifiques et l'enthousiasme qu'elle a apporté à ce travail. La confiance qu'elle avait en moi me réconfortait dans les moments les plus difficiles. Son expertise dans la RMN et ses expériences larges sur divers matériaux sont derrière le regard critique qu'elle avait pour ce travail. Je peux clairement dire que j'ai été chanceuse d'avoir eu un encadrement pareil, alliant compétences scientifiques du haut niveau et qualités humaines exceptionnelles. Merci pour ce sujet intéressant que vous avez proposé, pour votre temps, vos remarques, vos conseils et directives, votre enthousiasme à l'égard des résultats. Les mots me manquent pour exprimer ma gratitude à vous chers encadrants.

Cette thèse est en grande partie expérimentale. Il est clair que sans le soutien de plusieurs personnes compétentes dans diverses techniques expérimentales, ce travail

n'aurait pas été possible. Un grand merci à Dr. Myriam Duc pour sa patience, ses conseils et remarques très pertinentes sur le ciment en général et sur la XRD en particulier. Merci Myriam d'avoir mis à ma disposition plusieurs outils de ton laboratoire. Merci à Julien Vincent et à Dr. Mikael Thierry pour les essais d'analyses thermogravimétriques. Merci pour votre temps, votre organisation, et d'avoir toujours respecté les deadlines. Merci à Nadia Dominique pour les essais d'adsorption à l'azote. Je remercie également Jean Marc Plessier pour son aide et le temps passé sur les essais de Nano-indentation dont les résultats ne sont malheureusement pas présentés ici. Ce n'est qu'une partie remise. Et bien sûr, je remercie toute l'équipe technique du CERMES, Emmanuelle, Hocine, Baptiste, Marine, Xavier, Loïc, pour leurs disponibilités et leurs aides précieuses.

Je tiens également à remercier tout le laboratoire Navier et en particulier l'équipe géotechnique 'CERMES', qui offrent des conditions idéales de recherche en milieu académique mais aussi un environnement de travail propice et une ambiance exceptionnelle. Je n'oublierai jamais toutes ses discutions scientifiques enrichissantes qu'on a eu, ni les pots et les pauses cafés très agréables.

Mes remerciements vont également à mes amis et mes collègues. Merci à Zineb Abchir, Radja El Andaloussi, Layal Jradi, Youssef Abdullah, Sadek Feia, Yaghkob ikezouhene, Malik Belmekhtar, Katia Bellagh, Nicholas Collins Craft. Je n'oublierai jamais nos discutions autour des pauses café qui m'ont toujours fait voyager. Merci à Mouna Rifi, Amal Hriouech, Yassine El Assami, et beaucoup d'EHTPistes qui ont fait que mon passage à Paris soit agréable. Merci à Marcos Samudio et Hafsa Rahoui « cement guys! ». C'était très agréable d'avoir un collègue du Bureau qui parle le même langage cimentaire que toi et porte un grand enthousiasme pour ton travail et qui veux aussi comprendre le C-S-H. Merci à Hafsa qui comme Marcos, était à fond dans le ciment. Merci, pour ton sourire, ton optimisme et ton amitié. Je n'oublierai pas nos discussions de la signification des résultats de BET autour de tes délicieux tajines. On les comprendra un jour ces résultats ! Je te souhaite bon courage pour ta thèse ;). Merci à l'emblème de l'école des Ponts, Jeanine, qui sans son café la rédaction de cette thèse n'aurait pas été possible!

Mes remerciements ne peuvent s'achever sans une pensée pour mes parents, mes frères et sœurs (Souhayl, Hassan, Ghita). Leurs encouragements, amour, et présence ont été essentielles pour entamer cette phase de ma vie et la vivre le plus aisément possible. Particulièrement à ma mère Fatima El Harmassi qui m'a toujours poussé à donner le meilleur de Moi et a fait ce que je suis aujourd'hui.

Et si c'était à refaire ça serait avec plaisir !

Champs sur Marne, 27/11/2017

Sara

Contents

List of Figures

List of Tables

List of Abbreviations

Cement chemistry notation	
C	CaO
S	SiO_2
A	Al_2O_3
F	Fe_3O_3
$\bar{S}$	SO_3
H	H_2O
$\bar{C}$	CO_2
Cement phases	
C_3S	**T**ri calcium **S**ilicate
C_2S	**D**i calcium **S**ilicate
$C-S-H$	**C**alcium **S**ilicate **H**ydrate
CH	**C**alcium **H**ydroxide
$C_6A\bar{S}_3H_{32}$	**E**ttringite
$C_4A\bar{S}H_{12}$	**A**fm (Monosulfo-aluminate)
C_3AH_6	**Fe**-Siliceous hydrogarnet
$C_3(A,F)S_{0.84}H_{4.32}$	**H**ydrogarnet
$CaCO_3$	**C**alcite
Experiments and methods	
NMR	**N**uclear **M**agnetic **R**esonance
MIP	**M**ercury **I**ntrusion **P**orosimetry
XRD	**X** **R**ay **D**iffraction
TGA	**T**hermogravimetry **A**nalysis
SEM	**S**canning **E**lectron **M**icroscopy
BSE	**B**ack **S**cattered **E**lectrons
WVS	**W**ater **V**apor **S**orption
TEM	**T**ransmission **E**lectron **M**icroscopy
BJH	**B**arrett **J**oyner **H**alenda
BET	**B**runauer **E**mmett **T**eller
SANS	**S**mall **A**ngle **N**eutron **S**cattering
SAXS	**S**mall **A**ngle **x**-ray **S**cattering
IR	**I**nversion **R**ecovery
SR	**S**aturation **R**ecovery
CPMG	**C**arr **P**urcell **M**eiboom **G**ill
Other notations	
SSA	**S**pecific **S**urface **A**rea
RH	**R**elative **H**umidity
HD	**H**igh **D**ensity
LD	**L**ow **D**ensity

Chapter 1

Context and motivations

Cement is a widely manufactured and consumed material due to its cheap price, easy manufacturing and high mechanical properties. Particularly, it is widely used in the petroleum industry. During the process called primary cementing, a cement slurry is pumped to fill the annular space between the casing and the wellbore as presented in Figure 1.1. This cementing operation is very crucial in ensuring a well integrity during and after drilling. After cement set, the cement sheath has to ensure three important roles [1, 2]:

- Providing zonal isolation: This the most imperative role of a cement sheath. It consists in preventing fluids such as gas and water in one zone to be mixed with oil from another zone.
- Protecting the casing against corrosion: Cement sheath prevents fluids from the surrounding formation to reach the casing and hence, prevents its corrosion.
- Providing mechanical support for the casing.

During the life of an oil well the cement sheath is subjected to various mechanical and thermal loading endangering the well integrity during its exploitation and also after its abandon. Furthermore, when the cement slurry is pumped, it is hydrated under various environmental conditions. For instance, due to the geothermal gradient (about 25 °C per km) the cement sheath along a well is exposed to an increasing hydration temperature with depth. This causes a material potentially different in terms of its mechanical behaviour and its permeability along the well. It is well established that the mechanical properties of a cement paste are decreasing with increasing the hydration temperature [1]. The decrease of cement paste mechanical properties endangers the supporting functions of the cement sheath. The permeability also shows an increase with the increasing hydration temperature threatening the zonal isolation and the casing safety. The understanding and the modelling of the influence of temperature and pressure variation on the mechanical properties of a fresh and hardened cement paste has been a subject of research in Navier laboratory for several years. In the previous studies, the thermo-poro-mechanical and time dependent properties of cement paste have been evaluated experimentally [3–8]. The evaluated parameters have then been extrapolated to cement pastes with various W/C ratio and chemical composition using micromechanical modelling and homogenization methods [9–12]. The quantitative description of the microstructure is an essential input for micromechanical

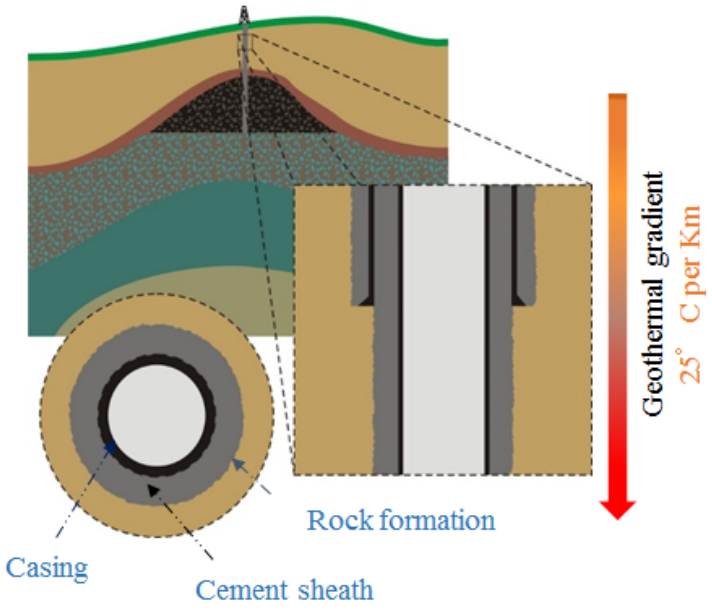

FIGURE 1.1: Cross Section of an Oil Well

modelling. Various approaches, for instance Powers and Brownyard [13] model or Tennis and Jennings [14] model provided a quantitative description of cement paste microstructure phases for various clinker compositions and water to cement ratio. These quantitative models of cement hydrates can only handle changes of the clinker chemical composition, the water to cement ratio and the hydration degree. The temperature and pressure effects on the microstructure are not considered in these models. Additionally, the decreasing mechanical properties and increasing permeability indicate that various changes occur at the level of the microstructure when the hydration temperature is increased. The essential motivation of this work is then to conduct a quantitative description of the microstructure in order to gain a better understanding on the influence of hydration temperature on the cement paste mechanical properties. Primordially, the volume assemblage has to be established for different curing temperatures. Therefore different experimental methods are used to characterise the mass assemblage of a cement paste. However, the values of C-S-H densities, that will help determining the volume assemblage at different curing temperatures are scarce in literature. This motivates a better and a fundamental understanding of the porosity variation within the C-S-H at increasing curing temperature. Along this manuscript, we will address two principal questions:

- How does the microstructure of cement in terms of chemical composition and pore structure evolve with increasing curing temperature for a class G cement?
- What are the origins behind the decline of the cement paste mechanical properties with increasing hydration temperature?

This manuscript is structured in five chapters after this one:

- Chapter 2: In this chapter, first a general introduction to the hydration of cementitious materials is presented. The essential parameters characterising the

C-S-H are recalled and discussed on the basis of different models describing C-S-H. Secondly, the main findings about the effect of temperature variation on the microstructure of cement paste and particularly of the C-S-H structure are reviewed. Finally, we present a review on the application of the homogenization techniques used to study poro-elastic properties of cementitious materials.

- Chapter 3: The material and methods used in the experimental investigation will be presented in this chapter. We will focus also on the choice of the drying method used prior to microstructural analysis. The method used to dry specimens in this study is compared to other available drying methods.
- Chapter 4: This chapter deals with the quantitative description of the mass assemblage of cement paste at different curing temperatures and also different ages. It focuses also on the description of the pore structure variation of cement paste at different hydration temperatures and ages.
- Chapter 5: This chapter concentrates on the analysis of the porosity results and phase assemblage obtained from Chapter 4 to determine the C-S-H chemical composition and density variations with curing temperature and time. The micromechanical modelling is used at this step in order to gain insight on the influence of temperature on the C-S-H pore structure and to explain the mechanisms behind deterioration of the mechanical properties of cementitious materials with increasing hydration temperature.
- Chapter 6: The conclusions are presented in chapter 6 together with the perspectives of this work.

Chapter 2

Litterature review

2.1 Introduction

This chapter presents an overview on the existing literature on the microstructure of cement. It first describes the leading chemical reactions between cement and water and the resultant hydration products. Secondly, the different models describing the cement porosity and explaining related phenomena are presented and discussed. The investigation of the cement microstructure and the properties related to, such as the total porosity and the specific surface area are very sensitive to the drying conditions. A review of different drying techniques is presented outlining the advantages and the drawbacks of each method in the evaluation of a given property. An overall comparison is then conducted to choose an appropriate drying method for the different experimental techniques that are going to be used in this study.

The present study aims primarily at describing quantitatively the effect of temperature on the microstructure of cement paste. Hence, a state of art on the effect of the curing temperature on the chemical composition, the pore structure and the mechanical properties is presented. Based on the quantitative description of the cement microstructure, micromechanical modelling is used in order to explore the degradation of mechanical properties at high temperatures. The necessary theoretical background for micromechanical analysis together of some application of the homogenization method are presented at the end of this chapter.

2.2 Cement hydration

The hardened cement paste results from the complex reactions of the four main clinker components namely alite (C_3S), belite (C_2S), celite (C_3A) and ferrite (C_4AF) with water, where C, S, A and F are abbreviations corresponding respectively to CaO, SiO_2, Al_2O_3 and Fe_3O_3. Cement grains develop interactions with the interstitial fluid resulting in dissolution of cement grains followed by precipitation of hydrates on the surface of grains [15]. Progressively, through these dissolution-precipitation reactions, hydrates form and replace the space initially occupied by grains and water. Hydrates first precipitate and cover the surface of cement grains and further grow into the available space [15, 16]. This process is schematically presented in Figure 2.1.

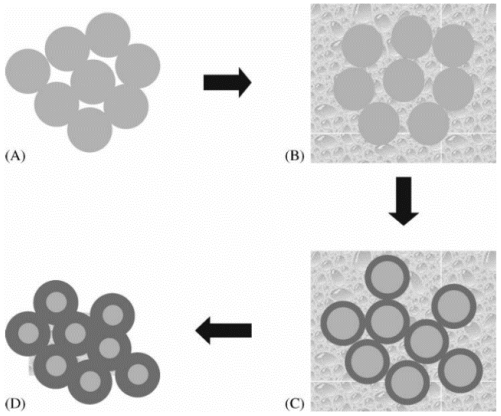

FIGURE 2.1: Representation of dissolution precipitation reactions of anhydrous grains with interstitial water [15]

The chemical reactions involved in dissolution-precipitation mechanisms translating the complex transformation of a cement slurry into a hardened cement paste are presented in the following for each clinker component.

2.2.1 C_3S and C_2S hydration

Reactions of C_3S and C_2S following Equations 2.1 and 2.2 [17] describe the hydration of the two major clinker components that occupy 80% of anhydrous cement mass. These reactions result in the development of C-S-H (calcium silicate hydrate) and CH (calcium hydroxide mineral) which occupy approximately 80% of hardened cement paste mass. The x and y, respectively C/S and H/S ratios are intrinsic characteristic to the C-S-H. These reactions are only approximate because x and y are variables and depend on the hydration conditions (P, T, W/C, RH), the age, the particle size, additives and the presence supplementary cementing materials. These two ratios characterizing the C-S-H will be addressed in Sections 2.4.1 and 2.4.2.

$$C_3S + (3 - x + y)\,H \rightarrow C_x{-}S{-}H_y + (3 - x)\,CH \tag{2.1}$$

$$C_2S + (2 - x + y)\,H \rightarrow C_x{-}S{-}H_y + (2 - x)\,CH \tag{2.2}$$

2.2.2 C_3A and C_4AF hydration

The hydration reactions of C_3A and C_4AF presented in 2.3 and 2.4 [18] are more complex than the ones of C_3S andC_2S. The hydrates formed from the hydration of C_3A depend on the presence of sulphate ions. When C_3A is hydrated in pure water, the hydration product is hydrogarnet C_3AH_6. This reaction releases a considerable amount a heat and causes a flash set of cement without any gain of mechanical properties. This undesirable effect has been overcome by the addition of gypsum $C\bar{S}H_2$ which changes the reaction and creates ettringite instead of hydrogarnet. When the sulfate ions are depleted, the ettringite becomes unstable and converts to other phases with less sulphate ions, mainly monosulfoaluminates, Afm. In a cement paste these phases can coexist simultaneously.

$$\begin{cases} 2C_3A + 21H \rightarrow C_4AH_9 + C_2AH_8 \rightarrow 2C_3AH_6 + 9H & \text{No sulfates} \\ 2C_3A + 3C\bar{S}H_2 + 26H \rightarrow C_6A\bar{S}_3H_{32} & \text{With sulfates} \\ 2C_3A + C_6A\bar{S}_3H_{32} + 4H \rightarrow 3C_4A\bar{S}H_{12} & \text{Sulfates depletion} \end{cases} \tag{2.3}$$

The C_4AF behaves in a similar manner to C_3A. It creates ferrite-ettringite ($C_6(A,F)\bar{S}_3H_{32}$) which is similar to ettringite, but this time some aluminium is replaced by iron in variable amounts as indicated by the brackets (A,F). The $(F,A)H_3$ is aluminium-iron hydroxide, an amorphous phase that can be also found in a cement paste.

$$\begin{cases} C_4AF + 3C\bar{S}H_2 + 21H \rightarrow C_6(A,F)\bar{S}_3H_{32} + (F,A)H_3 & \text{With sulfates} \\ C_4AF + C_6(A,F)\bar{S}_3H_{32} + 7H \rightarrow 3C_4(A,F)\bar{S}_3H_{12} + (F,A)H_3 & \text{Sulfates depletion} \end{cases} \tag{2.4}$$

2.2.3 Hydration kinetics

As stated above, the hydration of cement is regarded as process of subsequent dissolution precipitation steps. These different hydration processes are accompanied by a significant release of heat. The hydration process can be divided into five essential stages that are described below as indicated by the calorimetry experiments [16, 19] presented in Figure 2.2.

- Stage 1 (pre-induction period): This stage characterises the initial reaction resulting upon wetting cement paste. The duration of this period is of few minutes.
- Stage 2 (Induction period): This period is characterised by a slow down of the hydration reactions before an important increase in the reaction rate.
- Stage 3 (acceleration period): A period of several hours marked by a considerable release of heat. It is agreed this heat release originates from the nucleation and growth mechanisms.

- Stage 4 (deceleration period): An important decrease in the heat released from reactions is observed during this stage. This is probably due to the water depletion. It's also related to the difficulty of water to access anhydrous grains being surrounded by a less permeable product (Formed hydrates).
- Stage 5 (Curing phase): This phase corresponds to the ongoing hydration. It is mainly controlled by the diffusion of water through hydrates to further nucleate other grains in the anhydrous cement.

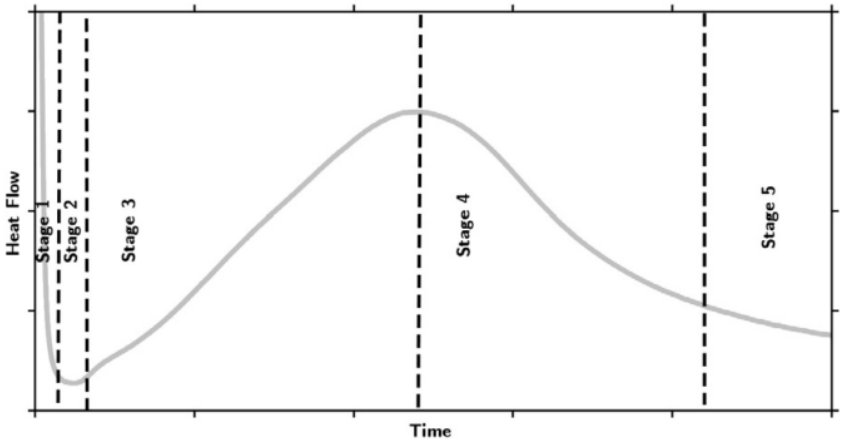

FIGURE 2.2: Rate of hydration of Alite with respect to time from isothermal calorimetry experiment [16]

2.3 Cement porosity and hydrates

The cement paste is a complex multiscale porous material. The pore sizes can range between several orders of magnitude from nano-metric spaces intrinsic to hydrate to large sub-milimetric air voids. This complexity derives from the major hydration product C-S-H that is porous itself. The C-S-H occupies 60% of the cement paste volume at hardened state and is responsible for its main mechanical properties. The understanding of C-S-H porosity is fundamental to understand many important phenomena related to the cement paste. For instance, the fine porosity controls creep and shrinkage of cement [20, 21]. Strength and permeability are mostly related to the larger porosity [20, 21]. Hence, understanding of cement porosity is of a key importance to understand cement properties and to assess its durability. In order to relate the different properties of cement paste to its porosity, several models have been proposed. These models tried to explain and gather the variations of cement properties (e.g, SSA) with physical parameters (e.g, W/C). In the following, we will present the challenging aspects of cement properties discussed by these models. We will present four models for porosity and state of water in C-S-H with a focus on the two most used and documented ones.

2.3.1 Challenging aspects of cement pore structure

Specific surface area SSA

The SSA of cement paste is a highly important parameter in explaining the strength and permeability of this material [20, 21]. However, the determination of cement paste SSA is very difficult. Different techniques provide different values of SSA and each technique normalises the SSA per respect to different references (dried mass, saturated volume, etc). Furthermore, the SSA determination is sensitive of the to the pretreatment method [22–24]. Another difficulty in assessing the true SSA of cement paste emerges from the pore structure of C-S-H, as the boundaries between the solid phase of C-S-H and its porosity are not clearly identified. While some methods measure a part of the SSA, others may measure higher values than the true SSA according to Thomas et al. [24]. The SSA of cement varies with various physical parameters controlling the hydration of cement (e.g. hydration degree, W/C, clinker composition, curing temperature, pressure). For instance, the SSA increases with hydration degree as the progressive hydration creates more C-S-H. The SSA also increases with W/C ratio as measured by Nitrogen and presented in Table 2.1. The water vapor however measures values of SSA that are independent of the W/C ratio (Table 2.1). The SSA and specially the disparity between the SSA as measured by Nitrogen and Water vapor are important elements when presenting a conceptual image of C-S-H.

SSA(m^2/g of dry paste)		
W/C	H_2O	N_2
0.35	208.0	56.7
0.40	202.6	79.4
0.50	194.6	97.3
0.57	193.8	132.2
0.70	199.6	139.6

TABLE 2.1: Variation of SSA of hardened cement paste with W/C as measured by Nitrogen and water vapor [23]

Sorption hysteresis and associated dimensional changes

Water vapor sorption isotherms obtained for cement paste exhibits an hysteresis between drying and re-wetting. The adsorption and desorption of water on cement paste is associated with dimensional changes (drying shrinkage & swelling). Understanding how water moves in and out cement paste can help explaining the observed dimensional changes of this latter. Elseways, associating the dimensional changes and the moisture properties of cement can help shedding light on the C-S-H and cement pore structure. The models that are going to be presented in what follows, were mostly based on the moisture properties of cement paste, dimensional changes and mechanical properties variation associated to different moisture conditions.

2.3.2 Classification of porosity in cement paste

Powers and Brownyard [13]

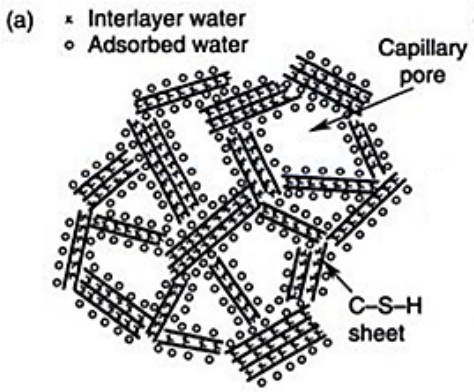

FIGURE 2.3: The structure of C-S-H after Powers and Brownyard model [21]

Powers and Brownyard provided the first complete description of hydrates [13], porosity and water state in hardened cement paste based on their studies of water vapor sorption isotherms and chemically bound water. They have proposed a model for the microstructure of cement and particularly the structure of its main binder C-S-H. In this model, the cement paste volume is regarded as an assembly of three separate components:

- Unreacted cement paste
- Hydration products
- Capillary pores

where hydration products are a mixture of C-S-H and crystalline hydrates. The high specific surface area of cement paste as measured by water vapor suggests a colloidal nature of this latter [13]. The water vapor sorption of cement exhibits an hysteresis that is commonly observed for slit-shaped materials. This hysteresis shape of water vapor isotherm indicates a layered structure of the cement building units as can be seen in Figure 2.3. Thus, cement is viewed as a colloid formed of small layered units that comes together to form a porous product. The Powers and Brownyard model classified water within cement paste based on its evaporability. The water contained in the cement paste after D-drying or oven drying at 105°C is refereed to as non-evaporable water. The evaporable water is the water removed by D-drying or oven drying at 105°C and was further classified into gel water and capillary water.

The cement porosity according to this model is the volume of paste occupied by evaporable water. The porosity within the cement pastes is then classified in two types as described below:

- Capillary porosity: contains the unreacted free water and not influenced by the C-S-H forces. It is located at least two water layers away from C-S-H [13].

- Gel porosity: the pores intrinsic to hydration products controlled by attractive surface forces of Van Der Waals. The gel pores include water comprised between layered units and adsorbed water held by surface forces. The quantity of gel pores is around four times the quantity of water forming a monolayer coverage on the C-S-H surfaces. Gel porosity occupies approximately 26% of the volume of the gel.

To explain the difference between the specific surface measured water and Nitrogen, Powers and Brownyard [13] put forward the difference between water molecule size and Nitrogen molecule size. Water having a molecule size of 0.325 nm while nitrogen diameter is about 0.405 nm [25]. An explanation that was not highly received due to small difference in size [21, 25].

The description of water state within cement paste allows understanding its dimensional behaviour. Regarding the volume change upon desorption and adsorption, Powers and Brownyard suggested that it is due to the disequilibrium between capillary tension and solid-liquid attraction. No volume change is observed when the magnitudes of these two forces are equal. Swelling is a result of water entering and forming a layer between solid surfaces on each side. Shrinkage is a result of solid-solid attractions that draw water outside the layer and brings the surfaces together. In other words, when the solid to liquid attraction overcomes the capillary tension, the water enters between solid surfaces and causes swelling upon re-wetting. However when, the capillary tension overcomes the solid-liquid attraction, water is withdrawn from layers and causes surfaces to come together.

Feldman and Sereda [26, 27]

The model provided by Feldman and Sereda [26, 27] is based on the studies of water sorption and length changes isotherms of cement together with the variation of the mechanical properties with moisture conditions. They proposed similarly to Powers and Brownyard [13] a colloidal nature of cement paste and a layered structure of C-S-H. These layers have however eccentric shapes [26, 27] resulting in larger capillary pores. Cement paste is a cluster of single irregular layers that come together randomly and form interlayer spaces (spaces between tobermorite sheets) and capillary pores, as can be seen in Figure 2.4.

Feldman and Sereda [26–28] have classified the water in cement pastes in three categories as in the model of Powers and Brownyard:

- Interlayer water: The water between tobermorite sheets.
- Adsorbed water: The water adsorbed on the outer surface of C-S-H.
- Free water: water inside the capillary pores.

Regarding the interlayer water they considered that it is lost irreversibly with the D-drying (i.e. upon wetting, water can enter interlayer spaces over the whole range of relative humidities). Regarding the specific surface area Feldman and Sereda [28] believed that water vapor measures a higher value than the effective surface area of cement. These larger values are the results of water being incorporated to interlayer

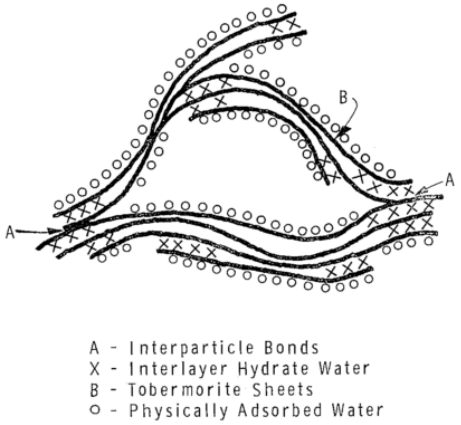

(a) C-S-H presentation

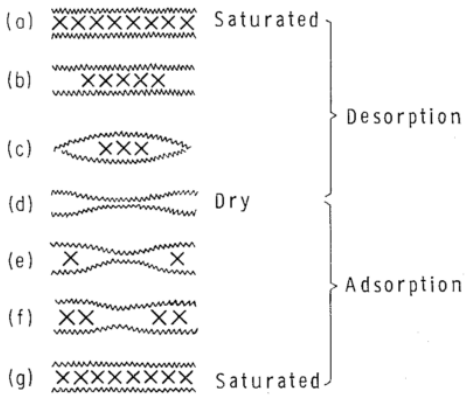

(b) Water movement in the C-S-H upon drying and wetinng

FIGURE 2.4: (a) Presentation of C-S-H particle after Feldman and Sereda model [26] (b) Modelling of water movement within cement paste upon dying and wetting [26]

spaces during adsorption. The Specific surface area provided by Nitrogen seems more reliable than the one provided by water. The change of $\mathrm{SSA}_{\mathrm{N}_2}$ with W/C is driven by the space change due to W/C. In fact, for lower W/C, the gel grows in a more confined spaces, turning some of the inter-particles spaces to interlayer spaces, that are not seen by Nitrogen and results in a smaller SSA. Regarding dimensional changes upon drying, Feldman and Sereda model associated the shrinkage over the range of [100%-35%] RH to capillary effects and the shrinkage below to 35% RH to the dehydration of hydration products.

Munich model [29]

The model developed by Wittmann [29] called the Munich model, describes the C-S-H as a three dimensional arrangement of colloidal particles. The interstices between these particles form the capillary pores. The colloidal particles do not have a pre-assumed internal structure (in Figure 2.5). They are bonded together by Van Der Waals forces. The particles arrangement is greatly influenced by moisture conditions. This model focuses on studying the role of water within a cement paste and the resulting dimensional changes, rather than providing a quantitative description of porosity and hydrates of cement paste. It considers the cohesion of a cement paste as a result of equilibrium between the repulsive pressure exerted by the strongly adsorbed film on the outer surface of particles and the attractive Van Der Walls forces trying to bring these surfaces together [29, 30]. Another important feature of this model is that it considers water vapor as unsuitable for measuring the specific surface area of cement because of the interaction of water vapor and the C-S-H structure. It agrees with the Feldman and Sereda model [26, 27] on this point.

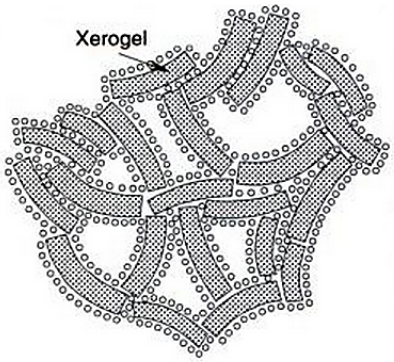

FIGURE 2.5: The structure of C-S-H after Wittman (Munich) model [21]

Tennis and Jennings model [14, 25]

Tennis and Jennings model [25, 31, 32] is the most complete and comprehensive model presented up to now. It was first presented by Tennis and Jennings in (1994-2000) [14, 25] and refereed to as (CM-I) and then refined in 2008 to the (CM-II) [31]. The model integrates various aspects of Feldman and Sereda's model and Powers and Brownyard's model. This model describes the cement paste as a colloid made up of particles called globules which flocculate to form the porous C-S-H network. The nanostructure of this globule has been elucidated through a combination of small angle neutron and X-Ray scattering techniques. The C-S-H globule morphology as proposed by [33] is presented in Figure 2.6. The globule is an equiaxed particle with a cross section of 5 nm diameter that has an internal sheet like structure similar to tobermorite. The globules are assumed to have an internal surface and internal water-filled porosity. We can distinguish three types of water within the C-S-H globules as detailed in the following and presented in Figure 2.6:

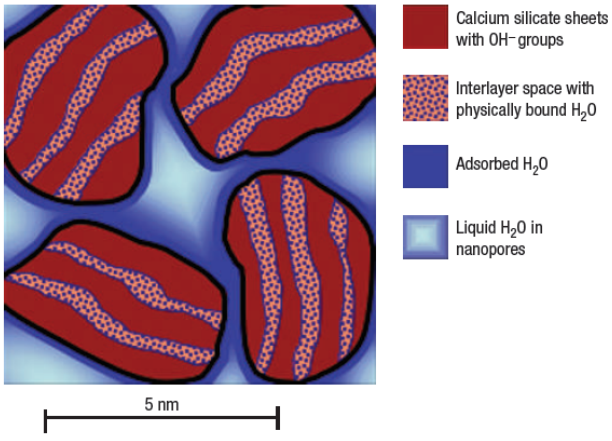

FIGURE 2.6: Schematic drawing of the C-S-H globule as determined from SANS and SAXS experiments [33]

- Physically adsorbed water: Water adsorbed on the outer surface present as a monolayer coverage of the C-S-H globules.
- Physically bound water: Water stacked within the globules present in the interlayer spaces.
- Chemically bound water: Water bound to calcium silicate sheets as hydroxyl groups (OH^-).

The Jennings model defines four types of pores (refer to Figure 2.7):

- Interlayer spaces and intraglobular pores (IGP): The CM-II with contrast to the CM-I distinguishes two locations of water within the globule: the interlayer spaces and the intraglobular pores with sizes of below 1 nm. The difference between these two types of very tiny pores is that removal of water from the interlayer spaces induces a collapse of the globule. However, the removal of water from the IGP does not induce any changes in the volume of the globule. It's worth mentioning that the distinction between these two water locations was suggested to explain the increase of C-S-H density observed during desorption up to 11% and the constant C-S-H density upon adsorption as shown in Feldman experiments [34]. In fact, desorption from 11% RH increases density (water being removed from the surface and interlayer spaces), but the resorption up to 11% RH does not change the density of C-S-H, meaning that water enter the IGP and adsorb on the surface without entering to interlayer spaces.
- Small gel pores (SGP): Pores filled with water trapped between the globules that are percolated to the outer regions. They have a characteristic size of 1 to 3 nm in diameter.
- large gel pores (LGP): pores or spaces created as a result of the overlap of globular flocks, with a characteristic size of 3 to 12 nm in diameter.
- Capillary pores: Pores filled with free water and non-intrinsic to the C-S-H. They are completely dried at around 85%RH. Jennings proposed a lower limit size of about 10 nm for capillary pores [18].

The Powers and Brownyard's model and the Jennings model both distinguishes gel pores. This designation is confusing as it refers to different pore regions, although both intrinsic to the C-S-H phase. The gel porosity of Powers and Brownyard's model includes the interlayer water as part of the gel porosity, while the Jennings model considers the gel porosity as the pores outside the globules. The interlayer spaces are not part of the gel porosity.

This classification of porosity within cement paste helps explaining the various reversible and irreversible dimensional changes. For instance, removal of water form LGP explains the irreversible shrinkage in the regions of high relative humidities [85%,40%]. This irreversible shrinkage is a result of reorganisation of globular flocks which come closer due to capillary stresses. Further drying removes water from SGP below 40%RH a point at which surface effects are dominant. Continuous drying below [20%-10%] removes water adsorbed in the surface and in the interlayer spaces which induces a collapse of the C-S-H layers. Upon re-adsorption water enters the interlayer spaces over the entire range of RH [36].

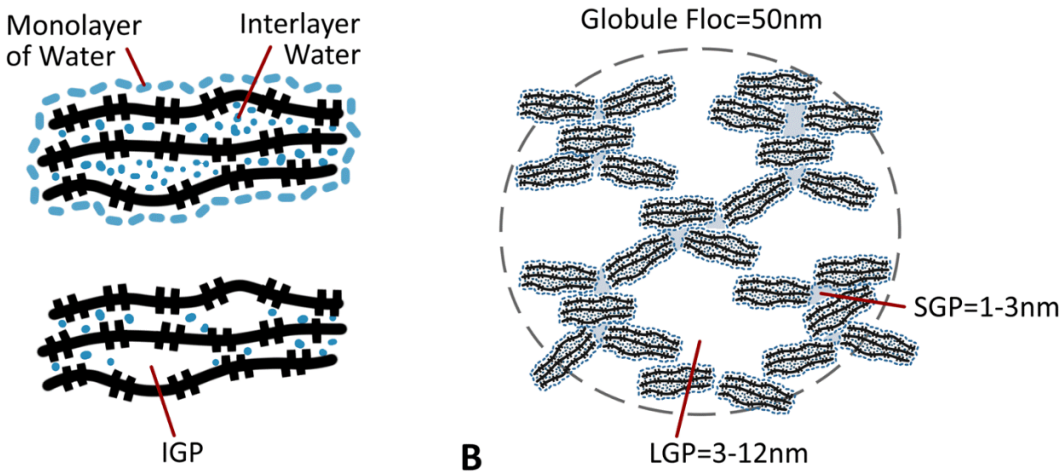

FIGURE 2.7: The description of the C-S-H porosity provided by Jennings [35]

Regarding the challenging measurements of SSA and essentially the differences between the SSA measured by water and Nitrogen and their evolution with the water to cement ratio, Tennis and Jennings [14, 25] suggested that the C-S-H is non distributed uniformly but rather fills the space in two different forms. For instance, the fact that water SSA measurements give higher values than Nitrogen SSA measurements, indicates that water can penetrates all the pores, but Nitrogen cannot. The pore region within C-S-H into which Nitrogen can penetrate is refereed to as LD C-S-H and the other pore region accessible to only water is refereed to as HD C-S-H. The difficulty of Nitrogen to penetrate HD C-S-H pores is associated to the more tightly packed pore structure of the latter. The quantities of the HD and LD C-S-H and their intrinsic porosities were obtained through fits of predicted properties of cement obtained by the model and the ones measured experimentally, e.g (Nitrogen SSA, Nitrogen porosity and capillary porosity). The quantities of these two regions varies with the degree of hydration and water to cement ratio, while their intrinsic porosities are independent of the hydration conditions. The intrinsic porosity of LD C-S-H and HD C-S-H are respectively 0.37 and 0.24 (see Figure 2.8). To sum up the CM-II findings, the C-S-H is perceived as an assembly of globules packing together in two different densities, composing the two C-S-H regions: HD C-S-H and LD C-S-H that forms the C-S-H gel.

Further evidence of two C-S-H types

The distinction between two C-S-H phases although not very realistic as one can imagine a continuous C-S-H density rather than two distinct densities, helps explaining various measurement inconsistencies about cementitious materials. Furthermore, others studies confirmed the existence of C-S-H packing in two densities. For instance, SANS allowed following the development of surface area during hydration [24]. The results of SSA of cement paste together with the heat released from cement paste for the first hours of hydration are shown in Figure 2.9. It can be seen that

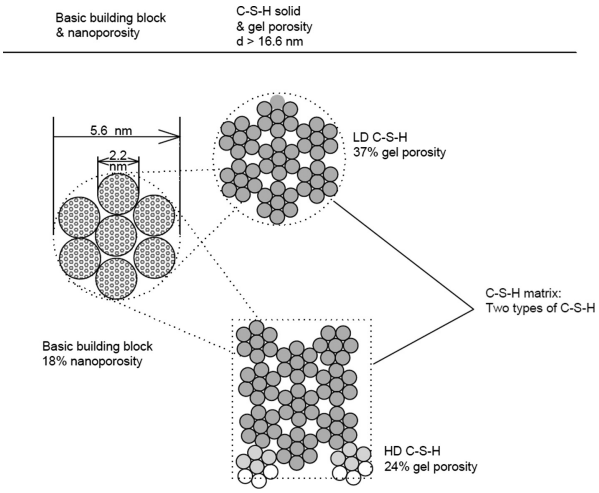

FIGURE 2.8: Characterisation of the C-S-H with its packing density as described by Jennings [37]

the surface area follows the evolution of heat flow until 24 hours of hydration, after which the SSA reaches a plateau while the heat continue increasing. This indicates that the SSA of early hydration products is higher than the SSA of the hydration products produced lately. Thomas et al. [24] suggested that this confirms the idea of two C-S-H types. The LD C-S-H associated to the higher SSA is formed at the first few hours of hydration and contributes to the development of SSA as measured by SANS experiments. The HD C-S-H which fills the space at late ages, does not contribute to the measured SSA of cement paste. Nano-indentation experiments confirmed the

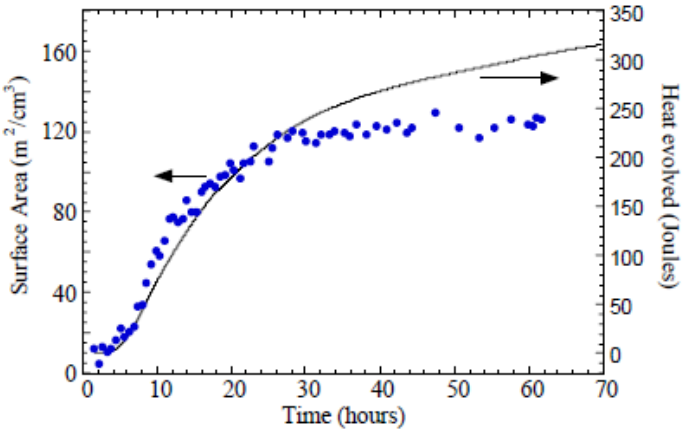

FIGURE 2.9: Surface area (solid circles) and heat evolved (line) for OPC/H2O cement as adapted from [24]

existence of two C-S-H types with different elastic properties [38–40]. They confirmed, similarly to Jennings, that their intrinsic properties are independent of the mix proportioning while their fractions may vary [39, 40]. Scrivener [41] observed two C-S-H morphologies based on SEM micrographs, a more and less dense C-S-H, corresponding respectively to the C-S-H that grows in more or less confined space. TEM experiments [42, 43] also detected two C-S-H types which were also assigned to

inner and outer product. The inner product grows at the surface of anhydrous grains, while the outer product grows at the inner product surfaces and fills the porous space. Recent studies motivated by the damaging preparation process of specimens for TEM, have used soft X-ray ptychographic microscopy to characterise the C-S-H morphology. They confirmed similarly to TEM, that the existence of an interglobular inner product and outer product with a fibrillar morphology [44].

Discussion on the Tennis and Jennings model

The globular nature of C-S-H widely admitted has been questioned by Brisard [45]. In fact, while simulating the small angles scattering curves, the simulated spectrum does not follow the experimental one, disproving the globular nature used in modelling the scattering curve. Beaudoin et al. [46–48] verified different features of the Jennings colloidal model of C-S-H and commented on their validity and here are some of his comments. For instance, the distinction between two different packing densities of C-S-H is based on SSA measurement of water vapor and Nitrogen. The water vapor sorption isotherm being irreversible makes BET calculation of SSA invalid according to Beaudoin et al. [46–48]. Beaudoin [46] suggests that all the calculations made by Tennis and Jennings to estimate SSA should be done on the reversible part of water sorption isotherm. He agrees on this point with Wittman [29] and Feldman and Sereda model [27]. Beaudoin et al. [47] explains that the large strain shrinkage, which triggered the colloidal model is largely justified by the layered model of Feldman and Sereda. Furthermore, Jennings [35] explains that upon adsorption up to 11%, water adsorbs on the surface and enters the IGP without entering interlayer spaces. Beaudoin et al. [46, 47] found this separation illogical as the water must enter the interlayer space in order to reach the IGP. Recent NMR studies [49–51] are also inconsistent with the existence of IGP. They differentiate between interlayer pore with size below 1 nm, gel pore of size between 2-5 nm and inter-hydrate pores of 10 nm size approximately [50, 51], but no IGP pores are detected [50].

2.3.3 Phase assemblage of cement paste

The mass and volume assemblage of hydrated cementitious materials are of great interest in understanding the strength development of these materials, particularly when using homogenization methods. However, due to the presence of amorphous phases, the determination of the mass and volume assemblage is not an easy task. There are two known models that allow the determination of the volume assemblage of cement paste for an ordinary Portland cement paste:

- The Powers and Brownyard hydration model: It allows establishing the volume assemblage as a function of the water-to-cement ratio and the hydration degree [13].
- The Tennis and Jennings hydration model: This model is more sophisticated than the one of Powers and Brownyard as it takes into account the chemical

composition of the cement clinker and the C-S-H for the evaluation of the volume fractions [25]. It also provides a more detailed volume assemblage comparing to the Powers and Brownyard model.

These models are presented and discussed in the following.

Powers and Brownyard model [13]

The Powers and Brownyard model considers the paste as an assembly of anhydrous clinker, hydration products ('called also the gel') and the water filling the capillary porosity, with respective volume fractions f_{ck}, f_{hyd} and f_w.

The volumetric fractions as a function of the water to cement ratio and the hydration degree are presented in the following as taken from [52], where ρ_{ck} is the clinker density, ρ_w the water density and W/C is the water to cement ratio:

$$f_{ck}(w/c, \alpha) = \frac{1-\alpha}{1+\frac{w}{c}\frac{\rho_{ck}}{\rho_w}} \tag{2.5}$$

$$f_{hyd}(w/c, \alpha) = \frac{0.68\alpha}{\frac{\rho_w}{\rho_{ck}}+\frac{w}{c}} \tag{2.6}$$

$$f_w(w/c, \alpha) = \frac{\frac{w}{c}-0.42\alpha}{\frac{\rho_w}{\rho_{ck}}+\frac{w}{c}} \tag{2.7}$$

Tennis and Jennings model [14]

The Tennis and Jennings model is based on the initial cement composition, C-S-H composition, water-to-cement ratio and degree of hydration. It consists of simple stoichiometric reactions for the hydration of the four dominant compounds in Portland cement: C_3S, C_2S, C_3A and C_4AF. The complete set of chemical reactions has been presented in Section 2.2. If the density and the averaged chemical composition (x, y) of C-S-H are known, the volume fractions of cement paste can be calculated from the chemical reactions presented in 2.2 with equations (2.1, 2.2, 2.3, 2.4). A numerical application can be found in [9, 40].

The Powers and Brownyard model permits to calculate the volume fractions in a simplified manner ignoring different microstructure phases, for an overall hydration degree. It seems also of limited application to provide quantitative description of volume assemblage due to capillary porosity dependency on temperature. The Tennis and Jennings model [25, 32] improves on the Powers and Brownyard model and assumes however separate hydration degrees to different phases. This allows a more accurate and detailed description of cement phases. Nevertheless, the knowledge of the C-S-H chemical composition and the density at different hydration temperatures is required in order to get the volume assemblage of cement with hydration temperature. These models limitations implicate that other numerical and experimental methods have to be used in order to establish the volume assemblage of the cement paste at different temperatures and determine the C-S-H chemical composition and density.

2.4 Chemical formulation

2.4.1 C/S ratio

The C/S ratio represents the calcium content of C-S-H per silicon content. As presented in section 2.2.1, the reactions producing C-S-H and CH are approximate because of the variable stoichiometry of the C-S-H. If one needs to evaluate the contents of the C-S-H and portlandite from these chemical reactions, as proposed by Tennis and Jennings, the average values of C/S and H/S ratios for specific hydration conditions have to be known. Yet, the C/S ratio does not have a unique value, it varies within a cement paste [53, 54]. An example is presented in Figure 2.10 for an ordinary cement paste for which the C/S ratio ranges from 1.2 to 2.3 with an average value of 1.75 [53].

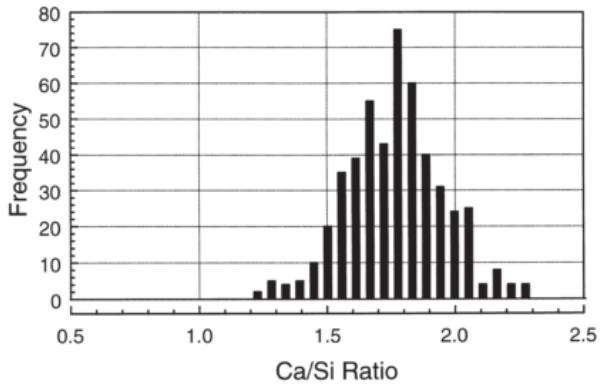

FIGURE 2.10: Ca/Si ratio frequency histogram for C-S-H in Portland cement pastes [53]

The C/S ratio varies also with the hydration conditions for instance water to cement ratio, age, cement mineral composition and the addition of supplementary materials. For instance, regarding the evolution of the C/S ratio with age, it has a bimodal distribution at the onset of hydration that tends to become homogeneous by the progressing hydration as suggested by Richardson [53]. The changes of the C/S ratio distribution from a bimodal to homogeneous was associated according to Richardson to a change in the morphology of C-S-H. The higher C/S ratios being associated to the inner product with a fine morphology and lower values are associated to the outer product with a fibrillar to a foil-like morphology. The densification of the outer C-S-H with progressing hydration transforms the bimodal distribution to a homogeneous one. Muller [55] has calculated the C/(S+A) ratio (where the A stands for the aluminium uptake of C-S-H) and confirmed that this ratio is decreasing with increasing hydration degree as shown in Figure 2.11(a). Muller studies [55] have also shown that lowering the W/C ratio increases the C/S ratio (Figure 2.11(b)).

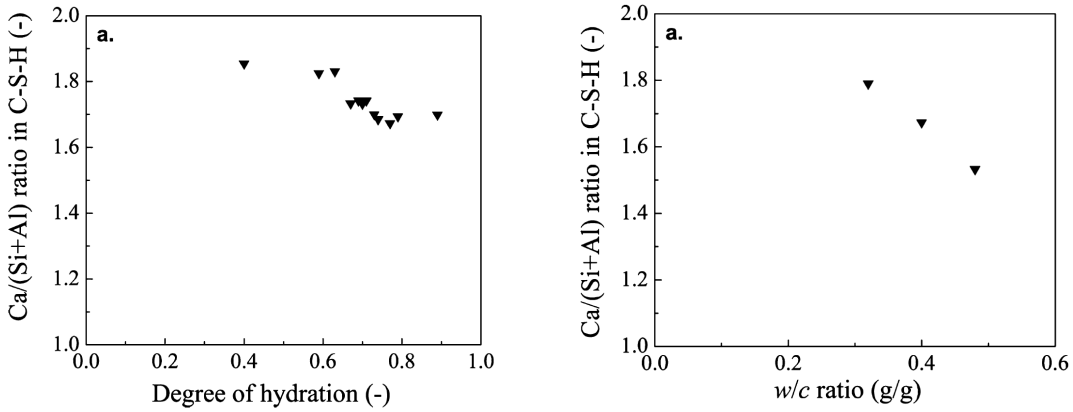

(a) (b)

FIGURE 2.11: Evolution of the C/S ratio of a white cement paste as obtained from NMR-based calculations (a) with the hydration degree and (b) with water to cement ratio [55]

2.4.2 H/S ratio

The H/S represents the water content of C-S-H per silicon content and has to be defined with respect to a specific drying state. For instance, for specific hydration conditions (W/C, age and composition) one can find different values of the H/S depending on the relative humidity or the used drying technique. This causes discrepancies in the data reported in the literature giving values ranging form 1.4 (Oven-dried or D-dried C-S-H) to 4 (Non-dried C-S-H) or even greater values for higher W/C ratio. Another way to define the water content of cement is by referring to different pore reservoirs within cement pore structure addressed in section 2.3. This description has been adopted by Jennings [35] as presented in Figure 2.12. This figure shows the variation of the H/S ratio with the location of water. For instance, a value of 1.8 is proposed for H/S ratio in interlayer water and 4 for C-S-H with saturated gel pores. The H/S ratio can vary also within a certain location with the drying. For instance, a globule with full interlayer spaces and encountered with a mono-layer of water has an H/S ratio of 2.1. If we remove the external layer adsorbed on the globule surface and leave the interlayer full of water we will find an H/S ratio equal to 1.8. If we start drying the interlayer we can reach smaller values of this ratio around 1.3-1.4 by D-drying and oven drying at 105°C for instance.

Similar to C/S ratio, the H/S ratio is considerably influenced by the hydration conditions (water to cement ratio, age, temperature, presence of additives). Muller [55] calculated an H/S ratio for both saturated C-S-H and dried C-S-H with full interlayer spaces for different water to cement ratio and different hydration degrees. The evolution of H/S ratio with water to cement and hydration degree is presented in Figure 2.13. It can be seen that the water content of saturated C-S-H is decreasing, while the water content of solid C-S-H is almost constant with increasing hydration degree. The decrease of C-S-H saturated water content is due to the consumption of the gel pore water as the hydration progresses to further nucleate solid C-S-H grains. Similarly, while increasing the W/C ratio, the saturated C-S-H water content is increasing

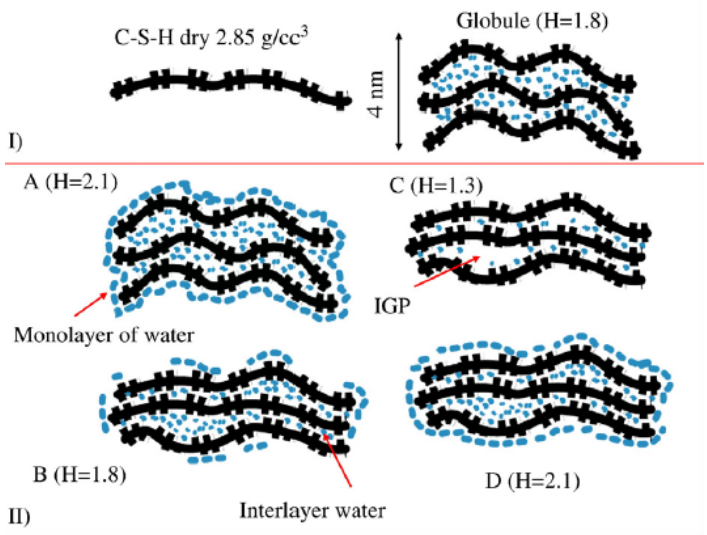

FIGURE 2.12: The water content of a C-S-H globules variation with respect to drying conditions [35]

while the water content of solid C-S-H remains quasi-unchanged.

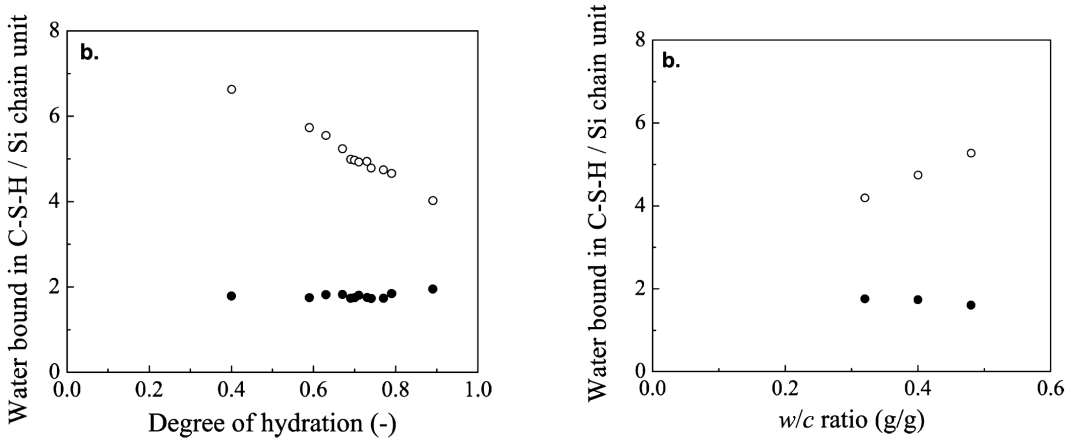

FIGURE 2.13: Evolution of the H/S ratio of C-S-H for both interlayer water and gel water (a) with the hydration degree and (b) water to cement ratio as obtained from NMR-based calculations on white cement [55]

2.4.3 Density

Figure 2.14 reports the variation of density of both crystalline C-S-H (tobermorite and jennite) and amorphous C-S-H (made of white cement or C_3S pastes) [56]. It can be seen that the density decreases with increasing H/S ratio. However, it increases with increasing C/S ratio. The C/S ratio and H/S ratio are both changing with the varying hydration conditions, resulting in a change of the C-S-H density.

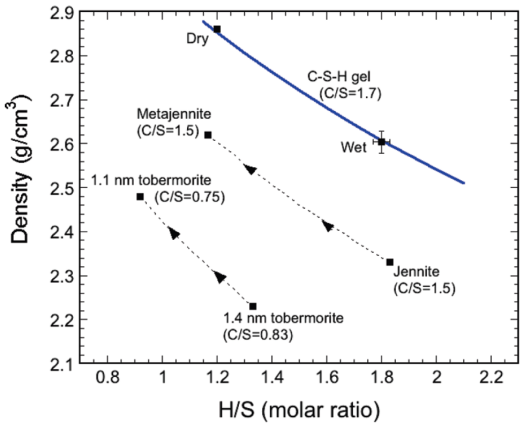

FIGURE 2.14: Evolution of density with water content for amorphous C-S-H resulting from cement paste and crystalline C-S-H corresponding to different C/S ratios as adapted from [56]

The density of C-S-H is however difficult to assess directly due to the amorphous nature of C-S-H and that this latter is intermixed with portlandite particles. The values reported in literature vary widely depending on the composition of cement, the method used for assessing the density and the pore volume excluded from measurement. For instance, the CM-II model reported values ranging from 1.83 $\mathrm{g/cm^3}$ up to 2.85 $\mathrm{g/cm^3}$ depending on the water content and the considered pore reservoirs [35]. Important values to be memorised are the density of solid C-S-H globules excluding the water monolayer coverage which is equal to 2.603 according to Allen et al. $\mathrm{g/cm^3}$ [33] and which decreases to 2.47 $\mathrm{g/cm^3}$ according to Jennings [35] when the water monolayer coverage is accounted for and finally the density of saturated C-S-H with its gel pores equal to 2.03 $\mathrm{g/cm^3}$ [35]. Feldman [57] reported value of 2.45 $\mathrm{g/cm^3}$ of the C-S-H density at 11%RH by Helium pycnometry and a value of 2.55 for solid C-S-H without the monolayer water coverage. Taylor suggested for a C-S-H with a chemical formula of $\mathrm{C_{1.75}SH_4}$ a value of 1.9 $\mathrm{g/cm^3}$ [20]. The work of Muller et al. [58] on the characterisation of the C-S-H enabled also the density of C-S-H to be determined. The saturated C-S-H density increases with hydration degree witnessing the densification of C-S-H with ongoing hydration as seen in Figure 2.15. An increase of the W/C causes the saturated C-S-H density to decrease, a result that is consistent with the increase of the BET surface area with increasing W/C and suggests a more open pore structure. However, the solid C-S-H density slightly decreases with increasing water to cement ratio and hydration degree.

2.4.4 Tobermorite-Jennite model

Similar to the pore structure, the special chemical composition of C-S-H has also been the subject of many models. Experiments of XRD, TEM and NMR spectroscopy showed similarity between the C-S-H structure and other natural crystals and minerals: tobermorite and jennite [59, 60]. Tobermorite is a rare crystalline calcium silicate hydrate that have been found in nature in the Northern Ireland with a chemical formula $\mathrm{C_4S_6H_6}$ and a C/S ratio equal to 0.83. Jennite $\mathrm{C_9S_6H_{11}}$ is another natural

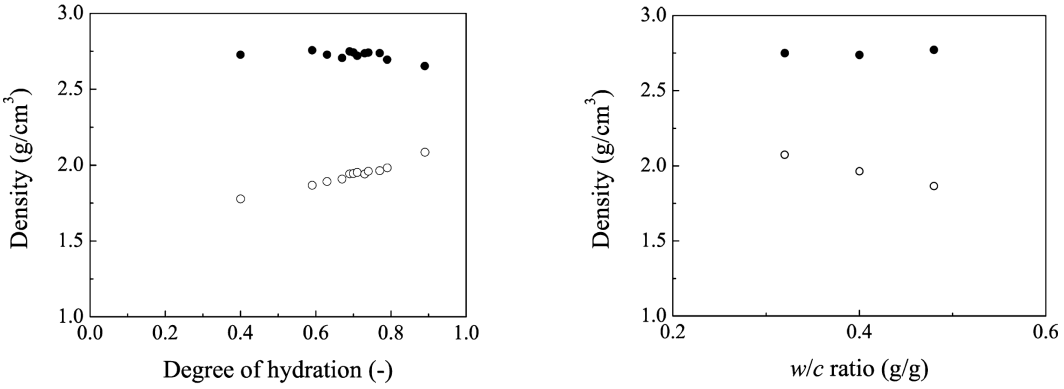

FIGURE 2.15: Density of C-S-H as obtained from NMR studies on white cement (a) with the hydration degree (b) with the water to cement ratio as adapted from [58] solid circles correspond to C-S-H solid and empty circles to saturated C-S-H

calcium silicate hydrate that has a structure similar to tobermorite but with a higher C/S ratio of 1.5. Tobermorite and jennite structures consist of a linear chain of silicate usually called dreierkette where the silicate tethrahedra connect themselves to the Ca^{2+} as presented in Figure 2.16. These dreierkette chains are repeated every 1.4 nm with the space between layers being filled by water molecules and calcium ions. To account for the high C/S ratio found in the C-S-H, Richardson [53, 60] suggested that the C-S-H can be modelled as a mixture of tobermorite & jennite or tobermorite & portlandite and different mechanisms were suggested to model these mixtures.

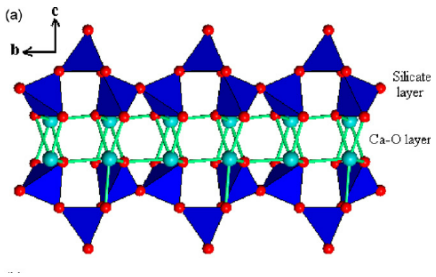

FIGURE 2.16: The structure of a tobermorite layer [61]

2.5 Drying methods of cement paste

The methods available for the characterization of cement microstructure such as Mercury porosimetry, water & gas adsorption, XRD, TGA, SEM and solid NMR, all require a complete removal of water from the specimen prior to testing. Removing water from microstructure is important for multiple reasons:

- stopping the hydration at a given age of maturation,

- some characterization methods such as MIP and N_2 adsorption require empty pores to enable the adsorption of the gas on the solid surface,
- removal of water reduces the risk of specimens carbonation and makes it easier to prepare the material (for instance: grinding and sieving cement powder for XRD experiments and solid state NMR analysis).

However, drying of cement paste either to arrest ongoing hydration or to assess total porosity has been shown to be very critical to the used method. In fact, drying methods may have a great influence on the crucial information obtained from these experiments (e.g : total porosity, Specific surface area) and can even damage the microstructure of the cement paste. We will present briefly the standard drying techniques used to remove water from hydrated cement pastes and their effects on the microstructure, with an emphasis on their impact on the evaluation of total porosity and specific surface area of cement paste.

2.5.1 Presentation of different drying techniques

The phase diagram presented in Figure 2.17 summarizes the conditions of pressure and temperature of different drying methods that are presented in the following. Drying requires transforming the water inside the specimens into vapor either by decreasing the pressure, increasing the temperature or decreasing the pressure at low temperatures.

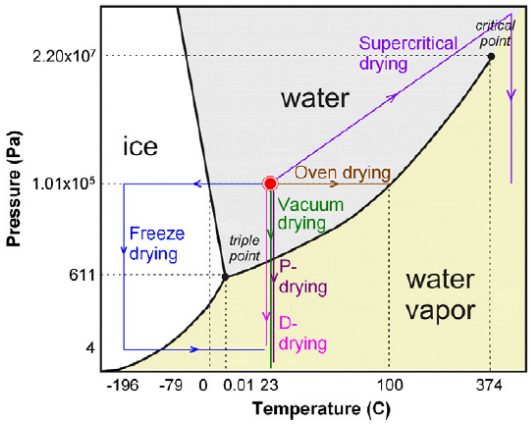

FIGURE 2.17: The phase diagram of water and the transitions between the phases for different drying methods. The red point indicates the initial state of water in the sample at atmospheric pressure and room temperature and the arrows indicate the paths followed during the drying process [62]

Oven drying at 105°C

Oven drying is one of the most used drying methods. The specimen is weighed and placed into an oven that is set at 105°C and at atmospheric pressure. The mass of

the specimen can be monitored periodically to follow the drying process. It is much quicker than the other techniques and water removal is complete after 24 h of drying for centimeter-sized specimens.

D-drying

The D-drying apparatus consists of a sealed container connected to a mechanical vacuum with a cooled trap (a mixture of solid CO_2 and alcohol at T=-79°C) keeping the pressure in the system below to 4.2 Pa and at room temperature (refer to 2.17). D-drying method is believed the most suitable drying technique, assumed to remove all the water except the chemically bound water and without introducing damage to the microstructure [20]. The water removed by this technique is refereed to as non-evaporable water. However, the extraction of water by this method is very slow and requires 14 days for the water to be completely removed.

Freeze drying

The specimen is placed directly into liquid nitrogen (-196°C) for five minutes. This very low temperature of liquid Nitrogen causes water to freeze immediately after immersion without exerting capillary stresses on the pores structure. The specimens are then placed in a freeze dryer at T= -77.7 °C. In these conditions, the ice water is then sublimated.

Solvent exchange

This method requires replacing the pore solution of hardened cement paste with organic liquids such as acetone, methanol or isopropanol. Cement paste is crushed finely and introduced in a large amount of solvent. This solvent has to be renewed many times. The replacement time depends on the size of the crushed cement grains and can take minutes to days. The organic solvent is then removed by gentle oven drying or vacuum drying. It's gentle drying method recognized for preserving the pore structure.

2.5.2 Impact of drying methods on the assessment of cement miscorstructure

Several comparative studies of different drying techniques were conducted on cement paste to examine the effect of drying on the microstructure. These previous studies examined the possible dehydration of hydration products and the changes of the pore structure for different drying techniques. The usually compared methods in literature are : Oven drying at 60°C and 105°C, vacuum-drying, and freeze-drying , D-drying. The essential conclusions drawn from the literature are summarized here for each method separately [21, 62–68].

Oven drying

It is reported to remove a part of the interlayer water. Hence, it results in an overestimation of the total porosity. It also causes severe and irreversible changes of the pore structure. Gallé [63] reported that oven drying at 105°C increases the median pore diameter and overestimates the capillary porosity as shown in Figure 2.18. Regarding the chemical composition, it has also been shown that oven-drying at 105°C dehydrates ettringite and Afm, and part of the C-S-H [21, 62, 67, 68]. Moreover, samples dried in oven experience a higher risk of carbonation [64, 68]. The dehydration of ettringite and Afm plus the enhanced carbonation risk make the use of oven-drying at 105°C inappropriate for experiments such as XRD, TGA and NMR. Oven drying at 105°C is far from being the drying method capable of preserving the microstructure. Oven drying at 60°C and 40°C are also common in the literature and are less harmful to the microstructure. In fact, at this temperature interlayer water is not removed, but we are not sure to empty all the gel pores. However, some of the risks mentioned for oven-drying at 105°C are still relevant, as for instance the ettringite dehydration (ettringite is unstable for temperatures above 40°C), and the carbonation risk. Oven drying either at 105°C or other temperature is not adequate to stop hydration of non-mature cement paste as it will accelerate its hydration and hence change the hydration degree. The SSA estimations obtained from BET experiments on oven-dried samples at 105°C show independent variation with the hydration degree, suggesting that oven drying cannot capture well the changes of SSA (Figure 2.19).

D-drying

The D-drying as mentioned previously is widely admitted to be a good drying method. Powers and Brownyard [13] for instance define the total porosity as the porosity evaluated by mass loss during D-drying. Jennings however mentioned that D-drying removes some of interlayer water [35]. Furthermore, other recent studies mentioned that D-drying has the same harmful implications on the microstructure comparing to oven drying at 105 °C [62, 69]. It overestimates the total porosity as it removes part of the chemically bound water to the C-S-H [62, 69]. It results almost in the same porosity as oven drying at 105°C in a CO_2 free environment. However, when comparing oven drying and D-drying it is found [64] that D-drying is more appropriate for a specimen treatment before evaluation of the SSA (Figure 2.19).

Freeze-drying

The total porosity obtained through freeze-drying is lower than the porosity measured by oven-drying at 105°C. It seems that freeze drying is a suitable technique for drying a cement based material, especially for a characterization through MIP [63]. However it probably introduces some changes at the nanoscale by creating micro-cracks [63, 70]. Also, it is accused for dehydration of ettringite [66, 70, 71]. Korpa et al. [65] found that freeze-drying is a good for estimating the SSA of cement paste.

Solvent exchange

Solvent replacement is a gentle drying method as a result of the low surface tension of the organic liquids. However, organic solvents can react with components [72]. For instance the portlandite is usually consumed by these organic liquids making the use of this technique inadequate for TGA experiments [68]. In addition to this, solvent

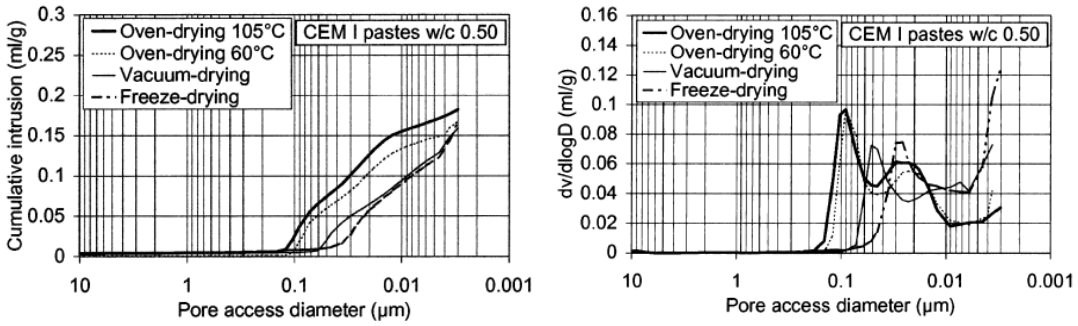

FIGURE 2.18: Comparison of different drying techniques on the pore structure through the use of mercury intrusion porosimetry after Galle [63]

molecules sorb into cement components and are not evacuated by simple drying [73]. Furthermore, this method requires sufficient time to enable total replacement of pore solution by the solvent, making it inaccurate for stopping the hydration at early age. Regarding the SSA of cement, solvent exchange causes too much variation in SSA and makes it difficult to trust the results obtained for specimens dried by solvent exchange according to Juenger et al. [64].

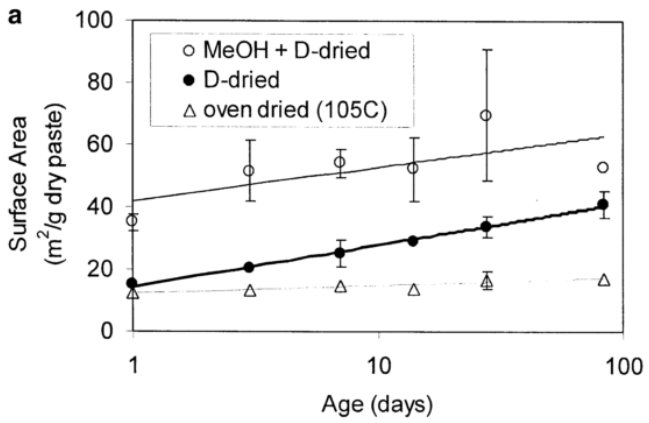

FIGURE 2.19: Comparison of the effect of different drying techniques on the measurement of specific surface area [64]

The different advantages and drawbacks of each of the above mentioned methods are summarized in table 2.2. A + grade marks that the drying method is adequate for use for the mentioned experiments and − grade marks its non-adequacy for the measurements, the reasons are mentioned above and some extrapolations are done by comparisons between similar methods in case the information is lacking in the literature. It can be clearly seen that there is no perfect drying method. The choice of the drying method has to be done according to each specific and desired property. However, it seems that if one wants to use one method to assess different properties freeze-drying is the most suitable to a large number of experimental methods.

Experiments Drying	OD 105(°C)	OD 40/60(°C)	DD	FD	SE
XRD	-	-	-	-	+
TGA	-	-	+	+	-
NMR	-	-	-	-	+
N2 (SSA)	-	-	+	+	-
N2 (porosity)	-	-	+	+	-
MIP	-	-	-	+	+
WVS	-	-	-	+	+
Carbonation risk	-	-	+	+	-
Early age hydration stoppage	-	-	-	+	-
Mature age hydration stoppage	+	+	+	+	+
Grade (+)	1/10	1/10	5/10	8/10	5/10

TABLE 2.2: A global grading of drying techniques regarding the pros and cons of these methods as reviewed from literature

2.6 Hydration temperature influence on cement paste

The effects of curing temperature on the cement paste hydration, chemical structure, pore structure and mechanical properties are detailed below.

2.6.1 Chemistry of hydration

The increase of curing temperature results in an acceleration of the precipitation-dissolution process. The hydration progresses rapidly for higher temperatures and then reaches a plateau as observed in Figure 2.20 from studies of Escalante et al. [74]. The samples hydrated at lower temperatures process slowly and the hydration evolves continuously in time and reaches even higher hydration degrees than the pastes hydrated at high temperatures. Regarding the chemistry of cement hydration in terms of the precipitated hydrates, it remains quasi-unchanged for hydration temperatures below 100°C and almost the same hydrates precipitate [20, 75, 76]. However, there are some exceptions. For instance, ettringite shows a thermal instability with increasing curing temperature [75]. Above 40°C it becomes unstable and converts to monosulphoaluminate. The quantities of the other hydrates (C-S-H, CH) remain constant at different temperatures in the range of 5°C and 50°C according to studies of Lothenbach et al. [75]. Above 100°C, several changes occur resulting in severe deterioration of mechanical properties with time and an increase of permeability, commonly called strength retrogression [20, 77, 78]. The phenomena related to strength retrogression are out of the scope in this study. Regarding variation of the chemical composition of C-S-H and its density with hydration temperature, Gajewicz [79] investigated using an approach similar to Muller et al. [50] these properties. The values of the C/(S+A) ratio, H/S ratio and C-S-H density are presented in Figure 2.21 at different temperatures. Gajewicz [79] didn't notice any variation of the C/(S+A) ratio under increasing curing temperature in the range of [10°C, 60°C], providing a value of 1.8 of this ratio which agrees with previous work of Gallucci et al. [80]. The H/S ratio of saturated C-S-H and solid C-S-H are both decreasing with increasing curing temperature. It is

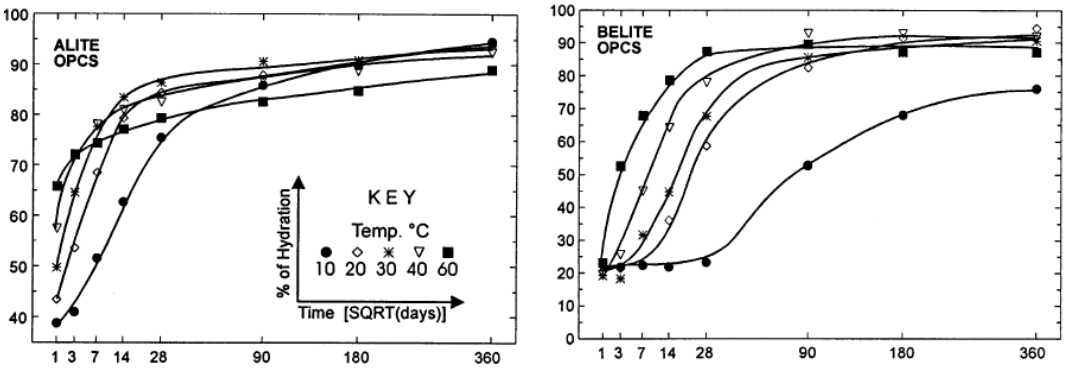

FIGURE 2.20: Hydration degree evolution of cement paste cured at different temperatures [74]

worth mentioning that Gallucci et al. [80] provided previously to Gajewiz [79] values of H/S ratio at different temperatures but those values accounted for interlayer water and a part of gel water. The density of solid and bulk C-S-H increases with curing temperature. The increase of solid C-S-H density was explained by the reduced number of C-S-H layers forming the globule as the temperature is increased, which is in agreement with the decrease of H/S ratio. The increase of bulk C-S-H density with temperature derives mainly form the increase in C-S-H solid density. The densities of C-S-H were calculated by Gallucci et al. [80] at different temperatures, but the obtained value at 20°C of 1.90 $\mathrm{g/cm^3}$ were lower than the widely trusted value of Jennings equal to 2.03 $\mathrm{g/cm^3}$. An up-scaling factor was then applied to obtain the densities of C-S-H at different temperatures as shown in Table 2.3.

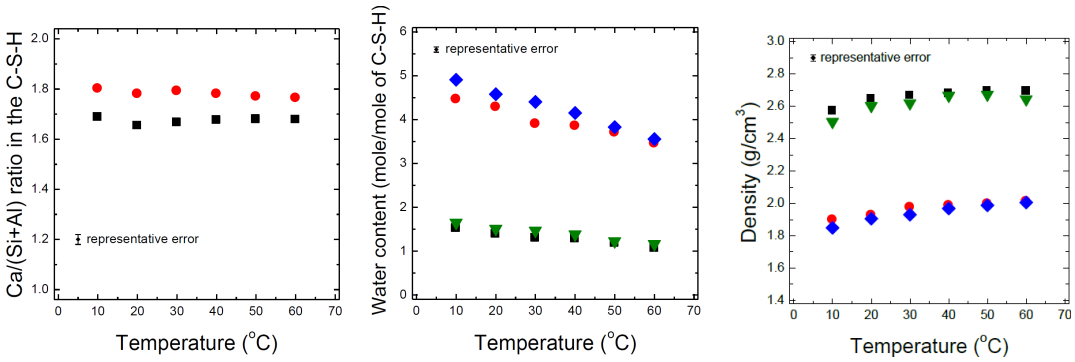

(a) C/S Ratio (b) H/S Ratio (c) Density

FIGURE 2.21: Evolution of C-S-H C/S ratio, H/S ratio and density with curing temperature for 28 days and 90 days [79], For (a) Red circles correspond to 28 days of hydration and black squares to 90 days while for (b) and (c) 28 days (triangles and diamonds) and 90 days old (squares and circles)

It seems that the morphology of C-S-H is also subjected to change when the curing temperature increases. Richardson [81] observed that elevated temperatures lead to a C-S-H with a fine texture of the inner product morphology and particles about half

T°C	5	20	40	60
Predicted density (g/cm^3)	1.79	1.90	2.04	2.13
Corrected density (g/cm^3)	1.91	2.03	2.18	2.27

TABLE 2.3: C-S-H density estimations [80]

size comparing to that of pastes hydrated at ambient temperature. The particles of C-S-H have a size of 3 nm to 4 nm. However, the outer product with its fibrillar structure tend to be much coarser at higher temperatures (refer to Figure 2.22). Richardson [81] also pointed out that the mean length of silicate chain increases with increasing curing temperature, a point that was confirmed by other researchers [80, 82, 83]

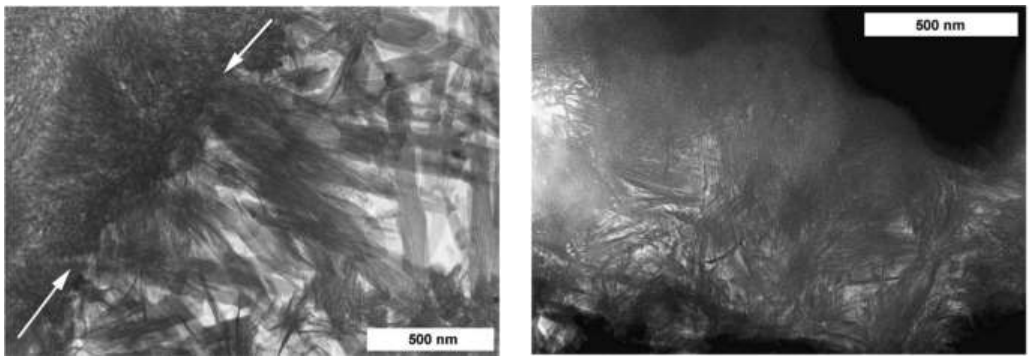

FIGURE 2.22: (a) TEM micrograph observations of Ip and Op for cement hydrated at 20°C and (b) at 80°C [84]

2.6.2 Pore structure of cement paste

The various studies, as found in the literature, agree on the coarsening effect of the hydration temperature of the cement pore structure [75, 80, 85–87]. The cumulative pore size distribution of a cement paste hydrated under different hydration temperatures as obtained from MIP shows that the higher the temperature the higher the total MIP porosity [85]. The changes in the pore structure are more marked in the range of 20 nm-100 nm showing an increase of the pore fraction associated to these pores [85]. Gallucci et al. [80] estimated the capillary through SEM image analysis for cement paste cured at different temperature and hydration degree. Results of Gallucci et al. [80] show that the capillary porosity is increasing with hydration temperature at a given hydration degree as shown in Figure 2.23. Gallucci et al. [80] confirm similarly to Bentur et al. [86] and Verbeck and Helmuth [87] that the increase of capillary porosity with increasing hydration temperature is not the result of limited hydration degree of pastes cured at high temperatures. Gallucci et al. [80] suggest that the increase of capillary porosity with increasing hydration temperature can be explained by the increase of C-S-H density. Lothenbach et al. [75] attributed the increase of the

capillary porosity mostly to the conversion of Aft phases to Afm phases. The latter being denser, contributes to the increase of capillary porosity. Lothenbach et al. [75] also mentioned that the denser inner product formed at high temperatures may contribute to this increase of capillary porosity. The more dense and stable configuration of inner C-S-H with increasing hydration temperature has been reported previously due to the increasing brightness of C-S-H in backscattered electron images [88–90]. Jennings et al. [91] reported that the increase of curing temperature causes the low density C-S-H to collapse toward a denser structure with fewer gel pores. Others authors however didn't notice any difference between inner and outer products based on analysis of grey level of BSE images [80]. Holly et al. [92] investigated the pore structure of white cement trough nuclear magnetic resonance and confirmed the increasing amount of capillary porosity. Holly et al. [92] found that after 40 days of hydration, the relaxation times associated to gel pores are decreasing with temperature suggesting smaller gel pores size, while the interlayer space size remains unchanged due to the constant relaxation times associated to interlayer water with increasing curing temperature. Gajewicz [79] by the use of NMR on white cement confirmed the constancy of interlayer-space sizes. The relaxation times associated to gel pores according to Gajewicz [79] are increasing with increasing temperature at mature ages suggesting bigger gel pores.

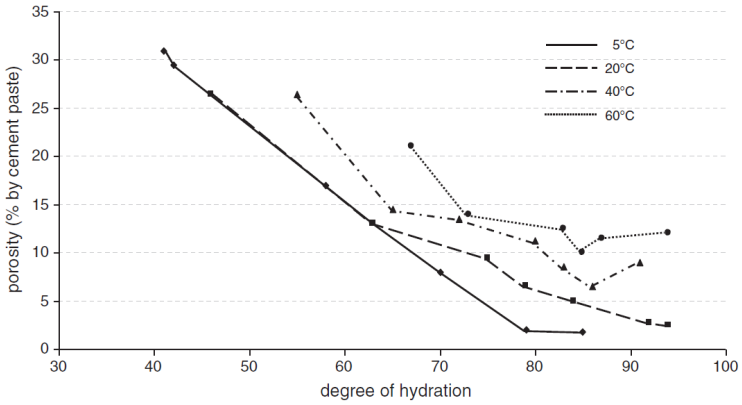

FIGURE 2.23: Evolution of capillary porosity with hydration temperature and hydration degree [80]

2.6.3 Mechanical properties

As presented in different parts of Section 2.6 cement pastes experience various changes in the microstructure when the hydration temperature is increased. These changes have a significant impact on the mechanical behaviour of cement paste. The effects of hydration temperature on the mechanical properties of cement has been widely studied and presented in the literature [20, 75, 85]. It has been agreed that temperature increase induces a considerable decrease in the mechanical properties for mature ages although the rapid development of strength at the start of hydration as observed in Figure 2.24(a). The rapid initial gain of strength is a result of acceleration of initial hydration, promoting a rapid formation of phases [16, 75, 85], as explained in

Section 2.6.1. This trend is confirmed from studies of Bourissai et al. [93] on the elastic properties of class G cement paste for two different temperatures at early ages. The results are presented in Figure 2.24(b) and show the continuous increase of the shear and bulk moduli of class G cement paste with age for both temperatures. After 20 hours of hydration the increase of elastic moduli slows down for 60°C, while it increases continuously for 20°C, similarly to the hydration degree evolution. The elastic properties of cement paste are higher for higher hydration temperatures at early ages. The results of Bourissai et al. [93] confirm the rapid gain in strength at high hydration temperatures previously mentioned in the literature [20, 74, 86]. The study of Bourissai et al. [93] was however limited to early hydration ages (up to one day of hydration).

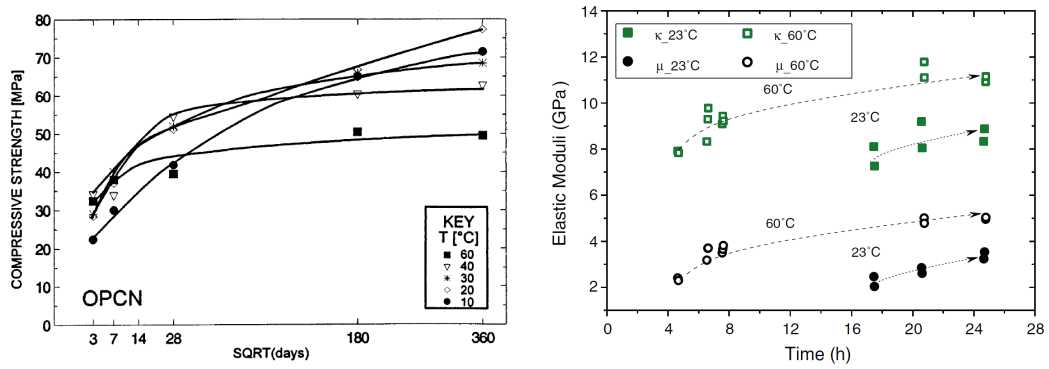

(a) (b)

FIGURE 2.24: (a) Development of compressive strength of a portland cement for different temperatures [74] (b) Evolution of dynamic elastic moduli of the class G cement paste with curing age and temperatures: 23°C (solid symbols) and 60°C (open symbols) [93]

Regarding the decrease of the mechanical properties, Verbeck and Helmuth [87] suggested that clinker grains are surrounded by a very dense hydrate that prevents further hydration. The lower hydration degree and the associated highly porous outer product will result in low mechanical properties. Verbeck and Helmuth's statements about the formation of a denser shell around clinker grains are confirmed by Kjellsen [89] SEM observations showing a denser inner product surrounded by a highly porous outer product at elevated curing temperatures. However, attempts to relate the decrease of mechanical properties to the limited degree of hydration of pastes cured at high temperatures are shown to be inconsistent [86]. Figure 2.25(a) shows that the compressive strength of cement paste for a given hydration degree is lower for high hydration temperatures. Figure 2.25(b) shows that Compressive strength-capillary porosity curves of cement paste cured at different temperatures are not identical, suggesting that the capillary porosity increase with increasing hydration temperature cannot explain the decrease of mechanical properties [86]. Lothenbach et al. [94] attributed the decrease in mechanical properties to the increase of capillary porosity. Zacak et al. [95] plot the compressive strength versus the non-evaporable water of cement [95] as shown in Figure 2.26 in order to gain insight on the origins decreasing mechanical properties of C_3S pastes. It is shown that the higher the temperature the lower the mechanical properties for a specific value of non-evaporable water. Moreover, the compressive

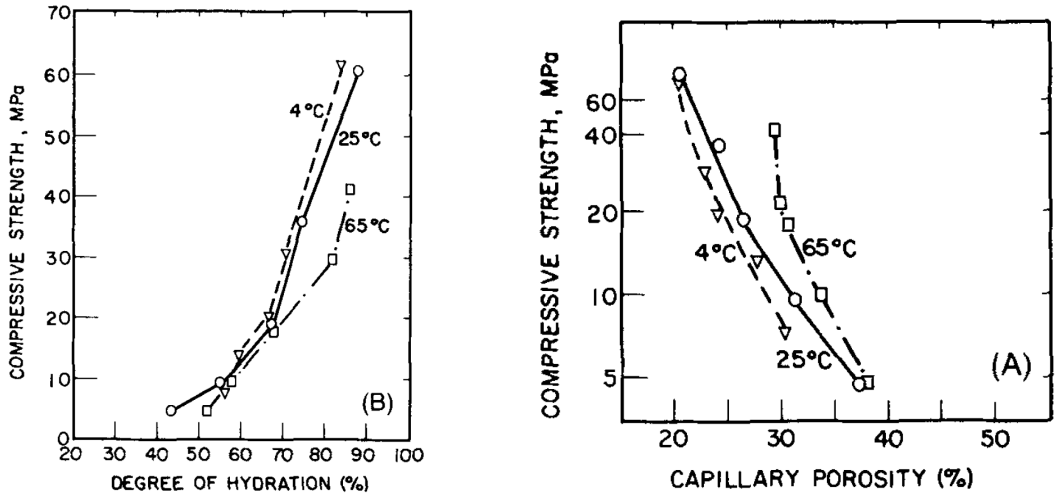

FIGURE 2.25: Evolution of cement paste strength with (a) the hydration degree and (b) the capillary porosity [86]

strength is increasing with the quantity of non-evaporable water with a more or less similar trend for different hydration temperatures. Zacak et al. [95] suggested that the hydration products formed at latter ages contribute similarly to the mechanical properties. The origin of the observed differences in mechanical properties are mainly due to the products formed at early hydration stages.

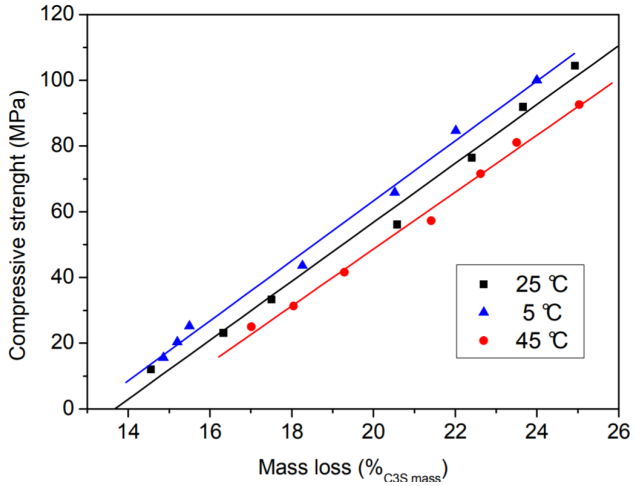

FIGURE 2.26: Evolution of the compressive strength of C3S pastes with their percentage of non-evaporable water at different temperatures [95]

2.7 Micromechanical modelling and upscaling methods

The homogenization procedures deal with the heterogeneous and composites materials and aim to define a homogeneous medium that has the same averaged macroscopic properties [96–98]. These homogenization procedures are particularly important for the studying of cement paste. For instance, the cement paste microstructure and mechanical properties are sensitive to various parameters and hydration conditions (i.e, cement composition, W/C, age of maturation, temperature, pressure, superplasticizers, etc). The complete poro-mechanical characterization of these parameters is often conducted using drained, undrained and unjacketed isotropic compression tests [3] which are time consuming because of the low permeability of cement. The homogenization procedures offer the possibility to investigate cement based materials and to examine the various parameters that might influence their mechanical behaviour [9, 40, 96, 98]. To predict mechanical properties micromechanical modelling requires a detailed description of the microstructure components in terms of volume fractions, mechanical properties and geometry. In the following, we present the theoretical background of the homogenization method, different microstructure representations of cement used for micromechanical modelling together with their respective applications. We also discuss the influence of the geometry of phases on the determined mechanical properties of cement.

2.7.1 Theoretical background of micromechancial modelling

Cement is a multiscale heterogeneous and porous material that exhibits different mechanical properties at different scales. Continuum micromechanics permits to address this scale difference and provides insights on the averaged mechanical properties of the cement paste. It is required to define a statistically homogeneous material with a representative elementary volume (REV) of size l. The REV has to be small enough compared to the size of the structure L and representative enough compared to the size d of the heterogeneities, yielding to $\mathrm{d} \ll \mathrm{l} \ll \mathrm{L}$ the so-called scale separation, an important criterion for the REV. Theoretical basis for the homogenization method and its main equations are recalled briefly in the following. A detailed derivation of equations can be found in [9, 11, 12, 97, 99] The micro-elasticity equations are derived from an REV submitted to a homogeneous strain boundary condition. The tensor of the overall effective moduli of the heterogeneous porous material $\mathbf{C}^{\mathrm{hom}}$, is given as:

$$\mathbf{C}^{\mathrm{hom}} = \langle \mathbf{c} : \mathbf{A} \rangle_V = \sum_{r=1}^{n} f_r \mathbf{c}_r \langle \mathbf{A} \rangle_{V_r} \tag{2.8}$$

Where $\langle \mathbf{A} \rangle_{V_r}$ is the average over the volume V_r of the strain localisation tensor of the phase r and $\mathbf{c}_r$ is the tensor of elastic moduli of different solid phases. In the isotropic case $\mathbf{C}^{\mathrm{hom}}$, $\langle \mathbf{A} \rangle_{V_r}$ and $\mathbf{c}_r$ can be reduced to the following:

$$\mathbf{C}^{\text{hom}} = 3K_d^{\text{hom}}\mathbf{J} + 2G^{\text{hom}}\mathbf{K} \tag{2.9}$$

$$\mathbf{c}_r = 3k_r\mathbf{J} + 2g_r\mathbf{K} \tag{2.10}$$

$$\langle \mathbf{A} \rangle_{V_r} = A_r^v\mathbf{J} + A_r^d\mathbf{K} \tag{2.11}$$

$\mathbf{J}$ is the volumetric part of the fourth-order symmetric unit tensor $\mathbf{I}$ and $\mathbf{K} = \mathbf{I} - \mathbf{J}$ is the deviatoric part. Where $\mathbf{I}$ is defined as $\mathbf{I}_{ijkl} = 1/2\left(\delta_{ik}\delta_{jl} + \delta_{il}\delta_{jk}\right)$ and δ_{ij} stands for the Kronecker delta. K_d^{hom} and G^{hom} are the homogenized bulk and shear moduli of the overall material, k_r and g_r are the bulk and shear moduli of the solid phase and A_r^v and A_r^d are volumetric and deviatoric strain localization coefficients. The strain localisation coefficients depend on the geometry of the inclusion. For an Eshelbian type morphology [100], i.e. an ellipsoidal inclusion embedded in a reference medium, A_r^v and A_r^d are estimated assuming the isotropy of the local and the reference medium and a spherical shape of particles following Eqs (2.12,2.13,2.14) as given by [96]:

$$A_r^v = \frac{\left(1 + \alpha_0\left(k_r/k_0 - 1\right)\right)^{-1}}{\sum_r f_r\left(1 + \alpha_0\left(k_r/k_0 - 1\right)\right)^{-1}} \tag{2.12}$$

$$A_r^d = \frac{\left(1 + \beta_0\left(g_r/g_0 - 1\right)\right)^{-1}}{\sum_r f_r\left(1 + \beta_0\left(g_r/g_0 - 1\right)\right)^{-1}} \tag{2.13}$$

where α_0 and β_0 are given in the following for spherical inclusions:

$$\alpha_0 = \frac{3k_0}{3k_0 + 4g_0}; \quad \beta_0 = \frac{6\left(k_0 + 2g_0\right)}{5\left(3k_0 + 4g_0\right)} \tag{2.14}$$

with k_0 and g_0 are respectively the bulk and shear moduli of the reference medium. The choice of the reference medium in Eqs (2.12) and (2.13) and the used homogenization scheme are mutually conditioned. One can distinguish two different homogenization schemes commonly applied for cementitious materials:

- The Mori-Tanaka scheme [101] where one phase can be identified as a matrix in which inclusions are embedded, and is supposed to play an important morphological role. This scheme supposes that inclusions do not interact with each others, which makes it appropriate for composite materials with small fractions of inclusions and where the matrix has the leading mechanical behaviour.
- The Self-consistent scheme identifies the matrix as the homogenized medium [102, 103]. The matrix properties are unknown in advance and are assessed through iterations. This model is adapted for materials where no element has the leading morphological role. It appears suitable for cementitious materials and has been used for various studies of cement pastes [9, 40].

2.7.2 Microstructure representation and application of homogenization method

As seen in previous sections of this chapter, the cement is a multiscale porous material that contains constituents with sizes ranging from some micrometers (capillary pores) to some nanometres (C-S-H particles). This imposes an homogenization of mechanical properties over different scales depending on the adopted microstructure representation. In the following are summarised some of the microstructure representations that have been used to describe the cement paste at different scales, the used homogenization scheme, the morphological assumptions and the applications they are used for.

Costantinides and Ulm [39] considered the porous C-S-H as a matrix where portlandite and clinker phases are enclosed as inclusions, which supposes a Mori-Tanaka scheme. The properties of the porous C-S-H matrix are obtained through a self-consistent homogenization of HD C-S-H inclusions ingrained in the LD C-S-H matrix. A spherical geometry is considered for all phases (refer to Figure 2.27). The micromechanical model based on this REV is used combined with nanoindentation experiments to investigate the effect of the two C-S-H types on the drop of elasticity caused by calcium leaching. Nanoindentation tests enabled estimating the elastic moduli of the HD and LD C-S-H and their volume fractions with respect to the C-S-H. The determined elastic properties of the two C-S-H types are used in a micromechanical model to highlight the mechanism of the decrease of elastic properties of cement paste caused by calcium leaching. It is suggested that the drop of elasticity of cement due to calcium leaching is the combined action of the increase of porosity due to portlandite dissolution and the loss of C-S-H elasticity resulting from its decalcification. They pointed out that the effect of decalcification is more significant on the loss of elasticity than the increase of porosity. Bernard et al. [40] used a similar micromechanical model for predicting elastic properties of hydrating cement paste but considered a Mori-Tanaka scheme for the two homogenisation steps. Ghabezloo [9], used also the microstructure representation proposed by Bernard et al. [40] but considered the self consistent scheme for the two homogenisation steps. A particular aspect of the model proposed by Ghabezloo is that the HD C-S-H phase is considered to be in undrained conditions as highlighted by experimental investigations of Ghabezloo et al. [3]. This micromechanical model is used for the extrapolation of the elastic and poro-elastic properties of a cement paste for different water to cement ratio and different chemical compositions [9, 10]. Sanahuja et al. [52] consider cement paste made up of clinker grains surrounded with a layer of denser inner product, ingrained in a matrix of low density C-S-H intermixed with capillary pores and used a Mori-Tanaka scheme for the homogenization of cement paste. The C-S-H gel and the C-S-H foam are homogenised through the self consistent scheme. A particular aspects of this model is the C-S-H particle shape which is supposed to be platelet-like (Figure 2.28). This model is used for predicting the elastic properties of hydrating cement paste.

Pichler and Helmich [104] modelled cement paste and mortar over three scales. The first two scales as presented in Figure 2.29 concern the homogenization of cement paste. The first step consists in an homogenization of a hydrate foam formed by

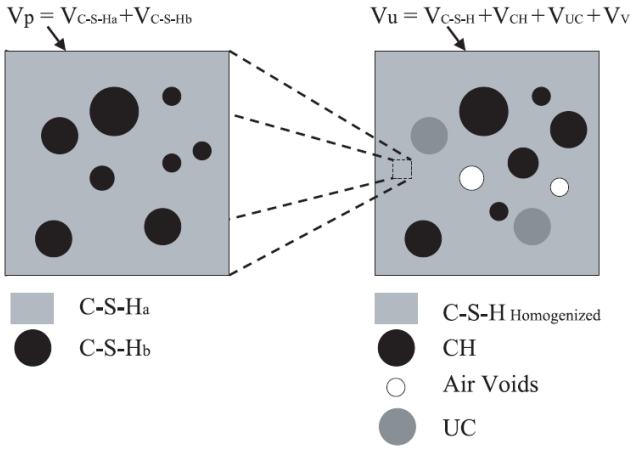

FIGURE 2.27: Representation of cement paste REV after Costantinides and Ulm [39]

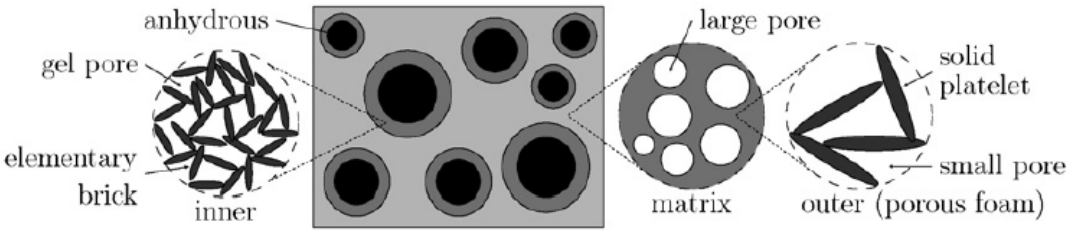

FIGURE 2.28: Representation of cement paste REV after Sanahuja et al. [52]

hydrates of a needle shape intermixed with spherical capillary pores and air voids through the self-consistent scheme. In a second step, spherical clinker grains embedded in the hydrate foam are homogenized through a Mori-Tanaka scheme to get the properties of cement paste. Pichler et al. [105] investigated through this model the effect of gel-space ratio and microstructural evolutions on the strength development of hydrating cement paste. In the different microstructure representations presented here different morphological aspects of inclusions were assumed, while some considered a spherical shape for hydrates [10, 39, 40], others regarded hydrates as needle-shaped [104, 106] or as platelets [52]. Stora et al. [107] and Pichler et al. [108] investigated the effect of the inclusion shapes on the micromechanical modelling of cement pastes properties. It is concluded that the spherical shape (infinite aspect ratio) lowers the apparent elastic stiffness of cement paste comparing to an acicular shape (aspect ratio of 1) [108]. The difference between predicted stiffness of acicular and spherical hydrates increases with increasing water to cement ratio and decreases with increasing hydration degree as seen in Figure 2.30. Pichler et al. [108] suggest that adopting a simple spherical shape for hydrates yields good estimates of elastic stiffness for mature cement pastes or cement pastes with low W/C. However, a cigar-like morphology seems more rational when modelling the properties of cement at early age. Stora et al. [107] compared the effect of inclusion shapes on modelling the properties of sound and leached cement paste [107]. While spherical inclusion shape yields good estimates of sound cement properties, it has an essential impact on leached cement paste,

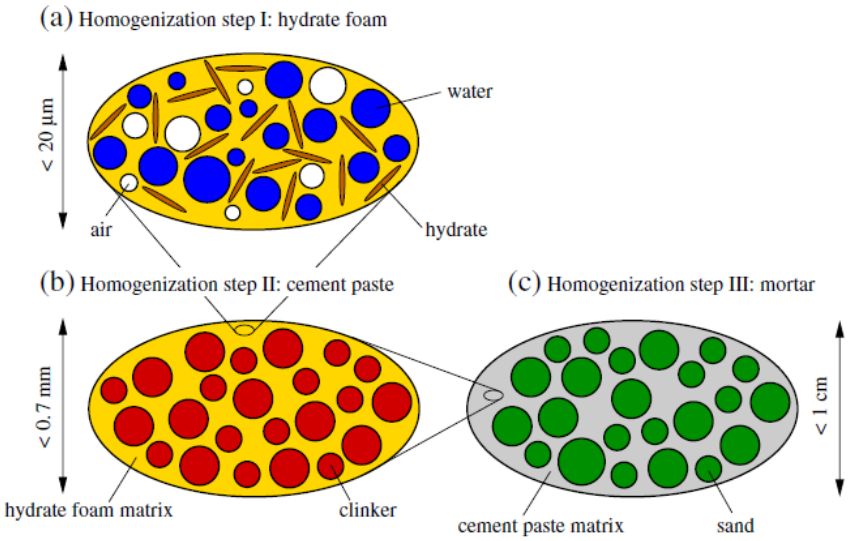

FIGURE 2.29: Representation of cement paste REV after Pichler and Helmich [104, 105]

which strengthens the evidence of approaching the shape of portlandite by more realistic morphologies for non-sound cement paste.

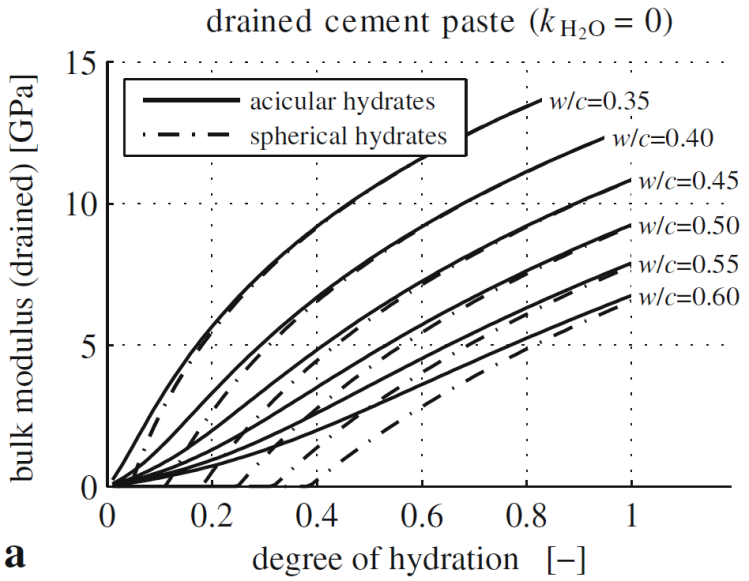

FIGURE 2.30: Predicted bulk modulus for drained cement paste at different W/C ratios using micromechanical modelling with different assumptions on hydrates shapes. Adapted from Pichler et al. [108]

2.8 Conclusions and knowledge gaps

This chapter introduced the variable aspects related to cementitious materials that are going to be used and discussed in this thesis. After a presentation of the leading hydration mechanisms, the different schematic and quantitative models describing the C-S-H structure have been presented. The available methods to dry cement pastes destined to various experiments are compared and their limitations and drawbacks are pointed out. A review of different findings regarding the effect of hydration temperature on cement microstructure has been presented and the trends of the main properties influenced by the hydration temperature were highlighted. The temperature has a significant influence on the microstructure of cement and its mechanical properties. It leads to an increase of the C-S-H density and an increase of the capillary porosity. It also results in some changes in the phase assemblage. All these changes cannot be quantified with the quantitative models of volume assemblage of Tennis and Jennings [14] or Powers and Brownyard [13] due to dependency of these models parameter on hydration temperature. Although the effect of temperature on the cement paste has been studied previously [75, 79, 80] an accurate quantitative evaluation of the microstructure is lacking, especially for a class G cement. For instance, evaluation of the C-S-H density, chemical composition and the related volume assemblage at different curing temperatures provided by recent studies of Gajewicz [79] concerns white cement paste. The complete characterization of the C-S-H pore structure in terms of HD and LD products at different hydration temperatures is also missing. These two limitations, concerning the volume assemblage and pore structure of cement explain the limited study of the effect of hydration temperature on cement paste mechanical properties though micromechanical modelling. Moreover, the origins behind the drop of elastic properties of cement with the increase of hydration temperature are conflicting. While some explains that this decrease in elastic properties is due to the increase of the capillary porosity [1, 20, 43], others showed that capillary porosity is a controlling factor but cannot fully describe the decrease of mechanical properties [86]. Further studies are needed, and this thesis is placed in the context of increasing the understanding of the effect of temperature on the evolution of cement based materials.

-

Chapter 3

Materials and methods

3.1 Introduction

This chapter is dedicated to the tested material and the experimental methods. The characterization of the microstructure is done by a combination of several methods. The chemical composition is investigated through X-Ray diffraction (XRD) combined with the Rietveld method, thermogravimetry analysis (TGA) and ^{27}Al NMR. The pore structure of hardened cement paste in this study is done by a combination of mercury intrusion porosimetry (MIP), Nitrogen and water vapor sorption (WVS) , ^{1}H nuclear magnetic resonance (^{1}H NMR). The macroscopic elastic properties of cement are evaluated through uniaxial compression tests.

The experimental methods used to probe cement microstructure are sensitive to drying methods. A comparison of some of these techniques is presented with the use of XRD, TGA, NMR, MIP, WVS.

3.2 Materials

The cement used in this study is a class G HSR (High Sulphate Resistant) cement provided by CBC company. This cement type has a specific chemical composition adapted for the use in oil-well constructions , water-wells and pipelines. The complexity of these constructions and the challenging conditions of temperature and pressure require controlling the thickening time, having a low viscosity, ensuring high resistance to aggressive environment, a high durability, and finally reduced segregation. API requirements for the chemical composition of this cement and physical properties are presented in Table 3.1.

Chemical composition		Physical properties	
Component	Wt %	Required property	Condition
Loss on ignition	3.0%	Free fluid (ml)	≤ 3.5
Insoluble residue	0.75%	Compressive Strength	
MgO	$\leq 6.0\%$	8h, 38°C at 10^5 Pa	$\geq 2.1 Mpa$
SO_3	$\leq 3.0\%$	8h, 60°C at 10^5 Pa	$\geq 10.3 Mpa$
C_3S	$\leq 65\%, \geq 48\%$	Thickening time (to 100 Bc)	$\leq 120 \geq 90$
C_3A	$\leq 3.0\%$	consistency after 30 min	$\leq 30 Bc$
C_4AF+2 *C_3A	$\leq 24\%$		
0.658*K_2O+Na_2O	$\leq 0.75\%$		

Table 3.1: API cement composition requirements and physical properties for a class HSR cement [109]

The phase composition of the tested cement clinker, obtained through XRF and also XRD combined with Rietveld Analysis are given in Table 3.2: The cement paste sam-

Chemical composition XRF		XRD - Rietveld	
Main oxides	Wt %	Phase Name	Wt %
SiO_2	19.14	C_3S Monoclinic	57.02
CaO	67.28	C_2S Beta	22.83
Al_2O_3	2.93	C_3A Cubic	1.33
Fe_2O_3	3.73	C_4AF	15.30
MgO	1.43	Gypsum	0.85
SO_3	2.5	Periclase	0.87
Na_2O	0.54	Calcite	0.65
TiO_2	0.40	Vaterite	0.88
LOI	2.40	Aragonite	0.27
K_2O	ns	Quartz	ns

ns: non significant

Table 3.2: Chemical composition of clinker from X-ray diffraction and Rietveld analysis

ples were prepared using a water to cement ratio of 0.44 according to the standard API requirements. The mix design of cement and the different used additives are presented in Table 3.3: The used water was distilled and degassed to remove different impuri-

Phase	Mass (g)
Cement	783.53
Water	339.54
Anti-foaming (D047)	6.27
Dispersant (D604AM)	9.47
Anti-settling (D153)	1.18

TABLE 3.3: The mix design for the preparation of 600 ml of cement slurry with a $w/c = 0.44$ and and density=1.90 $\mathrm{g/m^3}$

ties and air bubbles from the water. The water is mixed with the anti-sedimentation powder for 5 minutes at a velocity of 4000 rpm. The anti-foaming and the dispersant are then added successively and mixed for another 20 seconds. Finally, the cement powder is added and mixed for 35 seconds at 12000 rpm. After mixing, pastes were cured for different periods (1, 3, 7, 14, 28, 120 days) at different temperatures (7°C, 20°C, 40°C, 60°C, 90°C), under lime-saturated water in sealed containers to avoid water evaporation and carbonation of specimens.

3.3 Experimental methods

3.3.1 X-Ray diffraction analysis

X-Ray diffraction

The X-Ray diffraction or XRD is an outstanding tool used extensively to study the structure of crystalline materials and determine their composition. A typical experiment corresponds to bombing the material with a beam of X-rays. This causes the material to diffract the incidents rays in many directions characterized with angles. The experiment results in a list of angles and their associated intensities. The angles (or peak-positions) characterize the cell symmetry and size, and the intensities inform on the atomic distributions of atoms and are also related to the weight of the phase. The X-Ray diffraction has been widely used for the characterization of cementitious materials and the identification of the different hydration phases while varying the hydration conditions. In this study the XRD is used to determine the mass fractions of cement pastes hydrates and clinker phases.

The samples ground and sieved through the 32 μm mesh. Then, they have been mounted on sample holders by top loading passing through a 200 μm mesh to avoid segregation and preferred orientation. The surface of samples was cut off using a thin blade in perpendicular directions to avoid preferred orientation (PO) and minimize sample surface roughness. This preparation method has been shown to be less sensitive to preferred orientation than the ordinary compaction of samples [110].

The X-Ray patterns were obtained on a D8 advance diffractometer from Bruker operating at 35 kV and 40 mA, using CoKα (1.79 A) radiation at an angular step of 0.01°C per second between 3.0 ° and 80° [2θ] angles. The EVA software coupled

with the ICDD pdf-2 database enable the identification of the major phases present in the material.

Rietveld method

A quantitative analysis of the mineral phases identified with the X-ray diffraction pattern can be done using the Rietveld method. This method is based on a simulation of the whole XRD profile as a combination of the profiles of several single mineral phases. This is done by refining the structural parameters (lattice parameters, atomical positions and displacement parameters) and microstructural parameters (crystallite size and strain) of considered phases [111–113]. The refinement program adjusts the above-mentioned parameters in order to minimize the residual difference R_{wp} between the simulated profile y_{ci} and the measured one y_i using a non-linear least square algorithm [112]. The main equation used in the Rietveld refinements and the residual difference are given below:

$$y_{ci} = \sum\nolimits_p [S_p] \sum\nolimits_k p_k L_k F_k^2 G(2\theta_i - 2\theta_k) P_k + y_{cbi} \tag{3.1}$$

$$R_{wp} = \sum\nolimits_i W_i (y_i - y_{ci})^2 \tag{3.2}$$

where y_{ci} is the calculated intensity at a 2θ position and y_{cbi} is the background intensity at the i_{th} step. S_p is the scale factor of the p_{th} phase, L_k is the Lorentz and polarization factors for the k_{th} Bragg reflection. F_k is the structure factor, p_k is the multiplicity factor, P_k is the preferred orientation function, θ_{ik} is the Bragg angle for the k_{th} reflection, $G(2\theta_i - 2\theta_k)$ is the profile function and W_i is a weight factor taken equal to $W_i = 1/y_i$. For further details about the development of the equations of the structure factor and the profile function, one can refer to [111–115]. Compared to the single peak analysis method for phase quantification, the Rietveld method has the advantage of overcoming the peak overlap [112].

The difficulty in using the Rietveld method for hydrated cement pastes is related to the presence of poorly crystalline calcium silicate phases. This amorphous content yields to an increase of the hydrates mass fractions. This problem has been widely mentioned in the literature [111, 116]. Two-methods permit removing the contribution of amorphous material to crystalline phases: Internal and external method [117]. In this study the internal method has been used that requires the addition of a defined quantity of a standard material to the sample. The quantity of added standard material being known, the quantities of the other phases can hence be corrected [118–120]. We choose Corundum ($1\ \mu$m particle size powder) as an internal standard because of its non-reactivity with dried cement and adequacy in terms of absorption contrast for hydrated cement [68, Chapter 4]. $50\% - 50\%$ binary mixture of dried cement powder and Corundum was prepared following previous works [112, 121]. It should be mentioned that the Corundum has been added to the hardened cement paste after drying and grinding.

Refinement procedure

All Rietveld refinements reported in this study are done using commercial Topas 4.2 software. The refined parameters are the zero error, scale factors, lattice parameters, the preferred orientation according to the March Dollase model. The atomic positions and site occupancies of phases were kept fixed, except for C_4AF where a variable occupancy of aluminium and iron on tetrahedral and octahedral sites is expected [118]. The background has been described with a Chebyshev polynomial of the fifth order accompanied with the term 1/X. The considered phases in Rietveld refinements of hydrated cement pastes and their parameters are listed in Tab. 3.4.

The Rietveld refinement and the XRD experiments are used in this study to quantify the mass fractions of different hydrates and the hydration degree of clinker phases for various conditions of curing.

Phase	Formula	Crystal system	density
Alite	C_3S	Monoclinic/M3 Nishi et al. [122]	3.15
Belite	C_2S	Monoclinic/β Mumme et al. [123]	3.27
Aluminate	C_3A	Cubic	3.01
Brownmillerite	C_4AF	Orthorombic	3.73
Portlandite	CH	Rhombohedral	2.24
Calcite	$C\bar{C}$	Rhombohedral	2.71
Ettringite	$C_6A\bar{S}_3H_{32}$	Hexagonal	1.78

TABLE 3.4: Phases of cement microstructure considered in Rietveld refinements for hydrated cement pastes

3.3.2 Thermogravimetric analysis

Thermogravimetric analysis (TGA) is a technique in which the mass of a material submitted to a progressive heating is monitored as a function of temperature. It shows how the mass of a substance is altered due to changes of temperature. The mass difference is a result of degradation of the material, removal of moisture and the oxidation of components. A typical experiment corresponds to heating up a sample from room temperature to 1250°C at a fixed rate. It is widely used for the study of cement pastes to measure the bound water and the portlandite content. For ordinary cement pastes, we can distinguish three majors weight losses in TG and DTG curves (respectively, mass loss curve as a function of temperature and its derivative) associated to different reactions [124]:

- Up to 300°C: Dehydration of C-S-H and aluminates
- 400°C-550°C: Dehydroxylation of CH
- Above 600°C: Decarbonation of $CaCO_3$

It is a complementary method to XRD as it is able to detect amorphous phases. Furthermore, it seems more appropriate than XRD for measuring the portlandite content

for several reasons. First of all, the portlandite decomposition occurs in a unique interval. Secondly, TGA is able to detect even amourphous portlandite. Finally it is not sensitive to the preferred orientation as XRD [20, 68]. To quantify the total amount of portlandite the following expression is used [125, 126]:

$$f_{\mathrm{CH}}^{m} = L_{\mathrm{CH}} \frac{M_{\mathrm{CH}}}{M_{\mathrm{H_2O}}} + L_{\mathrm{CaCo_3}} \frac{M_{\mathrm{CH}}}{M_{\mathrm{CO_2}}} \tag{3.3}$$

where f_{CH}^{m} is the mass fraction of CH and M_X the molar mass of X. L_{CH} and L_{CaCo3} are the weight losses attributed to CH and $CaCO_3$ in their respective decomposition temperature domain. The first term accounts for the dehydroxylation of portlandite and the second term accounts for the carbonation of a certain quantity of portlandite, assuming that all the formed calcite is due to the portlandite carbonation. This carbonation process is supposed not to occur during TGA analysis under a nitrogen environment, but we suppose that the formation of calcite during the grinding process and preparation of material to XRD and TGA experiments is inevitable [68].

The quantification of C-S-H is quite difficult with this method as C-S-H, Aft and Afm phases loose their water in the same temperature range. Furthermore, the quantification of C-S-H relies on the knowledge of its molar mass and the number of water molecules in a C-S-H particle, which are not generally known and vary with the hydration conditions. The TGA experiments in this study are essentially destined to the evaluation of water bound to the C-S-H after drying and the assessment of portlandite content.

The experiments are carried out using a Netzsch Thermal Analyzer STA 409. Around 160 mg of powder is placed in a platinum crucible and heated up to 1250°C at a rate of 10°C/min under a nitrogen flow of 80 ml/min to prevent samples carbonation.

3.3.3 Mercury intrusion porosimetry

Mercury porosimetry (MIP) is a widespread tool for characterizing the porous structure of materials. The high surface tension of mercury opposes its entry into the pores, making it a non-wetting fluid. When increasing the pressure, the mercury is forced into the pores with an entry size depending on the applied pressure. Assuming a cylindrical pore geometry, the applied pressure can be related to equivalent pore sizes using the Washburn equation given below [21]:

$$P_{\mathrm{HG}} = \frac{4\gamma \cos(\theta)}{d} \tag{3.4}$$

Where d is the pore diameter in (m), γ is the surface tension of mercury (0.485 N/m), θ the contact angle between mercury and the pore surface. $\theta = 130°$ is commonly adopted for cement based materials [127–130] and is used in this work. The Washburn relation permits to evaluate the pore entry size corresponding to each pressure level (increased progressively) and to obtain a pore volume-pore size curve. It should be noted that the application of MIP for the characterization of the pore volume of

cement based materials has been often criticized in the literature (e.g. [131]) and its limitations have been pointed out. The most important failure of the MIP can be illustrated in Figure 3.1. In fact in situation (a) in Figure 3.1, the Washburn model will detect both pore sizes and their relative pore volumes. However, in situation (b) (Figure 3.1) it will assign all the intruded pore volume of large and small pores to the pore size of the small pore. Furthermore, situation (b) is very frequent in cement paste due to the so called ink-bottle effect that is often invoked to explain the hysteric behaviour of water or nitrogen sorption isotherm. This failure of the Washburn model will results in a wrong determination of the pore sizes and an underestimation of the volume of macropores attached to smaller pores. However, for capillary porosity estimations, other available methods for instance NMR [50] and SEM [80] have also their own limitations and give capillary porosity estimations which are sometimes lower than expected values. The MIP will be used in this study to investigate the capillary domain of porosity within a cement paste. Its limitations are going to be examined and argued. Specimens destined to MIP testing were freeze-dried prior to testing.

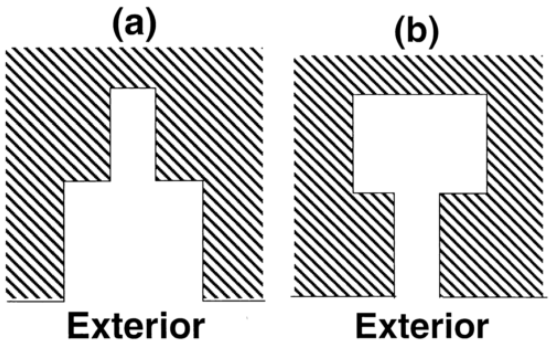

FIGURE 3.1: Illustration of (a) a small cylindrical pore connected to the exterior through a large cylindrical pore and (b) a large cylindrical pore connected to the exterior through a small pore

The porosimeter used in this study is an AutoPore IV 9500 from Micrometrics reaching a maximum pressure of 230 MPa corresponding to a pore size of 6 nm.

3.3.4 Sorption isotherm

Nitrogen sorption

Nitrogen adsorption and desorption (NAD) is a prominent method for studying the pore structure of materials. It has the advantage to cover the range of radii between 1 nm and 60 nm. The principal of the method relies on recoding the amount of adsorbed or desorbed nitrogen at different relative pressures, yielding a nitrogen adsorption/desorption isotherm. It usually serves determining the specific area of cement pastes and to study its porosity. The results of Nitrogen porosity and surface area measurements present some challenges in their interpretation when compared to results of water vapor sorption for instance [21]. Despite these complications in the

interpretation, the NAD experiments if interpreted properly, can provide useful information about the cement pore structure. NAD experiments require pretreatment of tested samples to enable adsorption of the Nitrogen. Yet, NAD experiments are very sensitive to the drying method and results vary depending on the amount of moisture removed by each drying methods [22, 64]. Among various drying methods compared in the study of Juenger et al. [64], the D-drying seemed the most consistent and reliable. The Freeze-drying however wasn't considered in the study of Juenger et al. [64]. Korpa et al. [65], showed that freeze-drying is preferred to D-drying and other common methods. In this study , we use freeze-drying to treat the specimens destined for BET experiments.

Water vapor sorption

Water vapor sorption isotherms correspond to the plot of water content of a material against the relative humidity RH. The water sorption isotherms were collected here through the gravimetric method. The experiments correspond to equilibrating specimens in a sealed desiccator at a given relative humidity. The RH within a desiccator is controlled by saturated salt solution in isothermal conditions (T= 20°C) as described in Table 3.5. Specimens destined to water vapour sorption were wet sawed from cylinders cured under water in sealed conditions to prevent external pre-drying and carbonation. Thin specimens of 4 to 5 mm of thickness were prepared in order to reach equilibrium within a reasonable time [132, 133]. The samples are equilibrated at a given relative humidity for at least six months, and then a step by step adsorption curve is collected. A measure of the sample weight before (m_{sat}) and after (m_{dry}) placing it in the desiccator is primordial in order to assess the saturation degree S_r of the sample for each relative humidity (RH) as giving by the equation below:

$$S_r(RH) = 1 - \frac{(m_{\mathrm{sat}} - m_{\mathrm{dry}}(RH))/\rho_{\mathrm{w}}}{\phi_{\mathrm{total}} m_{\mathrm{sat}}/\rho_{\mathrm{CP}}} \tag{3.5}$$

where ρ_{CP}, ρ_{w} and ϕ_{total} are respectively the saturated cement paste density, the water density and the cement total porosity. It can be seen that the evaluation of the S_r reposes on the determination of the total porosity of the sample. In the experiments related to water vapor sorption, drying at 105°C is commonly used to evaluate cement total porosity [134, 135]. Baroghel-Bouny [132, 133] however preferred drying at 3% that helps avoiding the less controlled environment of Oven-drying. In this study we collect two adsorption isotherm. The first one is conducted on an oven-dried specimen at 105 °C. The second one is acquired by adsorbing the water vapor starting from a relative humidity of 11 %RH.

BJH method

The pore size distribution of materials can be obtained from the isotherm sorption through the derivation of the cumulative pore volume with respect to the pore size. Several algorithms exist for the extraction of pores sizes. Among these algorithms the BJH (Barrett Joyner Halenda) method [136] is the most used for determining the

Saturated salt solution		
Name	Formula	Relative Humidity
Lithium chloride	LiCl	11%
Potassium acetate	CH_3CO_2K	20%
Magnesium chloride	$MgCl_2$	33%
Potassium carbonate	K_2CO_3	44%
Magnesium nitrate	MgN_2O6	55%
Sodium chloride	NaCl	75%
Ammonium sulfate	$(NH_4)_2SO_4$	81%
Sodium sulfite	Na_2SO_3	95.5%

TABLE 3.5: Relative humidity controlled by saturated salt solutions at ambient temperatures

pore size distribution. The basic equation used for the extraction of pore sizes is the Laplace-Kelvin equation. This equation determines the radius of a cylindrical pore into which capillary condensation occurs at a relative pressure. For a cylindrical pore the Laplace-Kelvin equation can be written as follows:

$$r_{\mathrm{k}} = -\frac{2\gamma\, V_{\mathrm{m}} \cos(\theta)}{RT \ln(RH)} \tag{3.6}$$

Where γ is the surface tension at the liquid–vapour interface, V_{m} is the molar volume of the liquid, θ is the contact angle between the liquid and the pore wall, R is the gas constant, and finally T is the temperature.

However, Laplace-Kelvin equation ignores the fact that adsorption inside the pore is not only caused by capillary condensation, but also by adsorption on the pore walls as presented in Figure 3.2. In a similar manner, it ignores the adsorbed film that remains on the pore walls while the capillary condensate evaporates during desorption. The

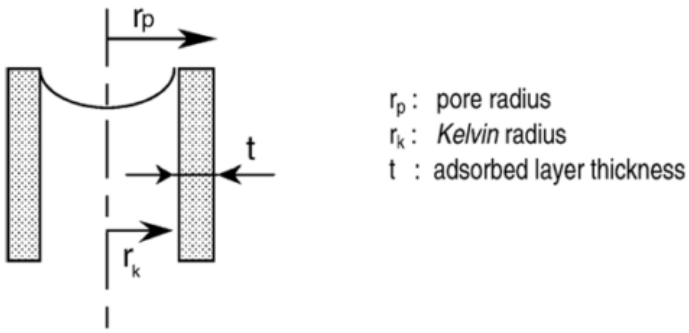

FIGURE 3.2: BJH model: the coexistence of capillary condensate and an adsorbed film within a cylindrical pore [132]

BJH method tries to correct this shortcoming of Laplace-Kelvin equation. In this method the Laplace-Kelvin equation is corrected by the addition of the film thickness t to the pore radius determined by the Laplace-Kelvin equation $\mathrm{r_k}$ to get the real pore

size of the pore r_p:

$$r_p = r_k + t \tag{3.7}$$

where t is the thickness of the adsorbed film. The thickness of this film vary with the relative pressure and the adsorbate and can be determined either experimentally [137, 138] or from theoretical calculations [21]. Experimental statistical thickness curves provided by Badmann et al. [138] and Hagymassy et al. [137] are very relevant for cement paste [132, 139] and provide comparable results. In this study the t-curve is taken from the experimental work of Hagymassy et al. [137]. The main equations of

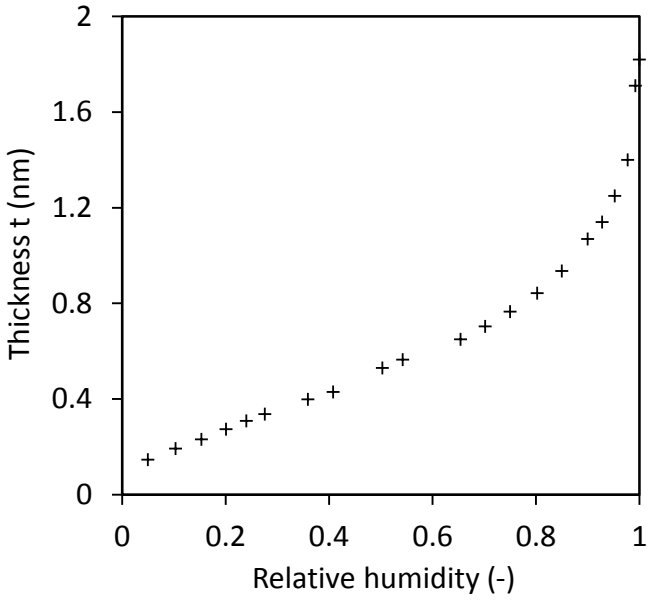

FIGURE 3.3: The thickness curve after Hagymassy et al. [140]

the BJH method are presented in the following after Llewellyn et al. [141]. The pore radius of a dried pore at a certain step is the average of the pore radii in contact with the non-wetting fluid between the start and the end of the step 3.8:

$$\overline{r}_{p,n} = \frac{(r_{p,n} + r_{p,n-1})}{2} \tag{3.8}$$

Regarding the distribution of adsorbate in pores, the removed moisture $\delta V_{p,n}$ is the sum of water from pores emptying from their capillary condensate and the water from the decrease of the film thickness as the relative pressure is lowered as presented in Figure 3.4 and recapitulated by Equation 3.9 [136].

$$\delta V_{p,n} = \left(\frac{\overline{r}_{p,n}}{\overline{r}_{p,n} - t_n}\right)^2 \left(\delta V_{l,n} - \delta t_n \left[\sum_{i=1}^{n-1} \Delta a_{p,i} \left(1 - \frac{t_n}{\overline{r}_{p,i}}\right)\right]\right) \tag{3.9}$$

where $\Delta a_{p,i} = \frac{2\delta V_{p,i}}{\overline{r}_{p,i}}$. This results in the cumulative surface area $a_{p,cum} = \sum_{i=1}^{n} \Delta a_{p,i}$

and the cumulative pore volume $V_{p,cum} = \sum_{i=1}^{n} \Delta V_{p,i}$ and also in the pore size distribution.

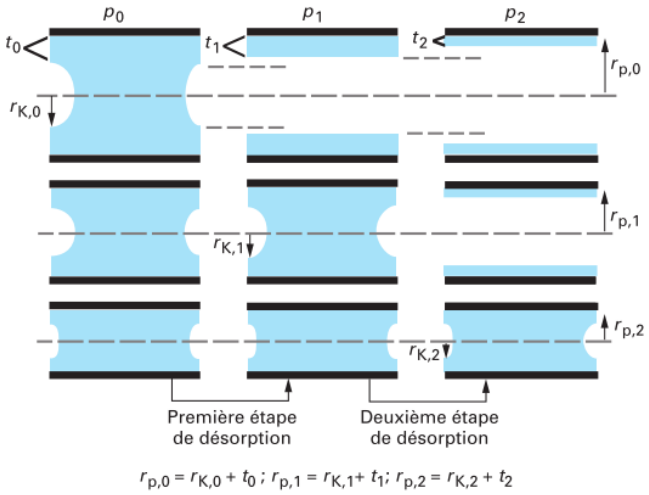

FIGURE 3.4: The first desorption steps of BJH model [141]

3.3.5 Scanning electron microscopy

Scanning electron microscopy (SEM) is a powerful observation method of the cement microstructure. The sample is subjected to a beam of electrons that colloid with atoms of the matter. These collisions generate signals that are detected and used to form the image. Different types of signals are generated depending on the nature of the collisions. The BSE signal (backscattered electrons) that will be used here are informative on the atomic number of the atoms in the sample. Hence, the intensities of BSE report the contrast of the chemical composition of the tested material. It essentially permits a visual identification of cement hydrates. We can distinguish within a cement paste between anhydrous clinker, portlandite, C-S-H and the pores as seen in Figure 3.5. It also gives an idea about the pore sizes and voids distribution. However, this technique has its limitations as well. It is not capable of detecting the smallest pores below 100 nm. It can only provide an idea about the very wide pores. Furthermore, the polishing procedure to make a flat surface prior to the analysis, induces cracks and overestimates the observed porosity. The evaluation of the porosity from the grey level of the image is another challenge in the use of SEM. The SEM-BSE images in this study are used for a visual identification of hydrates distribution and qualitative study of the pore structure.

Samples for SEM & BSE observations were impregnated in an epoxy resin (Figure 3.6) and kept under vacuum for 24 hours. They were then polished by decreasing the diamond powders diameters down to 1 μm. The samples then were vacuum-dried gently for 1 hour to remove the free water. Environmental scanning electron microscope (Env. SEM, Quanta 400from FEI company) coupled with energy dispersive X-ray spectrometry (EDX from EDAX company) are used to observe the microstructure of cement cured at different temperatures at an accelerating voltage of 15 kV.

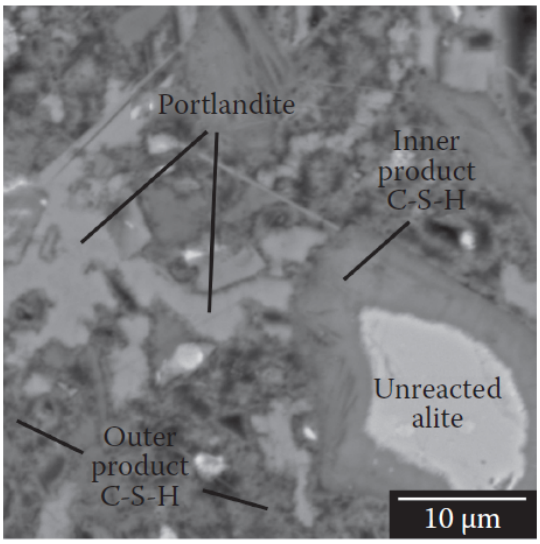

FIGURE 3.5: A typical BSE image on a hydrated cement paste[68]

Chemical X-ray microanalysis was carried out using a PGT Si(Li) energy dispersive spectrometer (EDS).

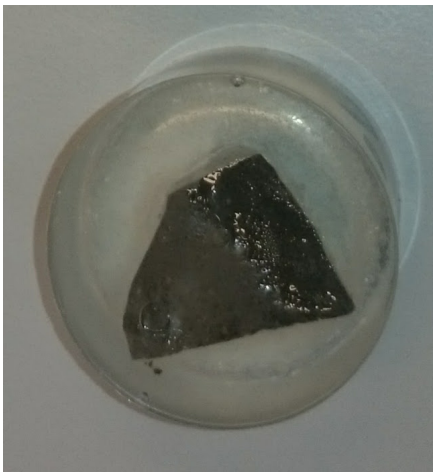

FIGURE 3.6: A sample impregnated in an epoxy resin prior to polishing

3.3.6 Nuclear magnetic resonance NMR

Basics of NMR method

^1H Nuclear magnetic resonance has proved to be a powerful non-destructive and non-invasive method for probing the water state in cement materials [49–51, 142–146]. The analysis of relaxation curves of cement water is of particular interest as it provides insight on the pore structure of cement, even de smallest pores that are not accessible to Nitrogen and Mercury intrusion. The nuclei of an atom is assimilated to a spherical charged particle that possesses a kinetic moment (I) and magnetic moment (μ) related

to each other with the equation below:

$$\mu = \gamma I \tag{3.10}$$

where γ is the gyromagnetic ratio. The spins of nuclei (magnetic moment) in the absence of an external magnetic field are oriented randomly. However, when they are exposed to a strong magnetic field B_0, the spins align themselves to the direction of the magnetic field. They precess around the axis defined by B_0 at a defined frequency called the Larmor frequency equal to $\omega_0 = \gamma B_0$. The ^1H nuclei has a quantum spin number $I = \frac{1}{2}$. This spin number defines the number of orientation states of a spin. For instance, for ^1H two energy states $(2\frac{1}{2}+1)$ can be defined: spin up state "parallel to the magnetic field" and spin down "antiparallel to the magnetic field". After the application of a static external field the number of spins in the upper energy level is slightly lower than that of the spins in the inferior energy level. The excess of spin in one energy state results in an excess of magnetization in the direction of the applied field B_0 (Figure 3.7(a)). After this step called polarisation (subjecting the matter to a static magnetic field), the net magnetization created along the Z-axis due to the energy difference between the states up and down can be handled in order to create other phenomena [21, 68, 147]. The application of another electromagnetic radiation B_1 oscillating perpendicular to B_0 at the Larmor frequency ω_0 tips the magnetization away from the z-axis. The spins are now spinning around B_0 and B_1 (Figure 3.7(b)). This oscillating field disturbs the equilibrium between the two energy levels. When the oscillating field is halted the initial distribution of spins up and down is regained, the process of regaining the equilibrium consists in releasing energy 'relaxation phenomenon'. The relaxation phenomenon occurs because an excess of energy and phase coherence are given to a nuclei by the application of an external field [21, 68, 147]. It consists of a release of the adsorbed energy and the return to equilibrium. It leads to the irradiation of a signal that is called NMR signal and which contains the invaluable information about the pore structure. More details on the NMR theory can be found in [21, 68, 147–149].

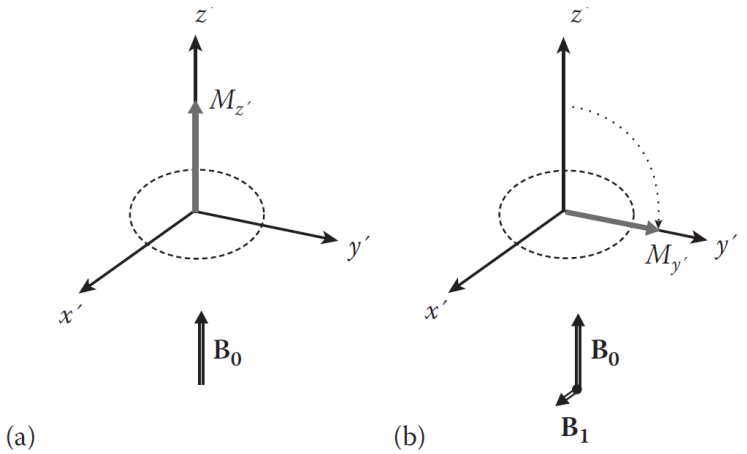

FIGURE 3.7: (a) The net magnetization along the z-axis after the application of a static field (b) excited spins after the application of an oscillating field (Figure adapted from [68])

Characterization method of NMR

The relaxation is characterized with two relaxation times, initiated by different mechanisms:

- T_2 value corresponds to the transverse relaxation, also called 'spin-spin' relaxation. It consists in the loss of coherence between the spins in the plane perpendicular to B_0. This relaxation time can be measured through a Carr-Purcell-Meiboom-Gill (CPMG) sequence.
- T_1 value corresponds to the longitudinal relaxation, also called 'spin-lattice' relaxation. It characterises the process that bring the magnetization again to the z-axis and establishes the initial Boltzmann distribution. The measurement of T_1 can be measured with inversion recovery or saturation recovery sequences.

The loss of coherence between spins occurs before the full recovery of magnetization on the z-axis. Thus, the T_2 is much shorter than T_1. A ratio of 4 between T_1 and T_2 at 20 MHz has been mentioned by McDonald et al. [146] for bulk liquids. In this study we will focus on the measurement of the T_1 relaxation time for two reasons: the first one is that these measurements are less sensitive to the field inhomogeneity, the second one is that we are working with grey cement with significant amount of paramagnetic impurities leading to a faster relaxation. As the T_2 are much smaller than T_1, an important part of the signal will be lost during T_2 measurement comparing to a T_1 measurement. The T_1 is measured by an inversion recovery sequence. It consists in an application of a 180° pulse followed by a 90° after an interval of time τ. The time τ is varied and the signal is fitted by an exponential curve to extract the values of T_1 as presented in Figure 3.8.

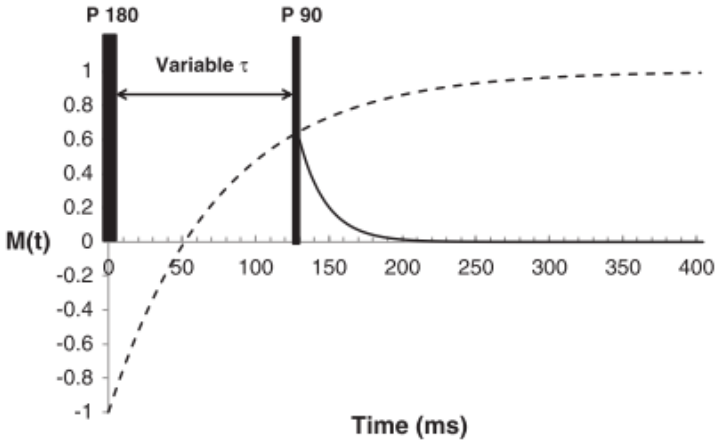

FIGURE 3.8: Inversion recovery pulse sequence to measure the T_1 relaxation time [51]

NMR studies were conducted a Bruker Minispec spectrometer operating at a hydrogen resonance frequency of 20 MHz. The samples are directly casted in NMR tubes with an internal diameter of 15 mm while ensuring a sample height around one centimeter. An inversion recovery sequences were programmed in order to get the T_1 relaxation time distributions at different temperatures. For each T_1 measurement, 60

different τ values were logarithmically distributed between 10 μs and 200 ms. 64 scans were accumulated for each measure with a recycle delay of 200 ms so that a complete relaxation measurement takes approximately 8 min.

Calculations of pore size

Considerable efforts have been devoted to the development of mathematical equations to extract the pore size distribution from NMR experiments. The most relevant model that is currently used by researchers for extracting the pore size from the NMR data is the Fast diffusion exchange model. This model considers two different magnetic varieties in the pore. A bulk phase with a specific relaxation time referred to as ${T_{1,2}}^{\text{bulk}}$ and a surface phase with a much faster relaxation described by ${T_{1,2}}^{\text{surf}}$. According to this model, the total recorded relaxation time is given by the following equation 3.11:

$$\frac{1}{T_{1,2}^{\text{obs}}} = \frac{\epsilon S}{V}\frac{1}{{T_{1,2}}^{\text{surf}}} + \frac{v-\epsilon S}{V}\frac{1}{{T_{1,2}}^{\text{bulk}}} \tag{3.11}$$

Where S, V and ϵ are respectively the pore surface, the pore volume and the water layer thickness. When the bulk relaxation time ${T_{1,2}}^{\text{bulk}}$ (seconds) is much greater than the surface relaxation time ${T_{1,2}}^{\text{surf}}$ (microseconds) the above mentioned equation is reduced to $\frac{1}{T_{1,2}} = \frac{\epsilon S}{V}\frac{1}{{T_{1,2}}^{\text{surf}}}$. This results in the following equation relating the pore relaxation time to the ratio of the volume of a pore V to its surface S:

$$\frac{1}{T_{1,2}} = \lambda\frac{S}{V} \tag{3.12}$$

Where λ is the surface relaxivity parameter supposed to be constant through the sample and depends essentially on the Fe^{3+} surface density, temperature, pore fluid composition and magnetic field strength. The determination of λ is problematic. Generally, one relaxation time from the NMR experiment is assigned to the median pore size obtained through MIP or Nitrogen pore size distribution and λ is obtained after measurement of ${T_{1,2}}^{\text{surf}}$. Another method that seems more accurate is to calculate the surface relaxivity from measurement of surface relaxation time ${T_{1,2}}^{\text{surf}}$ of a sample dried up to a monolayer coverage of water with a thickness of 0.28 nm [79, 150]. Drying cement paste up to 11% RH leaves a monolayer of water covering the surface of C-S-H [35]. The water molecule diameter equal to 0.28 nm, results in a surface relaxivity $\lambda = \frac{0.28}{{T_{1,2}}^{surf}}$. The surface relaxation time of cement equilibrated at 11%RH is equal to ${T_1}^{surf} = 129\mu$s providing a surface relaxivity of 2.17 nm/ms. A planar shape is assumed with a width equal to $d = 2\lambda{T_1}^{surf}$.

Data inversion

The inversion of the NMR signal in order to extract intensities and their relative relaxation times is done through a program made in our laboratory by Stéphane Rodts [49].

It is similar to the well known Contin program made by Provencher [151]. This program consist in approximating the relaxation data as a sum of mono-exponential signals. The stability of the fitting is ensured by the Tikhonov regularization constraint as presented in equation 3.13 by the addition of a non-negative constraint applied to the parameters a_p:

$$\mathrm{Min}_{a_p>0} \underbrace{\sum_i (s(t_i) - s_\infty + \sum_i a_p \exp(\frac{t_i}{T_p}))}_{\text{Leastsquarefit}} + \lambda \underbrace{\sum_p (a_{p-1} - 2a_p + a_{p+1})}_{\text{Tikhonovconstraint}} \quad (3.13)$$

where the a_p vs T_p is the distribution of relaxation time that we want to get. The regularization or parsimony λ is a constant that controls the sensitivity of the inversion by weighing the noise of the data. The choice of low λ may result in the resolution of non physical peaks. A high λ cannot resolve the different peaks of the microstructure. In the home made program a method for choosing the λ has been set depending on the noise of data. This automatic choice has been adopted here and seemed to be more repeatable and physical than fixing a constant parsimony parameter. The effect of λ on T_1 distribution is presented in Figure 3.9. The automatic parsimony parameter was reduced each time by 10^x where $x \in$ [1,2,3] starting from the one automatically determined up to 10^{-5}. The resolved peaks are getting thinner and one further peak is resolved. However, when varying the parsimony parameter of a T_2 experiment its effect is more pronounced, leading to the development of various tiny peaks at lower values of λ.

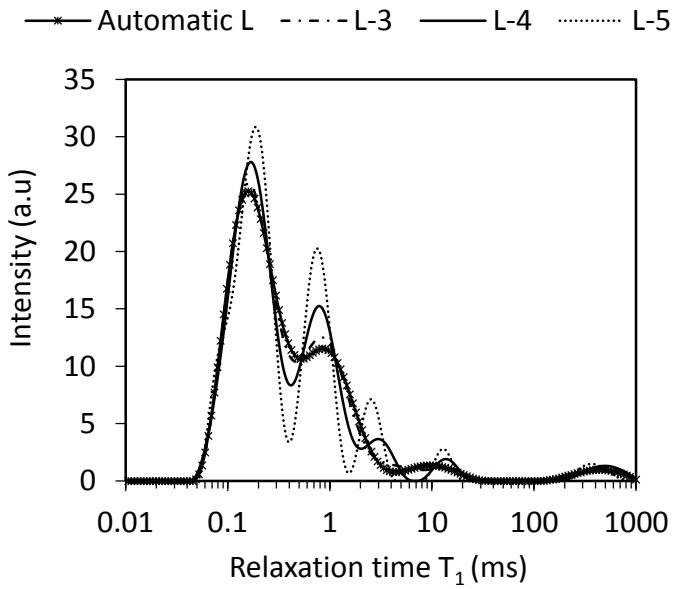

FIGURE 3.9: Influence of the parsimony parameter on the Laplace inversion

Effect of iron presence

Grey cement contains high amounts of Iron. This leads to a high concentration of paramagnetic ions in small pores, and causes a rapid drop of signal intensity leading to shorter relaxations times, caused by a higher relaxivity. The signal lifetime being shorten, leads to a significant loss of information for shorter relaxation times as some echoes are not recorded. For instance, in case of a T_2 measurement, solid echoes of portlandite and ettringite cannot be recorded as a result of high impurities concentrations [49, 51, 145]. In order to investigate the effect of the Iron presence in our T_1 measurements, two cement pastes prepared with different types of cement (White and Class G cement) at a water to cement ratio of 0.44 and hydrated for six months, are compared in Figure 3.10. It can be clearly seen that the relaxation times of grey cement are smaller than those of a white cement which is in agreement with the well established high relaxivity of grey cements. However, the description of the pore structure and the quantitative information regarding the intensity of each pore reservoir are still meaningful. Table 3.6 compares the ratio of T_1 of white and grey cement for an identified pore category and shows that this report is ranging from 4 to 5.25. The intensity of each pore category is providing consistent and comparable values which are almost equal for both white and grey cement. It should be noted that the slight discrepancies between the values obtained for a white cement paste and the grey one are not surprising, since their composition is different and should result in some differences in the microstructure. From this comparison it can be concluded that although the signal life time is shorten in the presence of Iron, quantitative interpretation of T_1 measurements is still relevant.

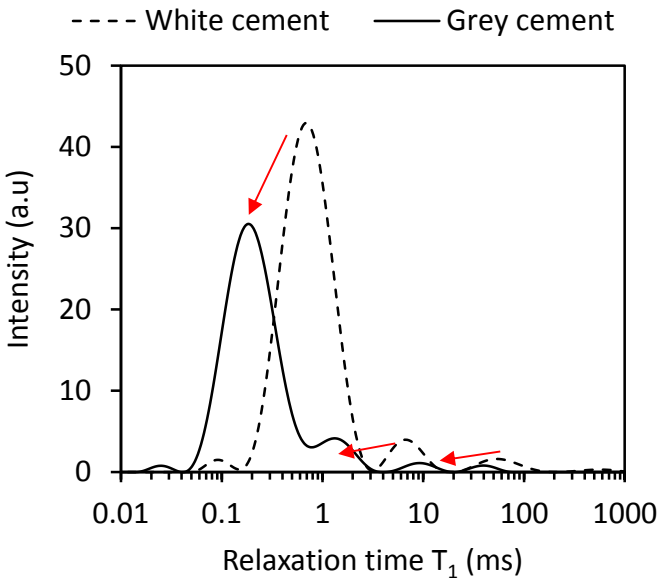

FIGURE 3.10: Comparison of T_1 relaxation times for white and grey cement

	T_1 (ms)		
	Peak_1	Peak_2	Peak_3
White cement	0.73	6.74	54.16
Class G cement	0.18	1.36	9.54
$\frac{{T_1}^{WC}}{{T_1}^{GC}}$	4.05	4.95	5.25
	Intensity relative to each peak		
White cement	0.91	0.05	0.03
Class G cement	0.89	0.08	0.028

TABLE 3.6: Comparison of relaxation times and peak intensities of white and grey cement paste hydrated for fix months

3.3.7 ^{27}Al solid state NMR

^{27}Al-SSNMR (solid state NMR) spectroscopy is a useful technique for analysing the local structure of both crystalline and amorphous materials [68, 147]. It provides insight on local structural ordering of atoms and their coordination. The key source of structural information in high-resolution NMR spectroscopy is the chemical shift. This chemical shift results from the shielding of the spin nucleus from the external magnetic field by the induced magnetic field due to electrons motions in the surrounding of nucleus. Here, we performed ^{27}Al magic-angle spinning nuclear magnetic resonance (MAS-NMR) experiments, at 208.5 MHz on a 18.8 T spectrometer equipped with a 3.2 mm probe head operating at a spinning frequency of 22 kHz. The record was carried out with 1 μs pulse length with a recycle delay of 0.5 s. The accumulation of 10000 scans permitted to have an appropriate signal to noise ratio for this cement. An experiment lasts approximately one hour. However, the obtained spectra are only qualitative because of the high iron amount in the cement paste and

it is recommended not to analyse quantitatively iron-rich cement pastes [68]. The ^{27}Al-NMR characterizations presented in this thesis were carried out in LAboratoire de Spectrochimie Infrarouge et Raman (LASIR) at Lille University of Science and Technology in France, by Julien Trébosc.

3.3.8 Uniaxial compression tests

Uniaxial compression test is one of the most common tests to characterise the mechanical behaviour of materials. It enables evaluating the compressive strength, the static Young's modulus and the Poisson's ratio of a material. The procedure of test is described by the ASTM 39 [152]. It consists of confining a specimen between two bearing blocks and controlling either the load or the displacement. The load is measured with a load sensor. Strains are measured through two strain gauges glued on the surface of the specimen perpendicular to each other. The results of this experiment yield curves of stress-strain or strain-strain. The maximum load over the cross sectional area gives the compressive strength. The slope over the elastic range of strain of the curve axial stress-axial strain yields the static Young's modulus. The Poisson's ratio is equal to the slope over the elastic domain of the curve radial strain-axial strain. Care should be paid to the surface of the specimens in contact with the bearing blocks that have to be smooth enough and perpendicular to the central line of the specimen to avoid stress concentration. Moreover, a length to diameter ratio of 2 has to be chosen in order to fulfil the standard requirements. Cylinders of length 8 cm and a diameter of 4 cm were tested.

3.4 Drying method effects on results of various characterization methods

As presented in the review of the influence of drying techniques on the microstructure in Chapter 2, the characterization of the cement microstructure is very critical to the drying method. The MIP, XRD, BET specific surface area and other experimental results vary significantly with the used drying method. Furthermore, the evaluation of the porosity of cement is very complicated as various porosity evaluation methods can result in different values for the total porosity. This is mainly due to the multiscale porosity of cement paste, covering sizes of several orders of magnitude, and to the fact that each method dries a certain pore reservoir. There exist different drying methods which are commonly used for porosity measurement. However which reservoir of porosity is being dried with each drying method is not well understood. Oven-drying as at 105°C has been used regularly, but it is considered to be non-accurate in estimating total porosity. As at 105°C a quantity of the water in the interlayer space, which is not regarded as porosity, evaporates [20, 63]. The quantity of evaporated interlayer water at 105°C is not clearly known. Another method which has been regularly used for cement paste is drying at 11% relative humidity which can be considered as a reference method based on previous studies of Feldman [153] showing that this condition corresponds to a full interlayer space with a monolayer of water encountering

the C-S-H globules. Hence, equilibrating a sample at 11% RH corresponds to a C-S-H with dried gel pores and full interlayer spaces. Freeze-drying is also regularly performed because of its rapidity, but the amount of water removed by freeze-drying is not known. In this study, we will compare two of the usually used methods for evaluating of the total porosity and stopping the hydration (oven-drying at 105°C and freeze-drying) with the drying at 11% RH that has been poorly compared to them. XRD, TGA, MIP, NMR and WVS are conducted on cement pastes hydrated for 4 months at 20°C and dried by different means: (Oven-drying: OD, Freeze-drying: FD and drying at 11% RH).

3.4.1 Thermogravimetric analysis TGA

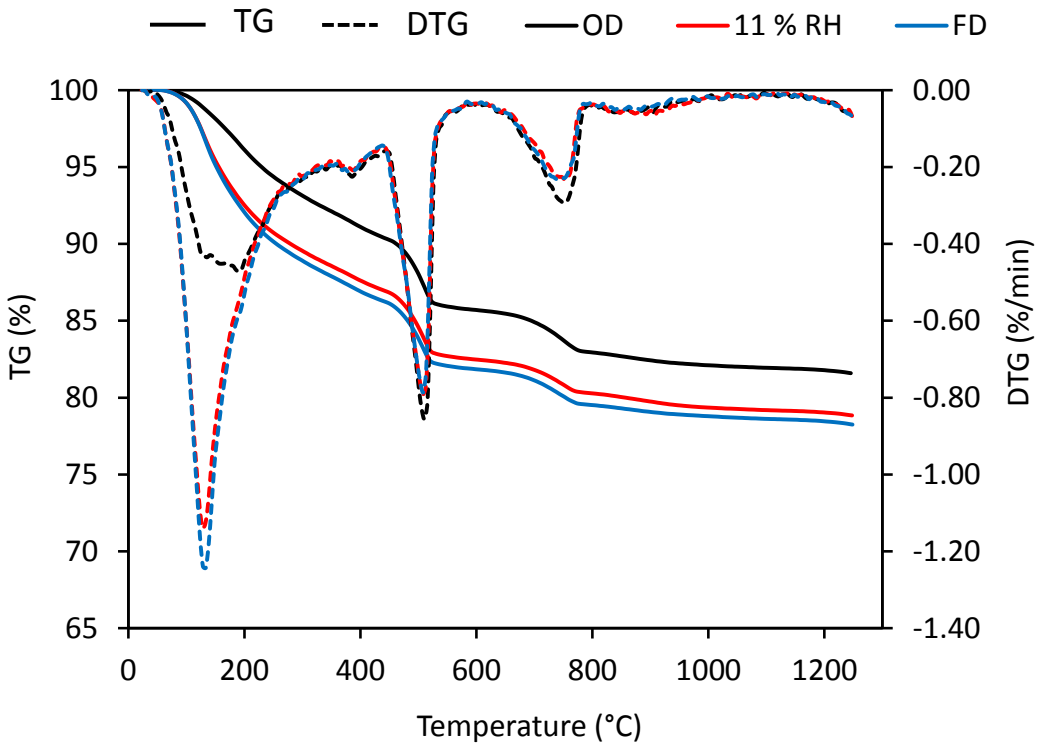

FIGURE 3.11: Thermogravimetric weight loss for cement class G cured at ambient temperature dried by different means (Oven-drying (OD), Freeze-drying (FD) and at 11% of relative humidity (11% RH)

The results of TGA experiments conducted on samples dried with different means are presented in Figure 3.11. It is worth recalling that the C-S-H dehydration occurs up to 300°C. The oven dried specimen at 105°C showed a smaller weight loss over the range associated to C-S-H, as compared to the ones of freeze-drying and 11% RH drying. However, the freeze dried specimen and the one dried at 11% RH present almost the same weight loss. Previous studies [153] suggested that the drying at 11% RH removes the gel pore water and leaves the interlayer full of water. By comparing the

TGA curves of oven-drying at 105°C and the drying at 11% RH, it can be confirmed that the oven-drying at 105°C removes a part of the interlayer water from the C-S-H. The oven-drying removes approximately 34% of interlayer water comparing to the drying at 11% RH as suggested from TGA experiments. This value agrees with previous findings of the H/S ratio. The H/S of an oven-dried C-S-H at a hardened state is equal to 1.4 [20, 35] and the H/S of an 11% RH-dried cement is around to 2.1 estimating 33.3%=$\frac{2.1-1.4}{2.1}$ of water loss during oven-drying comparing to drying at 11%.

The interesting similarity between TGA curves of freeze dried and 11% RH-dried samples illustrates that these two drying techniques empty almost the same pore reservoirs, with a negligible quantity of water residing in gel pores of freeze dried specimens as its curve departs slightly from TGA curve of 11%RH-dried ones. Given this similarity, we can conclude that freeze-drying removes the water in gel pores and leaves the interlayer spaces full of water and some physical water adsorbed on the surface of the C-S-H. Because of its rapidity compared to drying at 11% RH and the similarity of the the dried states, the freeze-drying may be preferred to dry specimens and to evaluate the total porosity. The porosity evaluated from the mass loss during freeze-drying can be assimilated to the cement total porosity. The quantity of water that lasts in the C-S-H after freeze-drying can be a good estimation of interlayer water. Regarding the portlandite content (associated to the range of 400°C-550°C), it seems that the compared drying techniques do not have an influence on the estimated CH content. The weight loss corresponding to portlandite is almost similar for the three methods. However, a slight increase of the carbonation degree (associated to the range of 600°C-900°C) of the specimens can be observed in case the oven-drying at 105°C is used because of the non-controlled environment. The portlandite and calcite contents are presented in the following.

3.4.2 X-Ray diffraction XRD and Rietveld analysis

The diffractograms of cement paste hydrated at ambient temperatures for four months and dried by three different means are presented in Figure 3.12. It seems that these hydration stoppage methods have the same influence on the microstructure of cement in terms of hydrates composition as the diffractograms are almost identical for the used drying methods. The mass assemblage obtained from Rietveld analysis on cement pastes hydrated at 20°C dried by different means is presented in Table 3.7. Similar to previous remarks, the phase assemblage is slightly influenced with the drying methods. The portlandite and the C-S-H content are quite similar for the used drying methods. Furthermore, the overall hydration degree is not influenced. An increase in the carbonation of the specimens can be noticed in the case of oven-drying because of the lack of control of CO_2 in the environment. These results confirm the findings of Collier et al. [66] regarding that these drying methods influenced slightly the obtained results. It should be noted, however, that this similarity may be partly due to the low ettringite content in our cement, since ettringite is the most sensitive hydrate to the drying method.

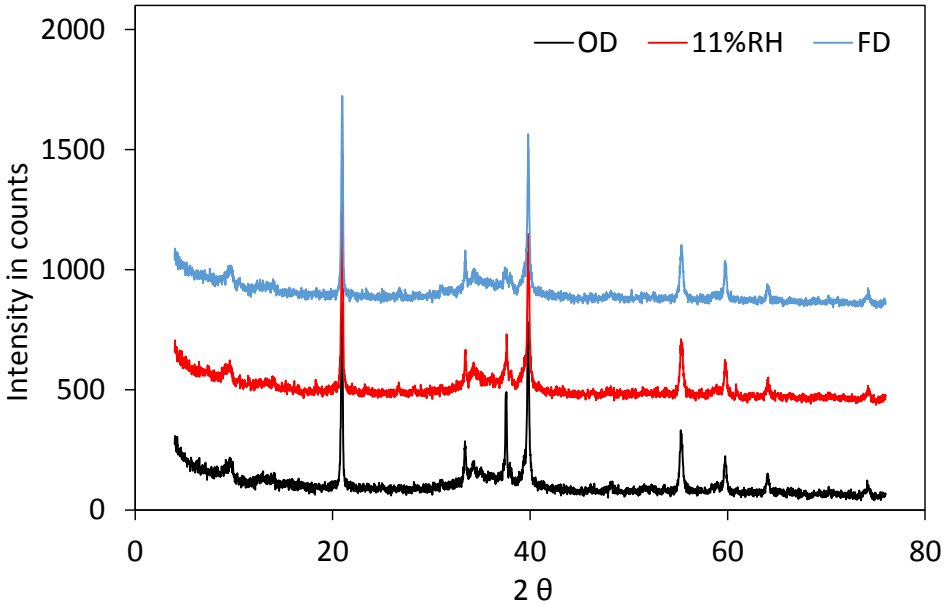

FIGURE 3.12: XRD of cement class G cured at ambient temperature dried by different means (Oven-drying (OD), Freeze-drying(FD) and at 11% of relative humidity (11%RH)

	Weight		
Phase	**FD**	**11%RH**	**OD**
C_2S beta (MUMME)	7.61	6.93	7.84
C_3S monoclinic (NISHI)	2.97	3.35	3.87
C_4AF	2.90	3.28	2.62
C_3A cubic	0.00	0.00	0.00
C-S-H	63.88	63.28	60.96
Portlandite	16.03	16.47	16.91
Calcite	6.61	6.69	7.80

TABLE 3.7: Phase assemblage of cement paste dried by different means, Oven-drying (OD), Freeze-drying (FD) and at drying 11% of relative humidity (11%RH). Portanldite and calcite are quantified from TGA analysis, clinker from XRD and C-S-H quantity is calculated to have the sum of different hydrates fractions equal to 1

3.4.3 Nuclear magnetic resonance NMR

The NMR has been used to study the effect of drying techniques on the microstructure of a cement paste. In Figure 3.13 we present NMR signal versus echo time acquired with a CPMG sequence (before Laplace inversion) for the mentioned drying methods. Inversion recovery sequences are used in this study except for this comparison where CPMG sequences are used. Again and similar to TGA experiment, the oven-dried specimens at 105°C have the smallest amount of water. The range of echo times where the oven-dried curve departs from the freeze-dried one and the 11%RH dried

one, is associated to the interlayer water (echo time < 0.1 ms). This confirms again the loss a significant part of interlayer water with oven-drying at 105°C. The curves associated to freeze-drying and 11%RH-drying almost coincide. A small difference can be observed in the range of echo times [0.1 ms, 1 ms] associated with gel pores, as there is a slight increase in signal intensity of the freeze dried specimens. These experiments are in accordance with the TGA curves. Firstly, the NMR confirms once again the striking similarity between the freeze-drying and the drying at 11%RH. It also informs us that a small fraction of water may reside in the gel pore after freeze-drying comparing to drying at 11%RH, as seen in the departure of the freeze dried curve form the 11%RH dried curve in the range of echo times [0.1 ms, 1 ms] associated with gel pores. We assume that the remaining fraction is insignificant. It can be concluded that the freeze-drying leaves the interlayer spaces full of water in addition to a very small fraction of the water in the gel pore as observed by TGA and NMR. The freeze-drying is thus a convenient method to dry specimens and to preserve their chemical composition for XRD and TGA experiments.

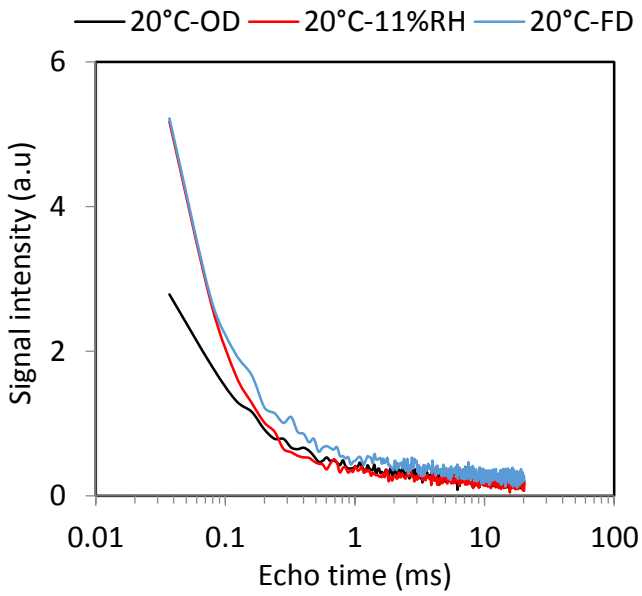

FIGURE 3.13: NMR signal of cement class G cured at ambient temperature dried by different means (Oven-drying: OD, Freeze-drying: FD and at 11% of relative humidity: 11%RH)

3.4.4 Mercury intrusion porosimetry (MIP)

In Figure 3.14 we present the pore size distribution and the cumulative porosity as obtained from mercury porosimetry for specimens that have been dried using three different methods.

As a point of fact, the drying technique has a considerable impact on the pore structure. As expected oven-drying at 105°C has the most significant influence on the pore structure. In fact, the total MIP porosity of oven dried samples is greater than

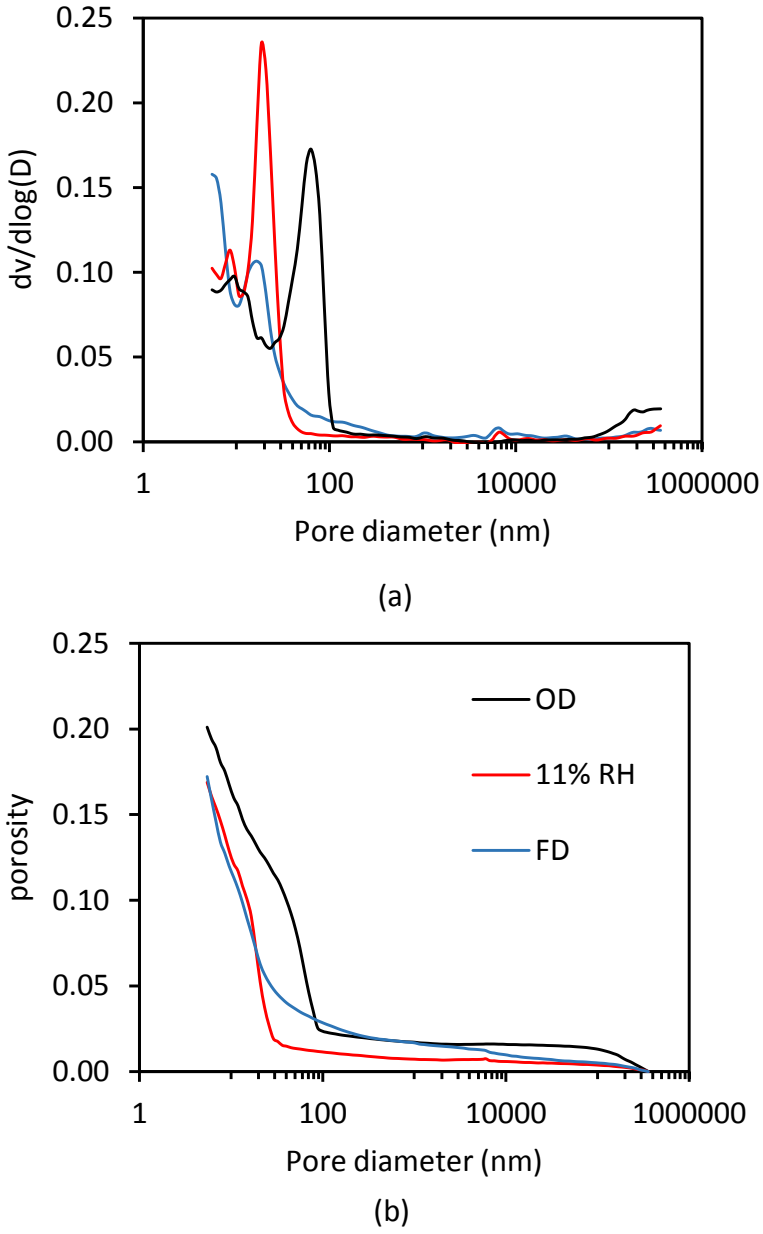

FIGURE 3.14: Comparison of different drying techniques by mercury porosimetry of cement paste dried by different means (Oven-drying: OD, Freeze-drying: FD and at 11% of relative humidity: 11%RH)

the total porosity of specimens dried by freeze-drying and drying at 11%RH. Furthermore, the pore family detected by MIP for the oven dried sample is displaced to larger pore sizes, confirming previous results [63]. This coarsening of the pore structure can be explained by the modification of the pore structure. The oven-drying at 105°C removes part of the interlayer water. The smallest pores are closed after water removal and a new family with bigger pores is created. However, The similarity between the freeze-drying and drying at 11% RH as observed by NMR and TGA is not reproduced by MIP for the whole range of pores sizes. Although, the total

porosity after FD and 11%RH-drying is the same, this latter is distributed differently. The fraction of macropore being higher for the freeze-dried specimens. It is reported that long-term drying does not influence the total porosity of a sample comparing to short-drying but it rather changes its distribution [154, 155]. A decrease in the finer porosity and an increase of the coarser porosity is generally observed [154]. However, we cannot compare the results presented here to the conclusions drawn in other works as the MIP identifies just a fraction of cement porosity. Nevertheless, it can be concluded that evaluating the porosity from MIP curves of either freeze-dried cement or 11%RH-dried cement yields comparable results for cumulative porosity above 20 nm.

3.4.5 Water vapor sorption (WVS)

Water vapor sorption is also sensitive to the drying method. Before acquiring the adsorption branch of the water sorption isotherm, a complete drying of the specimens is needed. Freeze-drying in not commonly used to dry specimens for WVS measurements because of the sample size. The oven-drying has been used regularly to remove water from the samples. However, as seen before in this study and in previous studies, the oven-drying at 105°C removes a considerable part of the interlayer water. We here examine if water re-enters the interlayer spaces. In Figure 3.15, we present the water vapor desorption branch together with adsorption branches for an oven-dried specimen at 105°C and a specimen dried progressively up to 11% RH. It can be seen a clear difference between these two adsorption branches. In fact, an important quantity of water removed by oven-drying is not regained comparing to the specimen dried progressively up to 11% RH. The adsorbed water content of cement at 11%RH contains a supplement of 32% of water comparing to the specimen oven-dried and re-saturated at 11% RH. This is consistent with the fraction of interlayer water removed by oven-drying as determined in TGA experiments 3.4.1. This for instance suggests that the part of interlayer water removed by oven-drying at 105°C is lost irreversibly. The significant departure between the two curves is observed for relative humidities above 35% RH. This range is mainly associated to capillary condensation. The differences in this range can be explained by the modification in the pore structure caused by oven-drying. As it was observed in the MIP examination of drying techniques, Oven-drying at 105°C destructs the smallest pores and creates a fictitious pore family with bigger pores. The main pore family detected by MIP on OD-dried sample ranges from 20 nm up 100 nm. This pore family will not be recovered by adsorption up to 81% RH as this relative humidity indicates with the use of Kelvin-Laplace equation a pore width of around 10 nm. The small water content up to 81% for oven dried samples (equal to 0.1) comparing to the water content obtained by progressive adsorption up to 81% RH (equal to 0.28), reflects the decrease of gel pore fraction after oven-drying and confirms similar previous observations [154]. The Oven-drying although very quick and practical method for drying a specimen before adsorption is to be avoided. Several changes result in a different pore structure and hence different adsorption curve that may mistake the information extracted from the adsorption such as the porosity and the specific surface area.

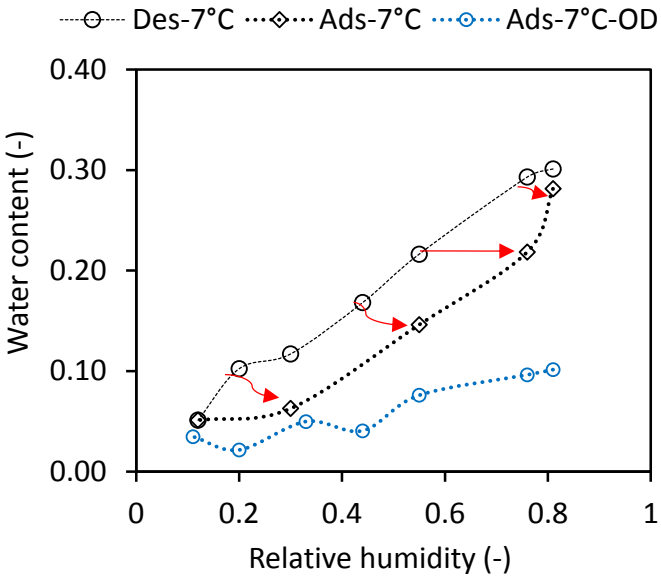

FIGURE 3.15: Water vapor sorption of cement class G cured at 7°C dried (Oven-drying: OD) , and dried progressively up to 11% of relative humidity: (Ads) stands for adsorption and (Des) for desorption, to enable comparison the total water content is taken from oven-drying at 105°C

3.5 Conclusions

The different methods used to characterise the microstructure and the macroscopic properties of cement paste have been presented. This experimental investigation gathers different techniques for the study of the chemical composition and the pore structure:

- Chemical composition: XRD analysed with the Rietveld method allows the estimation of the hydration degree of clinker phases and other crystalline phases. TGA however, seems more accurate when evaluating the portlandite content. Hence, a combination of these two methods is necessary in order to establish the mass assemblage of cement. TGA will be used also to determine the chemically bound water to C-S-H.
- Pore structure: The cement is a complex multiscale material. Each of the methods of the investigation of the porosity highlights a specific pore domain within a cement paste. A combination of several techniques is essential to cover the wide range of pore sizes in cement. The different used techniques are: MIP, BET, WVS, NMR.

  The different experimental methods used in this study require pretreatment of samples before testing. The hydration process in the investigated samples for

this study has been arrested using freeze-drying. This technique has been chosen because of its relative rapidity and adequacy with most of the used experimental methods. A detailed comparative study between freeze-drying, oven-drying and drying at 11%RH has been done. It is shown that freeze-drying and drying at 11%RH have almost the same influence on the cement paste microstructure, the freeze-drying has the advantage of being a very quick drying method comparing to 11%RH-drying. The freeze-drying can be used to evaluate the total porosity as it gives similar results to porosity evaluated by drying at 11%RH. The water left after freeze-drying can be assimilated to the interlayer water. However, when it comes to the pore structure, there are some differences in the range associated with macropores between freeze-drying and drying at 11%RH. The cumulative porosity obtained above 20 nm is quite similar for both freeze-dried and 11%RH-dried specimens, showing again that freeze-drying is acceptable for the study of the pore structure.

Chapter 4

Quantitative analysis of temperature effect on cement paste microstructure

4.1 Introduction

This chapter deals with the quantitative analysis of the effect of hydration temperature on a class G cement paste. The aim is to describe the mass assemblage and the pore structure of cement at different hydration temperatures and different maturation ages. Classical experiments X-Ray diffraction /Rietveld, thermo-gravimetric analysis and ^{27}Al NMR spectroscopy are used to describe the different hydrates of cement paste and their mass fractions. The porosity is investigated through a combination of various techniques to access the different porosity ranges: Mercury porosity, Nitrogen intrusion, water vapor sorption and ^{1}H NMR relaxometry experiments.

4.2 Phase assemblage

The development of the mass and volume assemblage of cement pastes are essential to explain the strength development of cementitious materials. As mentioned in Chapter 2, models that provide the mass assemblage of cement, for instance Tennis and Jennings model, needs a characterisation of the C-S-H density and chemical composition. The effect of hydration temperature on the mass and volume assemblage should be then studied experimentally. The classical experiments that enables determining the mass assemblage of cement microstructure are XRD and TGA analysis. XRD is used to assess the contents of the crystalline phases. TGA, overcoming the preferred orientation limitations of portlandite during XRD experiments, is used to assess the portlandite content. Other experiments such as ^{27}Al NMR are used in order to deepen the knowledge of the chemical composition of cement paste.

4.2.1 X-Ray diffraction and qualitative analysis

The powder diffraction patterns for the cement pastes cured at different temperatures are presented in Figure 4.1. These patterns show that the major crystalline phase formed during the hydration of class G cement is portlandite. Ettringite is formed in small quantities, below 2% as expected from the small quantity of C_3A in the Class G cement clinker (Table 3.2). X-Ray powder diffraction patterns suggest also that the major residual clinker phases are C_4AF and C_2S, which confirms the slow consumption of these two clinker phases [119, 125] comparing to C_3S that is almost completely depleted. Small quantities of Hibschite are also detected. The principal reflection of this phase is at about 39° (2θ) and is overlapped with the second reflection of portlandite. The portlandite being a highly crystalline phase, and hence exhibiting a symmetric diffraction peak, the non-symmetric part of its second peak is attributed to Hibschite. In the Hibschite phase identified in our cement a small amount of aluminium is replaced by iron, which may reflect a product formed from the hydration of ferrite phases. This qualitative analysis is relevant for the diffraction patterns collected for different curing conditions. However, the consumption of clinker phases is more pronounced with curing temperature, leading to a faster development of hydrates [75, 89, 94]. Furthermore, new phase appear with the elevation of temperature in the studied range. These phases are the katoite Ca_3Al_2 $[(OH)_4]_3$ and the dellaite C_6S_3H. Katoite is a calcium aluminate hydrate, member of hydrogrossular group. It is observed at high temperatures, starting from 60°C. The presence of katoite in class G cement pastes hydrated under elevated temperatures has been reported previously [156]. The strong intensities associated to katoite with increasing curing temperatures may also be explained by the fact that temperature favoured the development of katoite, which is, thermodynamically, a more stable phase than ettringite for which the stability decreases with increasing temperature according to previous studies [75]. The other observed phase when elevating the curing temperature is dellaite C_6S_3H, a crystalline calcium silicate hydrate with a C/S ratio of 2. No

evident conclusion can be made about the change of the dellaite quantity with temperature based on XRD patterns, as this phase shows strong overlapped peaks with residual clinker and amorphous C-S-H. The presence of this phase in geothermal cements has been previously reported [157]. The cement contains 15% of ferrite but apart from Hibschite, no Fe-containing phases are detected by XRD due to their poorly crystalline nature [158, 159]. This point is further discussed in Section 4.2.4.

The amorphous or short-range order phases scatter X-ray in many directions resulting in a large hump dispersed in a wide 2θ range instead of narrower peaks with high intensities relative to crystalline phases. The presence of amorphous content is evidenced here by the bump over the 2θ range [35°-40°]. Comparing the range associated to C-S-H for different curing temperatures, we observe that diffraction patterns associated to $T = 7$°C and $T = 20$°C exhibit narrower peaks in the 2θ range [35°-37°] comparing to $T = 60$°C and $T = 90$°C. This would suggest that the structure disorder is increasing with the elevating curing temperatures. The cement pastes cured at lower temperatures seem therefore to be more ordered than those cured at higher temperatures. The increasing degree of crystallinity in the structure of calcium silicate hydrate has been associated in a recent research to an increasing C/S ratio in C-S-H [160]. The lower temperature being related to higher C/S ratio, which has been previously mentioned in [81], may support the observed arrangement and the increasing order of the structure at low temperatures.

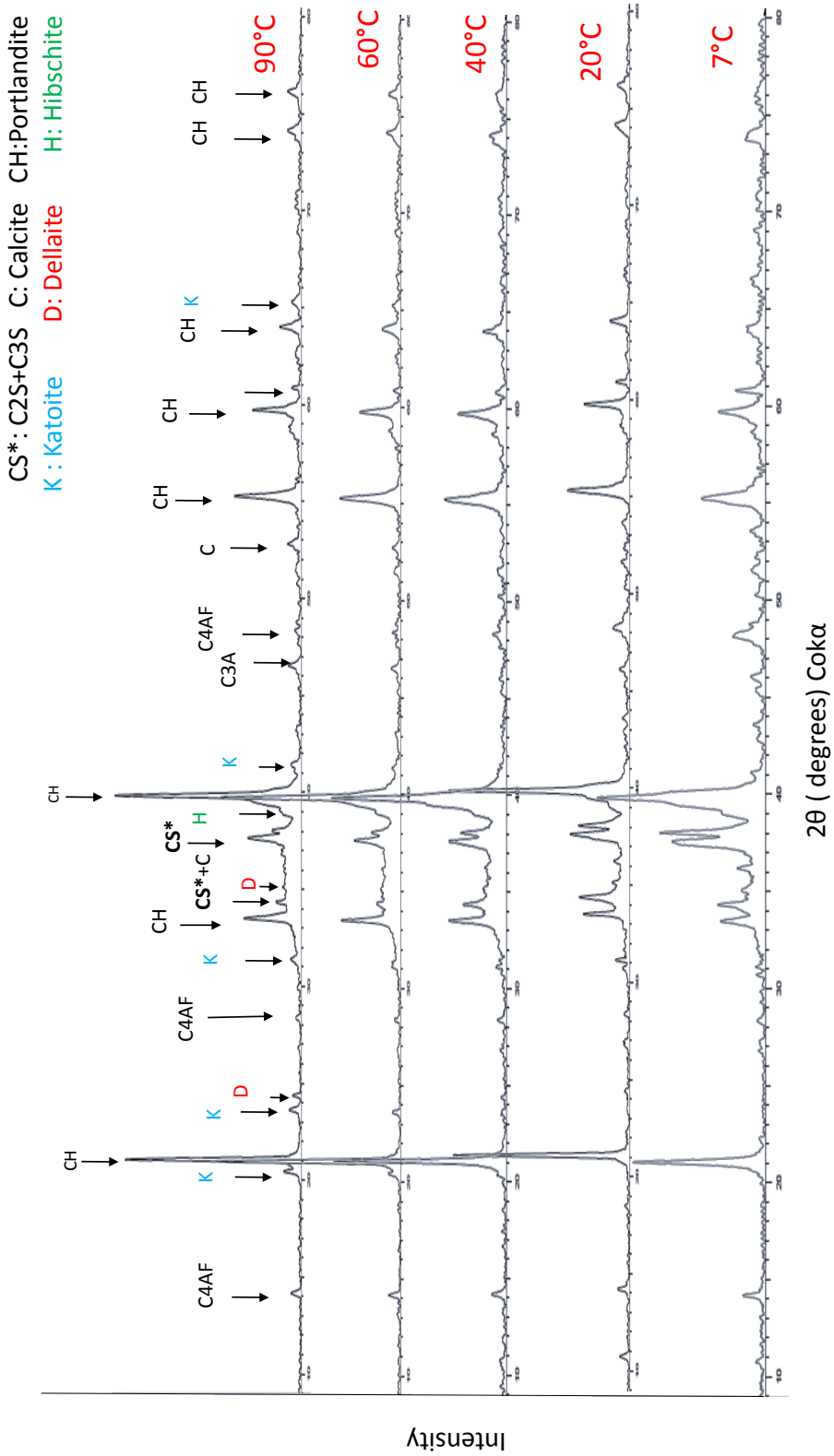

FIGURE 4.1: X-ray powder diffraction patterns with qualitative analysis of the major phases for cement class G cured at different temperatures T (°C)= 7, 20, 40, 60, 90

4.2.2 Thermogravimetric analysis

The results obtained from thermogravimetric tests are presented in Figure 4.2 in terms of the relative mass loss as a function of the temperature (TG, left y-axis) and the derivative of TG curve (DTG, right y-axis). The curves show four major weight losses.

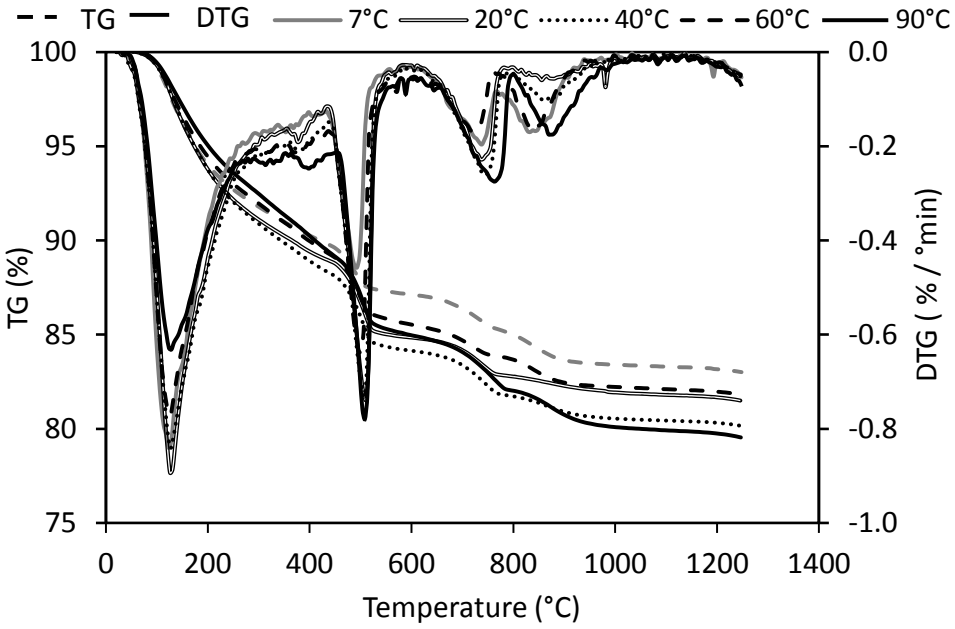

FIGURE 4.2: Thermogravimetric weight loss for class G cement paste cured at different hydration temperatures for 28 days

The first weight loss is mainly due to C-S-H, Afm and ettringite [161]. However, as presented above in the results of XRD experiments, the tested cement paste contains very small amounts of Afm and ettringite. This is mainly due to the small quantity of C_3A in the class G cement clinker. The second major weight loss observed at 450°C-550°C reflects the dehydration of portlandite. The third and forth losses are essentially due to the CO_2 departure from calcite. The existence of these two peaks can be seen as a sign of the carbonation of samples during preparation and storage [68, Chapter 5]. According to Sauman [162] and Morandeau et al. [163], the forth peak corresponds to well crystallized calcite, but the third one is attributed to allotropic forms of calcite (aragonite and vaterite). These two varieties of polymorph calcite turn into calcite around 500°C during heating. Being less stable, aragonite and vaterite decompose at lower temperatures than calcite. Vaterite, aragonite and calcite originate from the carbonation of C-S-H and portlandite [163]. However, it is difficult to state whether the formed calcite is due to the carbonation of portlandite or to the carbonation of C-S-H. The findings about this topic drawn in the literature are confusing. While some highlighted that the C-S-H and portlandite carbonate simultaneously [163], others mentioned that the carbonation of C-S-H occurs

when the portlandite is almost depleted [164, 165]. However, a consensus has been made that the carbonation of portlandite is more pronounced at the onset of carbonation. It can be clearly seen that our samples have undergone some carbonation similar to data presented in [68, Chapter 5] for samples carbonated during preparation and storage. However, when the carbonation rate is enhanced, the intensity of the forth peak is more pronounced as presented in the results of Morandeau et al. [163] and which is not the case here. As our samples are not intentionally carbonated as in [163] we assume that all the calcite formed is due to the portlandite carbonation as in [125]. It is worth noting that some analysis results will be influenced by this assumption and this will be discussed in the following. Aside from these four rapid weight losses, two more small weight losses can be identified. The first one is adjacent to C-S-H peak. This loss may originate from the dehydration of hydrogarnet that occurs above 250°C [166]. The second one is adjacent to the decomposition of portlandite. We deem that a part of this weight loss originates from the decomposition of dellaite which occurs above 600°C according to [167]. It can be observed that the weight losses that may potentially correspond to hydrogarnet and dellaite are more pronounced for higher hydration temperature. This combined with the XRD experiments strengthen the observations of the development of these two phases and the increase in their mass fractions with increasing hydration temperature.

To investigate how the hydrates develop with progressive hydration at different curing temperatures, we performed TGA experiments at different ages and two different extremes temperatures 20°C and 90°C. The TGA analysis are a good measure to the hydration degree. The TGA curves for cement cured at two different temperatures 20°C and 90°C are presented in Figure 4.3 and Figure 4.4. The description provided above holds for TGA analysis at different curing temperatures and maturation ages. It is seen that while the hydration of specimens cured at 20°C evolves continuously from 1 day up to four months, the specimens cured at 90°C reach their ultimate hydration degree at the very first days of curing. This is in accordance with previously mentioned trends in the literature, showing a rapid evolution of hydration degree of cement cured at higher temperatures. It also explains the rapid gain of strength for specimens cured at higher temperatures.

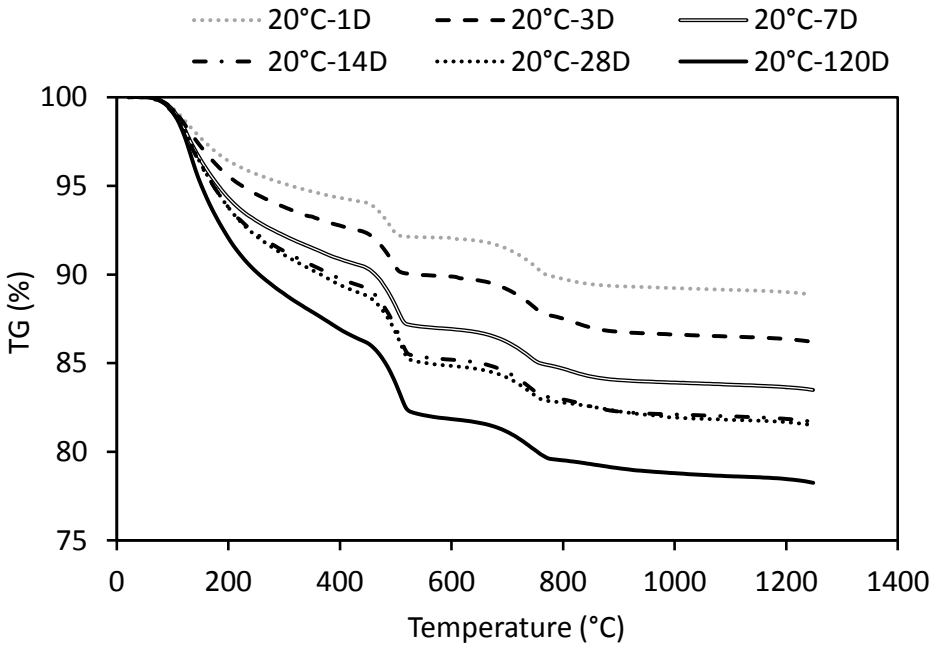

FIGURE 4.3: Thermogravimetric weight loss for class G cement paste cured at 20°C for different maturation ages

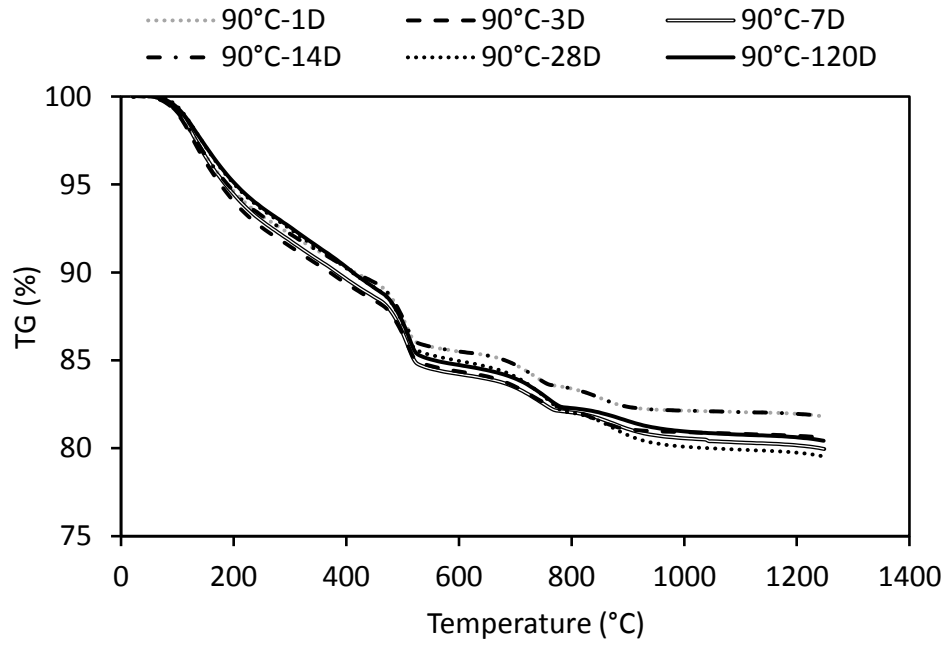

FIGURE 4.4: Thermogravimetric weight loss for class G cement paste cured at 90°C for different maturation ages

4.2.3 ^{27}Al solid state NMR

^{27}Al SSNMR spectra of cement paste hydrated under different temperatures are presented in Figure 4.5. These sepctra show six regions of resonance that are assignable to IV, V, and VI coordinated Al, with peak maxima around, 86 to 69 ppm, 35 ppm, 13.2 ppm, 10.8 ppm and 4.2 ppm respectively. The two regions of center-band resonances from tetrahedrally coordinated Al in the region (90-50 ppm), are present as impurities in Alite and Belite, or present in aluminate phases. The five coordinated Al are assigned to Al in the silicate chain of C-S-H. The signals in the region of (0 to 20 ppm) are assigned to octahedrally coordinated Al arising from Ettringite (13.2 ppm), Afm (10.8 ppm) and the third aluminate hydrate(TAH) (4.2 ppm) respectively. The third aluminate hydrate is associated to the Al at the outer surface of C-S-H. The peaks intensity relative to the ettringite reveals that this phase content is decreasing with increasing hydration temperature. No ettringite is found above 40°C. Whereas, the Afm content is increasing with the temperature. This is in agreement once again with the XRD observations and the findings of literature suggesting that the ettringite is not formed above 40°C due to its decreased stability and that is being replaced with Afm. The amount of TAH is almost not changing with temperature. The signal intensity from the four coordinated Al incorporated into the C-S-H structure seems constant up to 60°C and decreases slightly at 90°C.

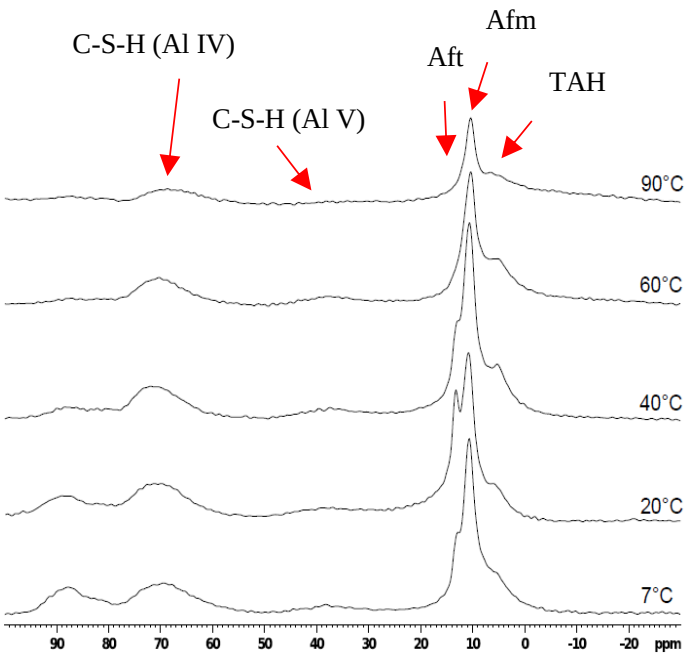

FIGURE 4.5: ^{27}Al SSNMR spectra of class G cement paste cured at different hydration temperatures for 28 days

4.2.4 Phase assemblage from combined Rietveld and TGA analysis

The quantitative evaluation of different phases in cement paste microstructure can be done through a combination of X-Ray diffraction/Rietveld method and thermogravimetric analysis. The portlandite content is taken from TGA analysis and corrected to account for the eventual carbonation process, as described in Eq. 3.3. We assume that the formed calcite is due to the carbonation of portlandite and not the carbonation of C-S-H. The mass fractions of clinker phases are determined from Rietveld analysis. Based on the result of XRD and TGA we build molar quantity balance on the major elements in cement CaO, SiO_2, Al_2O_3,Fe_2O_3 and SO_3 (Gypsum). The considered phases in the molar quantity balance are: C-S-H, CH, Al-ettringite, Al-monosulfate, residual clinker phases and Fe-containging siliceous hydrogarnet. In fact, the cement contains substantial amounts of ferrite, approximately 50% of this ferrite is hydrated, however, no Fe-containing product has been identified through XRD. The limitation of XRD experiments in identifying Fe-containing products is attributed in the literature to the amorphous nature of these products. It is reported that the hydration of Ferrite results in one or a combination of different hydrates i.e (Fe-ettringite, Fe-Afm, Fe-siliceous hydrogarnet and amourphous iron hydroxide). In a recent and more complete studies [159, 168], it is shown that the Fe-Ettringite and Fe-Afm are non stable materials and that the most stable hydration product resulting from ferrite hydration are the Al and Fe-siliceous hydrogarnet. Regarding these findings, we assume that the Fe-siliceous hydrogarnet is the Fe-containing product resulting from the hydration of Ferrite. The katoite is formed in small quantities and has been neglected in the mass assemblage. The molar quantity balance equations are given below:

$$\begin{cases} x n_{\mathrm{CSH}} + 6n_{\mathrm{Ett}} + 4n_{\mathrm{Afm}} + 3n_{\mathrm{Hydg}} = 3n_{\mathrm{C3S}} + 2n_{\mathrm{C2S}} + 3n_{\mathrm{C3A}} + 4n_{\mathrm{C4AF}} - n_{\mathrm{CH}} \\ n_{\mathrm{CSH}} + 0.84n_{\mathrm{Hydg}} = n_{\mathrm{C3S}} + n_{\mathrm{C2S}} \\ n_{\mathrm{Ett}} + n_{\mathrm{Afm}} + 0.9n_{\mathrm{Hydg}} = n_{\mathrm{C3A}} + n_{\mathrm{C4AF}} \\ n_{\mathrm{Hydg}} = n_{\mathrm{C4AF}} \\ 3n_{\mathrm{Ett}} + n_{\mathrm{Afm}} = n_{\mathrm{SO3}} \end{cases} \tag{4.1}$$

Where n_{z} is the molar quantity of phase z which can be either hydration product or consumed clinker phase. x is the C/S molar ratio in C-S-H. The molar quantity balance for different elements results in a non-linear system of five equations and five unknowns which can be solved numerically. The unknowns are: Ettringite, Afm, C-S-H, Hydrogarnet and the C/S molar ratio. The resulting molar quantities are used to evaluate the mass fractions of different phases by knowing their molar mass. According to Lothenbach et al. [75] ettringite is unstable at hydration temperatures higher than 50°C and AFm forms at the expenses of this phase. This has also been observed in the ^{27}Al NMR experiments, showing the formation of Afm at the expense of ettringite above 40°C. Interestingly, the resolution of the above system of equations for hydration temperatures 60°C and 90°C result in small negative values of ettringite molar quantity. For

these temperatures the ettringite molar quantity is imposed equal to zero and the other quantities are obtained by solving the first four equations.

The evaluated mass assemblage of cement pastes hydrated under different temperatures for 28 days is presented in Table 4.1. The mass fraction of portlandite shows a slight increase with increasing hydration temperature if comparing pastes cured at different temperatures and having a similar hydration degree. It also increases with the hydration degree for a specific temperature (For instance, 7°C and 20°C). The ettringite and Afm content are quite small. The ettringite mass fraction is decreasing with increasing hydration temperature, while the mass fraction of Afm is increasing. These observations are in good agreement with ^{27}Al NMR experiments. The C-S-H mass fraction is almost constant with increasing hydration temperature. Regarding the hydrogarnet, we found a fluctuating mass fraction depending on the hydration degree of ferrite which is also fluctuating with hydration temperature at 28 days of hydration. The hydrogarnet amount increases with progressing hydration of cement. The overall hydration degree of cement paste increases significantly from 7°C to 20°C at 28 days of hydration and only slight changes are observed for higher temperatures at the considered age. The pastes cured at low temperatures continue evolving with ages leading to an increase of the hydration degree. As stated above, based on XRD results, it can be clearly seen that C_3S is more consumed than the other clinker phases. C_2S and C_4AF generally react slowly confirming the low hydration degree corresponding to these phases at 28 days [118, 125].

Temperature (°C)	7	20	40	60	90
C-S-H	42.84	46.12	49.44	47.44	45.65
Portlandite	17.63	19.89	20.63	21.20	22.75
Ettringite	1.77	0.15	1.08	0.00	0.00
Afm	1.37	3.65	2.25	1.77	2.83
Si-Fe-Hydrogarnet	7.86	9.88	9.34	7.90	7.44
C_3S	7.02	4.17	4.73	3.96	3.17
C_2S	13.25	9.56	5.04	7.11	7.49
C_3A	0.81	0.28	0.52	1.05	0.55
C_4AF	7.66	5.45	5.80	7.22	7.58
Hydration degree	0.65	0.76	0.80	0.76	0.77

TABLE 4.1: Phase assemblage of cement pastes obtained from the combination of XRD-Rietveld and TGA analysis for cement class G cured at different temperatures for 28 days (mass fractions per respect to dry cement mass)

The mass assemblage obtained from a class G cement hydrated at 20°C for different curing ages is presented in Table 4.2. The portlandite and C-S-H are continuously increasing with the hydration degree. The ettringite content however is decreasing being replaced by Afm. The Si-Fe-Hydrogarnet is increasing with progressing hydration. It should be mentioned that the resolution of the above system of equations results in an evaluation of the C/S ratio in C-S-H (variable x), which will be presented later in section 5.2.2.

The uni-axial compression test are carried on pastes hydrated for four months at different temperatures. The results are compared with micro mechanical modelling. As for low temperatures the hydration progresses with time we add the mass assemblage corresponding to a hydration at 7°C for four months. The specimens cured at higher temperatures reach an ultimate hydration degree at the very early days of hydration. We deem that the mass assemblage for specimens cured at 60°C and 90°C is quasi-constant after 28 days of hydration.

	20°C						7°C
Days	1	3	7	14	28	120	120
C-S-H	32.85	35.79	40.9	44.7	46.12	48.26	48.48
Portlandite	12.65	14.93	18.13	19.00	19.89	21.14	22.1
Ettringite	1.62	0.23	0.22	0.76	0.15	0.00	0
Afm	1.87	3.81	3.70	2.81	3.65	4.74	4.09
Si-Fe-Hydrogarnet	8.75	9.92	9.53	9.46	9.88	12.14	12.44
C_3S	18.75	12.61	9.60	5.92	4.17	2.97	2.83
C_2S	14.13	13.98	10.15	9.26	9.56	7.61	7.83
C_3A	0.8	0.28	0.26	0.5	0.28	0.00	0.00
C_4AF	7.65	6.13	5.94	5.80	5.45	2.90	2.67
Hydration degree	0.53	0.61	0.68	0.72	0.76	0.83	0.83

TABLE 4.2: Phase assemblage of cement pastes obtained from the combination of XRD-Rietveld and TGA analysis for cement class G cured at 20°C for different hydration times and at 7°C for 120 days (mass fractions per respect to dry cement mass)

4.3 Porosity and pore size distribution

The multi-scale porosity of cement paste should be investigated through various porosimetry techniques capable of reaching various pore size ranges. In this study we used mercury intrusion porosimetry, water vapor sorption, Nitrogen sorption and NMR relaxometry in order to gain insights into the changes of the pore structure at different hydration temperatures and different maturation times.

4.3.1 Mercury intrusion porosity

Porosity variation at different hydration temperatures for a hardened state

The cumulative porosity and pore size distributions of cement pastes cured at different temperatures for 28 days as obtained from mercury porosimetry are presented in Figure 4.6. The results show one pore family with pore sizes ranging from 10 nm to 100 nm and the beginning of a second pore family with pore

sizes smaller than 10 nm. The median pore size is almost constant for temperatures ranging from 7°C to 40°C and increases significantly at 60°C. This trend was mentioned in the literature [20, 80, 89, 169] and reflects that higher temperatures lead to a coarsening of the porous structure. Pastes hydrated above 60°C have larger pore volume as observed by MIP compared to pastes cured at lower temperatures.

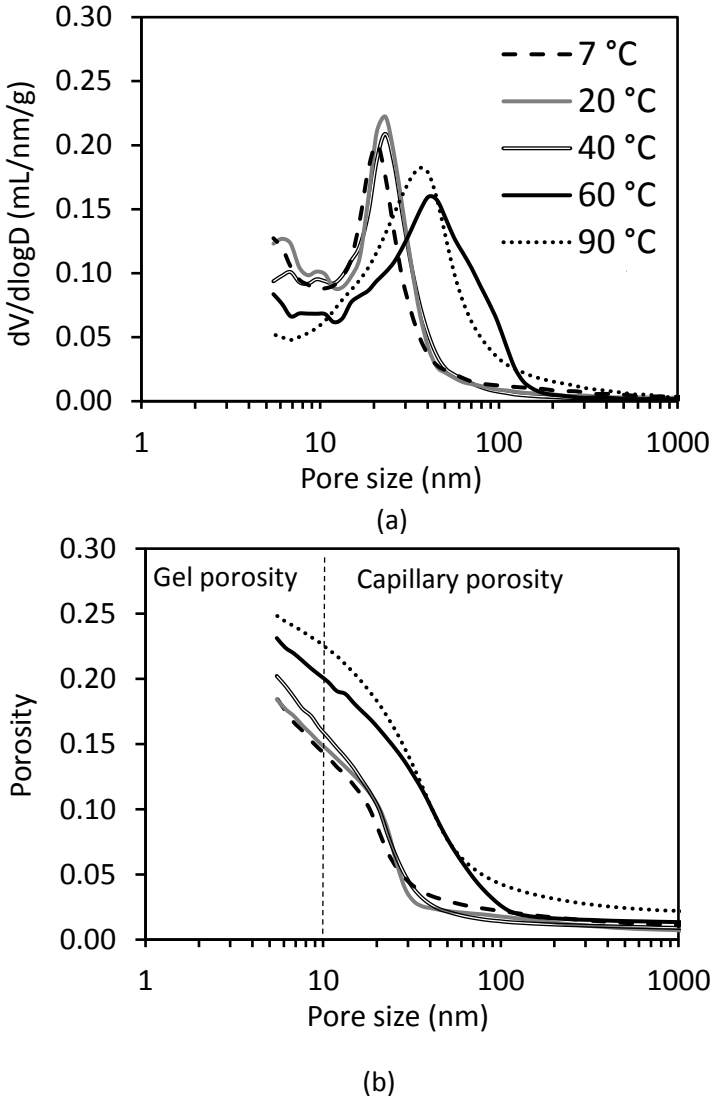

FIGURE 4.6: (a) Differential pore size distribution; (b) Cumulative intrusion curve as measured by MIP for a class G cement paste cured at different temperatures for 28 days (the dashed line corresponds to 10 nm)

The pore family observed by mercury intrusion corresponds to the capillary porosity and interestingly, the 10 nm pore size that corresponds to the lower limit of the pore family observed by mercury intrusion, has been considered as the lower limit of the size of the capillary pores [36]. Jennings [170] showed

that capillary pores empty at 85% RH. This has also been confirmed recently by NMR experiments that revealed a constant NMR intensity relative to capillary pores below 85% [50]. This threshold value of relative humidity when converted into pore size using the Kelvin equation indicates a pore size of 10 nm. Therefore, we assume that the capillary porosity is the porosity measured by mercury intrusion up to 120 MPa pressure corresponding to a pore size of about 10 nm, as shown in Figure 4.6 (a). MIP may result in an underestimation of the volume of the biggest pores in a material as they can potentially be accessible only through smaller pores. However, in this study a great part of the injected mercury volume corresponding to a wide range of pore sizes has been used to evaluate the capillary porosity. For this reason, the mentioned underestimation should be less significant on the evaluation of the capillary porosity presented here. Furthermore, recent studies by combining NMR and chemical shrinkage experiments validated the measurement of the capillary porosity through MIP [171]. The evaluated capillary porosity is presented in Figure 4.7 and shows an increase with increasing hydration temperature. This is in agreement with previous studies that showed through SEM experiments [80] or sorption isotherms [170] an increase of the capillary porosity with curing temperature. The increase of the capillary porosity may be explained by the development of denser hydration products as the curing temperatures increases [80, 172].

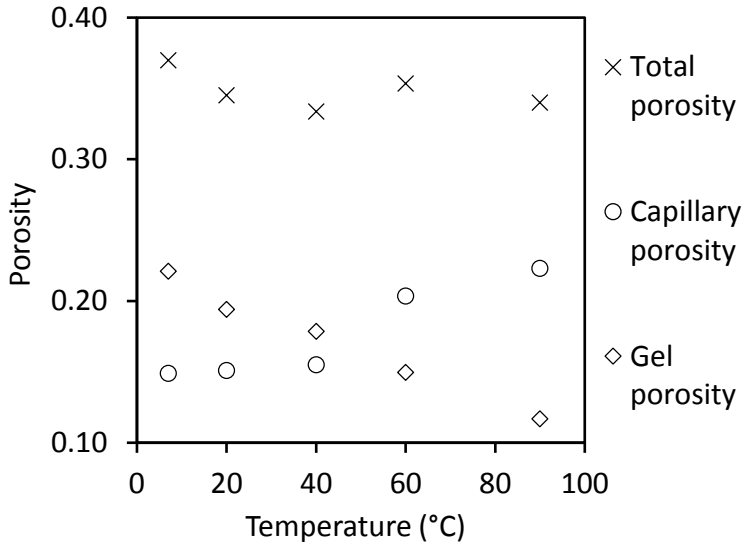

FIGURE 4.7: Evolution of total, capillary and gel porosity with hydration temperature for 28 days

Comparison between drying cement at 11% of RH and freeze drying showed that they empty almost the same pore reservoirs, the porosity measured by mass loss during freeze drying is thus assimilated to the total porosity. In Figure 4.7, the total porosity measured from mass loss during freeze drying is presented and shows a slight decrease with increasing curing temperature. The gel porosity can be evaluated by subtracting the capillary porosity from the total porosity. As can be seen in Figure 4.7, the calculated gel porosity is decreasing with the

curing temperature. The gel porosity decreases significantly by increasing the hydration temperature, while the mass fraction of C-S-H shows slight variations with increasing hydration temperature, as shown in Table 4.1. This highlights that the C-S-H becomes denser at elevated temperatures. The quantitative estimation of the C-S-H density with curing temperatures will be addressed in the following Chapter.

Porosity variation at different ages and temperatures

As seen in 4.2.2, the hydrates development with age depend on the hydration temperature. Lets now investigate how the hydrates fill progressively the space during hydration at different curing temperatures. The MIP pore size distributions for cement pastes cured at different hydration temperatures (7°C, 20°C, and 60°C) for different ages 1, 3, 7, 14 , 28 and 120 days are presented in Figures 4.8, 4.9 and 4.10. The cumulative porosity is decreasing continuously with the hydration time as the hydrates develop and fill the capillary space. For the lower curing temperatures (T=7°C and 20°C), the MIP pore size distributions show bimodal distributions of pores at the very first days, which turn into uni-modal ones as the hydration proceeds. The pore access diameter obtained through MIP is decreasing with increasing hydration degree. Besides, bigger capillary pores (10 μm, 0.1 μm) disappeared witnessing a densification of cement paste at the outer space of the C-S-H gel at early hydration ages and low temperatures. The MIP pore size distributions at 60 °C show however a unimodal distribution, large at the very first days of hydration and getting narrower by progressive hydration.

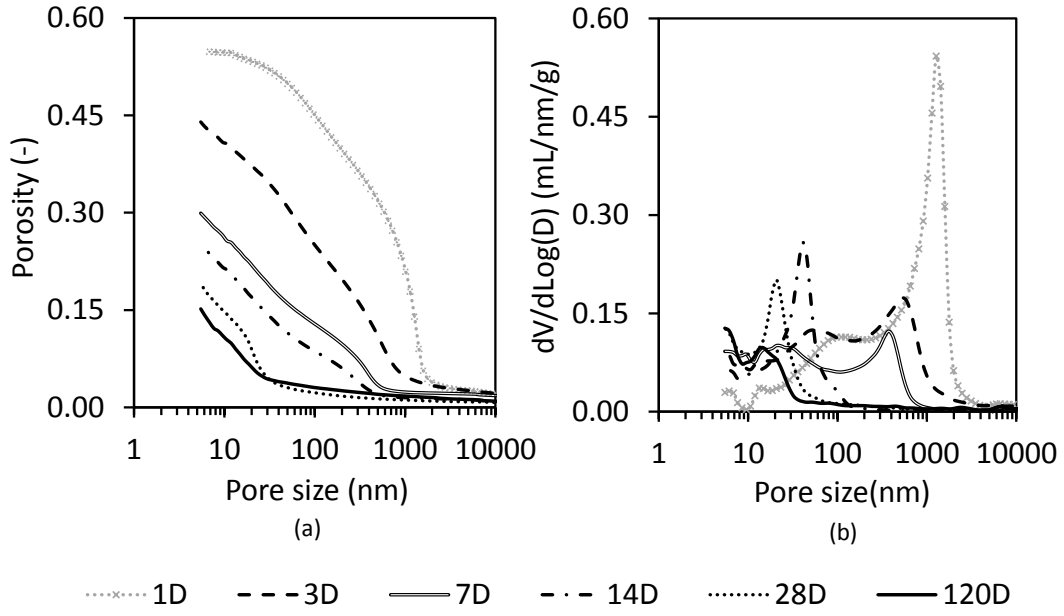

FIGURE 4.8: (a) Differential pore size distribution; (b) Cumulative intrusion curve as measured by MIP for a class G cement cured at 7 °C for different maturation ages

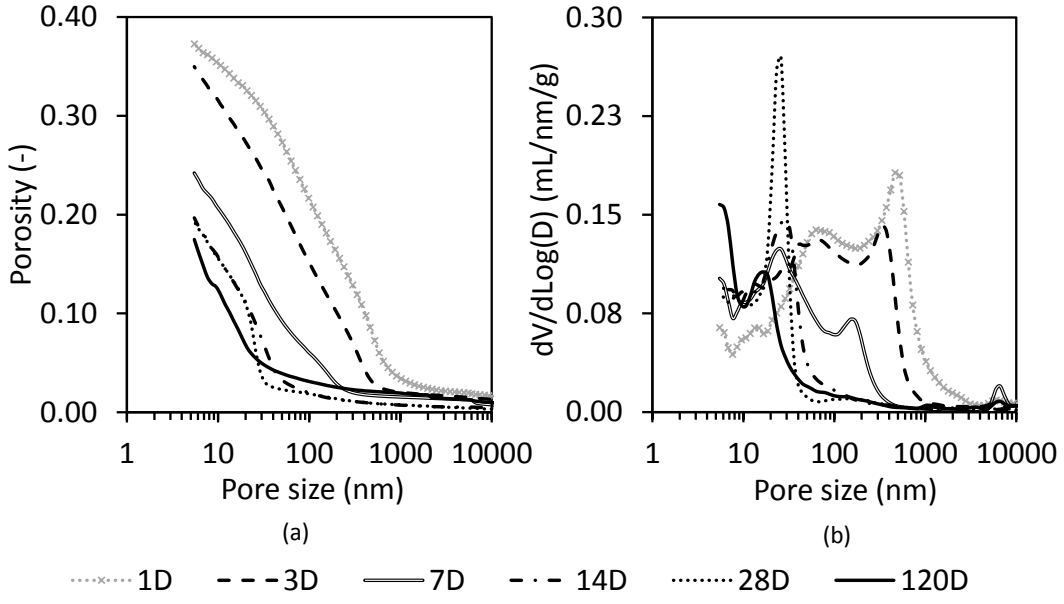

FIGURE 4.9: (a) Differential pore size distribution; (b) Cumulative intrusion curve as measured by MIP for a class G cement cured at 20 °C for different maturation ages

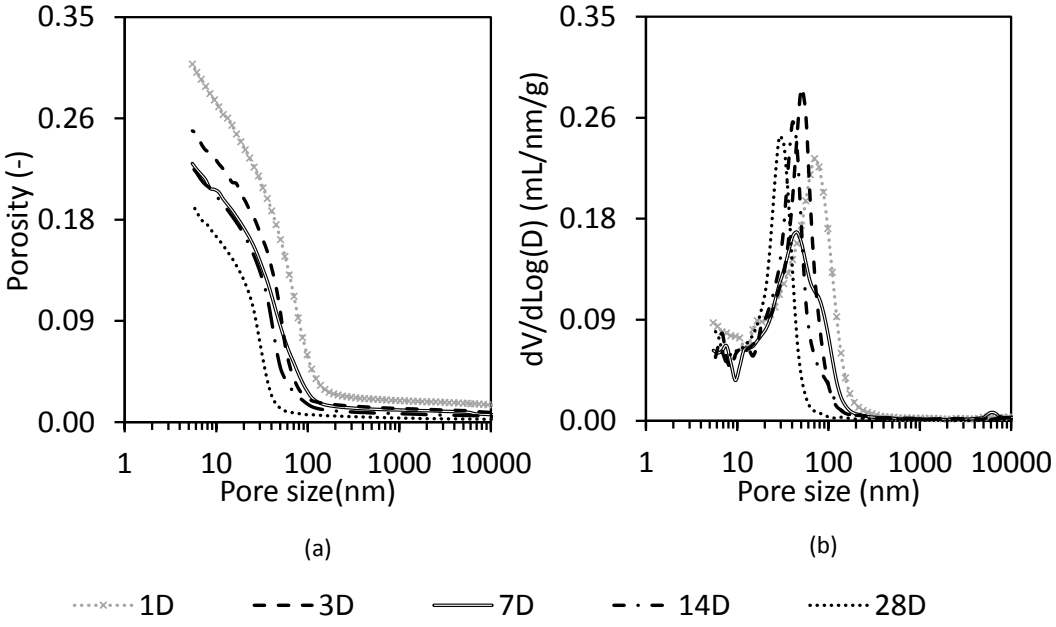

FIGURE 4.10: (a) Differential pore size distribution; (b) Cumulative intrusion curve as measured by MIP for a class G cement cured at 60 °C for different maturation ages

A quantitative evolution of the porosity with hydration time is drawn in Figure 4.11 for a cement paste hydrated under a hydration temperature of 20 °C. The total porosity and capillary porosity are gradually decreasing with proceeding age as the hydrates form and fill the space. The gel porosity increases at the first days of hydration and then starts decreasing after 28 days of hydration confirming observations of Muller et al. [58]. The increase of the gel porosity with progressive hydration derives from the development of the C-S-H gel with the hydration time. The latter decrease of the gel porosity is interpreted as a densification of the C-S-H gel by nucleation of solid C-S-H particles within gel pores. The densification is however not restricted to C-S-H gel pores as the capillary porosity continuously decreases with the hydration time, showing that hydrates develop also at the capillary spaces. All these observations are in accordance with different densification regimes presented by Königsberger et al. [173].

4.3.2 Water vapor sorption

Water vapor sorption isotherms at different temperatures

Water vapor sorption isotherms of cement cured at different temperatures are scarce in the literature. Few data exist on this subject, some were limited to the description of only the adsorption [174] or the desorption process [175] and others presented the isotherms of cement for limited range of temperatures

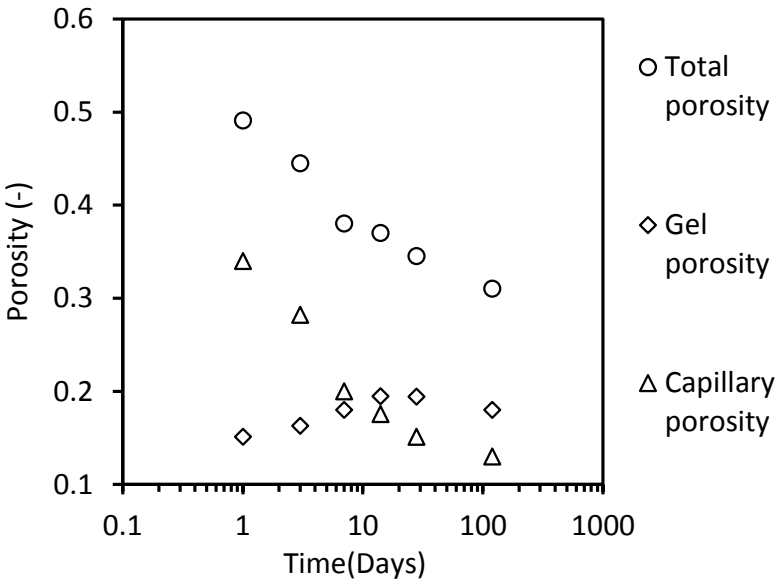

FIGURE 4.11: Evolution of total, capillary and gel porosity with time for a hydrating cement paste at 20°C

[176] for instance (20°C and 70°C). Other studies recently addressed the effect of heating temperature on the sorption isotherms after curing [135]. The full sorption isotherms (adsorption and desorption) of cement pastes cured at different temperatures for a wide range of temperatures for 7°C to 90°C are presented in Figure 4.12. For 20°C only the desorption branch is presented due to experimental accidents during acquisition of the adsorption branch. The dried mass reference is taken as the dried mass at 11%RH. In Figure 4.12 we can distinguish two regimes: a first non linear regime associated with the capillary domain and a second linear regime associated with multilayer adsorption. Samples hydrated at lower hydration temperatures exhibit almost a linear behaviour. The non linearity of the desorption isotherm appears starting from 20°C and increases significantly with increasing hydration temperatures. This is due to the increase of the capillary porosity with the curing temperature as it was observed from mercury intrusion porosimetry. It can be seen that the water weight loss is enhanced with increasing hydration temperature. The water content of cement hydrated at a given relative humidity is decreasing with temperature for both desorption and adsorption processes. The decreasing amount of desorbed water with increasing hydration temperature is in agreement with previously published results [175, 177]. However, previous studies showed hardly any variation of the adsorption branch with temperature. This is not the case here as the quantity of adsorbed water is lower for higher curing temperatures. An important feature of the isotherms is the hysteresis that is decreasing with increasing hydration temperature. This is further discussed in Section 4.3.3.

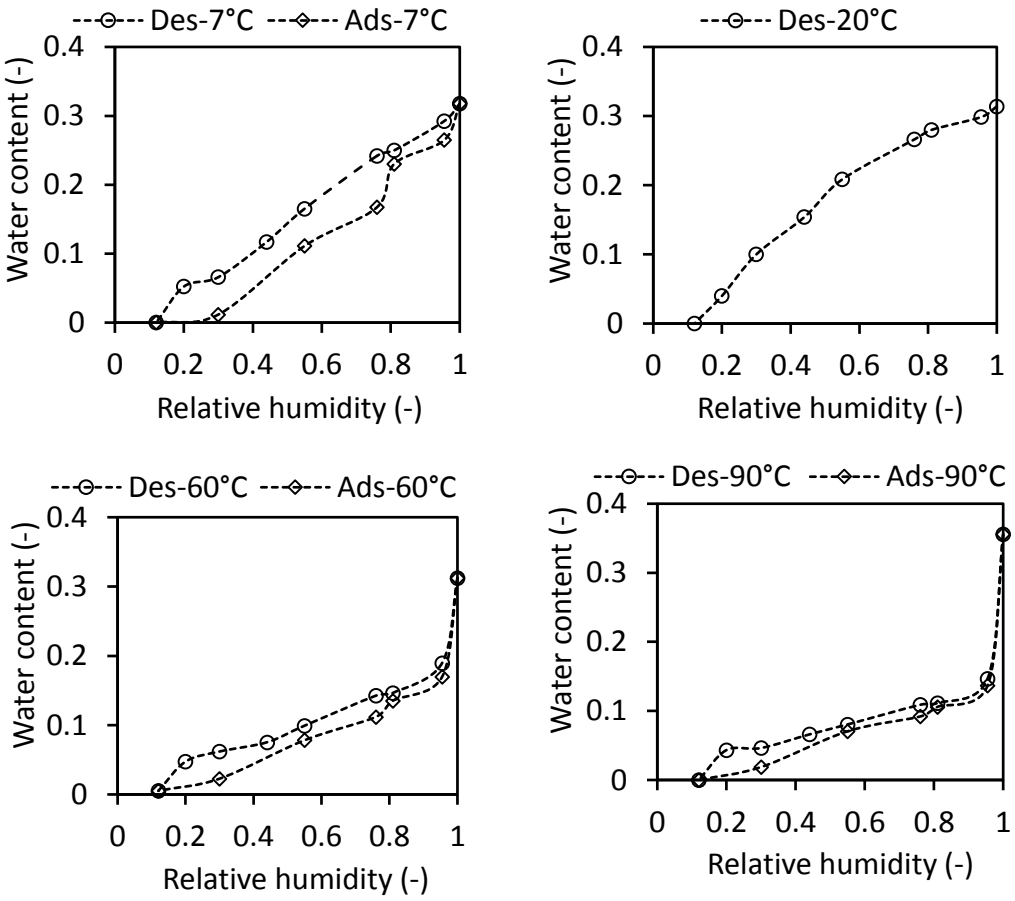

FIGURE 4.12: Water vapor sorption isotherms for a class G cement paste cured at different temperatures T (°C)= [7, 20, 60, 90] for four months

Pore size distributions from BJH analysis

The pore size distribution can be obtained from the water sorption isotherms using the BJH method. Results are presented in Figure 4.13 for both adsorption and desorption branches.

The desorption branch is usually chosen to extract pores entries as it is more stable from a thermodynamical point of view comparing to adsorption [21]. Here it can be seen that the differences between the adsorption and the desorption branches are quite small. The difference between desorption and adsorption branches is usually interpreted as a result of the desorption branch characterising pore entries and the adsorption branch characterising the pore widths. Here, we observe that there is a strong agreement between the adsorption and desorption branch for different pore sizes. However, some discrepancies start appearing in the range [2-5 nm] and these discrepancies decrease by increasing the hydration temperature. This correlates well with the decreasing hysteresis

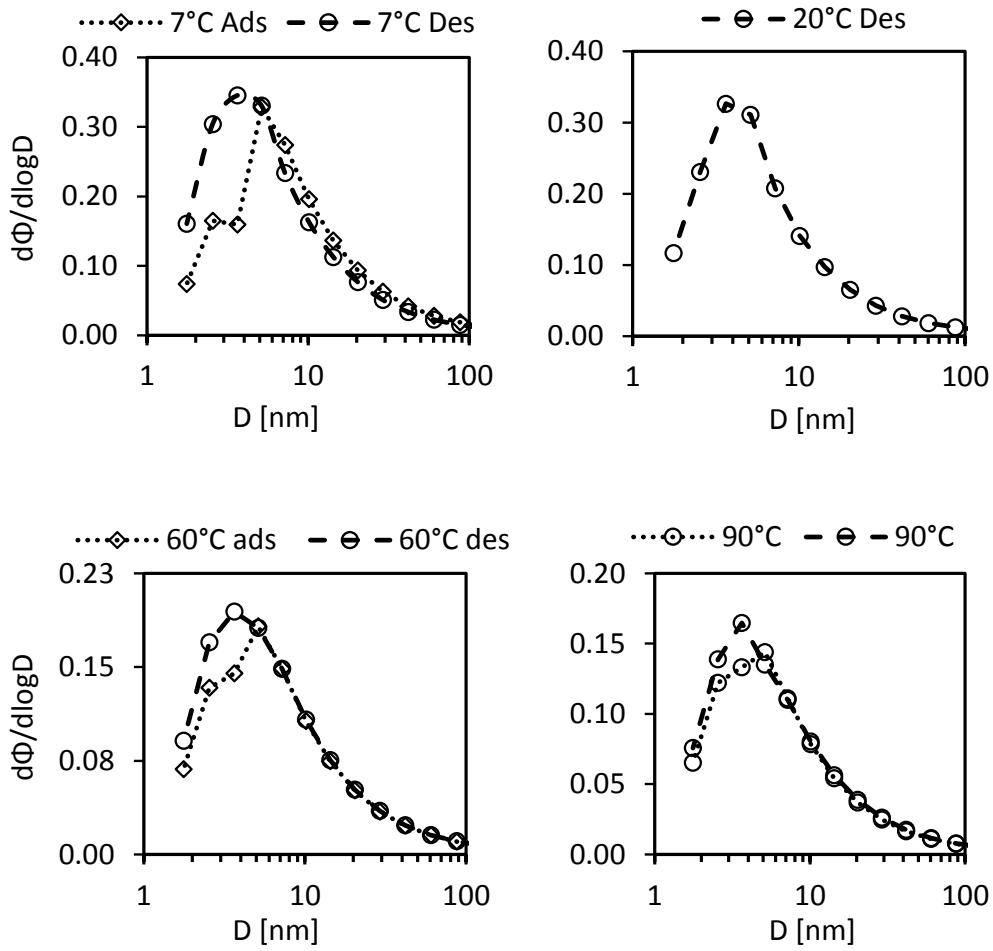

FIGURE 4.13: Pore size distributions obtained from BJH calculation on adsorption and desorption branches based of water sorption isotherm of cement pastes cured for 4 months at different temperatures T (°C)= 7, 20, 60, 90

when elevating the hydration temperature. Regarding pore sizes, the adsorption curves characterise a median pore size around 5 nm while the desorption branches characterise a median pore size of 3.5 nm. The pore size distributions as obtained from the adsorption branch are changing with temperature, while the ones obtained from the desorption branch are almost the same. Furthermore, the median pore size characterized by the desorption branch refers to a relative humidity of 0.36 RH which is similar to the cavitation pressure of water (around 0.35 RH). Thus, it seems reasonable to trust the adsorption branch for characterising a pore size distribution which showed some variation in the pore size distribution shape compared to the desorption branch. The pore family highlighted by water vapor sorption refers to gel pores. It can be understood

that the median pore size of gel pores is not changing with increasing curing temperature. The gel pore fraction is decreasing with temperature confirming previous observations.

4.3.3 Nitrogen sorption

The cumulative porosity with respect to the pore size of cement pastes cured at different temperatures as obtained from Nitrogen sorption is presented in Figure 4.14(a). Similarly to the MIP porosity, it can be clearly seen that the porosity intruded by Nitrogen is increasing significantly with temperature from 0.146 at 7°C to 0.182 at 90°C. However, this porosity does not correlate directly with capillary porosity. In Figure 4.14(b) the total porosity from Mercury and Nitrogen are both presented with respect to hydration temperature. In general, mercury intrusion gives higher values of porosity comparing to Nitrogen intrusion, although the Nitrogen is supposed to reach finer pores (up to 2 nm) as compared to mercury (up to 6 nm in our case). This is attributed to the difficulty of Nitrogen to condense in wide pores [21]. Therefore, the Nitrogen intrusion measures only a small fraction of capillary pores. Furthermore, it is shown in this study that the gel porosity is decreasing with increasing hydration temperature. As the Nitrogen intrusion measures an increasing pore volume with temperature, this pore volume cannot be assimilated with the gel porosity. Hence, it can be concluded that the Nitrogen pore volume correspond to a part of the capillary porosity and a part of the gel. These observations confirm the large difference between the specific surface area values of cement paste obtained by Nitrogen and Water.

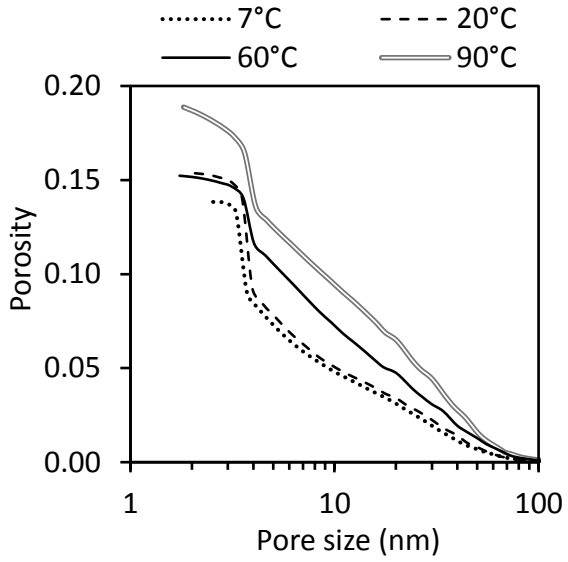

(a) a

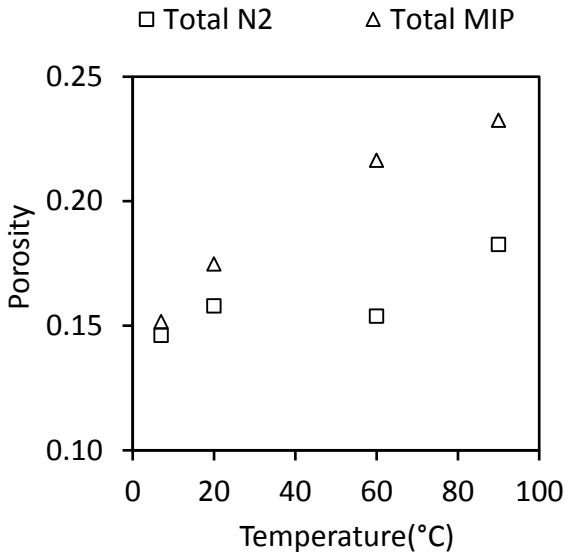

(b) b

FIGURE 4.14: (a) Cumulative porosity as obtained from Nitrogen and mercury porosimetry , (b) Comparison between total porosity as obtained from Nitrogen and mercury porosimetry of cement pastes cured for 4 months at different temperatures T(°C)= 7, 20, 60, 90

HD and LD porosity

Tennis and Jennings [14, 25] assumed that the C-S-H is distributed in two forms: Low and high density which are different in terms of their packing densities. This model assumes that some of C-S-H low density pores are accessible to Nitrogen, while none of high density pores are accessible to Nitrogen. The water however can enter both low density and high density C-S-H. This hypothesis permitted the evaluation of the HD and LD C-S-H intrinsic porosities (0.24 and 0.37 respectively), and their volume fractions inside C-S-H that vary with the hydration degree and W/C [25, 32]. The variation of these properties with other hydration parameters for instance the hydration temperature is poorly understood. It is usually assumed by some researchers that the properties of these two types of C-S-H for instance their intrinsic porosities are independent of the mix proportions and the hydration conditions [14, 32, 39], and only their volume fractions can vary. In this study, to characterise the pore volume of HD and LD variation with hydration temperature we follow the reasoning of Tennis and Jennings [14, 25] with some slight differences. We assume that LD and HD pores are both accessible to water. However, the Nitrogen can access the total pore volume of LD C-S-H and part of the capillary porosity. Furthermore, our analysis are based on the porosity results and not the SSA values due to complications of SSA estimations from water mentioned as the water is a part of the C-S-H particles. The analysis here is based on gathering the results of porosity obtained by different methods: Mercury porosity, Nitrogen porosity and water porosity. The capillary porosity as explained in Section 4.3.1 is taken from the cumulative porosity of mercury up to 10 nm. The total porosity is $\phi_{11\%\mathrm{RH}}$ the porosity measured by mass loss after drying at 11% of relative humidity. The gel porosity ϕ_{Gel} is regarded as the difference between the total porosity $\phi_{11\%\mathrm{RH}}$ and the capillary porosity. The gel porosity stands at the same time for the sum of the HD and LD porosities ϕ_{HD} and ϕ_{LD} respectively. Where ϕ_{HD} and ϕ_{LD} are porosities of HD and LD C-S-H with respect to the total volume of cement. Assuming that the Nitrogen access only to the LD C-S-H, we determine the pore volume of LD C-S-H from Nitrogen cumulative porosity as the intruded volume form 10 nm up to the end of intrusion. The 10 nm threshold is chosen again to determine the pore volume of LD in order be consistent with the determination of the capillary porosity. Finally the pore volume of HD is regarded as the difference between total porosity and the capillary porosity and LD porosity : $\phi_{\mathrm{HD}} = \phi_{11\%\mathrm{RH}} - \phi_{\mathrm{LD}} - \phi_{\mathrm{CAP}}$. This approach is summarized in Figure 4.15.

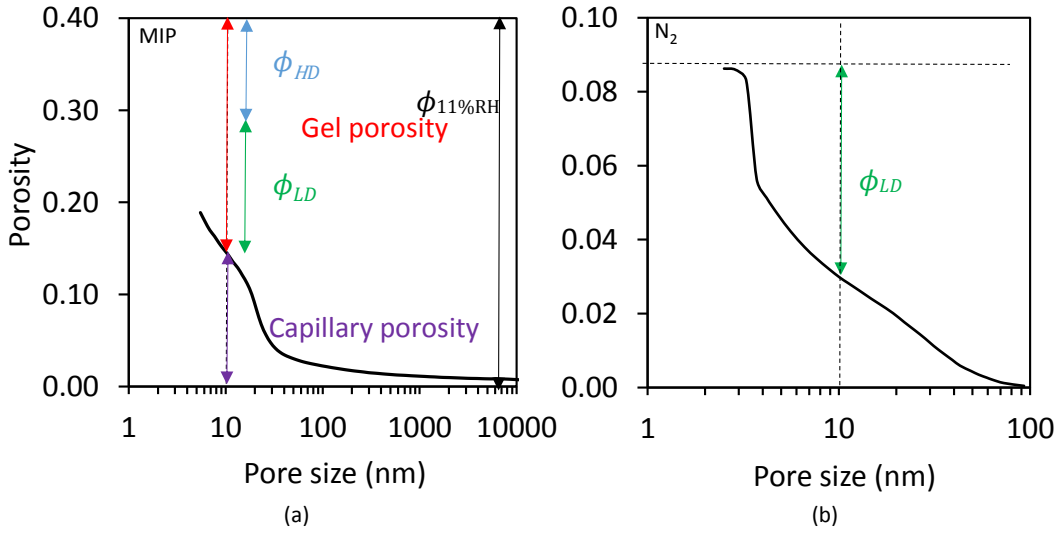

FIGURE 4.15: Scheme for determining the pore volume of LD and HD

The results of HD and LD porosities with respect to cement paste volume determined as follows are presented in Figure 4.16. The pore volume of LD is almost constant with temperature while the HD porosity decreases significantly with temperature. To compare the estimated values of HD and LD porosities lets calculate the ones predicted by Tennis and Jennings model [14, 25] for the same hydration conditions. At an overall hydration degree of 0.83 and a W/C=0.44 the volume fraction of LD and HD as estimated from the Tennis and Jennings model are respectively equal to 0.52 and 0.48. The determined hydration degree of alite and belite permit to estimate a volume fraction of 0.48 of C-S-H with respect to cement paste at four months of hydration. The pore volume of LD and HD with respect to cement paste calculated based on these values are reported in Figure 4.16. Estimations of LD and HD porosities in this work are in the range of values calculated by the Tennis and Jennings model [14, 25]. Estimations of the Tennis and Jennings model are however lower than the one calculated here. This derives mainly from the differences in the used assumption of a total LD pore volume accessible to Nitrogen or just some of the LD pores are accessible to Nitrogen. It's worth mentioning that considering a totally accessible LD porosity to Nitrogen didn't permit to obtain good fits of the evaluated porosities and the predicted ones by Tennis and Jennings model. We here consider a totally accessible LD porosity to Nitrogen for two reasons. Firstly, we find it unrealistic to distinguish between HD and LD based on their accessibility to nitrogen and to consider at the same time that a part of LD porosity is not accessible to Nitrogen. Secondly, the evaluated porosity non accessible to Nitrogen decreases significantly with temperature. If we assume that this porosity contains some of LD pores, the HD porosity will be smaller than the one evaluated in this study at high temperatures and may even vanish at 90°C. This suggests for instance that the C-S-H is mainly formed of low density at high temperature and contradict the well-established increase of C-S-H density.

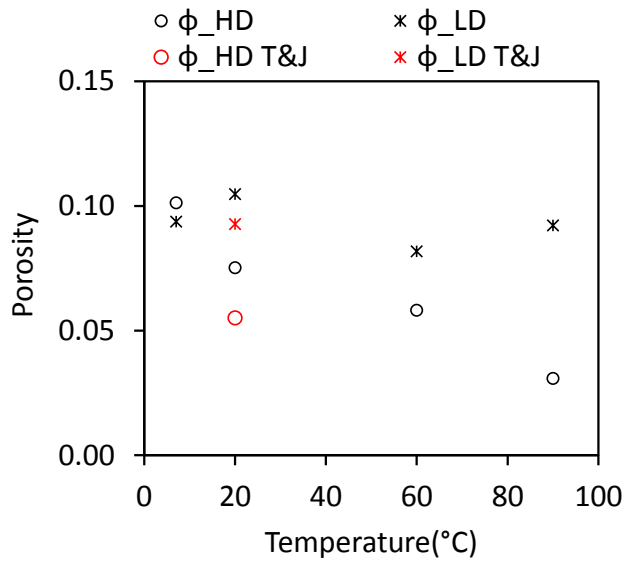

FIGURE 4.16: Variation of LD and HD pore volume with respect to cement paste volume for specimens hydrated for 4 months at different temperatures T(°C)= [7, 20, 60, 90]

Sorption hysteresis

The full sorption isotherms as collected from Nitrogen and water vapor of cement pastes cured at different hydration temperatures are presented in Figure 4.17 and Figure 4.12 respectively. An interesting feature of these isotherms is the diminishing hysteresis with elevating curing temperatures. The hysteresis is usually explained with the ink-bottle effect, the difference in contact angle between the receding and entering meniscus and finally, the water leaving the interlayer spaces irreversibly. It is worth noting that the hysteresis presented here does not include the contribution of the interlayer water, because the water vapor adsorption branch was obtained by progressively moving a specimen to higher relative humidities (e.g, from 11%RH to 33% RH and from 33% RH to 44% RH and so on). Moreover, the specimens used for Nitrogen were freeze-dried. In Section 3.4.1 we demonstrated that almost no interlayer water can be removed during freeze drying. The difference between the contact angle during adsorption and desorption cannot explain the reduced hysteresis as it is the same for the different specimens dried at T= 20°C. Hence, it can be concluded that the obtained hysteresis is mainly due to the ink-bottle effect. From this diminishing hysteresis, as it is associated with an ink-bottle effect, it can be understood that the necks controlling the desorption process are wider for higher curing temperatures.

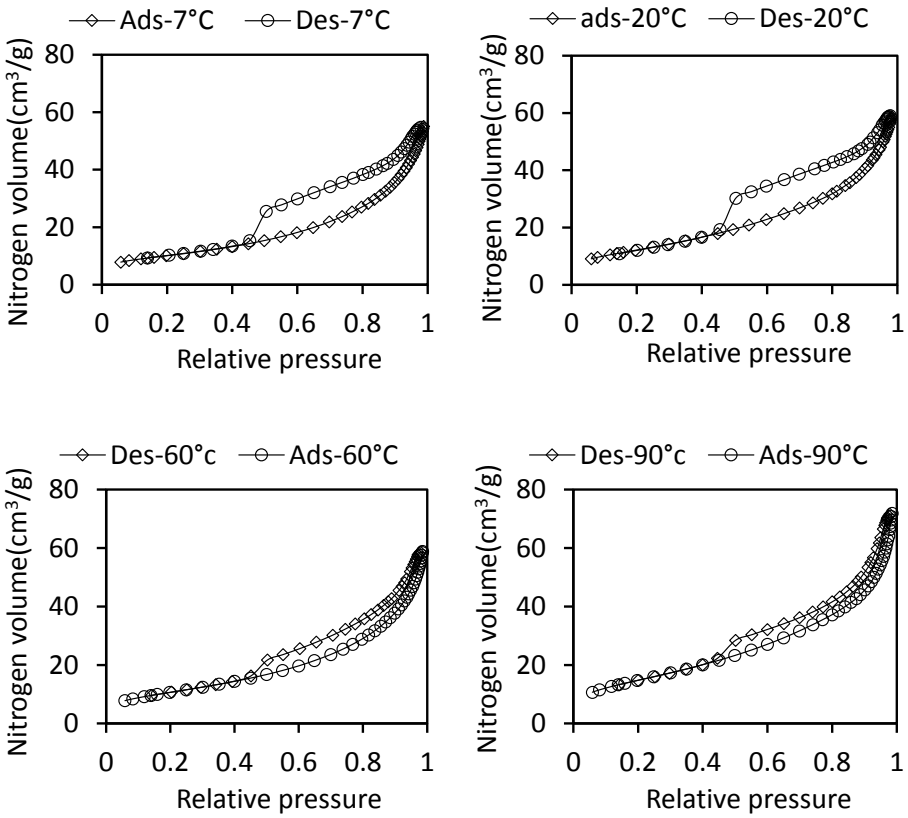

FIGURE 4.17: Nitrogen sorption measurement for a class G cement cured at different temperatures T (°C)= 7, 20, 60, 90 for 4 months

4.3.4 Nuclear magnetic resonance (NMR)

Chemical and mechanical setting times

The progressive early hydration has been followed by NMR at different temperatures for the first three days. The evolution of the relaxation time and the free induction decay signal are presented in Figure 4.18. The signal evolution illustrates water depletion due to progressive hydration. It can be seen that the increase of hydration temperature accelerates the water consumption showing an initial acceleration of hydration, which is a well-established result of calorimetry experiments [178, 179]. The relaxation time is also decreasing with the hydration temperature due to the increasing confinement level of water within the pores. The drop of relaxation time being faster at high temperatures indicates the rapid formation of a solid structure for specimens cured at high temperatures. The derivative of the T_1 relaxation time together with the heat flow curve of cement hydrated at 7°C are presented in Figure 4.19. The optimum of T_1 derivative is shown to correlate well with the optimum of the Vicat needle depth penetration derivative according to Wang et al. [142], permitting to define the time of mechanical setting. The slow down of the T_1 derivative

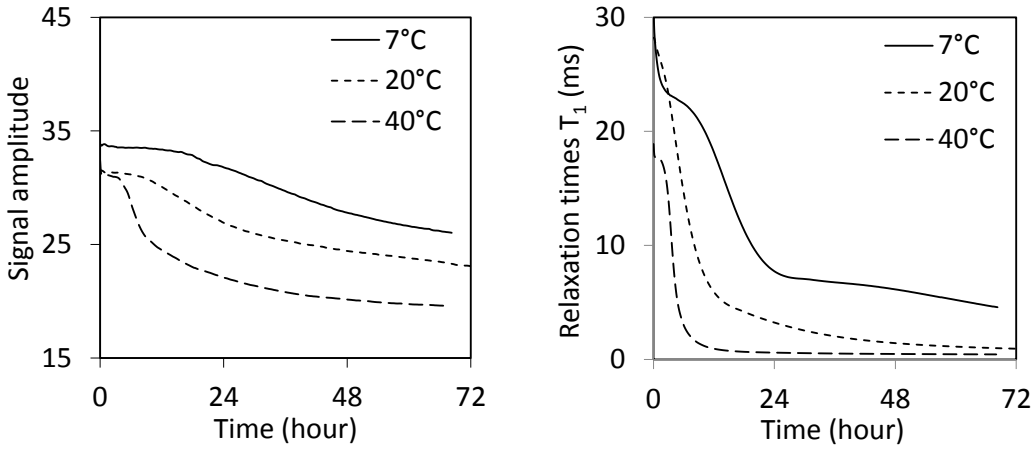

(a) (b)

FIGURE 4.18: Evolution of total NMR signal and relaxation time with the hydration time for different temperatures (T°C)=7, 20, 40

coincides with the optimum of the heat flow curve, making it possible to define the chemical setting time. The mechanical setting as perceived by Wang et al. [142] reveals the time for the percolation of a solid network while the chemical setting coincides with an important water depletion due to the precipitation of hydrates. It is worth mentioning that the mechanical setting here does not stand for the development of strength. It only corresponds to the formation of a defined structure. In this study, we found it interesting to correlate these characteristic times with the rheological behaviour of cement. We interpret the mechanical setting time as an indicator on the short term thixotropic reversible behaviour. The initial structure could be reproduced through a strong shearing. However, the chemical setting is seen as the long term thixotropic behaviour, corresponding to C-S-H particles bridging the clinker particles [180]. The mechanical and chemical setting times for class G cement taken as the time corresponding to the optimum of the T_1 derivative and the time at which the derivative equals zero, at different hydration temperatures are reported in Table 4.3. It is shown that both mechanical and chemical setting times are decreasing with increasing hydration temperature. The difference between these characteristic times is decreasing with increasing hydration temperatures. This permits identifying a characteristic time for workability loss of cement at different hydration temperatures. It is also consistent with the change in the hydration mechanism from diffusion control regime to reaction control regime. The delay between mechanical setting and chemical setting corresponds to a diffusion control regime. At high temperatures, the difference between mechanical setting times and chemical setting times is small comparing to low temperatures, reducing the time available for hydrates to diffuse leading to a more heterogeneous paste as highlighted by Verbeck [87].

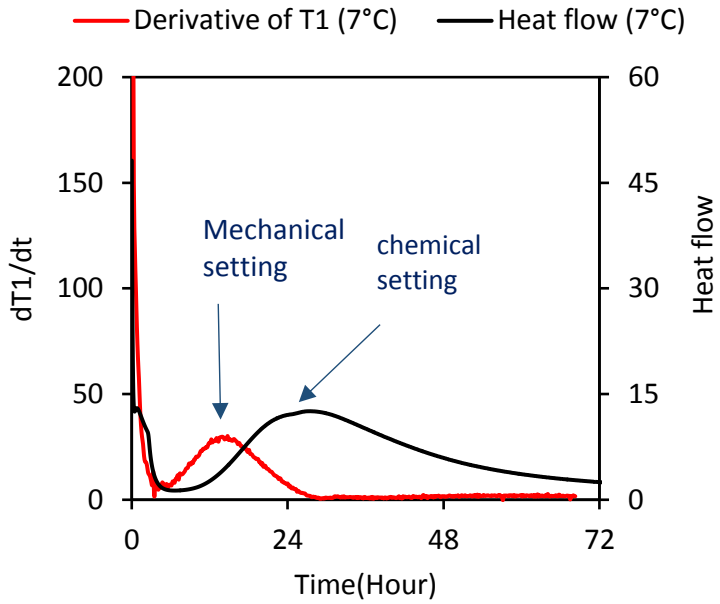

FIGURE 4.19: Derivative of the T_1 relaxation time curve and the heat flow curve of cement paste hydrating at 7°C indicating the chemical and mechanical setting of a cement paste

Temperature(°C)	Mechanical setting time (Hours)	Chemical setting time (Hours)
7	14.5	30
20	4.5	13
40	3.5	6

TABLE 4.3: Mechanical and chemical setting times at different temperatures

NMR pore size distribution at a hardened state

Figure 4.20 presents T_1 relaxation times of pastes cured at different hydration temperatures for 28 days. Generally, the relaxation time distribution exhibits four to three peaks. Based on the surface relaxivity evaluated in Section 3.3.6, the pore sizes can be calculated and assigned to different pore categories. The first peak with a relaxation time T_1=0.16 ms corresponds to interlayer water in C-S-H with a pore size of 0.70 nm at 7 and 20°C. A second peak at 7 and 20°C with T_1=0.90 ms and T_1=1.1 ms respectively corresponding to C-S-H gel pores with a characteristic size of 3.9 nm and 4.77 respectively. Finally, two or one side peaks that correspond to capillary pores. The evaluated pore size of interlayer spaces and gel pores are in accordance with other data in the literature estimating an interlayer spacing of 0.85 nm and a gel pore size of 2.5 nm [58]. However, it can be seen that the interlayer relaxation time increases slightly with increasing curing temperatures from 0.16 ms at 7 and 20°C to 0.20 ms at 40 and 60°C suggesting an increase of the interlayer space from 0.7

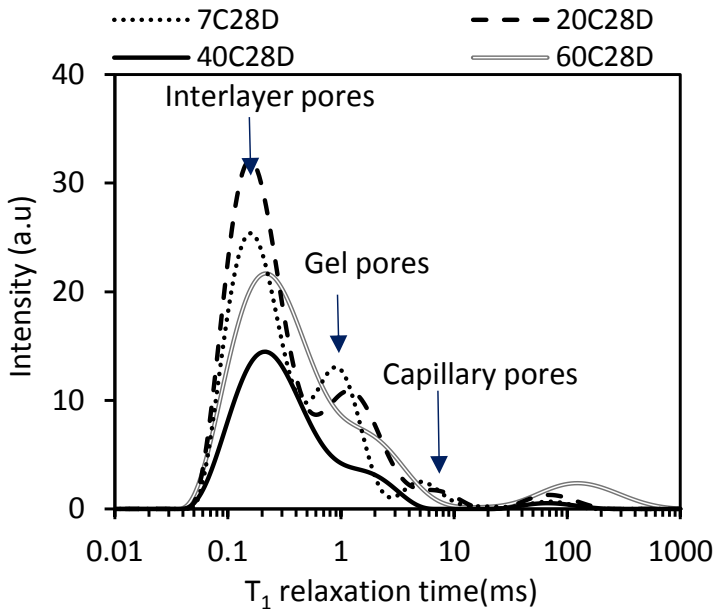

FIGURE 4.20: T1 relaxation time distribution obtained from NMR experiments at different temperatures T (°C)= 7, 20, 40, 60 for 28 days

nm to 0.87 nm. To our best knowledge this trend has not been observed in the literature. Gajewicz [79] and Holly et al. [92] have used ^{1}H NMR T_2 measurements to describe the pore structure of white cement with increasing hydration temperature and did not observe any variation of the interlayer spaces with hydration temperature. The increase of the interlayer space observed in this study is not fully understood. Regarding gel pores an increase in their size is noticed from 7°C to 20°C. Above 20°C, it seems that the median gel pore size is almost constant. However, the distribution is more spread at higher temperatures, spanning a wide range of pore sizes, on a contrary to lower temperatures where a sharp gel pore family is observed. The spread distribution of pore sizes at high hydration temperatures reflects the usually observed coarse structure. The gel pore size obtained from NMR confirms the pore size distribution obtained from BJH calculations on water vapor sorption indicating a pore size of 3.5-5 nm. The capillary porosity is however not well resolved with NMR. The efficiency of NMR experiments in characterizing a pore type rely on the saturation conditions of this pore. The capillary pores created by chemical shrinkage are unsaturated and hence cannot be seen by NMR leading to an underestimation of the capillary porosity by this method. Muller et al. [171] showed for instance that NMR combined with chemical shrinkage measurements provide estimations of capillary porosity that agree nicely with the MIP estimations of capillary porosity. A surprising feature of these NMR relaxation time distributions is the intensity relative to each pore category. The intensities suggest that an important fraction of water is contained in the interlayer spaces, while the common knowledge confirms that an important fraction of water is within gel pores. This inconsistency with previously published signal intensities makes

it difficult to interpret NMR intensities quantitatively, and motivates the use of other conventional methods to investigate the porosity within the cement paste.

Pore size distribution at different ages and temperatures

The NMR relaxation time distributions for cement pastes cured at different hydration temperatures (7°C, 20°C, 40°C and 60°C) for different ages (1, 3, 7, 14 , and 28 days) are presented in Figure 4.21. Similar to MIP, the relaxation times corresponding to low curing temperatures decrease progressively with ongoing hydration, witnessing the increase of confinement level of water within gel pores and then stabilise. The relaxation times corresponding to high curing temperatures stabilise after three days of hydration and the pore structure is frozen rapidly and does not evolve much.

Comparison between NMR and other conventional methods

The NMR pore size distribution presented above gives pore sizes of interlayer spaces and gel pores in accordance with other published data in the litterature, despite the high iron content of this class G cement. The pore size distribution obtained from NMR is compared with the pore size distribution obtained from MIP and BJH calculations on water sorption isotherm to investigate the limitations of each technique. The comparison is presented in Figure 4.22 for mature (120 days) and early age (1 day) cement pastes.

The pore size distributions obtained from different methods agree nicely despite the limitations of each technique. At a mature age the MIP curve covers the capillary pore range of the NMR pore size distribution. The BJH pore size covers both the capillary and the gel pore range. However, the pore size characterised by the BJH curve corresponds mostly to the gel pore family observed by NMR. Only NMR is capable of characterising the interlayer spaces. The agreement between MIP and NMR holds also for early age cement. The MIP curve shows a bimodal distribution over the capillary porosity at 20°C at 1 hydration day. NMR shows also a bimodal distribution of porosity over the same range of pores. However, the intensities relative to these two peaks seen by NMR and MIP are not similar. This may be explained by the capillary pores created by chemical shrinkage and that are not seen by NMR while they are well captured by MIP, leading to a higher intensity of MIP for the pores bigger than 100 nm. As mentioned in Section 4.3.1, the association of NMR and chemical shrinkage experiments for instance yields similar estimations of capillary porosity as the MIP [171].

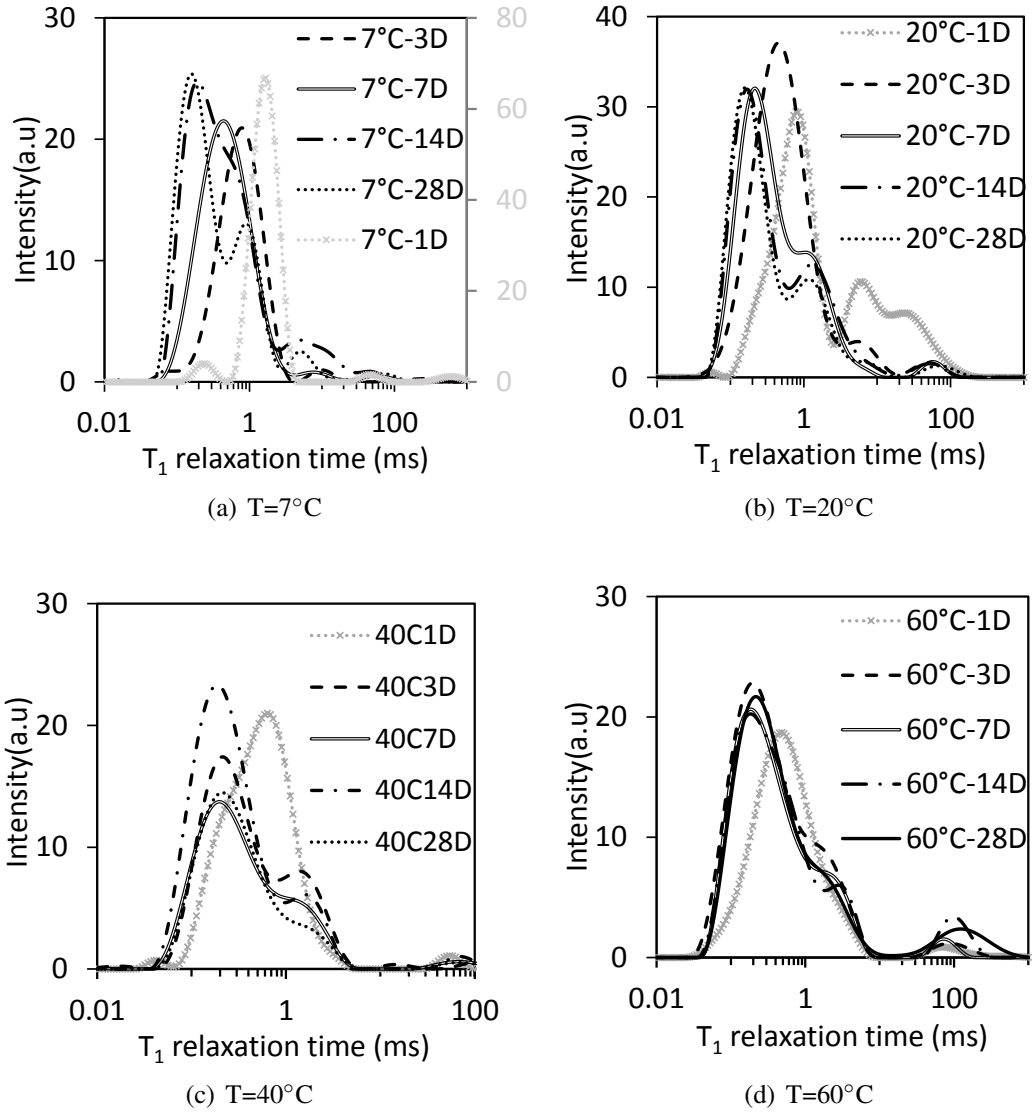

(a) T=7°C (b) T=20°C

(c) T=40°C (d) T=60°C

FIGURE 4.21: T_1 relaxation times obtained for specimens hydrated at different ages for T (°C)= 7, 20, 40, 60. The curve corresponding to 1 hydration day at 7°C can be read on the grey axis

4.3.5 Scanning electron microscopy

Scanning electron microscopy images of cement paste are presented in Figure 4.23 and show a visual distribution of hydrates and their porosity for specimens cured for four months at different temperatures. These images confirm the different observations presented above for cement pastes cured at different hydration temperatures. It is seen that the capillary porosity is increasing with increasing hydration temperature. Furthermore, the hydrates are less homogeneously distributed when the hydration temperature is increased. In Figure 4.23 a clear distinction in terms of density can be made between the hydrates and the surrounding matrix in which they are embedded. It seems that this matrix is getting porous with increasing hydration temperature. This visual observation

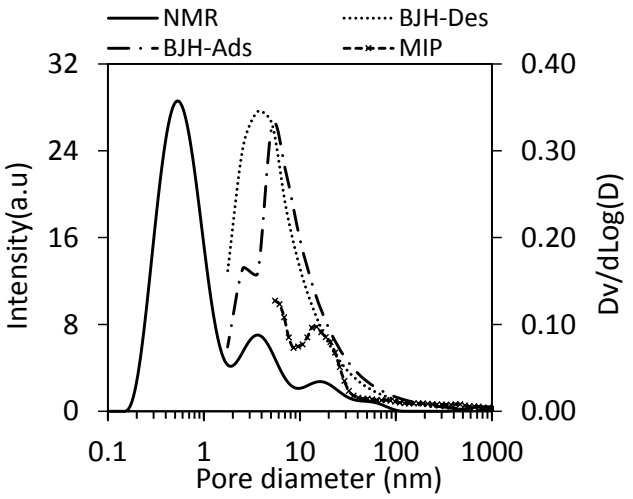

(a) T=7°C at 120 days of hydration

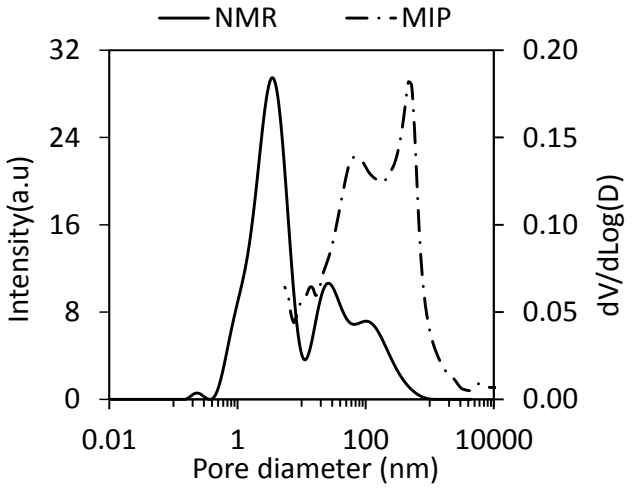

(b) T=20°C at 1 day of hydration

FIGURE 4.22: Comparison between NMR pore size distribution and the pore size distribution obtained from BJH analysis and Mercury intrusion

of cement paste at different hydration temperatures will help refining the microstructural representation of cement paste for micro-mechanical modelling.

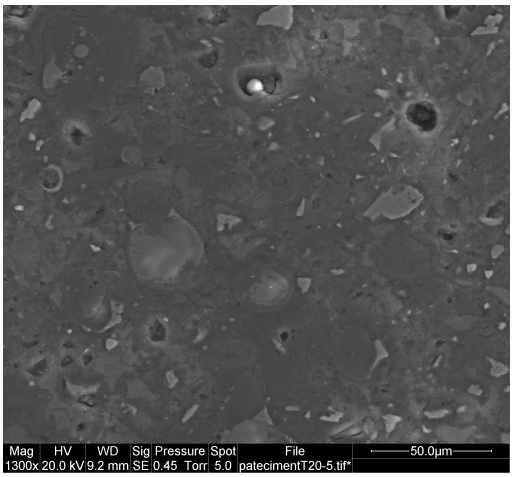

(a) T=20°

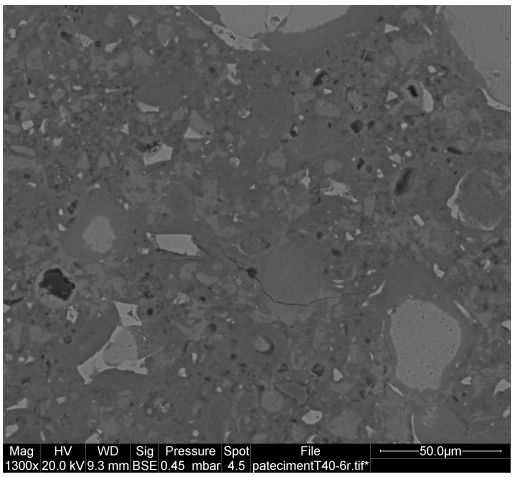

(b) T=40°

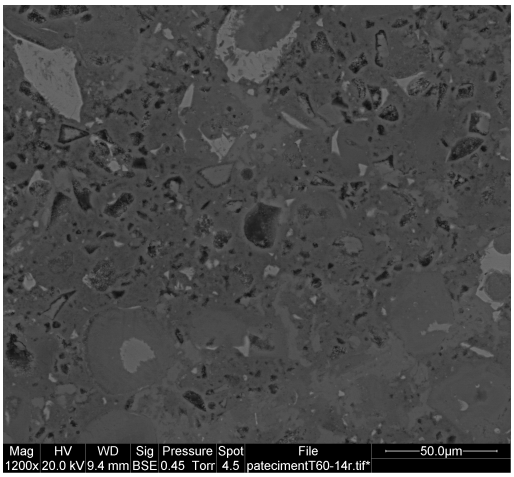

(c) T=60°

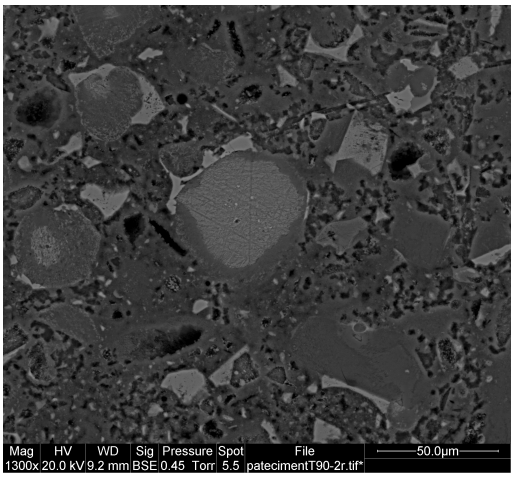

(d) T=90°

FIGURE 4.23: Microscopy observations on cement paste cured for four months at different temperatures T (°C)= 7, 20, 40, 60

4.3.6 Uniaxial compression tests

The results obtained from uniaxial compression tests conducted on class G cement samples cured at various hydration temperatures are presented in Figure 4.24. The uniaxial compression strength undergoes a significant decrease from 63 MPa at 7°C up to 47 MPa at 90°C. Similarly, the Young's modulus is reduced with increasing hydration temperature from 20.5 GPa at 7°C to 11.3 GPa at 90°C. In the same way the Poisson's ratio is declining from 0.27 at 7°C to 0.205 at 90°C.

These observations are in good agreement with well-established trends in the literature showing a decline of mechanical properties of cement when cured at high temperatures [20, 74]. This decrease of mechanical properties is generally attributed to the increase of capillary porosity generated by the enhanced heterogeneity of cement paste at elevated temperatures [20, 43, 74, 80]. In this

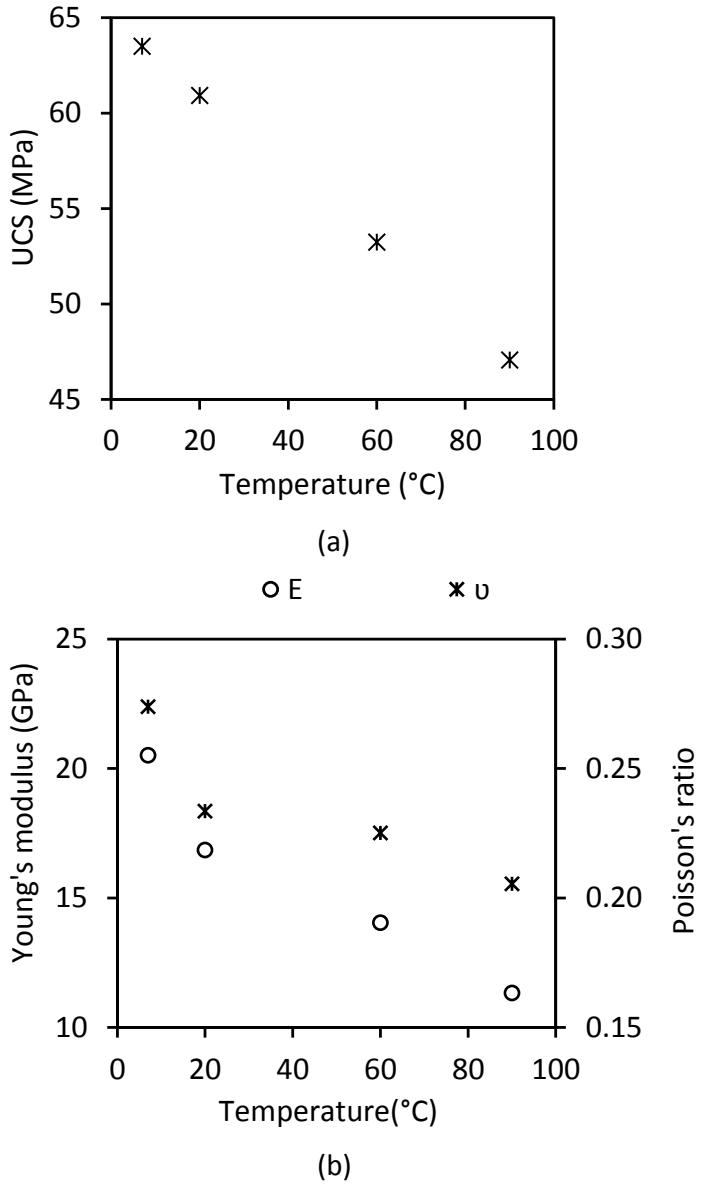

FIGURE 4.24: Elastic properties of cement paste cured for four months at different temperatures as obtained from uniaxial compressive strength (a) Uniaxial compression strength, (b) The Young's modulus and the Poisson's ratio

work, we will investigate how the increase of capillary porosity with increasing hydration temperature contributes to the decrease of the mechanical properties (Refer to section 5.3).

4.4 Conclusion

The cement paste microstructure has been characterized by performing X-Ray diffraction analysis combined with the Rietveld method, thermogravimetric analysis, mercury intrusion porosimetry, porosity evaluation by drying, Nitrogen and water vapor sorption and finally NMR relaxometry. The mass assemblage obtained from TGA and XRD is slightly affected by the hydration temperature. The different experimental methods agree on the increase of the capillary porosity and the decrease of the gel porosity by increasing the hydration temperature. Regarding hydrating cement pastes, the total and capillary porosity decreases with time as a result of progressive hydration. The gel porosity increases up to 28 days of hydration and then starts decreasing slightly as the C-S-H densifies within gel pores. The pore sizes obtained from MIP and BJH calculations on water vapor sorption show compatibility with the pore sizes obtained from NMR relaxation at mature and early ages. Association of water vapor sorption, capillary porosity and Nitrogen porosity following Tennis and Jennings [14, 25] schematic description of C-S-H permits quantifying the LD and HD pore volume with respect to cement paste. The LD pore volume is almost constant while the HD pore volume decrease significantly. At the macroscopic scale these different microstructural changes result in a significant decrease of the Young's modulus and Poisson's ratio of cement paste with increasing hydration temperature.

Chapter 5

Effect of the hydration temperature on the C-S-H

5.1 Introduction

The mass assemblage of a class G cement has been provided in the previous chapter for different curing temperatures and different hydration degrees at a curing temperature of 20°C. The porosity and pore size distribution obtained by different methods were also presented and showed agreement between each other. In this Chapter, the results of Chapter 4 are analysed in order to determine the C-S-H characteristics at different temperatures and hydration degrees at a curing temperature of 20°C. For instance, the C-S-H density, C/S and H/S molar ratios and the intrinsic HD and LD porosity are elucidated. The description of the microstructure at different hydration temperatures is used in a micro-mechanical model to gain insights into the origins of the decrease of mechanical properties of cement paste hydrated at high temperatures.

5.2 Charcterisation of the C-S-H chemical composition and density

5.2.1 Evaluation of C-S-H density

Few data in the literature exist on the effect of curing temperature on the C-S-H bulk density [79, 80] and the proposed values of this density at different curing temperatures are not close to each other. The direct measurement of C-S-H density is difficult due to its amorphous structure and the presence of portlandite finely intermixed with C-S-H particles. We propose here a simple indirect method to evaluate the C-S-H bulk density based on the experimental results presented previously. The C-S-H gel porosity ϕ_{gel} can be related to the C-S-H intrinsic porosity ϕ_{CSH} and its volume fraction f^V_{CSH} through the following expression:

$$\phi_{\text{gel}} = \phi_{\text{CSH}} f^V_{\text{CSH}} \tag{5.1}$$

The C-S-H intrinsic porosity can be further expressed in terms of the density of C-S-H solid ρ_s, the bulk density of C-S-H $\rho^{\text{bulk}}_{\text{CSH}}$ and the water density ρ_w as:

$$\phi_{\text{CSH}} = \frac{\rho_s - \rho^{\text{bulk}}_{\text{CSH}}}{\rho_s - \rho_w} \tag{5.2}$$

The C-S-H volume fraction f^V_{CSH} is linked to the mass fraction of saturated C-S-H, $f^{\text{sat}}_{\text{CSH}}$ through the following expression:

$$f^V_{\text{CSH}} = f^{\text{sat}}_{\text{CSH}} \frac{\rho_{\text{CP}}}{\rho^{\text{bulk}}_{\text{CSH}}} \tag{5.3}$$

where ρ_{CP} is the cement paste density. It is worth noting that the mass fraction of C-S-H evaluated in Section 4.2.4 corresponds to a freeze-dried C-S-H, $f^{\text{dry}}_{\text{CSH}}$. To evaluate the saturated C-S-H density, the saturated mass fraction $f^{\text{sat}}_{\text{CSH}}$ should be used. The dried and saturated mass fractions can be linked to each other with the following relation:

$$f^{\text{sat}}_{\text{CSH}} = f^{\text{dry}}_{\text{CSH}} \frac{\rho^{\text{bulk}}_{\text{CSH}}}{\rho^{\text{bulk}}_{\text{CSH}} - \phi_{\text{CSH}} \rho_w} \tag{5.4}$$

Using Eqs. 5.1, 5.2, 5.3, 5.4 and $\phi_{\text{gel}} = \phi_{\text{t}} - \phi_{\text{cap}}$ the following expression can be derived for the bulk C-S-H density:

$$\rho^{\text{bulk}}_{\text{CSH}} = \rho_{\text{s}} \frac{\rho_w(\phi_{\text{t}} - \phi_{\text{cap}}) + \rho_{\text{CP}} f^{\text{dry}}_{\text{CSH}}}{\rho_{\text{s}}(\phi_{\text{t}} - \phi_{\text{cap}}) + \rho_{\text{CP}} f^{\text{dry}}_{\text{CSH}}} \tag{5.5}$$

The inputs parameters for this expression are the density of C-S-H solid ρ_s, the mass fraction of freeze-dried C-S-H $f^{\text{dry}}_{\text{CSH}}$, the cement paste density ρ_{CP}, the total porosity ϕ_{t} and the capillary porosity ϕ_{cap}. The mass fraction of dried C-S-H is obtained from a mass balance of different hydrates as explained in Section

4.2.4. The total porosity and the capillary porosity are evaluated respectively by freeze drying and mercury porosimetry. The choice of C-S-H solid density is important for this analysis. The most admitted value of C-S-H solid density has been given by Allen et al. [33] using SANS & SAXS experiments and is equal to 2.603 g/cm^3. This density includes all the internal water of the C-S-H globule but excludes any adsorbed water at the globule's surface. As the drying at 11% RH leaves a monolayer of water on the C-S-H surface, the solid density of C-S-H at this condition is smaller than 2.603 [33]. Jennings [35] presented a solid density of globules equilibrated at 11% RH equal to 2.47 g/cm^3 which can be considered as the solid density of C-S-H globules in a freeze-dried cement paste, considering the similarity of freeze drying and 11% RH drying methods presented in Section 3.4.1. The density of C-S-H solid is considered to be independent of hydration conditions. Still, we admit that a change of the C-S-H solid density is possible. The changing chemical composition with temperatures will obviously affect this solid density [79].

C-S-H density at different temperatures

The bulk density of C-S-H has been evaluated for different hydration temperatures through the proposed method and presented in Figure 5.1. As expected, the C-S-H bulk density is increasing with increasing curing temperatures from 1.87 g/cm^3 at 7°C to 2.10 g/cm^3 at 90°C. The value of the bulk density evaluated at ambient temperature, equal to 1.96 g/cm^3, is close to the widely admitted value of C-S-H bulk density determined by Jennings [31], equal to 2.03 g/cm^3.

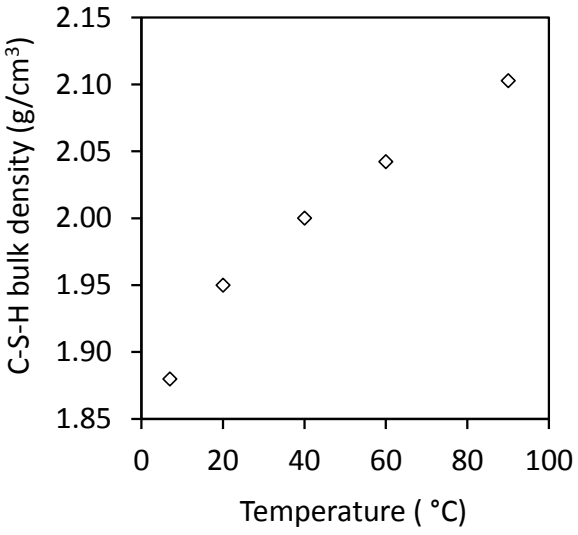

FIGURE 5.1: The evaluated C-S-H saturated density for different curing temperatures at 28 days of hydration

Gallucci et al. [80], reported values of the C-S-H bulk density at different curing temperatures that are higher than the one presented here. It's worth mentioning that a scaling factor has been applied to the densities obtained by Gallucci et al. [80] to be in accordance with the Jennings model predictions. Gajewicz [79] also reported the C-S-H bulk densities for white cement and the reported values of densities agree very well with the data presented here. For instance, Gajewicz [79] presented a density of 1.91 g/cm^3. and 2.01 g/cm^3 for 20°C and 60°C curing temperatures respectively, while we obtained 1.96 g/cm^3. and 2.04 g/cm^3 for the same hydration temperatures. Regardless of the experimental uncertainties, this good agreement gives confidence in our experimental results and the proposed method. It also provides quantitative estimations of the C-S-H density for another type of cement which presents some difficulties to be probed by other sophisticated methods such as NMR.

The intrinsic porosity of C-S-H can now be evaluated using Eq 5.2. The results, presented in Figure 5.2, show that the intrinsic porosity of C-S-H is decreasing significantly with increasing curing temperature from 0.40 at 7°C to 0.25 at 90°C at 28 days of hydration. The intrinsic porosity at 90°C is close to the HD intrinsic porosity of 0.24 provided by Tennis and Jennings [14].

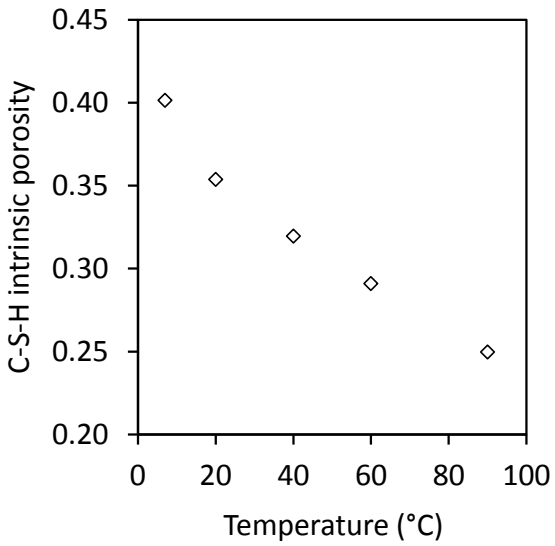

FIGURE 5.2: The intrinsic porosity of C-S-H for different curing temperatures at 28 days of hydration

The increase of the C-S-H bulk density with curing temperature was undeniable from increasing grey level of backscattered images of Gallucci et al. [80]. However, a debate has been raised on whether this changing grey level reflects a change of the C-S-H atomistic structure, or is due to an internal arrangement of C-S-H particles. It is here evidenced that regardless of C-S-H solid density (which is considered constant here), the decreasing internal porosity of C-S-H captures well the increase of C-S-H density. Nevertheless, we do not refute the

fact that the atomistic structure influences the C-S-H solid density. In fact, decreasing water content in C-S-H leads obviously to increasing solid density. As can be seen in Eq. 5.5, the saturated C-S-H density in our calculation is directly proportional to the C-S-H solid density ρ_s. Considering the relatively narrow range of the possible values of C-S-H solid density, it can only have a limited influence on the evaluation of C-S-H bulk density. Further work is needed to improve our knowledge about the C-S-H solid density under different curing conditions.

C-S-H density at 20°C at different ages

The C-S-H bulk density of a cement paste hydrated under 20°C for different curing ages is presented in Figure 5.3. It can be seen that the C-S-H bulk density is gradually increasing from 1.92 g/cm^3 after 1 day of hydration up to 1.99 g/cm^3 at 120 days. A considerable increase in density is noticed after 28 days of hydration. This is consistent with the noticed decrease of the gel porosity after 28 days as presented in Section 4.3.1 and suggests the development of C-S-H in more restricted spaces. In other words, it is the result of nucleation of solid C-S-H layers within the gel pores. Calculated densities at different ages are in a strong agreement with Muller et al. [58] estimations. The intrinsic

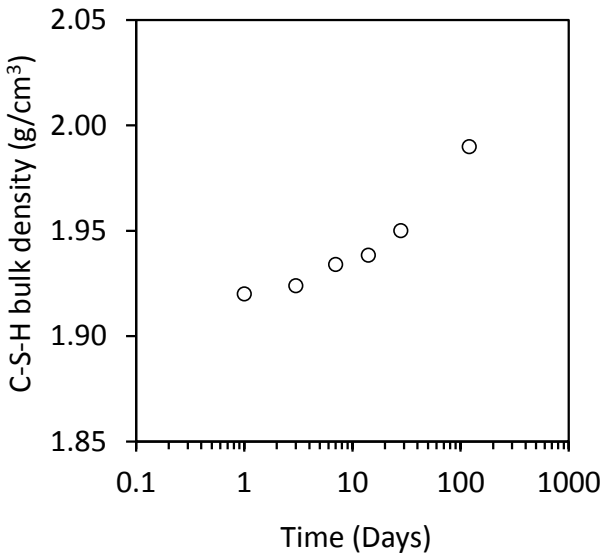

FIGURE 5.3: The evaluated C-S-H saturated density for different curing times at a hydration temperature of 20°C

porosity of C-S-H of a cement paste hydrated under 20°C for different curing ages is presented in Figure 5.4. The intrinsic porosity of C-S-H is decreasing from 0.374 at 1 day of hydration at 20°C to 0.326 at 120 days of hydration at the same temperature °C. The intrinsic porosity at early ages (0.374) is almost equal to the LD intrinsic porosity proposed by Tennis and Jennings [14] equal

to 0.37. This intrinsic porosity at 1 day of hydration supports the idea of development of one C-S-H type which is the low density C-S-H at early ages. The later decrease of C-S-H intrinsic porosity corresponds to the development of a high density C-S-H by nucleation of solid layers within the LD C-S-H. The intrinsic porosity at 120 days is equal to 0.326 and is in agreement with the intrinsic porosity provided by Tennis and Jennings [14] for the same hydration conditions 0.308=0.24*0.48+0.37*0.52.

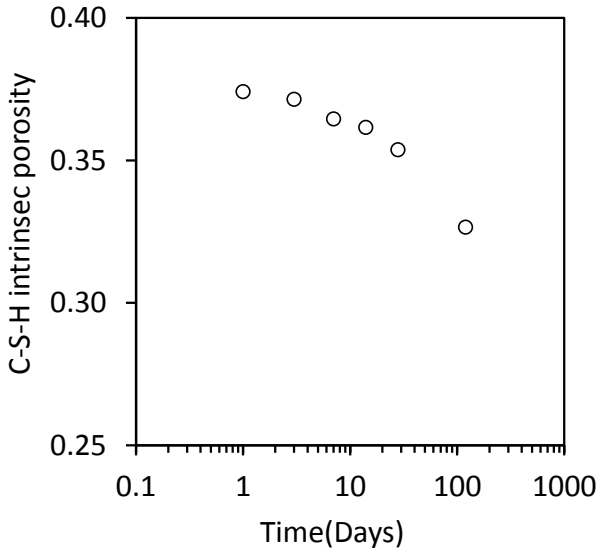

FIGURE 5.4: The intrinsic porosity of C-S-H for for different curing times at a hydration temperature of 20°C

5.2.2 C-S-H Chemical composition

This section is dedicated to evaluation of the influence of hydration temperature on the C-S-H composition in terms of C/S and H/S molar ratios. These ratios are defined in the following:

$$\mathrm{C/S} = \frac{n^{\mathrm{Ca}}_{\mathrm{CSH}}}{n^{\mathrm{Si}}_{\mathrm{CSH}}}; \quad \mathrm{H/S} = \frac{n^{\mathrm{H}}_{\mathrm{CSH}}}{n^{\mathrm{Si}}_{\mathrm{CSH}}} \tag{5.6}$$

Where $n^{\mathrm{Ca}}_{\mathrm{CSH}}$, $n^{\mathrm{Si}}_{\mathrm{CSH}}$ and $n^{\mathrm{H}}_{\mathrm{CSH}}$ correspond respectively to molar quantity of calcium, silicon and water in a C-S-H particle. The molar C/S ratio is derived from the resolution of the system of equations as mentioned in section 4.2.4. Regarding the H/S ratio, the molar quantity of chemically combined water in C-S-H can be estimated from the weight loss corresponding to C-S-H in TGA experiments. Within the temperature range associated to the dehydration of C-S-H other constituents like ettringite, Afm, hydrogarnet are also loosing water. Consequently to evaluate the water associated to C-S-H, the quantity of water

evaporated from the other phases in the same temperature range should be deduced. The molar contents of hydrogarnet has been evaluated through mass assemblage of the cement paste and its water content can be easily subtracted. Concerning ettringite and Afm, it should be recalled that the TGA experiments are performed here on freeze-dried samples. The freeze-drying seems to dehydrate ettringite and Afm [62] and probably for the same reason these two phases could not be observed in our XRD experiments. It seems thus reasonable to not subtract the water associated to ettringite and Afm from the TGA results as these phases may have been already dehydrated during the freeze drying. Therefore, the chemically combined water in C-S-H is evaluated by subtracting the water bounded to hydrogarnet from the total quantity of water removed until 300°C. The H/S ratio corresponding to the saturated C-S-H can be obtained by adding the molar quantity of water in gel pores per unit mass of dry paste to the value obtained for the dry C-S-H:

$$(\mathrm{H/S})_{\mathrm{sat}} = \frac{1}{n^{\mathrm{Si}}_{\mathrm{CSH}}} \left(n^{\mathrm{H}}_{\mathrm{CSH}} + \frac{\phi_{\mathrm{gel}} \rho_w}{(\rho_{\mathrm{CP}} - \phi_{\mathrm{t}} \rho_w) M_{\mathrm{H_2O}}} \right) \tag{5.7}$$

Where ρ_{CP} is the density of saturated cement paste and $M_{\mathrm{H_2O}}$ is the molar mass of water.

C-S-H chemical composition at different temperatures

The C/S ratios for different hydration temperatures as evaluated directly from the resolution of the set of Eqs. (4.1) are presented in Figure 5.5.

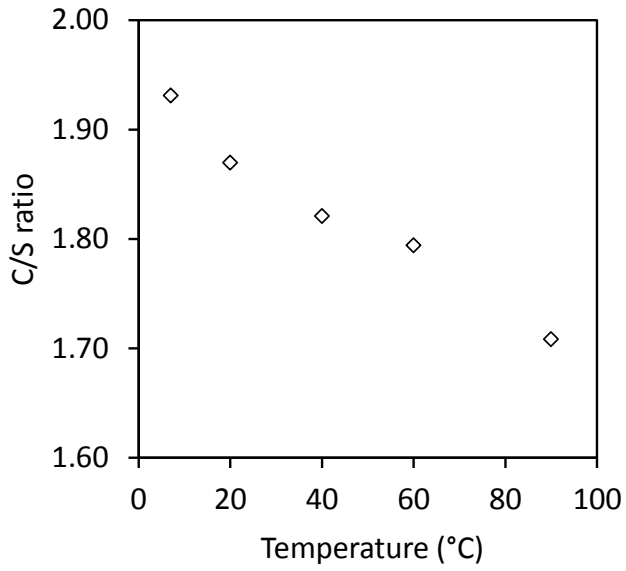

FIGURE 5.5: The evolution of the C/S ratio with respect to hydration temperature for a cement paste cured for 28 days at different temperatures

One can see a decrease of C/S ratio with increasing curing temperature, from 1.93 at 7°C to 1.71 at 90°C. The C/S ratio evaluated at ambient temperature, equal to 1.86, is higher than the generally admitted value of 1.75 regarded as the mean value of C/S molar ratio in C-S-H [20, 42, 53]. However, different values for the C/S ratio are presented in the literature. Escalante et al. [181] reported values ranging from 1.61 to 2.24 for C/S ratio. In other studies the same authors reported values of 2.06 and 2.07 based on EDS experiments [74]. Richardson et al. [53] reported values for the C/S ratio of 1.2 to 2.3. In a more recent study on a class G cement the C/S ratio at 30°C is found to be 1.84 ± 0.24 [126]. It appears that the values of C/S ratio vary widely in literature and rely on the used experimental techniques.

It is worth noting that the obtained values of C/S ratio depend on the evaluated quantity of portlandite from TGA results. As mentioned in section 4.2.2 we assumed that all the produced calcite comes from the carbonation of portlandite. If one assumes that a part of the calcite is produced as a result of the carbonation of C-S-H, this results in a smaller quantity of portlandite and leads to higher C/S ratios. As for example, if the first carbonation peak is arbitrarily attributed to C-S-H carbonation, it results in C/S ratios higher than 2.0 for hydration temperatures 7°C and 20°C, which is of course much higher than the admitted average values.

The evaluated H/S ratios for dry (corresponding to non evaporable-water or water within interlayer spaces) and saturated (corresponding to C-S-H with gel pores filled with water) conditions are given in Figure 5.6 for different hydration temperatures.

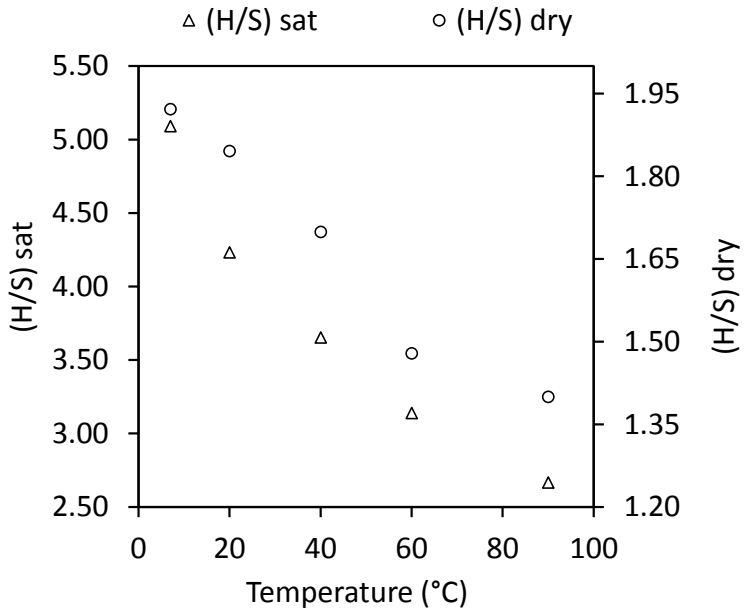

FIGURE 5.6: The evolution of the H/S ratio with respect to hydration temperature for a cement paste cured for 28 days at different temperatures

One can note a decrease of the H/S ratio with increasing curing temperature for both dry and saturated state. The dry (H/S) decreases from 1.92 at 7°C to 1.40 at 90°C and the saturated (H/S) varies from 5.1 at 7°C to 2.66 at 90°C. The evaluated value of H/S ratio for dried C-S-H cured at ambient temperature, equal to 1.85, compares well with the value of 1.8 given by Allen et al. [33] based on SANS and SAXS experiments, corresponding to interlayer water which does not include the layer of water at the surface of the globule. This has been confirmed in recent studies by Muller et al. [58] proposing a mean value of 1.8 for the interlayer water. The saturated H/S ratio evaluated at ambient temperature in this study is equal to 4.23, which is in agreement with the widely admitted value equal to 4 for a pure C-S-H [20, 35]. It is worth noting that the provided H/S ratios may be underestimated due to the eventual carbonation of C-S-H. Few data in the literature propose the H/S ratio for saturated C-S-H as most of the investigation techniques are destructive. In a recent study by Muller et al. [58] using NMR on a never dried cement paste,an H/S ratio equal to 4.4 is found respectively for w/c=0.40 which is compatible with the ratio of 4.23 found in this work for w/c=0.44.

The observed decreasing trend of H/S ratio with hydration temperature is compatible with the results of Bentur et al. [172] and Gallucci et al. [80] who both reported a decrease in the water content of C-S-H. However, the values calculated by Gallucci et al. [80] for the H/S ratio were bigger than the values admitted for interlayer water and lower than the values corresponding to a saturated C-S-H. They hence assigned the evaluated H/S ratio to interlayer water plus a part of water in gel pores. However, in this study a clear distinction between interlayer water and gel pore water has been made and provided coherent values with the widely admitted values. Gajewicz [79] clearly distinguished between interlayer water and gel pore water. The value provided of saturated H/S from for Gajewicz [79] studies are in agreement with the values of saturated H/S ratio proposed here. For instance at 20°C and 28 days the saturated H/S is equal to 4.24 according to Gajewicz [79] and a value of 4.23 is obtained here. However, the values corresponding to interlayer H/S ratio in this study are significantly different from the ones presented by Gajewicz [79]. For instance, the H/S ratio for a cement hydrated at 20°C for 28 days is equal to 1.45 according to Gajewicz [79] and a value of 1.85 is proposed here. One explanation for the difference between these values is that the measurements of Gajewicz [79] exclude the adsorbed water at the C-S-H surface, while the measurements in our study include the contribution of the adsorbed water. Regarding the decrease of H/S ratio, Thomas et al. [182] has interpreted this observation using sol-gel processing mechanisms, stipulating that the decrease in the molar H/S ratio is the result of the condensation reactions that take place in cement pastes. In fact, cement cured at elevated temperatures undergoes an enhanced rate of silicate polymerization [183] turning the monomeric species into polymeric species. This condensation reaction is accompanied by the release of a water molecule, which results in a diminution of C-S-H water content. Solid NMR experiments also confirmed this increasing rate of silicate polymerization with temperature as the mean chain length of silicate showed an increase with elevated curing

temperature [80, 183]. In a similar manner, the enhanced silicate polymerization rate yields to a decrease of the C/S ratio as reported before in [183]. The provided chemical composition of C-S-H is a simplified composition as it did not account for the eventual adsorption of sulphates or aluminium to the C-S-H. Indeed, some sulphates or aluminium may adsorb to the C-S-H, but it is shown that they have only a limited impact on its properties [80]. Furthermore, the quantity of sulphate present in the initial composition is very small and is mostly used to nucleate ettringite and Afm.

C-S-H chemical composition at 20°C at different ages

The C/S ratio at different ages is presented in Figure 5.7. This ratio is decreasing significantly the first 3 days and then stabilises around 1.84. The decrease of C/S ratio with age is in accordance with results from literature [53, 58].

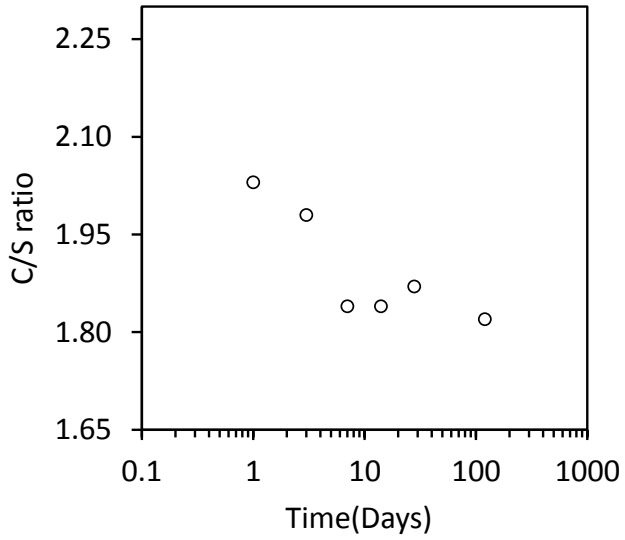

FIGURE 5.7: The evolution of the C/S ratio with respect to time at a hydration temperature of 20°C

The H/S ratio for dry and saturated C-S-H is presented in Figure 5.8. The dry H/S ratio increases with age from 1.23 at 1 day to 2.11 at 120 days. While the saturated H/S ratio decreases slightly with the hydration from 4.55 at 1 day to 4.27 at 120 days. These observations are different from what has been proposed recently by Muller et al. [58]. For instance, in [58] the saturated H/S ratio decreases from 6.65 at 1 day to 4.04 at 300 days of hydration. The observed decrease is much significant than what is observed here. Furthermore, the interlayer (or dry following the terminology used here) H/S obtained by Muller et al. [58] increases slightly at the first days of hydration and then stabilises after 7 days, while the one obtained here increases continuously with

the hydration time. The increase of dry H/S ratio may be seen as an increase of number of layers forming the C-S-H globules.

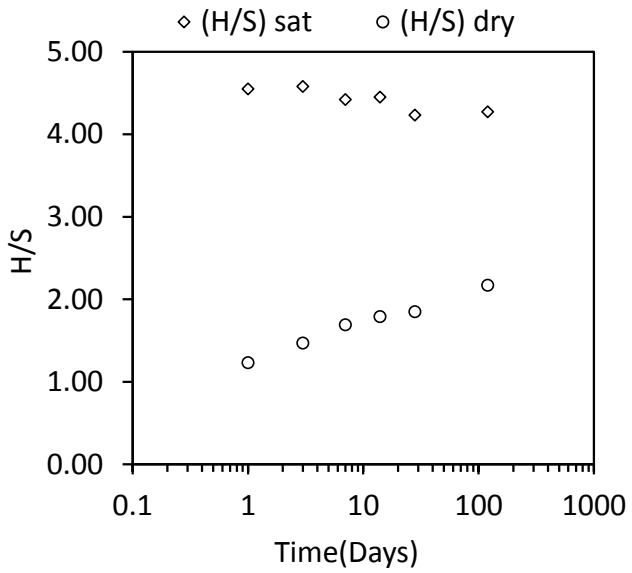

FIGURE 5.8: The evolution of the H/S ratio with respect to time at a hydration temperature of 20°C

5.2.3 Sensitivity analysis

The evaluation of the C-S-H chemical composition and density as presented in previous sections rely on various experimental results. Of course uncertainty in each measurement will have a certain influence on the evaluated parameters. For most of these methods it is quite difficult to define a numerical value for the precision or error on the results. For this reason, a sensitivity analysis is performed here in order to estimate the errors in the evaluated composition and density, based on an arbitrary 5% error in different experimental results. The results are presented in Table (5.1) for the cases in which the error is attributed to only one experimental result. It is shown that a 5% error induce a very small variation on the estimated C-S-H density, showing that the C-S-H density could be determined accurately. The chemical composition of C-S-H seems however to be more strongly concerned with the variation of the measured parameters. While the portlandite content and the C_3S and C_2S hydration degree have a limited effect on the C/S ratio, it seems that the dry and saturated H/S are the most sensitive to the measured parameters. The above analysis was based on an error attributed to only one parameter at each time. However, in reality, the errors on various parameters can happen simultaneously with different values and signs. In order to account for the errors accumulation, we performed an error analysis based on a randomly chosen error within the range of [-5%,5%], which can happen on every independently measured variable in our system of

Parameter changed by 5%	C/S	$(H/S)_{dry}$	$(H/S)_{sat}$	Density	C-S-H Fraction
Bound water ATG		5%	2 %	0.2%	0.9%
CH mass fraction	3%			0.3%	1.5%
Hydration degree of C_3S	2%	4.5%	4.5%	1%	5%
Hydration degree of C_2S	0.1%	1%	1%	0.5%	0.5%
Gel porosity			3%	1%	

TABLE 5.1: Error analysis on different evaluated C-S-H parameters (C/S, $(H/S)_{dry}$, $(H/S)_{sat}$, and density) for an arbitrary 5% error in an individual experimental result

equations. A Monte-Carlo type calculation has been performed to evaluate the range of values than can be obtained for each result. It is worth noting that the error added to different parameters is not necessarily the same. This is done for the hydration temperature of 7°C and the results are presented in Table (5.2) in terms of minimum and maximum values obtained in the worst cases for each parameter. It can be clearly seen that even in case of accumulated errors, the uncertainties on the results are higher than the case of single errors on an individual parameters, but however the uncertainties remain reasonable.

The experimental measured parameters in this study show coherence within repeatability and reproducibility tests, which provides confidence in the presented results. Moreover, the good quantitative and qualitative accordance with previously published results, as mentioned in different sections of the thesis, strengthen this confidence.

		Main results	Min values	Max values
C-S-H composition	C/S	1.93	1.83	2.03
	$(H/S)_{dry}$	1.92	1.75	2.12
	$(H/S)_{sat}$	5.1	4.74	5.61
	Density	1.88	1.85	1.93
Mass fractions	C-S-H	42.84	39.74	45.95
	Ettringite	1.77	1.46	2.07
	Afm	1.37	1.10	1.62
	Hydrogarnet	7.87	7.47	8.42

TABLE 5.2: Accumulated error analysis on different evaluated C-S-H parameters (C/S, $(H/S)_{dry}$, $(H/S)_{sat}$, density and mass fractions) for an arbitrary error chosen randomly within the range [-5%,+5%] introduced simultaneously to experimental results at 7°C

5.2.4 Nanoporosity of cement paste

The water content of cement paste has been determined from TGA analysis and resulted in the estimation of the H/S ratio. This water content is supposed to correspond to interlayer water. It can be thus interpreted in terms of nanoporosity of cement paste. By nanoporosity we refer to the porosity within the solid

C-S-H globules with respect to cement paste volume. This porosity is giving by the expression:

$$\phi^{\mathrm{CP}}_{\mathrm{Nanoporsity}} = \frac{V^{\mathrm{Interlayerwater}}_{\mathrm{CSH}}}{V_{\mathrm{CP}}} = \frac{\frac{n^{\mathrm{H}}_{\mathrm{CSH}} M_{\mathrm{H_2O}}}{\rho_w}}{V_{\mathrm{CP}}} \tag{5.8}$$

The nanoporosity evaluated along these lines is presented in Figure 5.9(a) for a cement hydrated under different curing temperatures for a maturation age of 28 days.

It is seen that the nanoporosity at 28 days of hydration is slightly decreasing although the hydration degree is almost similar for specimens hydrated at temperature above 20°C (around 0.77). The nanoporosity of samples hydrated at 7°C is however smaller than that of 20°C due to the lower hydration degree (0.65 at 28 days and 7°C). The nanoporosity evolution with curing age is presented in Figure 5.9(b) and is increasing with maturation age due to the progressive hydration. In fact, as the hydration progresses the C-S-H densifies and more interlayer spaces are created yielding to an increase of nanoporosity [50]. It is equal to 5% at the first hydration day and reaches 15% after 120 days of hydration at 20°C curing temperature. The value of nanoporosity estimated at 60°C and 90°C is equal to 11% with respect to total cement volume. It should be reminded that the TGA analysis of cement cured at different ages at 90°C showed minor variations, in fact, specimens hydrated at higher hydration temperatures reach rapidly an ultimate hydration degree. The nanoporosity is thus not supposed to change after 28 days of hydration for specimens hydrated at 60°C and 90°C. These results hence suggest that at a mature age, the nanoporosity of cement is decreasing with increasing hydration temperature. Few data in the literature reports the nanoporosity variation of cement paste with the hydration conditions. The only reported value is the one provided by Jennings [35] around 18% and corresponds to intrinsic C-S-H nanoporosity. Gajewicz studies [79] showed that the intensities relative to interlayer water within C-S-H are decreasing with increasing hydration temperature. When interpreted in terms of cement nanoporosity this decrease of interlayer NMR intensity suggests that the cement nanoporosity is decreasing from 15% at 10°C to 12% at 60°C, values in agreement with what is presented here.

5.2.5 Volume assemblage of cement at different temperatures

The volume assemblage obtained from the microstructure characterisation of cement paste hydrated at different temperatures is summarized in Table 5.3. Regarding the volume assemblage, the curing temperature increase impacts essentially on the capillary porosity and C-S-H volume fraction. It can be seen that the volume fraction of the C-S-H is decreasing with increasing curing temperature, while the capillary porosity is increasing. Both of these changes originate from the increasing C-S-H density with increasing curing temperature. The

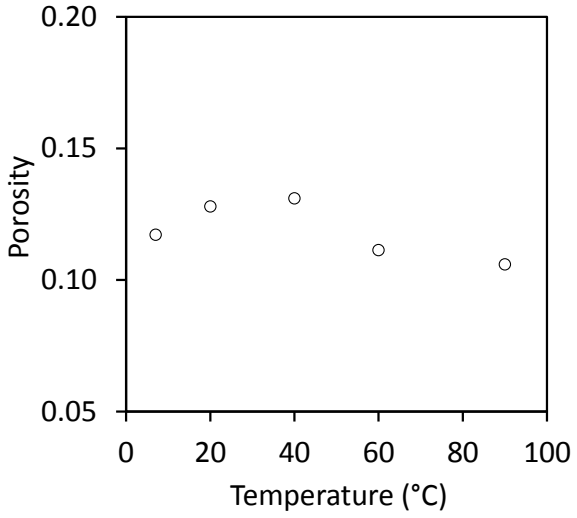

(a)

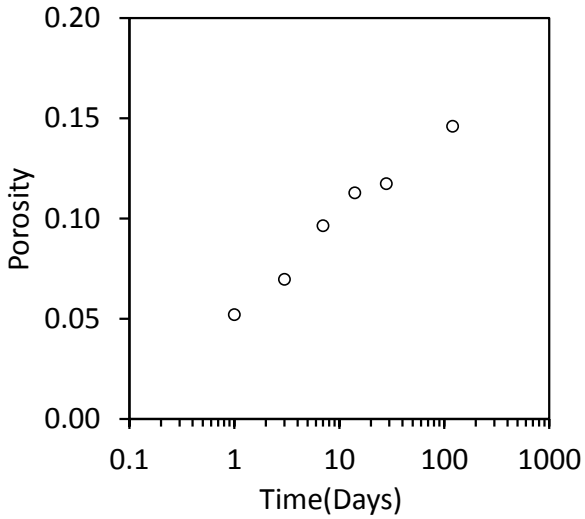

(b)

FIGURE 5.9: The nanoporosity of cement with respect to the total volume for (a) different hydration temperatures and (b) different hydration ages at a hydration temperatures of 20°C)

volume fraction of portlandite is almost constant with different curing temperatures for mature ages (i.e, 120 days for 7°C and 20°C and 28 days for 60°C and 90°C). The afm and hydrogarnet volume fractions are slightly increasing with the increase of hydration degree associated to aluminate and ferrite. The volume assemblage corresponding to four months of hydration will be used in micromechanical modelling. For 60°C and 90°C the volume assemblage determined at 28 days of hydration is used as the hydration degree is not supposed to change after 28 days of hydration at these hydration temperatures.

Ages			28 Days		120 Days	
Temperature(°C)	7	20	60	90	7	20
Volume fractions						
C-S-H	0.510	0.520	0.503	0.464	0.550	0.534
Portlandite	0.12	0.13	0.143	0.153	0.154	0.142
Afm	0.01	0.03	0.02	0.03	0.04	0.05
Hydrogarnet	0.04	0.05	0.042	0.040	0.067	0.067
Unhydrated clinker	0.014	0.10	0.095	0.093	0.069	0.068
Capillary voids	0.140	0.150	0.200	0.227	0.115	0.130
other information						
Density	1.89	1.95	2.04	2.10	1.95	1.99
C-S-H porosity	0.40	0.35	0.29	0.25	0.35	0.33

TABLE 5.3: The volume assemblage of cement paste hydrated for at different temperatures and other quantitative information needed for micromechanical modelling

5.2.6 Two C-S-H structures

In Section 4.3.3 the analysis of porosity results obtained by mercury porosimetry, water vapor sorption and Nitrogen sorption, permitted the estimation of the pore volume of LD and HD with respect to cement paste volume. The HD and LD pore volume are used in the following to further gain insight into the evolution of two C-S-H structures with curing temperature. The volume fraction (f^v_{CSH}) of C-S-H is related to the pore volume of LD and HD and their intrinsic porosities as stated by equation 5.9:

$$f^v_{\mathrm{CSH}} = \phi_{\mathrm{HD}} \cdot \frac{1}{\varphi_{\mathrm{HD}}} + \phi_{\mathrm{LD}} \cdot \frac{1}{\varphi_{LD}} \tag{5.9}$$

and the LD and HD fractions respectively of C-S-H are related to the volume fraction (f^v_{CSH}) of C-S-H and to the intrinsic porosities of HD and LD (φ_{HD} and φ_{LD}) respectively by equation 5.10 where $f^{\mathrm{CSH}}_{\mathrm{HD}} + f^{\mathrm{CSH}}_{\mathrm{LD}} = 1$:

$$\begin{aligned} f^{\mathrm{CSH}}_{\mathrm{LD}} &= \phi_{\mathrm{LD}}/\varphi_{\mathrm{LD}}/f^v_{\mathrm{CSH}} \\ f^{\mathrm{CSH}}_{\mathrm{HD}} &= \phi_{\mathrm{HD}}/\varphi_{\mathrm{HD}}/f^v_{\mathrm{CSH}} \end{aligned} \tag{5.10}$$

The volume fractions of C-S-H (f^v_{CSH}) at different temperatures are presented in Table 5.4 together with the porosities of HD and LD with respect to cement paste for different curing temperatures. The LD C-S-H porosities as obtained from NAD experiments are almost similar for different curing temperature and show only slight variations. Hence, their mean value is presented in table 5.4 for different curing temperatures.

Reporting the obtained values of these properties in equation 5.9 results in one equation for each temperature linking two variables (φ_{HD} and φ_{LD}). Given this equation, the LD C-S-H intrinsic porosity (φ_{LD}) is varied in the range of [0.2, 0.6] and the HD intrinsic porosity φ_{HD} is determined. In Figure 5.10, we plot

TABLE 5.4: Different porosities of cement paste per total volume and essential inputs for figure 5.10

Temperature(°C)	7	20	60	90
C-S-H Volume fraction f^v_{CSH}	0.550	0.534	0.503	0.464
Capillary porosity ϕ_{Cap}	0.115	0.130	0.200	0.227
Gel porosity ϕ_{Gel}	0.195	0.180	0.140	0.120
LD porosityϕ_{LD}	0.093	0.093	0.093	0.093
HD porosityϕ_{HD}	0.112	0.107	0.037	0.030
Total porosity $\phi_{11\%\mathrm{RH}}$	0.32	0.32	0.33	0.35
C-S-H Intrinsic porosity	0.35	0.33	0.29	0.25
C-S-H Density	1.95	1.98	2.04	2.10

the HD intrinsic porosity with respect to LD intrinsic porosity. The range of values corresponding to $\varphi_{\mathrm{LD}} < \varphi_{\mathrm{HD}}$ is omitted. The results for cement hydrated under various temperatures show that independently of the LD intrinsic porosity, the HD intrinsic porosity is decreasing with the curing temperature increase. This stands for an HD C-S-H that is getting denser at higher curing temperatures. Interestingly, the intrinsic porosity of C-S-H after one hydration day at 20°C is equal to 0.374 and is very close to the LD C-S-H intrinsic porosity. Furthermore, it is evidenced that the C-S-H that grows at the early hydration degrees is the low density C-S-H. This for instance, suggests that the LD intrinsic porosity at 20°C is equal to 0.37 similar to Tennis and Jennings propositions. For T=20°C, the predicted HD intrinsic porosity corresponding to an intrinsic LD porosity of 0.37 is equal to 0.31. The predicted HD intrinsic porosity is higher than the one provided by Tennis and Jennings model [14] equal to 0.24. It should be noted that we are not expecting getting the same intrinsic porosities as the Tennis and Jennings model as we assume a totally accessible LD porosity to Nitrogen, with an opposition to a partially accessible LD porosity assumed by Tennis and Jennings model [14]. Based on these observations we fix the LD and HD C-S-H intrinsic porosity for a hydration temperature of 20 °C at 0.37 and 0.31 respectively in what follows.

The microstructure characterization at this stage permits to obtain an expression linking the intrinsic porosities of LD and HD C-S-H (φ_{LD}, φ_{HD}) for different temperatures compatible with the calculated intrinsic porosities of C-S-H and the volume assemblage at different temperatures presented in Table 5.3. However, a more accurate quantitative evaluation of these intrinsic porosities is missing. In the following we will try to have an estimation of these porosities in the range of possible values using micromechanical modelling, based on a back analysis of experimentally evaluated macro-scale elastic parameters presented in 4.3.6.

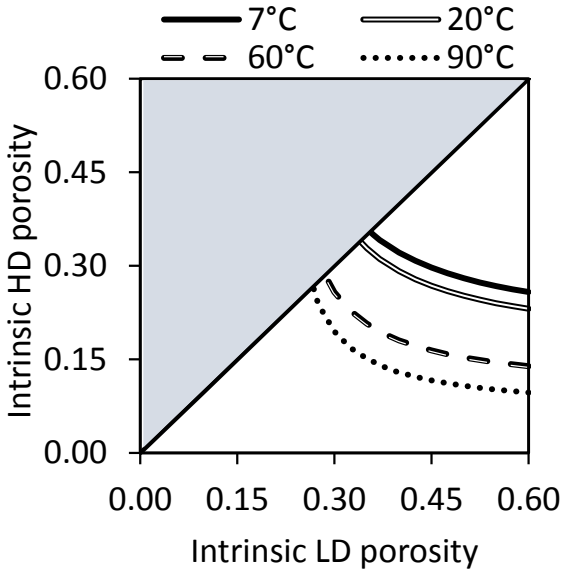

FIGURE 5.10: The variation of HD and LD intrinsic porosities with hydration temperature (results corresponding to four months of hydration)

5.3 Micromechancial modelling

The volume assemblage of cement paste is an essential input for micromechanical modelling. This volume assemblage has been presented for cement pastes cured at different hydration temperatures. Micromechanical modelling is carried in the following in order to highlight the origins of the decrease of elastic properties of cement.

5.3.1 Microstructure representation

Different microstructure representations can be used to upscale the elastic properties of cement. Generally the homogenisation of cement based materials is done in two steps to address the scale difference between the C-S-H phases and the cement paste [9, 11, 12, 39, 40, 99]. The first scale corresponds to the C-S-H with its gel pores with a scale length of the order of some nanometres. The second scale comprises C-S-H gel, crystalline hydrates, clinker inclusions and voids with a scale length of some microns. In the first step the properties of the C-S-H gel are determined through the homogenisation of the gel pores with the globules of solid C-S-H. In a second step the properties of cement paste composed of C-S-H gel, crystalline hydrates, clinker and voids are determined. The C-S-H in this homogenisation model can be considered either as one homogeneous phase or as two C-S-H phases with distinct properties [9, 40]. This classical two-scale microstructure representation of cement paste is

presented in Figures 5.11(a) and 5.11(b) with one and two C-S-H phases respectively. These microstructure representations have been applied successfully for modelling the mechanical behaviour of cement paste while varying the water to cement ratio and the hydration degree. We will show in the following that these microstructure representations are not appropriate for modelling the mechanical behaviour of cement paste with increasing hydration temperature. We consider a different representation of the microstructre which seems suitable to study the effect of hydration temperature on the mechanical behaviour of cement and that has been adopted recently by Königsberger [184] for modelling elastic properties of a hydrating cement paste with different water to cement ratio and hydration degree while taking into account the change of the C-S-H density. It consists of a representation of the cement paste microstructure over three scales. The first step concerns the homogenization of C-S-H solid globules and the gel pores in order to evaluate the elastic properties of the porous C-S-H. The second step consists in the homogenisation of the porous C-S-H with the capillary pores and yields the properties of the C-S-H foam or C-S-H matrix. In the third step the elastic properties of cement paste composed of clinker, crystalline hydrates and the C-S-H foam are evaluated based on the elastic properties of the C-S-H foam determined in the second step and the elastic properties of the other crystalline phases obtained from literature. The REVs of cement over three scales are presented in Figures 5.11(c) and 5.11(d) in case of one C-S-H phase or two C-S-H phases respectively. In the following we will examine the effect of these different microstructure representations and the assumptions made on the intrinsic porosities of HD and LD C-S-H for modelling the elastic properties of cement paste with different curing temperatures:

- 2S-1P: This configuration corresponds to the REV presented in Figure 5.11(a). It consists of considering the C-S-H as one homogeneous phase and the homogenisation of the elastic properties of cement paste is done over two scales. The intrinsic porosity of this homogeneous phase is decreasing by increasing the curing temperature, as presented in Table 5.3 and which is the result of the C-S-H being denser at higher temperatures.
- 2S-2P: This configuration will be considered to examine the effect of distinguishing between the HD and LD C-S-H phases on the homogenized properties. The REV corresponding to this microstructure is presented in Figure 5.11(b). The intrinsic porosities of HD and LD C-S-H phases are taken equal to 0.24 and 0.37, respectively, as provided by Tennis and Jennings [14]. The volume fraction of HD and LD are varied in order to describe the decreasing intrinsic porosity of C-S-H with increasing curing temperature, as presented in Table 5.5. This yields to an increase of the fraction of HD C-S-H with increasing curing temperature.
- 3S-1P: In this configuration, we consider the C-S-H as one homogeneous phase with decreasing intrinsic porosity (Table 5.3) and an homogenisation of the elastic properties of cement paste over three scales. The REV corresponding to this microstructure is presented in Figure 5.11(c). The fist step correspond to an homogenisation of C-S-H. In the second step

the homogenized properties of the matrix formed by porous C-S-H intermixed with capillary pores are determined. The third step consists of an homogenization of the C-S-H matrix with crystalline phases and clinker inclusions.

– 3S-2P: This configuration (Figure 5.11(d)) is similar to 3S-1P, while a distinction between the two C-S-H phases is made as in the configuration 2S-2P. The intrinsic porosities of HD and LD phases are taken equal to 0.24 and 0.37 respectively and their volume fractions are varied in order to describe the decreasing density of C-S-H as presented in Table 5.5.

Temperature(°C)	φ_{CSH}	$f_{\mathrm{LD}}^{\mathrm{CSH}}$	$f_{\mathrm{HD}}^{\mathrm{CSH}}$
7	0.35	0.87	0.13
20	0.33	0.70	0.30
60	0.29	0.43	0.57
90	0.25	0.14	0.86

TABLE 5.5: The volume fractions of C-S-H HD and LD determined in this study on the basis on C-S-H intrinsic porosity of C-S-H determined for different temperatures and the porosities of HD and LD determined by Tennis and Jennings [25, 32], φ_{HD}=0.24 and φ_{LD}=0.37

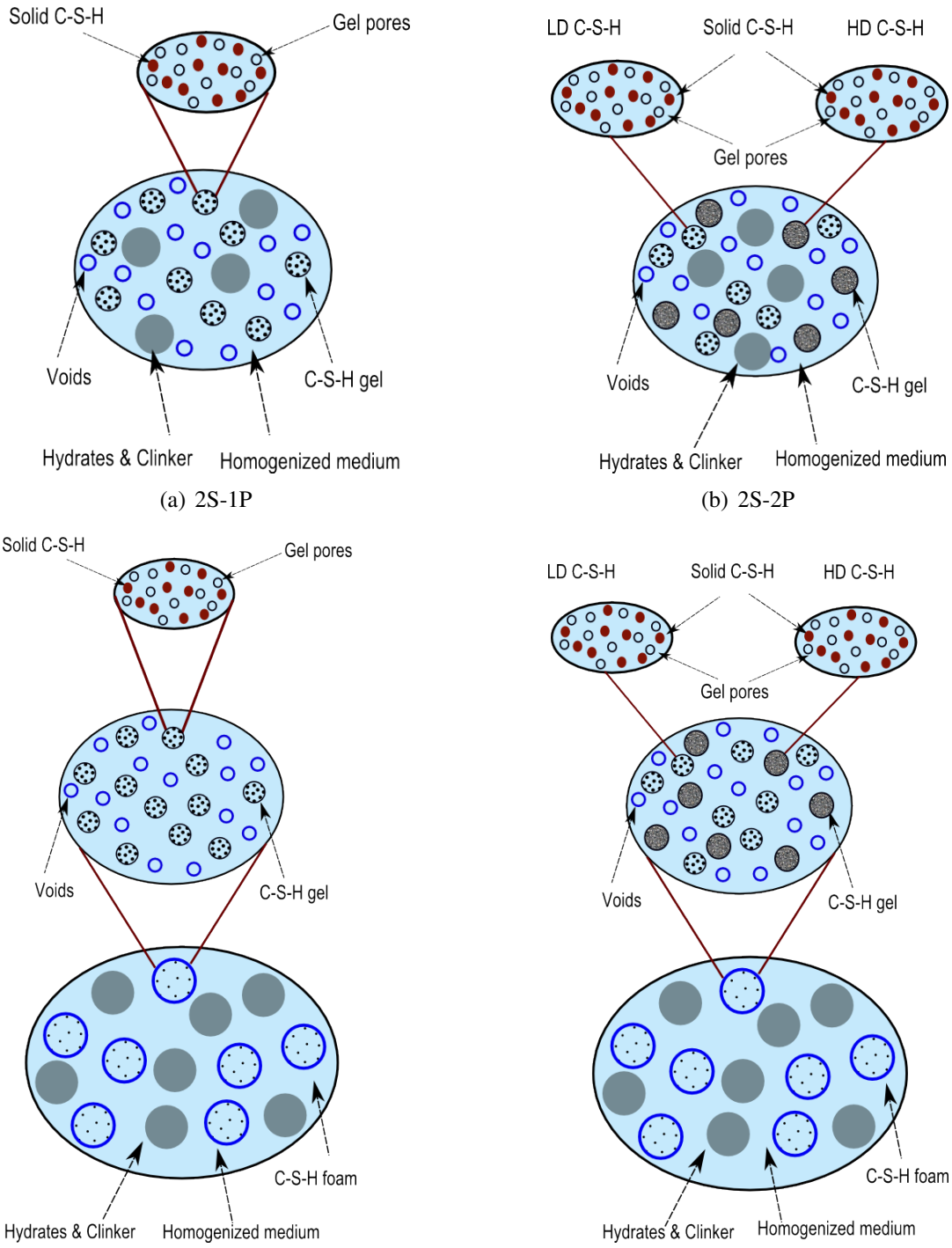

(a) 2S-1P (b) 2S-2P

(c) 3S-1P (d) 3S-2P

FIGURE 5.11: The REV representation of cement paste over different scales and considering different C-S-H representations: (a) two homogenisation steps with one homogeneous C-S-H phase, (b) two homogenisation steps with two homogeneous C-S-H phases, (c)three homogenisation steps with one homogeneous C-S-H phase, (d) three homogenisation steps with two homogeneous C-S-H phases

5.3.2 Elements for micromechanical modelling

The necessary inputs for the micromechanical modelling are the volume fractions of hydrates, elastic moduli of different phases and the intrinsic properties of the C-S-H (HD and LD) in case a distinction between these two C-S-H types is considered. The volume assemblage of cement has been presented in Table 5.3. The bulk and shear moduli of different crystalline phases are presented in Table 5.6. The bulk and shear moduli of solid C-S-H are calibrated based on the results of the elastic properties of cement determined at 20°C and and are also presented in Table 5.6 for different REVs presented in Figure 5.11. The calibration of the results based on elastic properties determined at 20°C is motivated by the availability of a complete description of solid C-S-H at this curing temperature in the literature. The determined bulk and shear moduli of C-S-H for the different REVs representations yield Young's moduli in the range of 46-50 GPa and Poisson ratio in the range of 0.23-0.27 which are compatible with previous studies [9, 99]. However, they are smaller than the parameters identified by Pellenq et al. [185], 67 GPa and 55 GPa for the Young's moduli respectively along x-z plane and y plane, and 0.30 for the Poisson's ratio. The difference between our estimations and those provided by Pellenq et al. [185] may be explained by the external layer of water encountering the C-S-H particles that reduces the mechanical properties of solid C-S-H in our case. The predicted properties of Pellenq et al. [185],exclude this external water layer.

The elastic parameters for other hydration temperatures will be assumed to be the same as the ones calibrated for 20°C. Of course, one can imagine that the variations of C-S-H chemical composition in terms of C/S and H/S ratios with hydration temperature can result in a variation of the mechanical properties of the solid C-S-H. Indeed, Plassard et al. [186] have reported experimental evidence of decreasing intrinsic elastic properties of C-S-H with a decreasing C/S ratio. Moreover, Constantinides and Ulm [39] showed that decalcification of C-S-H, which corresponds to a decrease of the C/S ratio, leads to a significant loss of elasticity. However, a decrease of H/S ratio increases the elastic properties of C-S-H. The influence of temperature on the chemical composition of C-S-H corresponds to a decrease of both C/S and H/S ratio. While the decrease of the C/S ratio is supposed to decrease the C-S-H elastic properties, the decrease of the H/S ratio will increase the elastic properties of C-S-H and may cancel the effect of C/S ratio. We therefore consider the C-S-H bulk and shear moduli constant with curing temperature. Furtherer work is definitely needed in order to verify this approximation.

5.3.3 Micromechanical modelling results

The microstructure description of cement at different hydration temperatures being presented, lets now investigate how do these different models apply to study the effect of hydration temperature on the elastic properties of cement. As mentioned in section 4.3.6, the experimental results show a significant reduction of the elastic properties of the cement paste with increasing hydration

Phase(°C)	k_s (GPa)	g_s (GPa)	
Clinker	113	53.6	[187]
Portlandite	40	16	[188–190]
Ettringite	28	10	[191]
Afm	40	16	[192]
Hydrogarnet	99.8	64.3	[193]
	C-S-H solid		Conditions of fit
2S-1P	26.9	16.1	20°C
2S-2P	26.2	17	(20°C, φ_{HD}=0.24, φ_{LD}=0.37)
3S-1P	34.6	18.2	20°C
3S-2P	34.6	19.4	(20°C, φ_{HD}=0.24, φ_{LD}=0.37)
3S-2P	30.5	20	(20°C, φ_{HD}=0.31, φ_{LD}=0.37)

TABLE 5.6: Bulk and shear moduli of different constituents of cement paste microstructure, xS-yP stands for x scales with y C-S-H phases

temperature. The elastic properties of cement determined experimentally will be compared with the predictions of the micromechanical modelling to examine various modelling assumptions and simplifications. We consider a self-consistent homogenization scheme for different homogenization steps and assume a spherical geometry for all phases. In case a distinction between HD and LD C-S-H is made, they will be considered differently in the homogenization procedure. In fact, regarding the small packing fraction of HD and its fine porosity, this phase is considered inactive during poro-mechanical testing as highlighted by experimental investigation of Ghabezloo [3] and Ghabezloo et al. [9]. The HD C-S-H behaves thus like a porous phase in undrained conditions. Hence in the second step of homogenization, the undrained bulk modulus of HD is used [9] (Refer to [9] for more details).

We examine different microstructure representations as highlighted in 5.3.1. The homogenized Young's modulus and Poisson's ratio corresponding to different microstructure representations introduced in Figure 5.11 are presented in Figure 5.12 and Figure 5.13, together with the elastic properties determined experimentally. It is shown that the homogenized properties of cement paste using a two-scale model, either by considering a homogeneous C-S-H phase or two distinct C-S-H phases are almost constant with increasing hydration temperature. This is in contradiction with the well established trend of experimental results showing a decrease of the mechanical properties of cement paste with increasing hydration temperature. It can be understood that the increase of the density of a homogeneous C-S-H phase and the resulting capillary porosity increase with increasing hydration temperature are not sufficient to simulate the drop of cement paste mechanical properties. The increasing hydration temperature, while promoting an increase of capillary porosity, that can initiate a drop of elastic properties of cement paste, renders the C-S-H gel denser and stiffer. The effect of increase of capillary porosity cancels the effect of increasing C-S-H density, resulting in elastic properties almost constant with increasing temperature. This two-scales model that applies very well for describing the evolution

of mechanical properties with water to cement ratio and with hydration degree [9, 40], is of limited application to describe the decline of the elastic properties of cement paste hydrated under different curing temperatures. The Young's modulus corresponding to the homogenisation of cement paste over three scales when considering the C-S-H as one homogeneous phase, is decreasing with increasing curing temperature. This result is in accordance with previously presented experimental trends. The prediction of the micromechanical model for the 60°C curing temperature are in good agreement with the experimental values. However, the predictions at the two extreme curing temperatures 7°C and 90°C are still far from the experimental predictions.

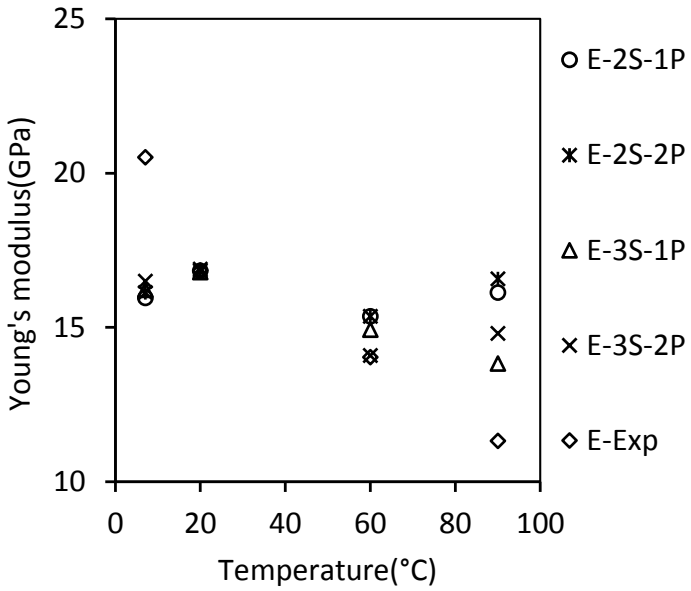

FIGURE 5.12: The homogenized Young's modulus of cement paste at different temperatures following different microstructure representations: (xS-yP stands for x scales with y C-S-H phases and Exp refers to experimentally determined properties)

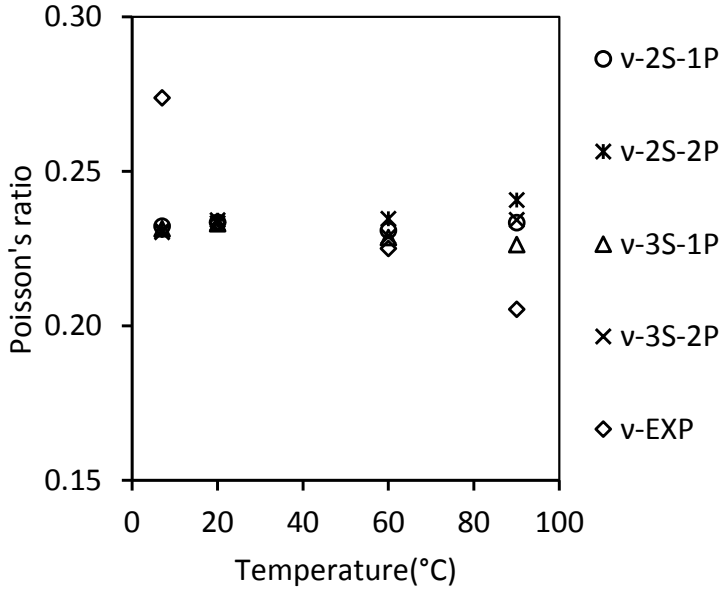

FIGURE 5.13: The homogenized Poisson's ratio of cement paste at different temperatures following different microstructure representations: (xS-yP stands for x scales with y C-S-H phases and Exp refers to experimentally determined properties)

It seems that the homogenisation of cement paste over three scales while the curing temperature is increased, showed variations compatible with experimental trends, although not fully quantitative. This microstructure representation shows that the capillary porosity initiates the decrease of the elastic properties of cement cured at high hydration temperatures, but it is not the only factor explaining this decrease. Lets now examine the effect of distinguishing between the two C-S-H types on the homogenized properties of cement through the three-scale model. We use the intrinsic porosities of HD and LD C-S-H determined by Jennings [32], together with their volumetric fractions constrained by the decrease of the C-S-H intrinsic porosity presented in Table 5.5. This configuration yields elastic properties of cement paste constant with increasing curing temperature. The distinction between the HD and LD C-S-H in this three-scale model with the same intrinsic porosities proposed by Jennings is again not suitable for describing the drop of elastic properties of cement with increasing curing temperature. This illustrates the non-adequacy of the constancy assumption made on the intrinsic porosities of HD and LD C-S-H with increasing curing temperature. It seems therefore, reasonable to consider the variations of the intrinsic porosities of LD and HD C-S-H with hydration temperature.

5.3.4 Evaluation of HD and LD intrinsic porosities via micromechanical modelling

As presented in Eq 5.9 and Figure 5.10, we can obtain a relation between the intrinsic porosities of HD and LD C-S-H for each hydration temperature, but at this stage we don't have sufficient information to determine the exact values of these porosities. This equation shows that the intrinsic porosity of the HD C-S-H is decreasing with increasing curing temperature. To shed light on the values of intrinsic porosities of LD and HD C-S-H we can try to use Eq 5.9 and the micromechanical modelling in order to fit their values for each hydration temperature. This can be done through a least square minimization of error between the calculated and experimentally evaluated elastic parameters while spanning different values of LD and HD intrinsic porosities verifying Equation 5.9. The evaluated intrinsic porosities and volume fractions of LD and HD C-S-H derived form micromechancial modelling associated to the experimental characterisation of the pore structure are presented in Table 5.7 and the homogenized elastic properties of cement paste are presented in Figure 5.14 for different temperatures.

Temperature(°C)	φ_{HD}	φ_{LD}	f_{LD}^{CSH}	f_{HD}^{CSH}
7	0.34	0.38	0.50	0.50
20	0.31	0.37	0.48	0.52
60	0.20	0.37	0.52	0.48
90	0.14	0.39	0.51	0.49

TABLE 5.7: The intrinsic properties of C-S-H HD and LD determined in this study though micromechanical modelling

The fitted HD porosity decreases significantly with hydration temperature as expected, while the LD intrinsic porosity is almost constant (0.37-0.39). The HD and LD volume fractions within the the C-S-H matrix are almost constant, around 0.50, for different temperatures. The The decreasing HD intrinsic porosity is in agreement with previous observations of Kjellsen [43] showing that the inner product becomes denser by increasing hydration temperature. Except for 7°C hydration temperature the evaluated values of elastic parameters are generally very close to the experimentally evaluated ones. We deem that the experimentally evaluated elastic properties of cement at 7°C are closer to the undrained properties. This is due to the lower permeability of the cement paste hydrated at 7°C. The undrained properties of cement at 7°C are equal to 18 GPa for the Young's modulus and 0.30 for the Poisson's ratio which are close to the experimental values of 20.5 GPa for the Young's modulus and 0.27 for the Poisson's ratio. We thus demonstrate that it is possible to reproduce the reduction of the elastic properties of the cement paste by increasing hydration temperature only by taking into account the existence of HD and LD C-S-H and the variations of their intrinsic porosities with temperature. An adaptation of the micro-structural representation of cement is also required to model the decrease of the mechanical properties of cement. It can be understood that the decrease of the mechanical properties of cement paste cured at high temperatures, is the

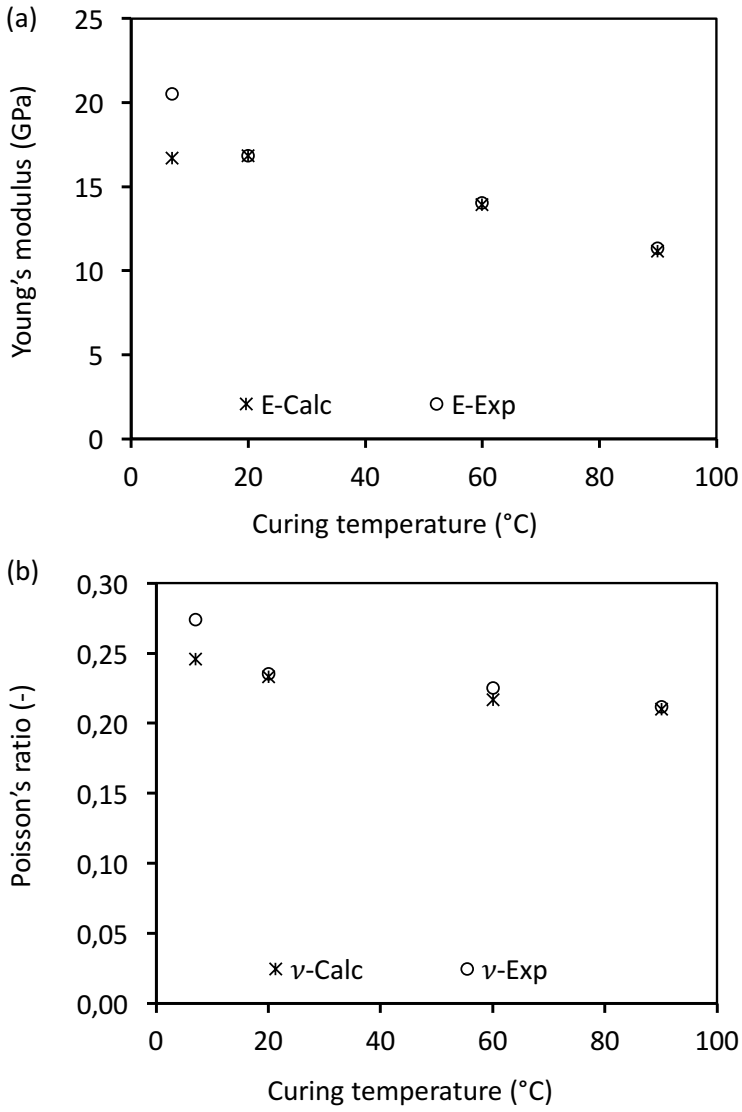

FIGURE 5.14: Homogenized Young's modulus and Poisson's ratio of cement paste at different temperatures using a three-scale homogenisation model with varying intrinsic porosities of LD and HD C-S-H (Exp: Determined experimentally, Calc: Calculated with micromechanical modelling

result of the decrease of the elastic properties of the matrix formed by the C-S-H gel intermixed with capillary pores. This conclusion can be confirmed by microscopy observations presented in Figure 4.23 for specimens cured for four months at different hydration temperatures. These images showed that the contrast between the hydrates encountering the clinker phases and the surrounding matrix in which they are embedded is increasing. This may indicate a clear difference in density between inner hydrates and the surrounding foam confirming the results of micromechanical modelling.

5.4 Conclusion

Analysis of the mass assemblage and porosity evaluations resulted in the characterisation of the C-S-H density and chemical composition for a class G cement paste hydrated for 28 days at different temperatures and for a cement hydrating at 20°C. The evaluated C-S-H bulk density varies from about 1.88 g/cm^3 at 7°C to about 2.10 g/cm^3 at 90°C. The evaluated C/S ratio decreases with increasing hydration temperature, from 1.93 at 7°C to 1.71 at 90°C. The same trend has also been observed for the variations of H/S ratio of saturated C-S-H which decreases with increasing curing temperature from 5.1 at 7°C to 2.66 at 90°C. The density of C-S-H and C/S and H/S molar ratios are evaluated also for a cement paste hydrating at 20°C. Regrading the variations of the C-S-H structure with maturation age, the density increased from 1.92 g/cm^3 at 1 day up to 1.99 g/cm^3 at 120 days of hydration. The C/S ratio decreases the first three days and then stabilises. The H/S of saturated C-S-H decreases slightly while the H/S of dry C-S-H increases progressively with hydration time.

Regarding the two C-S-H types porosity, an expression linking the HD and LD intrinsic porosities is obtained at different hydration temperatures based on porosity results and C-S-H volume fractions. This expression showed that the HD intrinsic porosity decreases significantly with increasing hydration temperature.

A self-consistent homogenisation model is used based on the quantitative description of volume assemblage. Results showed that the capillary porosity can not explain alone the decrease of the mechanical properties. The adoption of two C-S-H phases with varying their intrinsic properties is determining in the mechanical behaviour. The results of the performed multi-technique microstructure characterization are associated with the micromechanical model to back-analyse the intrinsic properties of HD and LD C-S-H. The results show an increase of the LD porosity and a significant decrease of the HD porosity with increasing hydration temperature. The decrease of cement paste elastic properties is thus explained as a consequence of the decrease of the elastic properties of the foam composed of C-S-H gel and capillary pores.

Chapter 6

Conclusions and perspectives

6.1 Conclusions

In oil and geothermal wells a cement sheath is placed between the formation rock and the casing and plays an important role for stability and sealing of the well. The knowledge of this cement sheath behaviour in well conditions is of great importance for the prediction of the well safety and analysis of cement sheath performances. Such an analysis requires a comprehensive constitutive law for the cement paste. An important difficulty for the characterization of the cement paste behaviour resides in its evolving nature, its complex microstructure and the high dependency of its properties to hydration conditions. For a complete characterization of the behaviour of such a complex and time-evolving material, the experimental methods should be associated with theoretical modelling among which the upscaling methods have been shown to be very promising. An important input for upscaling methods is a quantitative description of the microstructure along with the basic physical properties of its constituents. Yet, few quantitative information are available in the literature concerning the cement paste microstructure, particularly concerning the oil-well cements and challenging conditions of hydration in such environment. Among these conditions the hydration temperature, which is varying along the well due to geothermal gradient, has a great influence on cement microstructure and mechanical properties. The aim of this research work was therefore to provide a quantitative characterization of the microstructure of an oil-well cement paste with an emphasis on the role of hydration temperature, and to establish a link between the cement microstructure and its macro-scale mechanical properties by means of upscaling methods. These goals have been achieved as demonstrated throughout this manuscript. The general conclusions and findings are:

1. A multi-technique method is proposed for a quantitative characterization of the microstructure of a cement paste. This method is mainly based on a combination of several classical and widely available experimental methods, which can be considered as an important advantage, comparing to other available methods in the literature. Of course, it is based on a number of simplifications and assumptions, but despite the relative simplicity of the method, the good compatibility between the results of this work and

the well-established ones in the literature gives confidence in the proposed method.

2. This method is successfully used for a class G oil-well cement paste (a grey cement) hydrated under a wide range of hydration temperatures, between 7° and 90°C, covering a depth of around 2 km in an oil-well. The mass assemblage of cement has been evaluated for various temperatures and hydration degrees, along with the C-S-H density and chemical composition. These information, particularly for higher hydration temperature, are very scarce in the literature and to our best knowledge, are among the first ones for a class G cement. The various conclusions regarding the microstructure changes with hydration temperature and hydration degree are summarised below:

   (a) The mass assemblage evaluated by combining XRD-Rietveld and TGA analysis, shows slight variation with curing temperature change. A slight increase in the portlandite content is observed. A decrease of the ettringite content and an increase of Afm content are also noticed.

   (b) The porosity analysis by different methods shows a significant increase of capillary porosity and a decrease of the gel porosity by increasing hydration temperature. The increase of hydration temperature results also in a coarsening of the pore structure and a more heterogeneous distribution of hydrates.

   (c) Hydration at higher temperatures leads to a rapid evolution of the pore structure and the creation of a dense product at early ages. However, the Pore structure of cement paste cured at low temperatures evolves gradually with curing time leading to a continuous densification of cement paste.

   (d) The water vapor and Nitrogen sorption isotherms show a significant decrease of hysteresis by increasing hydration temperature.

   (e) Concerning the C-S-H chemical composition, $(\mathrm{C/S})$, $(\mathrm{H/S})_{\mathrm{dry}}$ and $(\mathrm{H/S})_{\mathrm{sat}}$ molar ratios are decreasing with increasing temperatures. The $(\mathrm{C/S})$ and $(\mathrm{H/S})_{\mathrm{sat}}$ decrease, while the $(\mathrm{H/S})_{\mathrm{dry}}$ increases with increasing hydration degree.

   (f) The C-S-H density is increasing with increasing hydration temperature. This explains the observed increase of the capillary porosity and the reduction of the gel porosity. The results show a progressive densification of the C-S-H during hydration. The densificaion derives form precipitation of C-S-H in the gel pores of the existing C-S-H.

   (g) The application of NMR yields satisfactory results comparing to other methods in terms of the pore size distribution although it is not fully quantitative. The application of NMR on grey cements should be further investigated and improved.

(h) The pore volume of LD C-S-H is slightly increasing and the pore volume of HD C-S-H decreases significantly with increase of hydration temperature. A relation linking the LD and HD intrinsic porosities is established for different hydration temperatures. This relation shows that the HD C-S-H intrinsic porosity decreases with increasing hydration temperature.

3. The quantitative microstructure information as obtained in this work has been used in micromechanical modelling to predict the elastic properties of the cement paste at different hydration temperatures. It has been shown that available microstructural representations of the cement paste in the literature are not adequate for modelling the decrease of the mechanical properties of cement paste with increasing hydration temperature. A three-scale representation of the cement microstructure is used and shown to be promising in modelling the observed experimental trends in the material behaviour. To our knowledge this is the first application of the upscaling methods to model the temperature-dependent behaviour of cement mechanical properties. This analysis showed that the reduction of the cement mechanical properties by increasing hydration temperature results from the weakening of the foam composed of the C-S-H gel intermixed with capillary pores.

4. The proposed micromechanical model, the quantitative microstructure information and the macro-scale experimental results of mechanical loading tests are associated for a back analysis of the internal pore structure of the C-S-H in terms of high density and low density packings and their dependency on the hydration temperature. The results showed a significant decrease of the HD intrinsic porosity and a slight increase of the LD intrinsic porosity by increasing hydration temperature. Even though the provided quantitative information should be considered as approximate due to the complexity of the used method, the results are new in the literature.

5. The findings of this research work permitted to gain a deeper insight into the cement paste microstructure, its dependency on the hydration temperature and the way it influences the mechanical properties of the material. These results constitute a practical tool for prediction of the mechanical properties of the cement paste under a wide range of hydration temperatures. This is an essential part of a modelling work-flow for prediction of the performances of a cement sheath in an oil well.

6.2 Perspectives

The work presented here can be further improved and extended in many ways:

- A multi-technique approach is proposed in this work to quantitatively characterise the microstructure of cement paste. This approach can be

completed by the use of Si solid state NMR. It can improve the determination of the hydration degree of alite and belite comparing to XRD-Rietveld.

- The micromechanical modelling and the back analysis of C-S-H intrinsic properties can be further improved and validated. A greater number of experimentally evaluated macro-scale parameters can permit to further constrain the fitted micro-scale C-S-H properties (elastic properties of C-S-H solid, HD and LD intrinsic porosities). It would be interesting to experimentally evaluate the elastic properties of cement paste at different hydration degrees and water to cement ratios for each hydration temperature. This permits to verify the predictive capacity of the micromechanical model and to improve the reliability of fitted parameters.
- In addition to the elastic properties, the hydration temperature increase results in a significant decrease of the strength of the cement paste. The micromechanical modelling, which is restricted in this work to the elastic properties, can be further extended to strength properties of the cement paste which is a very important information for designing oil-well cement sheath. It would be also interesting to investigate the effect of hydration temperature and the resulted microstructural changes on the permeability of the cement paste. The permeability is a very important property for insuring the zonal isolation which is the most important role of the cement sheath in an oil-well.
- The C-S-H growing at the early age is the D C-S-H as shown by various authors [14, 24]. Interestingly, the evaluated LD intrinsic porosity at 1 day hydration and a hydration temperature of 20°C is almost equal to the LD intrinsic porosity 0.37 as determined by [14]. Following the densification of C-S-H at different temperatures, as done here for a hydration temperature of 20°C, can help determining directly the LD intrinsic porosity for each hydration temperatures. The HD intrinsic porosity can then be determined easily using the established relation between HD and LD intrinsic porosities (Eq. 5.9).
- The homogenisation model is based on three scales, from nanometric scale associated to C-S-H gel, to micrometric scale associated to C-S-H foam and finally to millimetric scale of cement paste, spanning hence several orders of magnitude. It would be interesting to have more information on some intermediate scale to verify or improve the model and the performed back-analysis of micro-scale C-S-H properties. This can be done using nanoindentation experiments which permit to evaluate the mechanical properties at the C-S-H scale. Such results permit to further constrain the model and the back-analysed properties. Nanoindentation results have been used before for back-analysis of C-S-H intrinsic properties (e.g. [99]).
- The present work is restricted to temperatures up to 90°C. The hydration temperature may reach higher values up to 200°C in many oil-wells and

to 350°C in the most extreme cases exploited today. At these high temperatures the C-S-H undergoes a progressive metamorphosis resulting in a continuous decrease of the cement mechanical properties (e.g. uniaxial strength, Young's modulus) and an important increase of its permeability. This phenomenon is called strength retrogression. Even though the addition of silica fume and silica floor can prevent occurrence of strength retrogression, the microstructural origins behind this phenomenon are not well understood. The microstructure characterisation method as proposed in this study may help shedding lights of the mechanisms initiating strength retrogression. Furthermore, the experimental characterisation of class G cement microstructure with and without silica addition, may be used to develop a predictive micromechanical model for cement hydrated at high temperatures.

– The study here is limited to cement sheath in contact with pure water. In an oil-well the cement sheath can also be in contact with different gases for instance CO_2 and H_2S threatening the durability of the cement sheath. It would be interesting to investigate the effect of this kind of aggressive environment on the microstructure and mechanical properties.

Bibliography

1. Nelson, E. B. *Well cementing* (Elsevier, 1990).
2. Lavrov, A. & Torsæter, M. Physics and mechanics of primary well cementing. *SpringerBriefs in petroleum geoscience & engineering (* (2016).
3. Ghabezloo, S., Sulem, J., Guédon, S., Martineau, F. & Saint-Marc, J. Poromechanical behaviour of hardened cement paste under isotropic loading. *Cement and Concrete Research* **38,** 1424–1437 (2008).
4. Bois, A.-P. *et al.* Cement sheath integrity for CO 2 storage–An integrated perspective. *Energy Procedia* **37,** 5628–5641 (2013).
5. Ghabezloo, S., Sulem, J. & Saint-Marc, J. Evaluation of a permeability-porosity relationship in a low-permeability creeping material using a single transient test. *International Journal of Rock Mechanics and Mining Sciences* **46,** 761–768. ISSN: 13651609 (2009).
6. Ghabezloo, S., Sulem, J. & Saint-Marc, J. The effect of undrained heating on a fluid-saturated hardened cement paste. *Cement and Concrete Research* **39,** 54–64. ISSN: 00088846 (2009).
7. Vu, M. H., Sulem, J. & Laudet, J.-B. Effect of the curing temperature on the creep of a hardened cement paste. *Cement and Concrete Research* **42,** 1233–1241. ISSN: 00088846 (2012).
8. Vu, M. H. *et al.* Time-dependent behaviour of hardened cement paste under isotropic loading. *Cement and Concrete Research* **42,** 789–797 (2012).
9. Ghabezloo, S. Association of macroscopic laboratory testing and micromechanics modelling for the evaluation of the poroelastic parameters of a hardened cement paste. *Cement and Concrete Research* **40,** 1197–1210. ISSN: 00088846 (2010).
10. Ghabezloo, S. Multiscale modeling of the poroelastic properties of various oil-well cement pastes. *Journal of Multiscale Modelling* **2,** 199–215. ISSN: 1756-9737 (2010).
11. Ghabezloo, S. Micromechanics analysis of thermal expansion and thermal pressurization of a hardened cement paste. *Cement and Concrete Research* **41,** 520–532. ISSN: 00088846 (2011).
12. Ghabezloo, S. Effect of the variations of clinker composition on the poroelastic properties of hardened class G cement paste. *Cement and Concrete Research* **41,** 920–922. ISSN: 00088846 (2011).
13. Powers, T. C. & Brownyard, T. L. *Studies of the physical properties of hardened Portland cement paste* in *Journal Proceedings* **43** (1946), 101–132.

14. Tennis, P. D. & Jennings, H. M. A model for two types of calcium silicate hydrate in the microstructure of Portland cement pastes. *Cement and Concrete Research* **30,** 855–863 (2000).
15. Lesko, S., Lesniewska, E., Nonat, A., Mutin, J.-C. & Goudonnet, J.-P. Investigation by atomic force microscopy of forces at the origin of cement cohesion. *Ultramicroscopy* **86,** 11–21 (2001).
16. Scrivener, K. & Nonat, A. Hydration of cementitious materials, present and future. *Cement and Concrete Research* **41,** 651–665. ISSN: 00088846 (2011).
17. Brouwers, H. The work of Powers and Brownyard revisited: Part 1. *Cement and Concrete Research* **34,** 1697–1716. ISSN: 00088846 (2004).
18. Jennings, H. M., Thomas, J., Rothstein, D & Chen, J. Cements as porous materials. *Handbook of Porous Solids,* 2971–3028.
19. Bullard, J. W. *et al.* Mechanisms of cement hydration. *Cement and Concrete Research* **41,** 1208–1223 (2011).
20. Taylor, H. F. *Cement chemistry* (Thomas Telford, 1997).
21. Aligizaki, K. K. *Pore structure of cement-based materials: testing, interpretation and requirements* (CRC Press, 2005).
22. Litvan, G. G. Variability of the nitrogen surface area of hydrated cement paste. *Cement and Concrete Research* **6,** 139–143 (1976).
23. Mikhail, R. S. & Selim, S. A. Adsorption of organic vapors in relation to the pore structure of hardened Portland cement pastes. *Highway Research Board Special Report* (1966).
24. Thomas, J. J., Jennings, H. M. & Allen, A. J. The surface area of cement paste as measured by neutron scattering: evidence for two CSH morphologies. *Cement and Concrete Research* **28,** 897–905 (1998).
25. Jennings, H. M. & Tennis, P. D. Model for the Developing Microstructure in Portland Cement Pastes. *Journal of the American Ceramic Society* **77,** 3161–3172. ISSN: 0002-7820 (1994).
26. Feldman, R. F. & Sereda, P. J. A model for hydrated Portland cement paste as deduced from sorption-length change and mechanical properties. *Materials and structures* **1,** 509–520 (1968).
27. Feldman, R. & Sereda, P. A new model for hydrated Portland cement and its practical implications. *Engineering Journal* **53,** 53–59 (1970).
28. Feldman, R. F. & Ramachandran, V. S. Differentiation of interlayer and adsorbed water in hydrated Portland cement by thermal analysis. *Cement and Concrete Research* **1,** 607–620 (1971).
29. Wittmann, F. Interaction of hardened cement paste and water. *Journal of the American ceramic society* **56,** 409–415 (1973).
30. Ferraris, C. & Wittmann, F. H. Shrinkage mechanisms of hardened cement paste. *Cement and Concrete Research* **17,** 453–464 (1987).
31. Jennings, H. M., Thomas, J. J., Rothstein, D. & Chen, J. J. in *Handbook of porous solids* (eds Schüth, F., Sing, K. S. W. & Weitkamp, J.) 2971–3028 (Wiley-VCH Verlag GmbH, Weinheim, Germany, 2008).
32. Jennings, H. M. A model for the microstructure of calcium silicate hydrate in cement paste. *Cement and Concrete Research* **30,** 101–116. ISSN: 00088846 (2000).

33. Allen, A. J., Thomas, J. J. & Jennings, H. M. Composition and density of nanoscale calcium–silicate–hydrate in cement. *Nature materials* **6,** 311–316 (2007).
34. Feldman, R. Helium flow characteristics of rewetted specimens of dried hydrated Portland cement paste. *Cement and Concrete Research* **3,** 777–790 (1973).
35. Jennings, H. M. Refinements to colloid model of C-S-H in cement: CM-II. *Cement and Concrete Research* **38,** 275–289. ISSN: 00088846 (2008).
36. Pinson, M. B. *et al.* Hysteresis from Multiscale Porosity: Modeling Water Sorption and Shrinkage in Cement Paste. *Physical Review Applied* **3,** 064009. ISSN: 2331-7019 (2015).
37. Papatzani, S., Paine, K. & Calabria-Holley, J. A comprehensive review of the models on the nanostructure of calcium silicate hydrates. *Construction and Building Materials* **74,** 219–234. ISSN: 09500618 (2015).
38. Constantinides, G, Ulm, F. J. & Van Vliet, K. On the use of nanoindentation for cementitious materials. *Materials and structures* **36,** 191–196 (2003).
39. Constantinides, G. & Ulm, F.-J. The effect of two types of CSH on the elasticity of cement-based materials: Results from nanoindentation and micromechanical modeling. *Cement and concrete research* **34,** 67–80 (2004).
40. Bernard, O., Ulm, F.-J. & Lemarchand, E. A multiscale micromechanics hydration model for the early-age elastic properties of cement-based materials. *Cement and Concrete Research* **33,** 1293–1309 (2003).
41. Scrivener, K. L. Microstructure of concrete. *Materials Science of Concrete III, I, 1 pp.* **127** (1989).
42. Richardson, I. & Groves, G. Models for the composition and structure of calcium silicate hydrate (C S H) gel in hardened tricalcium silicate pastes. *cement and concrete research* **22,** 1001–1010 (1992).
43. Kjellsen, K. O. Heat curing and post-heat curing regimes of high-performance concrete: influence on microstructure and CSH composition. *Cement and Concrete Research* **26,** 295–307 (1996).
44. Bae, S. *et al.* Soft X-ray Ptychographic Imaging and Morphological Quantification of Calcium Silicate Hydrates (C–S–H). *Journal of the American Ceramic Society* **98,** 4090–4095. ISSN: 1551-2916 (2015).
45. Brisard, S. *Analyse morphologique et homogénéisation numérique: application à la pâte de ciment* PhD thesis (Université Paris-Est, 2011).
46. Beaudoin, J. J. On the Validity of Colloidal Models for Hydrated Cement Paste.
47. Beaudoin, J. J. & Alizadeh, R. A discussion of the paper "Refinements to colloidal model of C–S–H in cement: CM-II" by Hamlin M. Jennings. *Cement and Concrete Research* **38,** 1026–1027 (2008).
48. Beaudoin, J. J. & Alizadeh, R. A discussion of the paper "A multi-technique investigation of the nanoporosity of cement paste" by Hamlin M. Jennings, Jeffrey J. Thomas, Julia S. Gevrenov, Georgios Constantinides and Franz-Josef Ulm. *Cement and Concrete Research* **37,** 1373 (2007).

49. Faure, P. F. & Rodts, S. Proton NMR relaxation as a probe for setting cement pastes. *Magnetic resonance imaging* **26,** 1183–1196 (2008).
50. Muller, A., Scrivener, K., Gajewicz, A. & McDonald, P. Use of bench-top NMR to measure the density, composition and desorption isotherm of C–S–H in cement paste. *Microporous and Mesoporous Materials* **178,** 99–103 (2013).
51. Valori, A., McDonald, P. J. & Scrivener, K. L. The morphology of C–S–H: Lessons from 1 H nuclear magnetic resonance relaxometry. *Cement and Concrete Research* **49,** 65–81 (2013).
52. Sanahuja, J., Dormieux, L. & Chanvillard, G. Modelling elasticity of a hydrating cement paste. *Cement and Concrete Research* **37,** 1427–1439 (2007).
53. Richardson, I. The nature of C-S-H in hardened cements. *Cement and Concrete Research* **29,** 1131–1147. ISSN: 00088846 (1999).
54. Richardson, I. G. Model structures for C-(A)-S-H(I). EN. *Acta crystallographica Section B, Structural science, crystal engineering and materials* **70,** 903–23. ISSN: 2052-5206 (2014).
55. Muller, A. C. A. Characterization of porosity & CSH in cement pastes by ^{1}H NMR (2014).
56. Thomas, J. J., Jennings, H. M. & Allen, A. J. Relationships between Composition and Density of Tobermorite, Jennite, and Nanoscale CaO-SiO2- H2O. *The Journal of Physical Chemistry C* **114,** 7594–7601 (2010).
57. Feldman, R. Helium flow and density measurement of the hydrated tricalcium silicate - water system. *Cement and Concrete Research* **2,** 123 –136 (1972).
58. Muller, A., Scrivener, K., Gajewicz, A. & McDonald, P. J. Densification of C-S-H Measured by 1H NMR Relaxometry. *The Journal of Physical Chemistry C* **117,** 403–412. ISSN: 1932-7447 (2013).
59. Megaw, H. D. & Kelsey, C. Crystal structure of tobermorite. *Nature* **177,** 390–391 (1956).
60. Richardson, I. Tobermorite/jennite- and tobermorite/calcium hydroxide-based models for the structure of C-S-H: applicability to hardened pastes of tricalcium silicate, β-dicalcium silicate, Portland cement, and blends of Portland cement with blast-furnace slag, metakaol. *Cement and Concrete Research* **34,** 1733–1777. ISSN: 00088846 (2004).
61. Mostafa, N., Shaltout, A., Omar, H & Abo-El-Enein, S. Hydrothermal synthesis and characterization of aluminium and sulfate substituted 1.1 nm tobermorites. *Journal of Alloys and Compounds* **467,** 332–337 (2009).
62. Zhang, J. & Scherer, G. W. Comparison of methods for arresting hydration of cement. *Cement and Concrete Research* **41,** 1024–1036. ISSN: 00088846 (2011).
63. Gallé, C. Effect of drying on cement-based materials pore structure as identified by mercury intrusion porosimetry: a comparative study between oven-, vacuum-, and freeze-drying. *Cement and Concrete Research* **31,** 1467–1477 (2001).

64. Juenger, M. C. G. & Jennings, H. M. The use of nitrogen adsorption to assess the microstructure of cement paste. *Cement and Concrete Research* **31,** 883–892 (2001).
65. Korpa, A & Trettin, R. The influence of different drying methods on cement paste microstructures as reflected by gas adsorption: comparison between freeze-drying (F-drying), D-drying, P-drying and oven-drying methods. *Cement and Concrete Research* **36,** 634–649 (2006).
66. Collier, N., Sharp, J., Milestone, N., Hill, J. & Godfrey, I. The influence of water removal techniques on the composition and microstructure of hardened cement pastes. *Cement and Concrete Research* **38,** 737–744. ISSN: 00088846 (2008).
67. Snoeck, D. *et al.* The influence of different drying techniques on the water sorption properties of cement-based materials. *Cement and Concrete Research* **64,** 54–62 (2014).
68. Scrivener, K., Snellings, R. & Lothenbach, B. *A Practical Guide to Microstructural Analysis of Cementitious Materials* (Crc Press, 2016).
69. Thomas, J. J., Jennings, H. M. & Allen, A. J. Determination of the neutron scattering contrast of hydrated Portland cement paste using H 2 O/D 2 O exchange. *Advanced Cement Based Materials* **7,** 119–122 (1998).
70. Zhang, L & Glasser, F. Critical examination of drying damage to cement pastes. *Advances in cement research* **12,** 79–88 (2000).
71. Mantellato, S., Palacios, M. & Flatt, R. J. Impact of sample preparation on the specific surface area of synthetic ettringite. *Cement and Concrete Research* **86,** 20–28 (2016).
72. Beaudoin, J. J. *et al.* Solvent replacement studies of hydrated Portland cement systems: the role of calcium hydroxide. *Advanced Cement Based Materials* **8,** 56–65 (1998).
73. Knapen, E., Cizer, O., Van Balen, K. & Van Gemert, D. Effect of free water removal from early-age hydrated cement pastes on thermal analysis. *Construction and Building Materials* **23,** 3431–3438 (2009).
74. Escalante-Garcia, J. I. & Sharp, J. H. Variation in the Composition of C-S-H Gel in Portland Cement Pastes Cured at Various Temperatures. *Journal of the American Ceramic Society* **82,** 3237–3241 (1999).
75. Lothenbach, B., Winnefeld, F., Alder, C., Wieland, E. & Lunk, P. Effect of temperature on the pore solution, microstructure and hydration products of Portland cement pastes. *Cement and Concrete Research* **37,** 483–491. ISSN: 00088846 (2007).
76. Lesko, S., Lesniewska, E., Nonat, A., Mutin, J.-C. & Goudonnet, J.-P. Investigation by atomic force microscopy of forces at the origin of cement cohesion. *Ultramicroscopy* **86,** 11–21. ISSN: 03043991 (2001).
77. Barnes, P. & Bensted, J. *Structure and Performance of Cements, Second Edition* 584. ISBN: 0203477782 (2002).
78. Eilers, L., Root, R., *et al. Long-term effects of high temperature on strength retrogression of cements* in *SPE California Regional Meeting, 7-9 April, Long Beach, California* (1976).

79. Gajewicz, A. M. *Characterisation of cement microstructure and pore-water interaction by 1H Nuclear Magnetic Resonance Relaxometry* PhD thesis (University of Surrey, 2014).
80. Gallucci, E., Zhang, X. & Scrivener, K. Effect of temperature on the microstructure of calcium silicate hydrate (C-S-H). *Cement and Concrete Research* **53,** 185–195. ISSN: 00088846 (2013).
81. Richardson, I. The calcium silicate hydrates. *Cement and Concrete Research* **38,** 137–158. ISSN: 00088846 (2008).
82. Kim, J. J., Rahman, M. K. & Taha, M. M. R. Examining microstructural composition of hardened cement paste cured under high temperature and pressure using nanoindentation and 29Si MAS NMR. *Applied Nanoscience* **2,** 445–456 (2012).
83. Del Bosque, I. S., Martínez-Ramírez, S, Martín-Pastor, M & Blanco-Varela, M. Effect of temperature on C–S–H gel nanostructure in white cement. *Materials and structures* **47,** 1867–1878 (2014).
84. Richardson, I. Tobermorite/jennite-and tobermorite/calcium hydroxide-based models for the structure of CSH: applicability to hardened pastes of tricalcium silicate, β-dicalcium silicate, Portland cement, and blends of Portland cement with blast-furnace slag, metakaolin, or silica fume. *Cement and Concrete Research* **34,** 1733–1777 (2004).
85. Kjellsen, K. O., Detwiler, R. J. & Gjørv, O. E. Pore structure of plain cement pastes hydrated at different temperatures. *Cement and concrete research* **20,** 927–933 (1990).
86. Bentur, A., Berger, R. L., Kung, J. H., Milestone, N. & Young, J. Structural properties of calcium silicate pastes: II, Effect of curing temperature. *Journal of the American Ceramic Society* **62,** 362–366 (1979).
87. Verbeck, G. J. *Structures and physical properties of cement paste, Invited Paper* in *5th International Symposium on the Chemistry of Cement, Tokyo* (1968), 1–32.
88. Scrivener, K. L. The effect of heat treatment of inner product C S H. *Cement and Concrete Research* **22,** 1224–1226 (1992).
89. Kjellsen, K. O., Detwiler, R. J. & Gjørv, O. E. Backscattered electron imaging of cement pastes hydrated at different temperatures. *Cement and Concrete Research* **20,** 308–311. ISSN: 00088846 (1990).
90. Famy, C, Scrivener, K. & Crumbie, A. What causes differences of CSH gel grey levels in backscattered electron images? *Cement and Concrete Research* **32,** 1465–1471 (2002).
91. Jennings, H. M., Thomas, J. J., Gevrenov, J. S., Constantinides, G. & Ulm, F.-J. A multi-technique investigation of the nanoporosity of cement paste. *Cement and Concrete Research* **37,** 329–336 (2007).
92. Holly, R, Reardon, E., Hansson, C. & Peemoeller, H. Proton spin–spin relaxation study of the effect of temperature on white cement hydration. *Journal of the American Ceramic Society* **90,** 570–577 (2007).
93. Bourissai, M., Meftah, F., Brusselle-Dupend, N., Lecolier, É & Bonnet, G. Evolution of the Elastic Properties of an Oilwell Cement Paste at Very Early Age under Downhole Conditions: Characterization and Modelling.

Oil & Gas Science and Technology–Revue d'IFP Energies nouvelles **68,** 595–612 (2013).

94. Lothenbach, B., Matschei, T., Möschner, G. & Glasser, F. P. Thermodynamic modelling of the effect of temperature on the hydration and porosity of Portland cement. *Cement and Concrete Research* **38,** 1–18. ISSN: 00088846 (2008).
95. Zacak, M., Garrault, S., Korb, J. & Nonat, A. *Effect of temperature on the development of CSH during early hydration of C3S* in *12 th International Congress on the Chemistry of Cement* (2007), W1–06.
96. Zaoui, A. Continuum micromechanics: survey. *Journal of Engineering Mechanics* **128,** 808–816 (2002).
97. Dormieux, L., Kondo, D. & Ulm, F.-J. *Microporomechanics* (John Wiley & Sons, 2006).
98. Suquet, P. *Continuum micromechanics* (Springer, 2014).
99. Ulm, F.-J., Constantinides, G & Heukamp, F. Is concrete a poromechanics materials?—A multiscale investigation of poroelastic properties. *Materials and structures* **37,** 43–58 (2004).
100. Eshelby, J. D. *The determination of the elastic field of an ellipsoidal inclusion, and related problems* in *Proceedings of the Royal Society of London A: Mathematical, Physical and Engineering Sciences* **241** (1957), 376–396.
101. Mori, T. & Tanaka, K. Average stress in matrix and average elastic energy of materials with misfitting inclusions. *Acta metallurgica* **21,** 571–574 (1973).
102. Hershey, A. The elasticity of an isotropic aggregate of anisotropic cubic crystals. *Journal of Applied mechanics-transactions of the ASME* **21,** 236–240 (1954).
103. Hill, R. A self-consistent mechanics of composite materials. *Journal of the Mechanics and Physics of Solids* **13,** 213–222 (1965).
104. Pichler, B. & Hellmich, C. Upscaling quasi-brittle strength of cement paste and mortar: A multi-scale engineering mechanics model. *Cement and Concrete Research* **41,** 467–476 (2011).
105. Pichler, B. *et al.* Effect of gel–space ratio and microstructure on strength of hydrating cementitious materials: An engineering micromechanics approach. *Cement and Concrete Research* **45,** 55–68 (2013).
106. Termkhajornkit, P., Vu, Q. H., Barbarulo, R., Daronnat, S. & Chanvillard, G. Dependence of compressive strength on phase assemblage in cement pastes: Beyond gel–space ratio—Experimental evidence and micromechanical modeling. *Cement and Concrete Research* **56,** 1–11 (2014).
107. Stora, E, He, Q.-C. & Bary, B. Influence of inclusion shapes on the effective linear elastic properties of hardened cement pastes. *Cement and concrete research* **36,** 1330–1344 (2006).
108. Pichler, B., Hellmich, C. & Eberhardsteiner, J. Spherical and acicular representation of hydrates in a micromechanical model for cement paste: prediction of early-age elasticity and strength. *Acta Mechanica* **203,** 137–162 (2009).
109. John, B. Class G and H Basic Oil Well Cements. *World Cement* (1992).

110. Chen, C.-W. *A mineralogical approach to use the non-qualified fine aggregates in asphalt concrete pavement* PhD thesis (Université Paris-Est, 2016).
111. Aranda, M. A. G., De la Torre, A. G. & Leon-Reina, L. Rietveld Quantitative Phase Analysis of OPC Clinkers, Cements and Hydration Products. *Reviews in Mineralogy and Geochemistry* **74,** 169–209. ISSN: 1529-6466 (2012).
112. Bish, D. L. & Post, J. E. Quantitative mineralogical analysis using the Rietveld full-pattern fitting method. *American Mineralogist* **78,** 932–940 (1993).
113. Toby, B. H. R factors in Rietveld analysis : How good is good enough ? *International Centre for diffraction Data Data,* 67–70 (2006).
114. Le Saoût, G., Kocaba, V. & Scrivener, K. Application of the Rietveld method to the analysis of anhydrous cement. *Cement and Concrete Research* **41,** 133–148. ISSN: 00088846 (2011).
115. De Noirfontaine, M.-N., Dunstetter, F., Courtial, M., Gasecki, G. & Signes-Frehel, M. Polymorphism of tricalcium silicate, the major compound of Portland cement clinker. *Cement and Concrete Research* **36,** 54–64. ISSN: 00088846 (2006).
116. Snellings, R., Salze, A. & Scrivener, K. Use of X-ray diffraction to quantify amorphous supplementary cementitious materials in anhydrous and hydrated blended cements. *Cement and Concrete Research* **64,** 89–98. ISSN: 00088846 (2014).
117. Snellings, R., Bazzoni, A. & Scrivener, K. The existence of amorphous phase in Portland cements: Physical factors affecting Rietveld quantitative phase analysis. *Cement and Concrete Research* **59,** 139–146. ISSN: 00088846 (2014).
118. Saoût, G. L., Füllmann, T., Kocaba, V. & Scrivener, K. *Quantitative study of cementitious materials by X-ray diffraction/ Rietveld analysis using an external standard* in *12th International Congress on the Chemistry of Cement.* (2007).
119. Scrivener, K., Füllmann, T., Gallucci, E., Walenta, G. & Bermejo, E. Quantitative study of Portland cement hydration by X-ray diffraction/Rietveld analysis and independent methods. *Cement and Concrete Research* **34,** 1541–1547. ISSN: 00088846 (2004).
120. Jenkins, R & Snyder, R. *Introduction to x-ray powder diffractometry* (John Wiley & Sons, 1996).
121. Suda, Y., Saeki, T. & Saito, T. Relation between chemical composition and physical properties of CSH generated from cementitious materials. *Journal of Advanced Concrete Technology* **13,** 275–290 (2015).
122. Nishi, F., Takeuchi, Y. & Maki, I. Tricalcium silicate Ca3O [SiO4]: the monoclinic superstructure. *Zeitschrift für Kristallographie-Crystalline Materials* **172,** 297–314 (1985).
123. Mumme, W., Hill, R., Bushnell-Wye, G & Segnit, E. Rietveld crystal structure refinements, crystal chemistry and calculated powder diffraction data for the polymorphs of dicalcium silicate and related phases. *Neues Jahrb. Mineral. Abh* **169** (1995).

124. Alarcon-Ruiz, L., Platret, G., Massieu, E. & Ehrlacher, A. The use of thermal analysis in assessing the effect of temperature on a cement paste. *Cement and Concrete research* **35,** 609–613 (2005).
125. Kocaba, V. *Development and evaluation of methods to follow microstructural developments of cementitious systems including slags* PhD thesis (École Polytechnique Fédérale de Lausanne, 2010).
126. Krakowiak, K. J. *et al.* Nano-chemo-mechanical signature of conventional oil-well cement systems: Effects of elevated temperature and curing time. *Cement and Concrete Research* **67,** 103–121. ISSN: 00088846 (2015).
127. Zeng, Q., Li, K., Fen-Chong, T. & Dangla, P. Analysis of pore structure, contact angle and pore entrapment of blended cement pastes from mercury porosimetry data. *Cement and Concrete Composites* **34,** 1053–1060 (2012).
128. Zeng, Q., Li, K., Fen-Chong, T. & Dangla, P. Pore structure of cement pastes through NAD and MIP analysis. *Adv Cem Res* **28,** 23–32 (2016).
129. Cook, R. A. & Hover, K. C. Mercury porosimetry of hardened cement pastes. *Cement and Concrete research* **29,** 933–943 (1999).
130. Cook, R. A. & Hover, K. C. Mercury porosimetry of cement-based materials and associated correction factors. *Construction and Building Materials* **7,** 231–240 (1993).
131. Diamond, S. Mercury porosimetry: An inappropriate method for the measurement of pore size distributions in cement-based materials. *Cement and Concrete Research* **30,** 1517 –1525 (2000).
132. Baroghel-Bouny, V. Water vapour sorption experiments on hardened cementitious materials: Part I: Essential tool for analysis of hygral behaviour and its relation to pore structure. *Cement and Concrete Research* **37,** 414–437 (2007).
133. Baroghel-Bouny, V. Water vapour sorption experiments on hardened cementitious materials. Part II: Essential tool for assessment of transport properties and for durability prediction. *Cement and Concrete Research* **37,** 438–454 (2007).
134. Brue, F., Davy, C. A., Skoczylas, F., Burlion, N. & Bourbon, X. Effect of temperature on the water retention properties of two high performance concretes. *Cement and Concrete Research* **42,** 384–396 (2012).
135. De Burgh, J. M. & Foster, S. J. Influence of temperature on water vapour sorption isotherms and kinetics of hardened cement paste and concrete. *Cement and Concrete Research* **92,** 37–55 (2017).
136. Barrett, E., Joyner, L. & Halenda, P. The determination of pore volume and area distributions in porous substances. 1-Computations from nitrogen isotherms. *J. Am. Chem. Soc.* **73,** 373–380 (1951).
137. Hagymassy, J., Odler, I., Yudenfreund, M., Skalny, J. & Brunauer, S. Pore structure analysis by water vapor adsorption. III. Analysis of hydrated calcium silicates and portland cements. *Journal of Colloid and Interface Science* **38,** 20–34 (1972).

138. Badmann, R., Stockhausen, N. & Setzer, M. J. The statistical thickness and the chemical potential of adsorbed water films. *Journal of Colloid and Interface science* **82,** 534–542 (1981).
139. De Burgh, J. M., Foster, S. J. & Valipour, H. R. Prediction of water vapour sorption isotherms and microstructure of hardened Portland cement pastes. *Cement and Concrete Research* **81,** 134–150 (2016).
140. Hagymassy, J., Brunauer, S. & Mikhail, R. S. Pore structure analysis by water vapor adsorption: I. t-curves for water vapor. *Journal of Colloid and Interface Science* **29,** 485–491 (1969).
141. Rouquerol, F., Luciani, L., Llewellyn, P., Denoyel, R. & Rouquerol, J. Texture des matériaux pulvérulents ou poreux. *Techniques de l'ingénieur. Analyse et caractérisation* **2,** p1050–1 (2003).
142. Wang, B., Faure, P., Thiéry, M. & Baroghel-Bouny, V. 1 H NMR relaxometry as an indicator of setting and water depletion during cement hydration. *Cement and Concrete Research* **45,** 1–14 (2013).
143. Faure, P. & Caré, S. Suivi par IRM et par T 1 de l'effet du couplage hydratation–séchage sur la microstructure de pâte de ciment. *Comptes Rendus Chimie* **9,** 548–555 (2006).
144. Faure, P. F., Caré, S., Magat, J. & Chaussadent, T. Drying effect on cement paste porosity at early age observed by NMR methods. *Construction and Building materials* **29,** 496–503 (2012).
145. McDonald, P. J., Rodin, V & Valori, A. Characterisation of intra-and inter-C–S–H gel pore water in white cement based on an analysis of NMR signal amplitudes as a function of water content. *Cement and Concrete Research* **40,** 1656–1663 (2010).
146. McDonald, P., Korb, J.-P., Mitchell, J & Monteilhet, L. Surface relaxation and chemical exchange in hydrating cement pastes: a two-dimensional NMR relaxation study. *Physical Review E* **72,** 011409 (2005).
147. Blümich, B. *Essential NMR: for Scientists and Engineers* (Springer Science & Business Media, 2005).
148. Lynden-Bell, R. M. & Harris, R. K. *Nuclear magnetic resonance spectroscopy* (Appleton-Century-Crofts, 1969).
149. Callaghan, P. T. *Translational dynamics and magnetic resonance: principles of pulsed gradient spin echo NMR* (Oxford University Press, 2011).
150. D'Orazio, F., Bhattacharja, S., Halperin, W. P., Eguchi, K. & Mizusaki, T. Molecular diffusion and nuclear-magnetic-resonance relaxation of water in unsaturated porous silica glass. *Physical Review B* **42,** 9810 (1990).
151. Provencher, S. W. A constrained regularization method for inverting data represented by linear algebraic or integral equations. *Computer Physics Communications* **27,** 213–227 (1982).
152. ASTM, C. 39, Standard test method for compressive strength of cylindrical concrete specimens. *Annual book of ASTM standards* **4** (1996).
153. Feldman, R. F. Factors affecting Young's modulus-porosity relation of hydrated Portland cement compacts. *Cement and Concrete Research* **2,** 375–386 (1972).

154. Gajewicz, A., Gartner, E, Kang, K, McDonald, P. & Yermakou, V. A 1 H NMR relaxometry investigation of gel-pore drying shrinkage in cement pastes. *Cement and Concrete Research* **86,** 12–19 (2016).
155. Maruyama, I., Nishioka, Y., Igarashi, G. & Matsui, K. Microstructural and bulk property changes in hardened cement paste during the first drying process. *Cement and Concrete Research* **58,** 20–34 (2014).
156. Nauleau, É. *Évolution au cours du temps des propriétés physiques et mécaniques des matériaux cimentaires d'un puit géothermique basse énergie* PhD thesis (Université Paris-Est, 2013).
157. Kurdowski, W. in, 603–659 (Springer Netherlands, Dordrecht, 2014). ISBN: 978-94-007-7945-7.
158. Dilnesa, B. Z. *Fe-containing hydrates and their fate during cement hydration: thermodynamic data and experimental study* PhD thesis (ÉCOLE POLYTECHNIQUE FÉDÉRALE DE LAUSANNE, 2011).
159. Vespa, M., Wieland, E., Dähn, R. & Lothenbach, B. Identification of the Thermodynamically Stable Fe-Containing Phase in Aged Cement Pastes. *Journal of the American Ceramic Society* **98,** 2286–2294 (2015).
160. Geng, G., Kilcoyne, D. A., Benmore, c. J. & Monteiro, P. J. M. *Multi-technology Investigation of the Atomic Structure of Calcium Silicate Hydrates Multi-technology Investigation of the Atomic Structure of Calcium* in *14th International Congress on the Chemistry of Cement, 13-16 octobre 2015, Beijing, China* (2015).
161. Bhatty, J. I. *et al.* in *Compositional Analysis by Thermogravimetry* (ASTM International, 1988).
162. Šauman, Z. Carbonization of porous concrete and its main binding components. *Cement and Concrete Research* **1,** 645–662. ISSN: 00088846 (1971).
163. Morandeau, A., Thiéry, M. & Dangla, P. Investigation of the carbonation mechanism of CH and C-S-H in terms of kinetics, microstructure changes and moisture properties. *Cement and Concrete Research* **56,** 153–170. ISSN: 00088846 (2014).
164. Branch, J., Kosson, D., Garrabrants, A. & He, P. The impact of carbonation on the microstructure and solubility of major constituents in microconcrete materials with varying alkalinities due to fly ash replacement of ordinary Portland cement. *Cement and Concrete Research* **89,** 297 – 309 (2016).
165. Sevelsted, T. F. & Skibsted, J. Carbonation of C–S–H and C–A–S–H samples studied by sup 13C, sup 27Al and sup 29Si MAS NMR spectroscopy. *Cement and Concrete Research* **71** (2015).
166. Rivas-Mercury, J., Pena, P., de Aza, A. & Turrillas, X. Dehydration of $Ca_3Al_2(SiO_4)y(OH)_{4(3-y)}$ $(0 < y < 0.176)$ studied by neutron thermodiffractometry. *Journal of the European Ceramic Society* **28,** 1737–1748. ISSN: 09552219 (2008).
167. Garbev, K., Gasharova, B., Beuchle, G., Kreisz, S. & Stemmermann, P. First Observation of $\alpha-Ca_2[SiO_3(OH)](OH) - Ca_6[Si_2O_7][SiO_4](OH)_2$ Phase Transformation upon Thermal Treatment in Air. *Journal of the American Ceramic Society* **91,** 263–271. ISSN: 1551-2916 (2008).

168. Dilnesa, B., Wieland, E, Lothenbach, B, Dähn, R & Scrivener, K. Fe-containing phases in hydrated cements. *Cement and Concrete Research* **58,** 45–55 (2014).
169. Bentur, A. Effect of curing temperature on the pore structure of tricalcium silicate pastes. *Journal of colloid and interface science* **74,** 549–560 (1980).
170. Jennings, H. M., Thomas, J. J., Gevrenov, J. S., Constantinides, G. & Ulm, F.-J. A multi-technique investigation of the nanoporosity of cement paste. *Cement and Concrete Research* **37,** 329–336. ISSN: 00088846 (2007).
171. Muller, A. & Scrivener, K. A reassessment of mercury intrusion porosimetry by comparison with 1H NMR relaxometry. *Cement and Concrete Research* **100,** 350–360 (2017).
172. Bentur, A., Berger, R. L., Kung, J. H., Milestone, N. & Young, J. Structural properties of calcium silicate pastes: II, effect of curing temperature. *Journal of the American Ceramic Society* **62,** 362–366 (1979).
173. Königsberger, M., Hellmich, C. & Pichler, B. Densification of CSH is mainly driven by available precipitation space, as quantified through an analytical cement hydration model based on NMR data. *Cement and Concrete Research* **88,** 170–183 (2016).
174. Daian, J.-F. Condensation and isothermal water transfer in cement mortar Part I—Pore size distribution, equilibrium water condensation and imbibition. *Transport in porous media* **3,** 563–589 (1988).
175. Poyet, S. & Charles, S. Temperature dependence of the sorption isotherms of cement-based materials: heat of sorption and Clausius–Clapeyron formula. *Cement and Concrete Research* **39,** 1060–1067 (2009).
176. Hundt, J. & Kantelberg, H. Sorptionsuntersuchungen an Zementstein, Zementmörtel und Beton (1978).
177. Ishida, T., Maekawa, K. & Kishi, T. Enhanced modeling of moisture equilibrium and transport in cementitious materials under arbitrary temperature and relative humidity history. *Cement and concrete research* **37,** 565–578 (2007).
178. Zhang, J., Weissinger, E. A., Peethamparan, S. & Scherer, G. W. Early hydration and setting of oil well cement. *Cement and Concrete research* **40,** 1023–1033 (2010).
179. Pang, X., Jimenez, W. C. & Iverson, B. J. Hydration kinetics modeling of the effect of curing temperature and pressure on the heat evolution of oil well cement. *Cement and Concrete Research* **54,** 69–76 (2013).
180. Roussel, N., Ovarlez, G., Garrault, S. & Brumaud, C. The origins of thixotropy of fresh cement pastes. *Cement and Concrete Research* **42,** 148–157 (2012).
181. Escalante-Garcia, J., Mendoza, G & Sharp, J. Indirect determination of the Ca/Si ratio of the CSH gel in Portland cements. *Cement and concrete research* **29** (1999).
182. Thomas, J. J. & Jennings, H. M. A colloidal interpretation of chemical aging of the C-S-H gel and its effects on the properties of cement paste. *Cement and Concrete Research* **36,** 30–38. ISSN: 00088846 (2006).

183. Cong, X. & Kirkpatrick, R. Effects of the temperature and relative humidity on the structure of C-S-H gel. *Cement and Concrete Research* **25,** 1237–1245. ISSN: 00088846 (1995).
184. Königsberger, M. *Multiscale microstructural modeling in cement and concrete : from hydration to poroelasticity, creep, and strength* PhD thesis (Technische Universität Wien, 2016).
185. Pellenq, R. J.-M. *et al.* A realistic molecular model of cement hydrates. *Proceedings of the National Academy of Sciences* **106,** 16102–16107 (2009).
186. Plassard, C., Lesniewska, E., Pochard, I. & Nonat, A. *Intrinsic elastic properties of Calcium Silicate Hydrates by nanoindentation* in *12th International Congress on the Chemistry of Cement* (2007), 44.
187. Acker, P. *et al.* Micromechanical analysis of creep and shrinkage mechanisms. *Creep, Shrinkage and Durability Mechanics of Concrete and other quasi-brittle Materials, Cambridge, MA,* 15–25 (2001).
188. Monteiro, P. J. & Chang, C. The elastic moduli of calcium hydroxide. *Cement and Concrete Research* **25,** 1605–1609 (1995).
189. Holuj, F, Drozdowski, M & Czajkowski, M. Brillouin spectrum of Ca (OH) 2. *Solid State Communications* **56,** 1019–1021 (1985).
190. Haecker, C.-J. *et al.* Modeling the linear elastic properties of Portland cement paste. *Cement and Concrete Research* **35,** 1948–1960 (2005).
191. Speziale, S. *et al.* Single-crystal elastic constants of natural ettringite. *Cement and Concrete Research* **38,** 885–889 (2008).
192. Kamali, S. *Comportement et simulation des matériaux cimentaires en environnement agressifs: lixiviation et température* PhD thesis (Cachan, Ecole normale supérieure, 2003).
193. O'Neill, B., Bass, J. D. & Rossman, G. R. Elastic properties of hydrogrossular garnet and implications for water in the upper mantle. *Journal of Geophysical Research: Solid Earth* **98,** 20031–20037 (1993).

List of publications and conference participations

Journal papers

- S. Bahafid, S. Ghabezloo, M. Duc, P. Faure, J. Sulem, Effect of the hydration temperature on the microstructure of Class G cement: C-S-H composition and density, Cem. Concr. Res. 95 (2017) 270–281.
- S. Bahafid, S. Ghabezloo, P. Faure, M. Duc, J. Sulem, Study of the pore structure of cement paste with the hydration temperature : Experimental investigation and micromechanical modelling. Submitted to cement and concrete research in September 2017.

Conference papers

- S. Bahafid, M. Duc, S. Ghabezloo, P. Faure, J. Sulem, Influence of curing temperature on the chemical composition and density of C-S-H in an oil-well cement paste. The 36th Cement and Concrete Science Conference 2016 (Cardiff).
- S. Bahafid, S. Ghabezloo, M. Duc, P. Faure, J. Sulem,, Microstructure Characterization and Micromechanical Modelling of Cement Pastes Hydrated at Different Temperatures, Proceedings of the 6th Biot Conference on Poromechanics 2017 (Paris).
- S. Bahafid, S. Ghabezloo, P. Faure, M. Duc, J. Sulem, Micromechanical Modelling of Cement Pastes Hydrated at Different Temperatures, The 37th Cement and Concrete Science Conference 2017 (London).

Oral presentations and posters

- Presentation of a poster at Alert geomaterials workshop (2015, Aussois)
- Presentation of a poster at Alert geomaterials workshop (2016, Aussois)
- Oral presentation at the 36th cement and concrete science – (2016, Cardiff, UK)
- Oral presentation at the 8th multiscale materials modeling – (2016, Dijon, France)
- Oral presentation at the EMI International Conference – (2016, Metz, France)
- Oral presentation at the GDRI workshop (2016, Paris, France)
- Oral presentation at the Sixth Biot Conference (2017, Paris, France)
- Oral presentation at the 37th cement and concrete science – (2017, London, UK)

Cement and Concrete Research 95 (2017) 270–281

Contents lists available at ScienceDirect

Cement and Concrete Research

journal homepage: www.elsevier.com/locate/cemconres

Effect of the hydration temperature on the microstructure of Class G cement: C-S-H composition and density

Sara Bahafid[a,1], Siavash Ghabezloo[a,*], Myriam Duc[b], Pamela Faure[a], Jean Sulem[a]

[a]Laboratoire Navier, UMR 8205, Ecole des Ponts ParisTech, IFSTTAR, CNRS, UPE, Champs-sur-Marne, France
[b]Université Paris-Est, Ifsttar, GERS/SRO, France

ARTICLE INFO

Article history:
Received 8 April 2016
Received in revised form 18 December 2016
Accepted 10 February 2017

Keywords:
hardened cement paste
microstructure
C-S-H
porosity
C-S-H density

ABSTRACT

Curing temperature has a significant influence on cement paste microstructure and the properties of its principal hydrate C-S-H. In this paper, the effect of the hydration temperature in the range of 7 °C to 90 °C on the microstructure of a class G oil-well cement is studied. This is done by combining various experimental methods, including X-ray diffraction associated with the Rietveld analysis, thermo-gravimetric analysis, mercury intrusion porosimetry and porosity evaluation by drying. The experimental results show an increase of the capillary porosity and a decrease of the gel porosity by increasing the hydration temperature. This is attributed to a decrease of the C-S-H intrinsic porosity and a corresponding increase of the C-S-H density for higher curing temperatures. The experimental results are used in a simple analysis method to evaluate the density of C-S-H, as well as its C/S ratio and H/S ratio in dry and saturated conditions. The evaluated C-S-H density varies from 1.88 g/cm^3 at 7 °C to 2.10 g/cm^3 at 90 °C. The results also show a decrease of molar C/S ratio with increasing hydration temperature from 1.93 at 7 °C to 1.71 at 90 °C and of the H/S ratio from 5.1 at 7 °C to 2.66 at 90 °C.

1. Introduction

Understanding the microstructure of cement is a key step for producing green cements and improving the behavior of cement-based materials. The cement hydration process and the resulting microstructure are highly dependent on the cement formulation and the hydration conditions. Particularly, the hydration temperature has a significant influence on the cement paste microstructure and on its physical and mechanical properties [1–3]. This is for instance important for understanding the behavior and properties of oil-well cements. Indeed, in the structures of oil, gas and geothermal wells, a cement sheath is placed between the casing and the surrounding rock. This cement sheath plays a major role in providing zonal isolation along the well (i.e., it excludes fluids such as water or gas in one zone from oil in another zone), in protecting the casing against corrosion and in providing mechanical support [4–6]. Due to the geothermal gradient (about 25 °C per km) the cement sheath along a well is exposed to a hydration temperature increasing with depth which influences its microstructure and consequently its mechanical properties. The effect of hydration temperature on cement has been previously studied and presented in the literature [3,7–10]. It has been agreed that temperature variation induces considerable changes in the microstructure and the mechanical behavior. Higher temperatures accelerate the dissolution precipitation processes of anhydrous cement, promoting a rapid formation of phases and yielding to faster development of initial strength [3,7,8]. For hydration temperatures below 100 °C the chemistry of cement hydration remains quasi-unchanged and almost the same hydrates precipitate [7,9,10]. However, some phases (e.g., ettringite) show a thermal instability with increasing curing temperature [7]. Above 100 °C, several changes occur resulting in severe deterioration of mechanical properties with time, commonly called strength retrogression [9,11,12].

The structure of the main binder of cement, calcium silicate hydrate commonly mentioned as C-S-H, is highly sensitive to the hydration temperature. Its bulk density increases with the curing temperature [13] and its morphology changes [14,15]. Richardson [14] showed that elevated temperatures lead to a C-S-H with a fine texture morphology and particles about half size comparing to that of pastes hydrated at ambient temperature. Furthermore, elevated temperature enhances C-S-H polymerization causing a decrease in the C/S ratio [14].

The aim of this paper is to present an experimental study of the effect of the hydration temperature on the microstructure of

* Corresponding author.
E-mail address: siavash.ghabezloo@enpc.fr (S. Ghabezloo).
[1] Siavash Ghabezloo, Laboratoire Navier/CERMES, Ecole des Ponts ParisTech, 6-8 Av. Blaise Pascal, Cité Descartes, Champs sur Marne, 77455 Marne la Vallée Cedex 2, France.

http://dx.doi.org/10.1016/j.cemconres.2017.02.008
0008-8846/

cement paste. This study is performed on a class G cement (according to API classification), which is the most commonly used cement in oil wells. The hydration temperature is varied between 7 °C and 90 °C (7 °C, 20 °C, 40 °C, 60 °C, 90 °C), which is the temperature range corresponding to depths below 2 km, in which the class G cement is generally used without any particular additive (e.g. silica fume). Our main objective through this study is to quantify the major components of the cement paste microstructure with respect to the curing temperature and to provide information on the stoichiometry and the bulk density of C-S-H. X-ray diffraction, analyzed with the Rietveld method and combined with thermogravimetric analysis enable a quantitative description of mass fractions of cement hydrates. Mercury porosimetry and total porosity measurements are used for the characterization of gel and capillary porosity evolution with hydration temperature. A combination of the abovementioned methods permits the evaluation of the C/S and H/S ratios, C-S-H bulk density and intrinsic porosity with temperature in the studied range.

The present study is a continuation of research work of coauthors on the behavior of hardened class G cement paste. In previous studies, the thermo-poro-mechanical and time dependent properties of the tested cement paste have been evaluated experimentally [5,6,16-19]. The evaluated parameters have then been extrapolated to cement pastes with various w/c ratio and chemical composition using micromechanical modeling and homogenization method [20–23]. The quantitative characterization of the effect of hydration temperature on the cement paste microstructure, as presented in this paper, can be used in the micromechanical modeling of oil-well cements for evaluation of their thermo-poro-mechanical properties for various hydration temperatures, corresponding to different depths along an oil well.

2. Cement hydration and microstructure

A brief review is presented here on cement hydration reactions and microstructure to provide the necessary information for further analysis and discussions of the experimental results on microstructure characterization. The cement hydration is the result of complex chemical reactions between the cement clinker and water involving the dissolution of clinker phases and the precipitation of hydration products. The most important reactions correspond to the consumption of the most abundant clinker phases, namely Alite (C_3S) and Belite (C_2S). These two reactions result in the development of crystalline CH (calcium hydroxide), called portlandite, and C-S-H, a generic name given to any amorphous or poorly crystalline calcium silicate phase in cement pastes and illustrating its allotropic occurrence [9]. The structure of C-S-H varies within a cement paste and a variety of C-S-H, with different C/S ratios, can be observed. Based on TEM (Transmission Electron Microscopy) analysis, Richardson [24] has shown that the C/S ratio in cement paste covers a wide range of values with an average of 1.75. An average value of 4 is also generally admitted for the H/S ratio of a saturated C-S-H [9,25,26] and of 1.8 for C-S-H with full interlayer water [27]. Note that the given average values for C/S and H/S ratio correspond to an ordinary cement hydrated at ambient temperature. The variability of C-S-H chemical composition makes the reaction process very complex and the reaction formulation are only approximate. To account for the variable stoichiometry of C-S-H, the reactions expressing the hydration of Alite and Belite have been reformulated by Brouwers [25] as:

$$C_3S + (3 - x + y)H \rightarrow C_x - S - H_y + (3 - x)CH \quad (1)$$

$$C_2S + (2 - x + y)H \rightarrow C_x - S - H_y + (2 - x)CH \quad (2)$$

where x and y stand respectively for the C/S and H/S ratios. The C-S-H structure has been approximated either by a Tobermorite or Jennite [15]. The variability of C/S ratio and the disorder of C-S-H has been interpreted by removal of bridging silicate tetrahedral [15,24]. This defect tobermorite model has been readdressed recently to approximate the C-S-H structure [28].

The cement paste is a porous material with a porous structure covering an impressive range of pore sizes from sub-nanometer (size of interlayer pores) to sub-millimeter (size of air voids). Between these extreme pore sizes, one can distinguish different types of porosities depending on the considered scale. The complexity comes from the main binder of cement, C-S-H which is porous itself with a pore volume commonly called gel porosity. Several microstructural models have been proposed to describe the porous structure of cement and C-S-H. One of the most widely cited models is the one proposed by Jennings et al. [29–31], describing the C-S-H as a granular structure made up of a basic building bloc called globule, with a layered structure similar to Tobermorite. This model classifies water in cement paste into three categories:

1. Interlayer water: corresponding to water packed between C-S-H solid layers. This water is filling spaces of less than 1 nm, drying only at very low relative humidity. This interlayer porosity is a part of the C-S-H building bloc (Globule).
2. Water in gel pores: corresponding to water filling the spaces between packed globules. These pores can be further divided into two categories depending on their size defining small gel pores and large gel pores.
3. Water in capillary porosity: water in pores of size above 10 nm, drying at 85% RH [31].

The results of this paper are going to be discussed and analyzed according to the Jennings model [31]. For more extensive information on cement microstructure the reader can refer to milestone books and papers which address this subject in detail [8,9,11,25,26,32,33].

3. Materials and methods

This section is dedicated to a presentation of the tested cement paste, sample preparation method and experimental techniques used in this study.

3.1. Materials

The cement paste samples were prepared using a class G cement at a water to cement ratio of 0.44 according to the standard API requirements and following the procedure described by Ghabezloo et al. [5]. After mixing, pastes were cured for 28 days at different temperatures, under lime-saturated water in sealed containers to avoid water evaporation and carbonation of specimens. The samples are cured at five different curing temperatures: 7 °C, 20 °C, 40 °C, 60 °C, and 90 °C. After 28 days of curing, the hydration process has been arrested using a freeze-dryer. This technique has been chosen because of its relative rapidity and as it is supposed to cause less damage to the microstructure than oven drying [34]. The freeze drying according to [35] didn't appear to cause major differences on the XRD patterns compared to other drying techniques. However, the same method has been reported to degrade ettringite and monosulfate and dehydrate C-S-H [33]. Nevertheless, there is no blameless method for drying the cement without affecting its microstructure. Even solvent exchange that has been widely adopted to be suitable for XRD experiments has been recently criticized for altering some hydration products [35]. After drying, some samples were ground in

a tungsten ball mill and sifted in a 32 μ m sieve. The prepared powder is destined to XRD and TGA experiments. Several samples were prepared to assess the repeatability of the measurements.

3.2. Experimental methods

The characterization of the effect of hydration temperature on the cement paste microstructure in this study is done by a combination of several experimental methods: X-ray diffraction combined with Rietveld method, thermogravimetric analysis, mercury intrusion porosimetry, porosity measurement by freeze drying. These methods are described below.

3.2.1. X-ray diffraction

The X-ray diffraction allows the identification of the main crystalline phases in materials and has been widely used for the characterization of cements. When combined with the Rietveld method, it enables the quantification of these phases. The X-ray patterns were obtained on a D8 advance diffractometer from Bruker operating at 35 kV and 40 mA, using CoK (1.79 A) radiation at an angular step of 0.01 °C per second between 3.0° and 80° [2θ] angles. The EVA software coupled with the ICDD pdf-2 database enables the identification of the major phases present in the material.

3.2.2. Rietveld method

A quantitative analysis of the mineral phases identified on the X-ray diffraction pattern can be done using the Rietveld method. This method is based on a simulation of the whole XRD profile as a combination of the profiles of several single mineral phases. This is done by refining the structural parameters (lattice parameters, atomical positions and displacement parameters) and microstructural parameters (crystallite size and strain) of considered phases [36–38]. The refinement program adjusts the above-mentioned parameters in order to minimize the residual difference R_{wp} between the simulated profile y_{ci} and the measured one y_i using a non-linear least squares algorithm [37]. The main equation used in the Rietveld refinements and the residual difference are given below:

$$y_{ci} = \sum_p [S_p] \sum_k p_k L_k F_k^2 G(2\theta_i - 2\theta_k) P_k + y_{cbi} \quad (3)$$

$$R_{wp} = \sum_i W_i (y_i - y_{ci})^2 \quad (4)$$

where y_{ci} is the calculated intensity at a 2θ position and y_{cbi} is the background intensity at the i_{th} step. S_p is the scale factor of the p_{th} phase, L_k is the Lorentz and polarization factors for the k_{th} Bragg reflection. F_k is the structure factor, p_k is the multiplicity factor, P_k is the preferred orientation function, θ_{ik} is the Bragg angle for the k_{th} reflection, $G(2\theta_i - 2\theta_k)$ is the profile function and W_i is a weight factor taken equal to $W_i = 1/y_i$. For further details about the development of the equations of the structure factor and the profile function, one can refer to Refs. [36–40]. Compared to the single peak analysis method for phase quantification, the Rietveld method has the advantage of overcoming the peak overlap [37]. The difficulty in using the Rietveld method for hydrated cement pastes is related to the presence of poorly crystalline calcium silicate phases. This amorphous content yields an increase of the hydrates mass fractions. This problem has been widely mentioned in the literature [36,41]. Two-methods permit removing the contribution of amorphous material to crystalline phases: Internal and external method [42]. In this study the internal method that requires the addition of a defined quantity of a standard material to the sample has been used. The quantity of added standard material being known, the quantities of the other phases can hence be corrected [43–45]. We choose Corundum (1 μ m particle size powder) as an internal standard because of its non-reactivity with dried cement and adequacy in terms of absorption contrast for hydrated cement [46, Chapter 4]. 50%–50% binary mixture of dried cement powder and corundum was prepared following previous works [37,47]. It should be mentioned that the corundum has been added to the hardened cement paste after drying and grinding.

3.2.3. Refinement procedure

All Rietveld refinements reported in this study are done using commercial Topas 4.2 software. The refined parameters are the zero error, scale factors, lattice parameters, the preferred orientation according to the March Dollase model. The atomic positions and site occupancies of phases were kept fixed, except for C_4AF where a variable occupancy of aluminum and iron on tetrahedral and octahedral sites is expected [43]. The background has been described with a Chebyshev polynomial of the fifth order accompanied with the term 1/X. The considered phases in Rietveld refinements and their parameters are listed in Table 1.

3.2.4. Thermogravimetric analysis

Thermogravimetric analysis (TGA) is a technique in which the mass of a material submitted to a progressive heating is monitored as a function of temperature. It shows how the mass of a substance is altered due to changes of temperature. The mass difference is a result of degradation of the material, removal of moisture and the oxidation of components. A typical experiment corresponds to heating up a sample from room temperature to 1250 ° C at a fixed rate. For cement pastes, we can distinguish three majors weight losses in TG and DTG curves (respectively, mass loss curve as a function of temperature and its derivative) associated to different reactions [50]:

- Up to 350 °C: Dehydration of C-S-H and aluminates
- 400 °C–550 °C: Dehydroxylation of CH
- Above 600 °C: Decarbonation of $CaCO_3$

The experiments are carried out using a Netzsch Thermal Analyzer STA 409. Around 160 mg of powder is placed in a platinum crucible and heated up to 1250 °C at a rate of 10 °C/min under a nitrogen flow of 80 ml/min to prevent samples carbonation. TGA is often used to determine the portlandite content as its decomposition occurs in a unique interval. To quantify the total amount of portlandite the following expression is used [51,52]:

$$f_{CH}^m = L_{CH} \frac{M_{CH}}{M_{H_2O}} + L_{CaCo3} \frac{M_{CH}}{M_{CO_2}} \quad (5)$$

where f_{CH}^m is the mass fraction of CH and M_X the molar mass of X. L_{CH} and L_{CaCo3} are the weight losses attributed to CH and $CaCO_3$ in their respective decomposition temperature domain. The first term accounts for the dehydroxylation of portlandite and the second term accounts for the carbonation of initial portlandite into calcite, assuming that all the formed calcite is due the portlandite carbonation. This carbonation process is supposed not to occur during TGA analysis under a nitrogen environment, but we suppose that the formation of calcite during the grinding process and preparation of material to XRD and TGA experiments is inevitable.

Table 1
Phases of cement microstructure considered in Rietveld refinements.

Phase	Formula	Crystal system	Density
Alite	C_3S	Monoclinic/M3 Nishi et al. [48]	3.15
Belite	C_2S	Monoclinic/β Mumme et al. [49]	3.27
Aluminate	C_3A	Cubic	3.01
Brownmillerite	C_4AF	Orthorombic	3.73
Portlandite	CH	Rhombohedral	2.24
Calcite	$CaCO_3$	Rhombohedral	2.71

The quantification of C-S-H is quite difficult with this method as C-S-H and AFM phases loose their water at the same temperature range. Furthermore, the quantification of C-S-H relies on the knowledge of its molar mass and the number of water molecules in a C-S-H particle, which are not generally known and vary with the hydration conditions.

3.2.5. Mercury intrusion porosimetry

Mercury porosimetry (MIP) is a widespread tool for characterizing the porous structure of materials. The high surface tension of mercury opposes its entry into the pores, making it a non-wetting fluid. When increasing the pressure, the mercury is forced into the pores with an entry size depending on the applied pressure. Assuming a cylindrical pore geometry, the applied pressure can be related to equivalent pore sizes using the Washburn equation given below [34]:

$$P_{HG} = \frac{4\gamma\cos(\theta)}{d} \quad (6)$$

where γ is the surface tension of mercury (0.485 N/m), θ the contact angle between mercury and the pore surface ($\theta = 130^\circ$), and d is the pore diameter in (m). The experiments are performed on freeze-dried cement paste samples. The Washburn relation permits to evaluate the pore entry size corresponding to each pressure level (increased progressively) and to obtain a pore volume-pore size curve. The porosimeter used in this study is an AutoPore IV 9500 from Micrometrics reaching a maximum pressure of 230 MPa corresponding to a pore size of 6 nm. It should be noted that the application of MIP for characterization of the pore volume of cement based materials has been sometimes criticized in the literature (e.g. Ref. [53]) and its limitations have been pointed out. This is particularly due to the ink-bottle effect and also accessibility problems resulting in underestimation of the macropores by this method. Other available methods for capillary porosity evaluation like NMR [54] and SEM [13] have also their own limitations and give capillary porosity estimations which are sometimes lower than expected values.

4. Experimental results, analysis and discussions

4.1. X-ray diffraction and qualitative analysis

The phase composition of the tested cement clinker, obtained through XRF and also XRD combined with Rietveld analysis is given in Table 2.

The powder diffraction patterns for the cement pastes cured at different temperatures are presented in Fig. 1. These patterns show that the major crystalline phase formed during the hydration of class G cement is portlandite. Ettringite is formed in small quantities, below 2% as expected from the small quantity of C_3A in the Class G cement clinker (Table 2). X-ray powder diffraction patterns suggest also that the major residual clinker phases are C_4AF and C_2S, which confirm the slow consumption of these two clinker phases [44,51] comparing to C_3S that is almost completely depleted. Small quantities of Hibschite are also detected. The principal reflection of this phase is at about 39°(2θ) and is overlapped with the second reflection of portlandite. The portlandite being a high crystalline phase, and hence exhibiting a symmetric diffraction peak, the non-symmetric part of its second peak is attributed to Hibschite. In the Hibschite phase identified in our cement a small amount of aluminum is replaced by iron, which may reflect a product formed from the hydration of ferrite phases. This qualitative analysis is relevant for the diffraction patterns collected for different curing conditions. However, the consumption of clinker phases is more pronounced with curing temperature, leading to a faster development of hydrates [2,7,55]. Furthermore, new phase appear with the elevation of temperature in the studied range. These phases are the katoite $Ca_3Al_2[(OH)_4]_3$ and the dellaite C_6S_3H. Katoite is a calcium aluminate hydrate, member of hydrogrossular group. It is observed at high temperatures, starting from 60 °C. The presence of katoite in class G cement pastes hydrated under elevated temperatures has been reported previously by [56]. The strong intensities associated to katoite with increasing curing temperature may be explained by the fact that temperature favored the development of katoite, which is, thermodynamically, a more stable phase than ettringite for which the stability decreases with increasing temperature according to Ref. [7]. The other observed phase when elevating temperature, dellaite C_6S_3H, is a crystalline calcium silicate hydrate with a C/S ratio of 2. No evident conclusion can be made about the change of the dellaite quantity with temperature based on XRD patterns, as this phase shows strong overlapped peaks with residual clinker and amorphous C-S-H. The presence of this phase has been previously reported in geothermal cements [57]. Regarding the hydration of ferrite it is not easy to detect any Fe-containing phase. Previous studies reported that the most stable Fe-containing phases are Al and Fe-siliceous hydrogarnet or an amorphous Iron hydroxide [58,59]. Both of these components are hard to detect with X-ray considering their poorly crystalline structure. We deem in this study that Fe-siliceous hydrogarnet has formed during the hydration of ferrite and we will quantify it in the following.

The amorphous or short-range order phases scatter X-ray in many directions resulting in a large hump dispersed in a wide 2θ range instead of narrower peaks with high intensities relative to crystalline phases. The presence of amorphous content is evidenced here by the bump over the 2θ range [35° –40°]. Comparing the range associated to C-S-H for different curing temperature, we observe that diffraction patterns associated to $T = 7$°C and $T = 20$°C exhibit narrower peaks in the 2θ range [35° –37°] comparing to $T = 60$ °C and $T = 90$ °C. This would suggest that the structure disorder is increasing with the elevating temperatures. The cements cured at lower temperature seem therefore to be more ordered than those cured at higher temperature. The increasing degree of crystallinity in the structure of calcium silicate hydrate has been associated in a recent research to an increasing C/S ratio in C-S-H [60]. The lower temperature being related to higher C/S ratio, which has been previously mentioned in Ref. [14], may support the observed arrangement and the increasing order of the structure at low temperatures.

Table 2
chemical composition of clinker from X-ray diffraction and Rietveld analysis.

Chemical composition XRF		XRD - Rietvveld	
Main oxides	Wt%	Phase name	Wt%
SiO_2	19.14	C_3S monoclinic	57.02
CaO	67.28	C_2S beta	22.83
Al_2O_3	2.93	C_3A cubic	1.33
Fe_2O_3	3.73	C_4AF	15.30
MgO	1.43	Gypsum	0.85
SO_3	2.5	Periclase	0.87
Na_2O	0.54	Calcite	0.65
TiO_2	0.40	Vaterite	0.88
LOI	2.40	Aragonite	0.27
K_2O	ns	Quartz	ns

ns: non-significant.

4.2. Thermogravimetric analysis

The results obtained from thermogravimetric tests are presented in Fig. 2 in terms of the relative mass loss as a function of the temperature (TG, left y-axis) and the derivative of TG curve (DTG, right y-axis). The curves show four rapid weight losses. The first weight

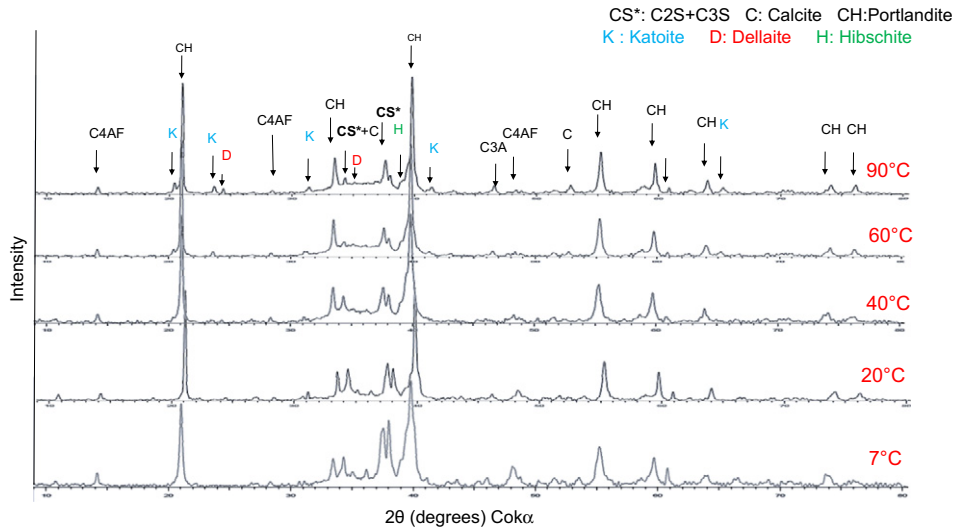

Fig. 1. X-ray powder diffraction patterns with qualitative analysis of the major phases for cement class G cured at different temperatures T (°C) = 7, 20, 40, 60, and 90.

loss is mainly due to C-S-H, Afm and ettringite [61]. However, as presented above in the results of XRD experiments, the tested cement paste contains very small amounts of Afm and ettringite. This is mainly due to the small quantity of C_3A in the class G cement clinker. The second major weight loss observed at 450 °C–550 °C reflects the dehydration of portlandite. The third and forth losses are essentially due to the CO_2 departure from calcite. The existence of these two peaks can be seen as a sign of the carbonation of samples during preparation and storage [46, Chapter 5]. According to Sauman [62] and Morandeau et al. [63], the forth peak corresponds to well crystalized calcite, but the third one is attributed to allotropic forms of calcite (aragonite and vaterite). These two varieties of polymorph calcite turn into calcite around 500 °C during heating. Being less stable, aragonite and vaterite decompose at lower temperatures than calcite. Vaterite, aragonite and calcite originate from the carbonation of C-S-H and portlandite [63]. However, it is difficult to state whether the formed calcite is due the carbonation of portlandite or to the carbonation of C-S-H. The findings about this topic drawn in the literature are confusing. While some highlighted that the C-S-H and portlandite carbonate simultaneously [63], others mentioned that the carbonation of C-S-H occurs when the portlandite is almost depleted [64,65]. However, a consensus has been made that the carbonation of portlandite is more pronounced at the onset of carbonation. It can be clearly seen that our samples have undergone some carbonation similar to data presented in Ref. [46, Chapter 5] for samples carbonated during preparation and storage. However, when the carbonation rate is enhanced, the intensity of the forth peak is more pronounced as presented in the results of Morandeau et al. [63] and which is not the case here. As our samples are not intentionally carbonated as in Ref. [63], we assume that all the calcite formed is due to the portlandite carbonation as in Ref. [51]. It is worth noting that some analysis results will be influenced by this assumption and this will be discussed in the following. Aside from these four rapid weight losses, two more small weight losses can be identified. The first one is adjacent to C-S-H peak. This loss may originate from the dehydration of hydrogarnet that occurs above 250 °C [66]. The second one is adjacent to the decomposition of portlandite. We deem that a part of this weight loss originates from the decomposition of dellaite which occurs above 600 °C according to [67]. It can be observed that the weight losses that may potentially correspond to hydrogarnet and dellaite are more pronounced with for higher hydration temperature. This combined with the XRD experiments strengthen the observations of the development of these two phases and the increase in their mass fractions with increasing hydration temperature.

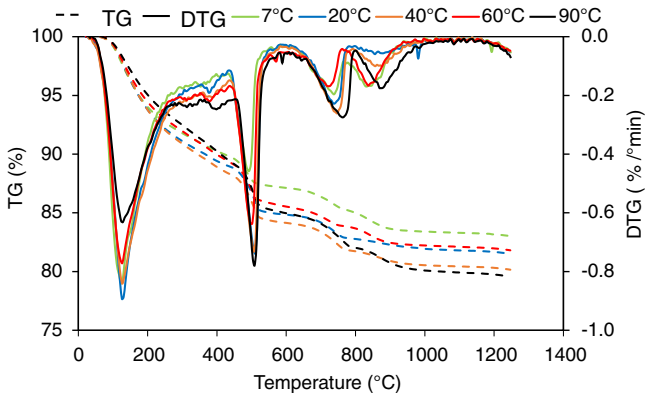

Fig. 2. Thermogravimetric weight loss for cement class G cured at different temperatures.

4.3. Phase assemblage of cement hydrate from combined Rietveld and TGA analysis

The quantitative evaluation of different phases in cement paste microstructure can be done through a combination of X-ray diffraction/Rietveld method and thermogravimetric analysis. The portlandite content is taken from TGA analysis and corrected to account for the eventual carbonation process, as described in Eq. (5). The mass fractions of clinker phases are determined from Rietveld analysis. Based on the result of XRD and TGA we build molar quantity balance of the major elements in cement CaO, SiO_2, Al_2O_3, Fe_2O_3 and SO_3 (Gypsum). The considered phases in the molar quantity balance are: C-S-H, CH, Al-ettringite, Al-monosulfate, residual clinker phases and Fe-containing siliceous hydrogarnet considered as the most stable phases resulting from the hydration of Ferrite [68]. The katoite

is formed in small quantities and has been neglected in the mass assemblage. The molar quantity balance equations are:

$$\begin{cases} xn_{CSH} + 6n_{Ett} + 4n_{Afm} + 3n_{Hydg} = 3n_{C3S} + 2n_{C2S} + 3n_{C3A} + 4n_{C4AF} - n_{CH} \\ n_{CSH} + 0.84n_{Hydg} = n_{C3S} + n_{C2S} \\ n_{Ett} + n_{Afm} + 0.9n_{Hydg} = n_{C3A} + n_{C4AF} \\ n_{Hydg} = n_{C4AF} \\ 3n_{Ett} + n_{Afm} = n_{SO_3} \end{cases} \quad (7)$$

where n_z is the molar quantity of phase z which can be either hydration product or consumed clinker phase. x is the C/S molar ratio in C-S-H. The molar quantity balance for different elements result in a non-linear system of five equations and five unknowns which can be solved numerically. The unknowns are: Ettringite, Afm, C-S-H, Hydrogarnet and the C/S molar ratio. The resulting molar quantities are used to evaluate the mass fractions of different phases. According to Lothenbach et al. [7] ettringite is unstable at hydration temperatures higher than 50 °C and AFm forms at the expenses of this phase. Interestingly, the resolution of the above system of equations for hydration temperatures 60 °C and 90 °C results in small negative values of ettringite molar quantity. For these temperatures the ettringite molar quantity is imposed equal to zero and other quantities are obtained by solving the first four equations. The evaluated mass assemblage of cements hydrated under different temperatures are presented in Table 3. The mass fraction of portlandite shows a slight increase with increasing hydration temperature, with a more pronounced increase from 7 to 20 °C and slighter increase for higher temperatures. This lower portlandite quantity at 7 °C is compatible with the higher C_3S and C_2S content observed at this temperature. The ettringite and Afm content are quite small, less than 2% and are fluctuating with increasing hydration temperature. The C-S-H mass fraction increases with hydration temperature between 7 to 40 °C and shows a slight decrease for higher temperatures. Regarding the hydrogarnet, we found a fluctuating mass fraction depending on the hydration degree of ferrite which is also fluctuating with hydration temperature. The overall hydration degree of cement paste increases significantly from 7 °C to 20 °C and only slight changes are observed above this range at the considered age. As stated above, based on XRD results, it can be clearly seen that C_3S is more consumed than the other clinker phases. C_2S and C_4AF generally react slowly confirming the low hydration degree corresponding to this phase [43,51]. It should be mentioned that the resolution of the above system of equations results also in an evaluation of the C/S ratio in C-S-H (variable x), which will be presented later in Section 4.6.

Table 3
Phase assemblage of cement pastes obtained from the combination of XRD-Rietveld and TGA analysis for cement class G cured at different temperatures.

Temperature (°C)	7	20	40	60	90
C-S-H	42.84	46.12	49.44	47.44	45.65
Portlandite	17.63	19.89	20.63	21.20	22.75
Ettringite	1.77	0.15	1.08	0.00	0.00
Afm	1.37	3.65	2.25	1.77	2.83
Si–Fe-Hydrogarnet	7.86	9.88	9.34	7.90	7.44
C_3S	7.02	4.17	4.73	3.96	3.17
C_2S	13.25	9.56	5.04	7.11	7.49
C_3A	0.81	0.28	0.52	1.05	0.55
C_4AF	7.66	5.45	5.80	7.22	7.58

4.4. Porosity and pore size distribution

4.4.1. Drying method for total porosity measurement

Evaluating the total porosity of cement is very complicated as various porosity evaluation methods can result in different values for the total porosity. There exist different drying methods which are commonly used for porosity measurement. However, which reservoir of porosity is being dried with each drying method is not well understood. Oven drying at 105 °C has been used regularly, but it is considered to be non-accurate in estimating total porosity. At 105 °C, a quantity of the water in the interlayer space, which is not regarded as porosity, evaporates. The quantity of evaporated interlayer water at 105 °C is not clearly known. Another method which has been regularly used for cement paste is drying at 11% relative humidity which can be considered as a reference method based on previous studies of Feldman [69] and Jennings [31] who clarified that this condition corresponds to a full interlayer space with a monolayer of water encountering the C-S-H globules. Hence, equilibrating a sample at 11% RH corresponds to a C-S-H with dried gel pores and full interlayer spaces. These drying techniques for evaluation of the total porosity are compared here with the freeze drying method which is used in this study for preparation of the sample for microstructure characterization experiments (e.g. MIP, TGA) and needs much less time compared to 11% drying. This comparison is done by performing thermogravimetric analysis on hardened cement pastes cured during four months at 20 °C and dried using these methods (Oven drying: OD, Freeze drying: FD and 11% RH drying).

The results of TGA experiments are presented Fig. 3 and show a smaller weight loss associated to C-S-H for 105 °C dried sample, as compared to the ones of freeze drying and 11% RH drying. These latter present almost the same weight loss. It can thus be confirmed that the oven drying at 105 °C removes approximately 30% of the interlayer water from the C-S-H. The interesting similarity between TGA curves of freeze dried and 11% RH-dried samples illustrates that these two drying techniques empty almost the same pores reservoir. Given this similarity, we can conclude that freeze drying removes the water in gel pores and leaves the interlayer spaces full of water and some physical water adsorbed on the surface of the C-S-H. Because of its rapidity compared to drying at 11% RH the freeze drying is preferred to dry specimens in this study and can be regarded as a quick method for evaluating total porosity of a cement paste. It's worthwhile mentioning that the fourth peak corresponding to the crystalline calcite is almost absent in Fig. 3, as compared to the result presented in Fig. 2. This can be due to the fact that the samples had a shorter storage period before the experiments presented in Fig. 3,

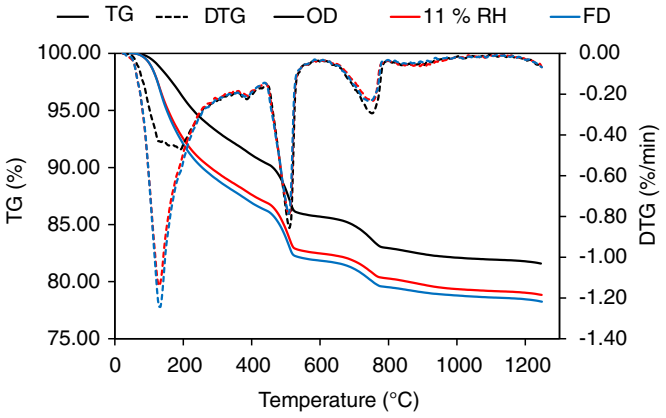

Fig. 3. Thermogravimetric weight loss for cement class G cured at ambient temperature dried by different means (Oven drying: OD, Freeze drying: FD and at 11% of relative humidity.

and thus undergone a lower degree of carbonation corresponding to preparation and storage.

4.4.2. Effect of temperature on cement paste porosity

The cumulative porosity and pore size distributions of cement pastes cured at different temperatures as obtained from mercury porosimetry are presented in Fig. 4. The results show one pore family with pore sizes ranging from 10 to 100 nm and the beginning of a second pore family with pore sizes smaller than 10 nm. The median pore size is almost constant for temperatures ranging from 7 °C to 40 °C and increases significantly at 60 °C. This trend was mentioned in the literature [1,2,9,13] and reflects that higher temperatures lead to a coarsening of the porous structure. Pastes hydrated above 60 °C have larger capillary pore volume compared to pastes cured at lower temperatures. This has also been explained by polymerization reactions starting around 60 °C [70]. The pore family observed by mercury intrusion corresponds to the capillary porosity and interestingly, the 10 nm pore size that corresponds to the lower limit of the pore family observed by mercury intrusion, has been considered as the lower limit of the size of the capillary pores [71]. Jennings [72] showed that capillary pores empty at 85% RH. This has also been confirmed recently by NMR experiments that revealed a constant NMR intensity relative to capillary pores below 85% [54]. This threshold value of relative humidity when converted into pore size using the Kelvin law indicates a pore size of 10 nm. Therefore, we assume that the capillary porosity is the porosity measured by mercury intrusion up to 120 MPa pressure corresponding to a pore size of about 10 nm, as shown in Fig. 4 (a). As mentioned in Section 3.2.5, the MIP may result in an underestimation of the volume of the biggest pores in a material as they can potentially be accessible only through smaller pores. However, in this study a great part of the injected mercury volume corresponding to a wide range of pores sizes has been used to evaluate the capillary porosity. For this reason, the mentioned underestimation should be less significant on the evaluation of the capillary porosity presented here. The evaluated capillary porosity is presented in Fig. 5 and shows an increase with increasing hydration temperature. This is in agreement with previous studies that showed through SEM experiments [13] or sorption isotherms [72] an increase of the capillary porosity with curing temperature. The increase of the capillary porosity may be explained by the development of denser hydration products as the curing temperature increases [13,73]. In Fig. 5, the total porosity measured from mass loss during freeze drying is also presented and shows a slight decrease with increasing curing temperature. The gel porosity can be evaluated by subtracting the capillary porosity from the total porosity. As can be seen in Fig. 5, the calculated gel porosity is decreasing with the curing temperature. The gel porosity decreases significantly by increasing the hydration

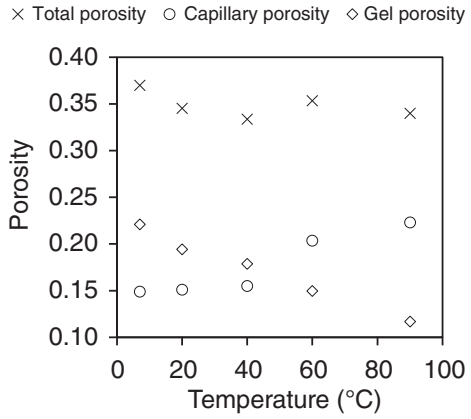

Fig. 5. Evolution of total, capillary and gel porosity with temperature.

temperature, while the mass fraction of C-S-H shows slighter variation with temperature, as shown in Table 3. This highlights that the C-S-H becomes denser at elevated temperatures. This point will be addressed in the following section.

4.5. Evaluation of C-S-H density

Few data in the literature exist on the effect of curing temperature on the C-S-H bulk density. It is difficult to assess this density considering the amorphous structure of C-S-H and the presence of portlandite intermixed with C-S-H particles. We propose here a simple method to evaluate the C-S-H bulk density based on the experimental results presented previously. The C-S-H gel porosity ϕ_{gel} can be related to the C-S-H intrinsic porosity ϕ_{CSH} and its volume fraction f^{V}_{CSH} through the following expression:

$$\phi_{gel} = \phi_{CSH} f^{V}_{CSH} \tag{8}$$

The C-S-H intrinsic porosity can be further expressed in terms of the density of C-S-H solid ρ_s, the bulk density of C-S-H ρ^{bulk}_{CSH} and the water density ρ_w as:

$$\phi_{CSH} = \frac{\rho_s - \rho^{bulk}_{CSH}}{\rho_s - \rho_w} \tag{9}$$

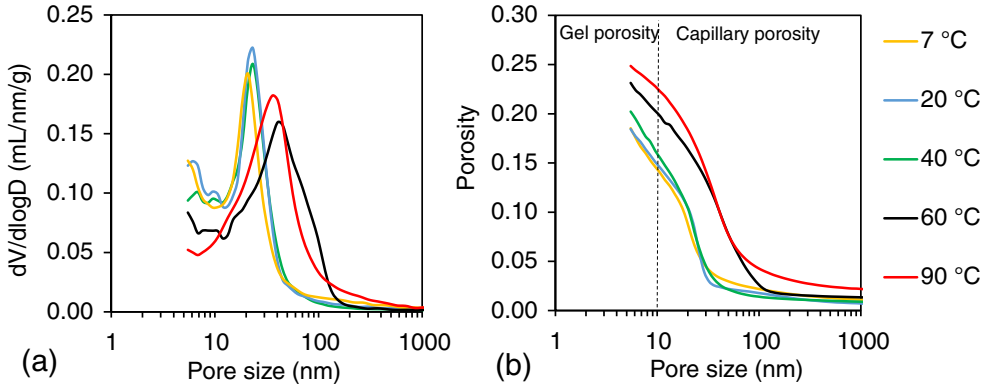

Fig. 4. (a)Differential pore size distribution; (b) Cumulative intrusion curve as measured by MIP for a class G cement cured at different temperatures (the dashed line corresponds to 10nm).

The C-S-H volume fraction f_{CSH}^{V} is linked to the mass fraction of saturated C-S-H, f_{CSH}^{sat} through the following expression:

$$f_{CSH}^{V} = f_{CSH}^{sat} \frac{\rho_{CP}}{\rho_{CSH}^{bulk}} \tag{10}$$

where ρ_{CP} is the cement paste density. It is worth noting that the mass fraction of C-S-H evaluated in Section 4.3 corresponds to a freeze-dried C-S-H, f_{CSH}^{dry}. To evaluate the saturated C-S-H density, the saturated mass fraction f_{CSH}^{sat} should be used. The dried and saturated mass fractions can be linked to each other with the following relation:

$$f_{CSH}^{sat} = f_{CSH}^{dry} \frac{\rho_{CSH}^{sat}}{\rho_{CSH}^{sat} - \phi_{CSH}\rho_w} \tag{11}$$

Using Eqs. (8), (9), (10), (11) and $\phi_{gel} = \phi_t - \phi_{cap}$, the following expression can be derived for the bulk C-S-H density:

$$\rho_{CSH}^{bulk} = \rho_s \frac{\rho_w(\phi_t - \phi_{cap}) + \rho_{CP} f_{CSH}^{dry}}{\rho_s(\phi_t - \phi_{cap}) + \rho_{CP} f_{CSH}^{dry}} \tag{12}$$

The input parameters for this expression are the density of C-S-H solid ρ_s, the mass fraction of freeze-dried C-S-H f_{CSH}^{dry}, the cement paste density ρ_{CP}, the total porosity ϕ_t and the capillary porosity ϕ_{cap}. The mass fraction of dried C-S-H is obtained from a mass balance of different hydrates as explained in Section 4.3. The total porosity and the capillary porosity are evaluated respectively by freeze drying and mercury porosimetry. The choice of C-S-H solid density is important for this analysis. The most admitted value of C-S-H solid density has been given by [27] using diffraction experiments and is equal to 2.603 g/cm^3. This density includes all the internal water of the C-S-H globules but excludes any adsorbed water at the globules surface. As the 11% RH drying leaves a monolayer of water on the C-S-H surface, the solid density of C-S-H at this condition is smaller than 2.603 [27]. Jennings [31] presented a solid density of globules equilibrated at 11% RH equal to 2.47 g/cm^3 which can be considered as the solid density of C-S-H globules in a freeze dried cement paste, considering the similarity of freeze drying and 11% RH drying methods as presented in Fig. 3. The density of solid C-S-H is considered to be independent of hydration conditions. Still, we admit that a change of the C-S-H solid density is possible. The changing chemical composition with temperatures will obviously affect this solid density.

The bulk density of C-S-H has been evaluated for different hydration temperatures through the proposed method and presented in Fig. 6. As expected, the C-S-H bulk density is increasing with hydration temperatures from 1.88 g/cm^3 at 7 °C to 2.10 g/cm^3 at 90 °C. The value of the bulk density evaluated at ambient temperature, equal to 1.95 g/cm^3, is close to the widely admitted value of C-S-H bulk density determined by Jennings [74], equal to 2.03 g/cm^3.

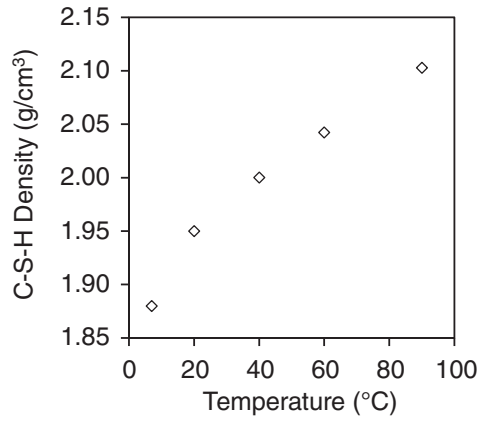

Fig. 6. The evaluated C-S-H saturated density for different curing temperatures.

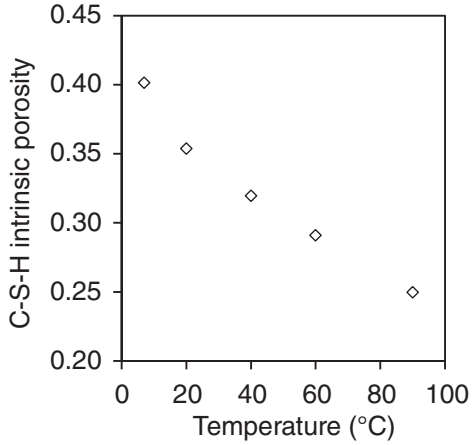

Fig. 7. The intrinsic porosity of C-S-H for different curing temperatures.

The intrinsic porosity of C-S-H can now be evaluated using Eq. (9). The results, presented in Fig. 7, show that the intrinsic porosity of C-S-H is decreasing significantly with increasing curing temperature from 0.40 at 7 °C to 0.25 at 90 °C.

The increase of the C-S-H bulk density with curing temperature was undeniable from increasing grey level of backscattered images of Gallucci et al. [13]. However, a debate has been raised on whether this changing grey level reflects a change of the C-S-H atomistic structure, or is due to an internal arrangement of C-S-H particles. Through this study, we evidenced that regardless of C-S-H solid density (which is considered constant here), the decreasing internal porosity of C-S-H captures well the C-S-H densification. Nevertheless, we do not refute that the variation of the atomistic structure will influence the C-S-H solid density. In fact, decreasing water content in C-S-H leads obviously to increasing solid density. As can be seen in Eq. (12), the saturated C-S-H density in our calculation is directly proportional to the C-S-H solid density ρ_s. Considering the relatively narrow range of the possible values of C-S-H solid density, it can only have a limited influence on the evaluation of C-S-H bulk density. Further work is needed to improve our knowledge about the C-S-H solid density under different hydration conditions.

4.6. C-S-H chemical composition

This section is dedicated to evaluation of the influence of hydration temperature on the C-S-H composition in terms of C/S and H/S molar ratios. Contradictory results are reported in the literature concerning the influence of hydration temperature on C/S ratio. According to Gallucci et al. [13], while some authors reported a decrease in the C/S ratio [75], others mentioned an increase of this ratio with temperature [76]. Concerning the H/S ratio, recent results of Gallucci et al. [13] show a decrease of this ratio by increasing hydration temperature. These ratios are defined in the following:

$$C/S = \frac{n_{CSH}^{Ca}}{n_{CSH}^{Si}}; \quad H/S = \frac{n_{CSH}^{H}}{n_{CSH}^{Si}} \tag{13}$$

where n_{CSH}^{Ca}, n_{CSH}^{Si} and n_{CSH}^{H} correspond respectively to molar quantity of calcium, silicon and water in a C-S-H particle. The molar C/S ratio is derived from the resolution of the system of equations as

mentioned in Section 4.3. Regarding the H/S ratio, the molar quantity of chemically combined water in C-S-H can be estimated from the weight loss corresponding to C-S-H in TGA experiments. Within the temperature range associated to the dehydration of C-S-H other constituents like ettringite, Afm, hydrogarnets are also loosing water. Consequently to evaluate the water associated to C-S-H, the quantity of water evaporated from the other phases in the same temperature range should be deduced. The molar contents of hydrogarnets has been evaluated through mass assemblage of the cement paste and its water content can be easily subtracted. Concerning ettringite and Afm, it should be recalled that the TGA experiments are performed here on freeze-dried samples. The freeze-drying seems to degrade or dehydrate ettringite and Afm [33] and probably for the same reason these two phases could not be observed in our XRD experiments. It seems thus reasonable to not subtract the water associated to ettringite and Afm from the TGA results as these phases may have been already dehydrated during the freeze drying. Therefore, the chemically combined water in C-S-H is evaluated by subtracting the water bounded to hydrogarnets from the total quantity of water removed until 350 °C. The H/S ratio corresponding to the saturated C-S-H can be obtained by adding the molar quantity of water in gel pores per unit mass of dry paste to the value obtained for the dry C-S-H:

$$(\mathrm{H/S})_{\mathrm{sat}} = \frac{1}{n^{\mathrm{Si}}_{\mathrm{CSH}}}\left(n^{\mathrm{H}}_{\mathrm{CSH}} + \frac{\phi_{\mathrm{gel}}\rho_w}{(\rho_{\mathrm{CP}} - \phi_t\rho_w)M_{\mathrm{H_2O}}}\right) \quad (14)$$

where ρ_{CP} is the density of saturated cement paste and $M_{\mathrm{H_2O}}$ is the molar mass of water.

The C/S ratios for different hydration temperatures are evaluated directly from the resolution of the set of Eqs. (7) and are presented in Fig. 8. One can see a decrease of C/S ratio with increasing curing temperature, from 1.93 at 7 °C to 1.71 at 90 °C. The C/S ratio evaluated at ambient temperature, equal to 1.87, is in agreement with the generally admitted value of 1.75 regarded as the mean value of C/S molar ratio in C-S-H [9,24,77]. However, different value for the C/S ratio are presented in the literature. Escalante et al. [78] reported values ranging from 1.61 to 2.24 for C/S ratio. In other studies the same authors reported values of 2.06 and 2.07 based on EDS experiments [75]. Richardson et al. [24] reported values for the C/S ratio of 1.2 to 2.3. In a more recent study on a class G cement the C/S ratio at 30 °C is found to be 1.84 ± 0.24 [52]. It appears that the values of C/S ratio vary widely in literature and depend on the used experimental techniques.

It is worth noting, that the obtained values of C/S ratio depend on the evaluated quantity of portlandite from TGA results. As mentioned in Section 4.2, we assumed that all produced calcite comes from the carbonation of portlandite. If one assumes that a part of the calcite is produced as a result of the carbonation of C-S-H, this results in a smaller quantity of portlandite and leads to higher C/S ratios. As for example, if the first carbonation peak is arbitrarily attributed to C-S-H carbonation, it results in C/S ratios higher than 2.0 for hydration temperatures 7 °C and 20 °C, which is of course much higher than the admitted average values.

The evaluated H/S ratios for dry (corresponding to non-evaporable-water) and saturated (corresponding to C-S-H with gel pores filled with water) conditions are given in Fig. 9 for different hydration temperatures. One can note a decrease of H/S ratio with increasing curing temperature for both dry and saturated state. The dry (H/S) decreases from 1.92 at 7 °C to 1.40 at 90 °C and the saturated varies from 5.1 at 7 °C to 2.66 at 90 °C. The evaluated value of H/S ratio for dried C-S-H at ambient temperature, equal to 1.85, compares well with the value of 1.8 given by Allen et al. [27] based on SANS and SAXS experiments, corresponding to interlayer water which does not include the layer of water at the surface of the globule. This has been confirmed in recent studies by Muller et al. [79] proposing a mean value of 1.8 for the interlayer water. The saturated H/S ratio evaluated at ambient temperature in this study is equal to 4.23, which is in agreement with the widely admitted value equal to 4 for a pure C-S-H [9,31]. It is worth noting that the provided H/S ratios may be underestimated due to the eventual carbonation of C-S-H. Few data in the literature propose the H/S ratio for saturated C-S-H as most of the investigation techniques are destructive. In a recent study by Muller et al. [79] using NMR on a never dried cement paste, H/S ratios equal to 4.4 and 5.3 are found respectively for $w/c = 0.40$ and $w/c = 0.48$. These results are compatible with the ratio of 4.23 found in this work for $w/c = 0.44$. The observed decreasing trend of H/S ratio with hydration temperature is compatible with the results of Gallucci et al. and Bentur et al. [13,73] who both reported a decrease in the water content of C-S-H. However, the values calculated by Gallucci et al. [13] for the H/S ratio were bigger than the values admitted for interlayer water and lower than the values corresponding to a saturated C-S-H. They hence assigned the evaluated H/S ratio to interlayer water plus a part of water in gel pores. However, in this study a clear distinction between interlayer water and gel pore water has been provided and showed coherence with the widely admitted values. Regarding the decrease of H/S ratio, Thomas et al. [80] has interpreted this observation using sol–gel processing mechanisms, stipulating that the decrease in the molar H/S ratio is the result of the condensation reactions that take place in cement pastes. In fact, cement cured at elevated temperatures undergoes an enhanced rate of silicate polymerization [81] turning the monomeric species into polymeric species. This condensation reaction is accompanied by the release of a water molecule, which result in a diminution of C-S-H water content. Solid NMR experiments also confirmed this

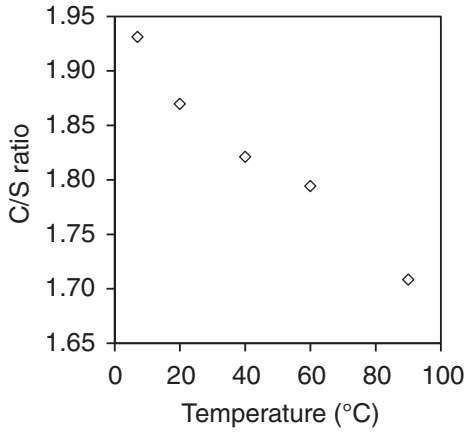

Fig. 8. The evolution of the C/S ratio with respect to temperature.

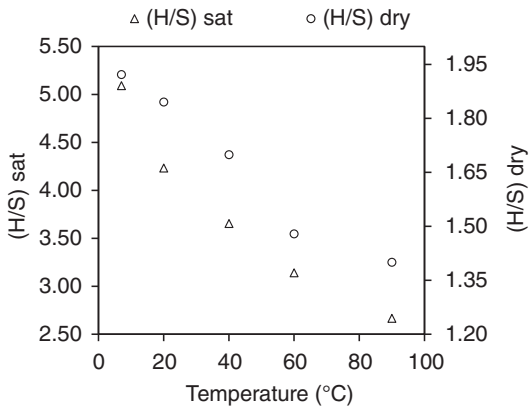

Fig. 9. The evolution of the H/S ratio with respect to temperature.

increasing rate of silicate polymerization with temperature as the mean chain length of silicate showed an increase with elevated curing temperature [13,81]. In a similar manner, the enhanced silicate polymerization rate yields to a decrease of the C/S ratio as reported before in [81]. The provided chemical composition of C-S-H is a simplified composition as it did not account for the eventual adsorption of sulphate or aluminum to the C-S-H. Indeed, some sulphates or aluminum may adsorb to the C-S-H, but it is shown that they have only a limited impact on it's properties [13].

The evaluation of C/S and H/S ratios permits an evaluation of the molar masses of dried and saturated C-S-H, presented in Fig. 10. The results show a decrease of C-S-H molar mass with increasing hydration temperature for both dried and saturated state. The saturated molar mass decreased from 260 g/mol at 7 °C to 204 g/mol at 90 °C and the dried molar mass decreased from 203 g/mol at 7 °C to 181 g/mol at 90 °C.

Various results in the literature mentioned a more or less linear relationship between C/S and H/S ratios and also between these ratios and the C-S-H bulk density [47,82]. The evaluated H/S ratios are plotted in Fig. 11 against the C/S ratios. One can see that the saturated H/S ratio shows an almost linear variation with the C/S ratio.

4.7. Sensitivity analysis

The evaluation of the C-S-H chemical composition and density as presented in previous sections rely on various experimental results. Of course uncertainty in each measurement will have a certain influence on the evaluated parameters. For most of these methods, it is quite difficult to define a numerical value for the precision or error on the results. For this reason, a sensitivity analysis is performed here in order to estimate the errors in the evaluated composition and density, based on an arbitrary 5% error in different experimental results. The results are presented in Table 4 for the cases in which the error is attributed to only one experimental result. It is shown that a 5% error induce a very small variation on the estimated C-S-H density, showing that the C-S-H density could be determined accurately. The chemical composition of C-S-H seems however to be more strongly concerned with the variation of the measured parameters. While the portlandite content and the C_3S and C_2S hydration degree have a limited effect on the C/S ratio, it seems that the dry and saturated H/S are the most sensitive to the measured parameters.

The above analysis was based on an error attributed to only one parameter at each time. However, in reality, the errors on various parameters can occur simultaneously with different values and signs. In order to account for the errors superposition, we performed an error analysis based on a randomly chosen error within the range of [−5%, 5%], which can occur on every independently measured variable in our system of equations. A Monte-Carlo type calculation has been performed to evaluate the range of values that can be obtained for each result. It is worth noting that the error added to different parameter is not necessarily the same. This is done for the hydration temperature of 7 °C and the results are presented in Table 5 in terms of minimum and maximum values obtained in the worse cases for each parameter. It can be clearly seen that even in case of accumulated errors, the uncertainties on the results higher than the case of errors on an individual results, but however the uncertainties remain reasonable.

The experimental measured parameters in this study show coherence within repeatability and reproducibility tests, which gives confidence in our results. Moreover, the good quantitative and qualitative accordance with previously published results, as mentioned in different sections of the paper, strengthens this confidence.

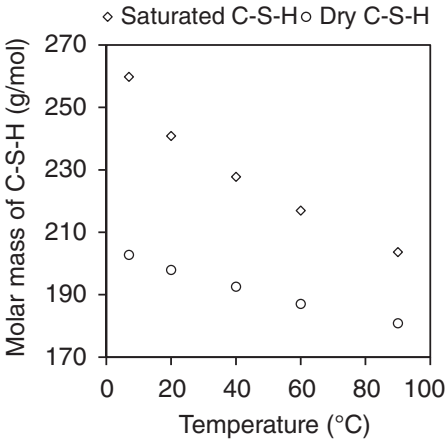

Fig. 10. The variation of saturated and dry C-S-H molar mass with curing temperature.

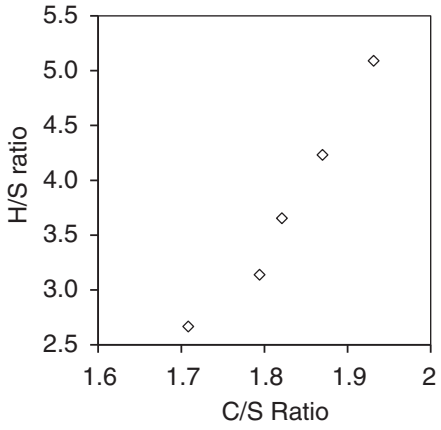

Fig. 11. The variation of H/S ratio with C/S ratio (results corresponding to different hydration temperatures).

5. Conclusions

A multi-technique experimental study has been performed to investigate the influence of the hydration temperature, between 7 °C and 90 °C on the microstructure of cement paste and more particularly on the C-S-H bulk density and chemical composition. The cement paste samples have been prepared using a class G oil-well cement and $w/c = 0.44$ and cured for 28 days in saturated conditions at 7, 20, 40, 60 and 90 °C. The cement paste microstructure has been characterized by performing X-ray diffraction analysis combined with the Rietveld method, thermogravimetric analysis, mercury intrusion porosimetry and porosity evaluation by drying. The experimental results show an increase of the capillary porosity and a slight decrease of the total porosity, resulting in a decrease of the gel porosity by increasing the hydration temperature. An analysis method has been proposed to evaluate the C-S-H bulk density and intrinsic porosity by combining the results of the above-mentioned experiments. The results show a decrease of the C-S-H intrinsic porosity

Table 4
Error analysis on different evaluated C-S-H parameters (C/S, $(H/S)_{dry}$, $(H/S)_{sat}$, and density) for an arbitrary 5% error in an individual experimental result.

Parameter changed by 5%	C/S	$(H/S)_{dry}$	$(H/S)_{sat}$	Density	C-S-H fraction
Bound water ATG		5%	2%	0.2%	0.9%
CH mass fraction	3%			0.3%	1.5%
Hydration degree of C_3S	2%	4.5%	4.5%	1%	5%
Hydration degree of C_2S	0.1%	1%	1%	0.5%	0.5%
Gel porosity			3%	1%	

Table 5
Accumulated error analysis on different evaluated C-S-H parameters (C/S, $(H/S)_{dry}$, $(H/S)_{sat}$, density and mass fractions) for an arbitrary error chosen randomly within the range [−5%, +5%] introduced simultaneously to experimental results at 7 °C.

		Main results	Min values	Max values
C-S-H composition	C/S	1.93	1.83	2.03
	$H/S_{(dry)}$	1.92	1.75	2.12
	$H/S_{(dry)}$	5.1	4.74	5.61
	Density	1.88	1.85	1.93
Mass fractions	C-S-H	42.84	39.74	45.95
	Ettringite	1.77	1.46	2.07
	Afm	1.37	1.10	1.62
	Hydrogarnet	7.87	7.47	8.42

and a corresponding increase of the C-S-H bulk density by increasing hydration temperature. This can clearly explain the observed increase of the capillary porosity for higher curing temperatures. The evaluated C-S-H bulk density varies from about 1.88 g/cm^3 at 7 °C to about 2.10 g/cm^3 at 90 °C. The analysis of the experimental results permitted to evaluate the C-S-H chemical composition in terms of C/S ratio and also H/S ratio for dry (corresponding to chemically bounded water) and saturated (corresponding to C-S-H with gel pores filled with water) conditions. The evaluated C/S ratio decreases with increasing hydration temperature, from 1.93 at 7 °C to 1.71 at 90 °C. The same trend has also been observed for the variations of H/S ratio of saturated C-S-H which decreases with increasing curing temperature from 5.1 at 7 °C to 2.66 at 90 °C. The quantitative characterization of the effect of hydration temperature on the cement paste microstructure, as presented in this paper, can be used in the micromechanical modeling of oil-well cements for evaluation of their thermo-poro-mechanical properties for various hydration temperatures, corresponding to different depths along an oil well.

Acknowledgments

This work has benefited from a French government grant managed by ANR within the frame of the national program Investments for the Future ANR-11-LABX-022-01. The authors would like to thank Julien Vincent and Mickael Saillio (Division of Material Physicochemistry of Ifsttar) for performing TGA experiments. They would like also to thank Pipat Termkhajornkit (LafargeHolcim R&D) and André Garnier (Total) for fruitful discussions.

References

[1] A. Bentur, Effect of curing temperature on the pore structure of tricalcium silicate pastes, J. Colloid Interface Sci. 74 (2) (1980) 549–560.
[2] K.O. Kjellsen, R.J. Detwiler, O.E. Gjørv, Backscattered electron imaging of cement pastes hydrated at different temperatures, Cem. Concr. Res. 20 (2) (1990) 308–311.
[3] K.O. Kjellsen, R.J. Detwiler, O.E. Gjørv, Pore structure of plain cement pastes hydrated at different temperatures, Cem. Concr. Res. 20 (6) (1990) 927–933.
[4] E.B. Nelson, Well Cementing, Elsevier. 1990.
[5] S. Ghabezloo, J. Sulem, S. Guédon, F. Martineau, J. Saint-Marc, Poromechanical behaviour of hardened cement paste under isotropic loading, Cem. Concr. Res. 38 (12) (2008) 1424–1437.
[6] A.-P. Bois, M.-H. Vu, S. Ghabezloo, J. Sulem, A. Garnier, J.-B. Laudet, Cement sheath integrity for CO_2 storage—an integrated perspective, Energy Procedia 37 (2013) 5628–5641.
[7] B. Lothenbach, F. Winnefeld, C. Alder, E. Wieland, P. Lunk, Effect of temperature on the pore solution, microstructure and hydration products of Portland cement pastes, Cem. Concr. Res. 37 (4) (2007) 483–491.
[8] K. Scrivener, A. Nonat, Hydration of cementitious materials, present and future, Cem. Concr. Res. 41 (7) (2011) 651–665.
[9] H. Taylor, Cement Chemistry, Thomas Telford Services Ltd. 1997.
[10] S. Lesko, E. Lesniewska, A. Nonat, J.-C. Mutin, J.-P. Goudonnet, Investigation by atomic force microscopy of forces at the origin of cement cohesion, Ultramicroscopy 86 (1-2) (2001) 11–21.
[11] P. Barnes, J. Bensted, Structure and Performance of Cements, Second edition ed., vol. 2002. 2002.
[12] L. Eilers, R. Root, Long-term Effects of High Temperature on Strength Retrogression of Cements, SPE California Regional Meeting, 7–9 April, Long Beach, California, Society of Petroleum Engineers. 1976,
[13] E. Gallucci, X. Zhang, K. Scrivener, Effect of temperature on the microstructure of calcium silicate hydrate (C-S-H), Cem. Concr. Res. 53 (2013) 185–195.
[14] I. Richardson, The calcium silicate hydrates, Cem. Concr. Res. 38 (2) (2008) 137–158.
[15] I. Richardson, Tobermorite/jennite- and tobermorite/calcium hydroxide-based models for the structure of C-S-H: applicability to hardened pastes of tricalcium silicate, β-dicalcium silicate, Portland cement, and blends of Portland cement with blast-furnace slag, metakaol, Cem. Concr. Res. 34 (9) (2004) 1733–1777.
[16] S. Ghabezloo, J. Sulem, J. Saint-Marc, Evaluation of a permeability–porosity relationship in a low-permeability creeping material using a single transient test, Int. J. Rock Mech. Min. Sci. 46 (4) (2009) 761–768.
[17] S. Ghabezloo, J. Sulem, J. Saint-Marc, The effect of undrained heating on a fluid-saturated hardened cement paste, Cem. Concr. Res. 39 (1) (2009) 54–64.
[18] M.H. Vu, J. Sulem, J.-B. Laudet, Effect of the curing temperature on the creep of a hardened cement paste, Cem. Concr. Res. 42 (9) (2012) 1233–1241.
[19] M.H. Vu, J. Sulem, S. Ghabezloo, J.-B. Laudet, A. Garnier, S. Guédon, Time-dependent behaviour of hardened cement paste under isotropic loading, Cem. Concr. Res. 42 (6) (2012) 789–797.
[20] S. Ghabezloo, Association of macroscopic laboratory testing and micromechanics modelling for the evaluation of the poroelastic parameters of a hardened cement paste, Cem. Concr. Res. 40 (8) (2010) 1197–1210.
[21] S. Ghabezloo, Multiscale modeling of the poroelastic properties of various oil-well cement pastes, J. Multiscale Model. 2 (3-4) (2010) 199–215.
[22] S. Ghabezloo, Micromechanics analysis of thermal expansion and thermal pressurization of a hardened cement paste, Cem. Concr. Res. 41 (5) (2011) 520–532.
[23] S. Ghabezloo, Effect of the variations of clinker composition on the poroelastic properties of hardened class G cement paste, Cem. Concr. Res. 41 (8) (2011) 920–922.
[24] I. Richardson, The nature of C-S-H in hardened cements, Cem. Concr. Res. 29 (8) (1999) 1131–1147.
[25] H. Brouwers, The work of Powers and Brownyard revisited: part 1, Cem. Concr. Res. 34 (9) (2004) 1697–1716.
[26] H. Brouwers, The work of Powers and Brownyard revisited: part 2, Cem. Concr. Res. 35 (10) (2005) 1922–1936.
[27] A.J. Allen, J.J. Thomas, H.M. Jennings, Composition and density of nanoscale calcium-silicate-hydrate in cement, Nat. Mater. 6 (4) (2007) 311–316.
[28] B. Lothenbach, A. Nonat, Calcium silicate hydrates: solid and liquid phase composition, Cem. Concr. Res. 78 (2015) 57–70.
[29] H.M. Jennings, P.D. Tennis, Model for the developing microstructure in Portland cement pastes, J. Am. Ceram. Soc. 77 (12) (1994) 3161–3172.
[30] H.M. Jennings, A model for the microstructure of calcium silicate hydrate in cement paste, Cem. Concr. Res. 30 (1) (2000) 101–116.
[31] H.M. Jennings, Refinements to colloid model of C-S-H in cement: CM-II, Cem. Concr. Res. 38 (3) (2008) 275–289.
[32] S. Papatzani, K. Paine, J. Calabria-Holley, A comprehensive review of the models on the nanostructure of calcium silicate hydrates, Construct. Build Mater. 74 (2015) 219–234.
[33] J. Zhang, G.W. Scherer, Comparison of methods for arresting hydration of cement, Cem. Concr. Res. 41 (10) (2011) 1024–1036.
[34] K.K. Aligizaki, Pore Structure of Cement-based Materials: Testing, Interpretation and Requirements, CRC Press. 2005.
[35] N. Collier, J. Sharp, N. Milestone, J. Hill, I. Godfrey, K. Garbev, B. Gasharova, G. Beuchle, S. Kreisz, P. Stemmermann, The influence of water removal techniques on the composition and microstructure of hardened cement pastes, Cem. Concr. Res. 38 (6) (2008) 737–744.
[36] M.A.G. Aranda, A.G. De la Torre, L. Leon-Reina, Rietveld quantitative phase analysis of OPC clinkers, cements and hydration products, Rev. Mineral. Geochem. 74 (1) (2012) 169–209.
[37] D.L. Bish, J.E. Post, Quantitative mineralogical analysis using the Rietveld full–pattern fitting method, Am. Mineral. 78 (9-10) (1993) 932–940.
[38] B.H. Toby, R factors in Rietveld analysis: how good is good enough ? International Centre for diffraction Data Data (December 2005), 2006, 67–70.
[39] G. Le Saoût, V. Kocaba, K. Scrivener, Application of the Rietveld method to the analysis of anhydrous cement, Cem. Concr. Res. 41 (2) (2011) 133–148.
[40] M.-N. de Noirfontaine, F. Dunstetter, M. Courtial, G. Gasecki, M. Signes-Frehel, Polymorphism of tricalcium silicate, the major compound of Portland cement clinker, Cem. Concr. Res. 36 (1) (2006) 54–64.
[41] R. Snellings, A. Salze, K. Scrivener, Use of X-ray diffraction to quantify amorphous supplementary cementitious materials in anhydrous and hydrated blended cements, Cem. Concr. Res. 64 (2014) 89–98.
[42] R. Snellings, A. Bazzoni, K. Scrivener, The existence of amorphous phase in portland cements: physical factors affecting Rietveld quantitative phase analysis, Cem. Concr. Res. 59 (2014) 139–146.
[43] G.L. Saoût, T. Füllmann, V. Kocaba, K. Scrivener, Quantitative study of cementitious materials by X-ray diffraction/Rietveld analysis using an external standard, 12Th International Congress on the Chemistry of Cement., 2007,
[44] K. Scrivener, T. Füllmann, E. Gallucci, G. Walenta, E. Bermejo, Quantitative study of Portland cement hydration by X-ray diffraction/Rietveld analysis and independent methods, Cem. Concr. Res. 34 (9) (2004) 1541–1547.

[45] R. Jenkins, R. Snyder, Introduction to X-ray Powder Diffractometry, John Wiley & Sons. 1996.
[46] K. Scrivener, R. Snellings, B. Lothenbach, A Practical Guide to Microstructural Analysis of Cementitious Materials, CRC Press. 2016.
[47] Y. Suda, T. Saeki, T. Saito, Relation between chemical composition and physical properties of CSH generated from cementitious materials, J. Adv. Concr. Technol. 13 (5) (2015) 275–290.
[48] F. Nishi, Y. Takeuchi, I. Maki, Tricalcium silicate Ca_3O [SiO_4]: the monoclinic superstructure, Z. Krist. Crystalline Mater. 172 (1-4) (1985) 297–314.
[49] W. Mumme, R. Hill, G. Bushnell-Wye, E. Segnit, Rietveld crystal structure refinements, crystal chemistry and calculated powder diffraction data for the polymorphs of dicalcium silicate and related phases, Neues Jb. Mineral. Abh. 169 (3). (1995).
[50] L. Alarcon-Ruiz, G. Platret, E. Massieu, A. Ehrlacher, The use of thermal analysis in assessing the effect of temperature on a cement paste, Cem. Concr. Res. 35 (3) (2005) 609–613.
[51] V. Kocaba, Development and Evaluation of Methods to Follow Microstructural Developments of Cementitious Systems Including Slags, Ph.D. thesis. École Polytechnique Fédérale de Lausanne. 2010.
[52] K.J. Krakowiak, J.J. Thomas, S. Musso, S. James, A.-T. Akono, F.-J. Ulm, Nano-chemo-mechanical signature of conventional oil-well cement systems: effects of elevated temperature and curing time, Cem. Concr. Res. 67 (2015) 103–121.
[53] S. Diamond, Mercury porosimetry: an inappropriate method for the measurement of pore size distributions in cement-based materials, Cem. Concr. Res. 30 (10) (2000) 1517–1525.
[54] A. Muller, K. Scrivener, A. Gajewicz, P. McDonald, Use of bench-top NMR to measure the density, composition and desorption isotherm of C-S-H in cement paste, Microporous Mesoporous Mater. 178 (2013) 99–103.
[55] B. Lothenbach, T. Matschei, G. Möschner, F.P. Glasser, Thermodynamic modelling of the effect of temperature on the hydration and porosity of Portland cement, Cem. Concr. Res. 38 (1) (2008) 1–18.
[56] É. Nauleau, ÉVolution au cours du temps des propriétés physiques et mécaniques des matériaux cimentaires d'un puit géothermique basse énergie, Université Paris-Est. 2013.
[57] W. Kurdowski, Cement and Concrete Chemistry, Springer Netherlands, Dordrecht, 2014, 603–659. (Ch. Special Cements)
[58] B.Z. Dilnesa, Fe-containing Hydrates and Their Fate During Cement Hydration: Thermodynamic Data and Experimental Study, Ph.D. thesis. ÉCOLE POLYTECHNIQUE FÉDÉRALE DE LAUSANNE. 2011.
[59] M. Vespa, E. Wieland, R. Dähn, B. Lothenbach, Identification of the thermodynamically stable fe-containing phase in aged cement pastes, J. Am. Ceram. Soc. 98 (7) (2015) 2286–2294.
[60] G. Geng, D.A. Kilcoyne, c. J. Benmore, P.J.M. Monteiro, Multi-technology Investigation of the Atomic Structure of Calcium Silicate Hydrates. Multi-technology Investigation of the Atomic Structure of Calcium, 14Th International Congress on the Chemistry of Cement, 13-16 October 2015, Beijing, China, 2015.
[61] J.I. Bhatty, K.J. Reid, D. Dollimore, G.A. Gamlen, R.J. Mangabhai, P.F. Rogers, T.H. Shah, The Derivation of Kinetic Parameters in Analysis of Portland Cement for Portlandite and Carbonate by Thermogravimetry, Compositional Analysis by Thermogravimetry ASTM International. 1988.
[62] Z. Šauman, Carbonization of porous concrete and its main binding components, Cem. Concr. Res. 1 (6) (1971) 645–662.
[63] A. Morandeau, M. Thiéry, P. Dangla, Investigation of the carbonation mechanism of CH and C-S-H in terms of kinetics, microstructure changes and moisture properties, Cem. Concr. Res. 56 (2014) 153–170.
[64] J. Branch, D. Kosson, A. Garrabrants, P. He, The impact of carbonation on the microstructure and solubility of major constituents in microconcrete materials with varying alkalinities due to fly ash replacement of ordinary Portland cement, Cem. Concr. Res. 89 (2016) 297–309.
[65] T.F. Sevelsted, J. Skibsted, Carbonation of C-S-H and C-A-S-H samples studied by sup 13c, sup 27al and sup 29si MAS NMR spectroscopy, Cem. Concr. Res. 71 (2015) 56–65.
[66] J. Rivas-Mercury, P. Pena, A. de Aza, X. Turrillas, Dehydration of $Ca_3Al_2(SiO_4)$ $y(OH)_{4(3-y)}(0 < y < 0.176)$ studied by neutron thermodiffractometry, J. Eur. Ceram. Soc. 28 (9) (2008) 1737–1748.
[67] First observation of $\alpha - Ca_2[SiO_3(OH)](OH) - Ca_6[Si_2O_7][SiO_4](OH)_2$ phase transformation upon thermal treatment in air, J. Am. Ceram. Soc. 91 (1) (2008) 263–271.
[68] B. Dilnesa, E. Wieland, B. Lothenbach, R. Dähn, K. Scrivener, Fe-containing phases in hydrated cements, Cem. Concr. Res. 58 (2014) 45–55.
[69] R.F. Feldman, Factors affecting Young's modulus–porosity relation of hydrated Portland cement compacts, Cem. Concr. Res. 2 (4) (1972) 375–386.
[70] A. Bentur, R.L. Berger, J.H. Kung, N. Milestone, J. Young, Structural properties of calcium silicate pastes: II, effect of curing temperature, J. Am. Ceram. Soc. 62 (7-8) (1979) 362–366.
[71] M.B. Pinson, E. Masoero, P.A. Bonnaud, H. Manzano, Q. Ji, S. Yip, J.J. Thomas, M.Z. Bazant, K.J. Van Vliet, H.M. Jennings, Hysteresis from multiscale porosity: modeling water sorption and shrinkage in cement paste, Phys. Rev. Appl. 3 (6) (2015) 064009.
[72] H.M. Jennings, J.J. Thomas, J.S. Gevrenov, G. Constantinides, F.-J. Ulm, A multi--technique investigation of the nanoporosity of cement paste, Cem. Concr. Res. 37 (3) (2007) 329–336.
[73] A. Bentur, R.L. Berger, J.H. Kung, N. Milestone, J. Young, Structural properties of calcium silicate pastes: II, effect of curing temperature, J. Am. Ceram. Soc. 62 (7-8) (1979) 362–366.
[74] H.M. Jennings, J.J. Thomas, D. Rothstein, J.J. Chen, Cement as Porous Materials, in: F. Schüth, K.S.W. Sing, J. Weitkamp (Eds.), Handbook of Porous Solids, Wiley-VCH Verlag GmbH, Weinheim, Germany, 2008, pp. 2971–3028. Ch. 6.
[75] J.I. Escalante-Garcia, J.H. Sharp, Variation in the composition of C-S-H gel in Portland cement pastes cured at various temperatures, J. Am. Ceram. Soc. 82 (11) (1999) 3237–3241.
[76] M.C. Lewis, Heat Curing and Delayed Ettringite Formation in Concretes., Imperial College London (University of London). 1996. Ph.D. thesis
[77] I. Richardson, G. Groves, Models for the composition and structure of calcium silicate hydrate (C-S-H) gel in hardened tricalcium silicate pastes, Cem. Concr. Res. 22 (6) (1992) 1001–1010.
[78] J. Escalante-Garcia, G. Mendoza, J. Sharp, Indirect determination of the Ca/Si ratio of the CSH gel in Portland cements, Cem. Concr. Res. 29 (12) (1999) 1999–2003.
[79] A. Muller, K. Scrivener, A. Gajewicz, P.J. McDonald, Densification of C-S-H measured by 1h NMR relaxometry, J. Phys. Chem. C 117 (1) (2013) 403–412.
[80] J.J. Thomas, H.M. Jennings, A colloidal interpretation of chemical aging of the C-S-H gel and its effects on the properties of cement paste, Cem. Concr. Res. 36 (1) (2006) 30–38.
[81] X. Cong, R. Kirkpatrick, Effects of the temperature and relative humidity on the structure of C-S-H gel, Cem. Concr. Res. 25 (6) (1995) 1237–1245.
[82] I.G. Richardson, Model structures for C-(A)-S-H(I), Acta Crystallogr. Sect. B: Struct. Sci. Cryst. Eng. Mater. 70 (Pt 6) (2014) 903–923.